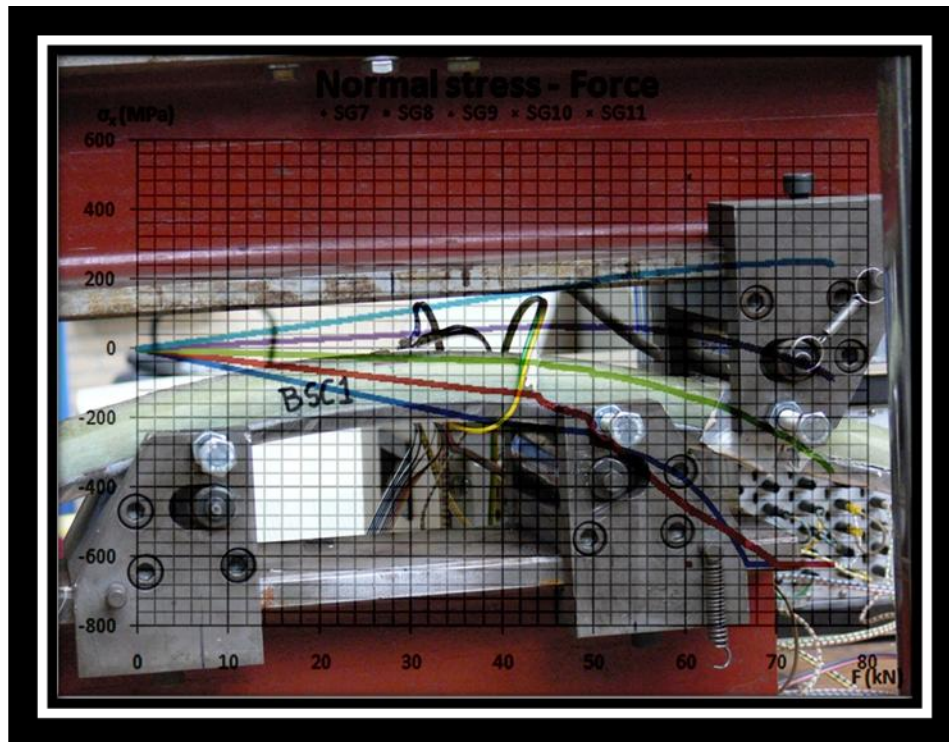


Faculty of Civil Engineering & Geosciences

Strengthening of Steel Bridges by GFRP Plates



COURSE: CT 5060 – MSc THESIS

NAME: KOUREPINIS VASILEIOS

STUDENT NUMBER: 1337297

TABLE OF CONTENTS

1. PROBLEM DESCRIPTION.....	1
1.1 Introduction.....	1
1.2 Orthotropic bridge deck.....	1
1.3 Fatigue cracks in orthotropic bridge decks	2
1.3.1 Fatigue cracks in the deck plate	2
1.3.2 Fatigue cracks in the longitudinal weld between deck plate and trough web..	6
2. FRP COMPOSITES	8
2.1 Introduction.....	8
2.2 Materials	8
2.2.1 Fibres.....	8
2.2.2 Matrix.....	11
2.2.3 Composite materials.....	14
2.2.4 Adhesives	15
2.3 Manufacturing methods	17
2.3.1 Pultrusion	18
2.3.2 Hand layup	21
2.4 Durability	23
2.4.1 General	23
2.4.2 Temperature effects.....	23
2.4.3 Moisture	24
2.4.4 UV light exposure	24
2.4.5 Alcalinity and acidity	25
2.4.6 Galvanic corrosion	25
2.4.7 Creep, stress rupture, stress corrosion.....	25
2.4.8 Fatigue.....	26
2.4.9 Impact.....	26
3. PROPOSED STRENGTHENING METHOD	27

3.1 Introduction.....	27
3.2 Configuration of proposed solution.....	27
3.3 Preliminary analytical solution.....	28
3.3.1 Case 1: Steel plate without FRP plate.....	32
3.3.2 Case 2: Steel plate with FRP plate.....	32
3.3.3 Expected stress reduction factor (SRF).....	34
4. EXPERIMENTS AND RESULTS	36
4.1 Introduction.....	36
4.2 Tensile tests on GFRP specimens	36
4.2.1 Specimen and tensile test description	36
4.2.2 Specimen failure pattern	38
4.2.3 Tensile test results.....	43
4.3. Bending tests on GFRP plates.....	47
4.3.1 Specimen and bending test description.....	47
4.3.2 Specimen failure pattern	50
4.3.3 Bending test results	54
4.4 Bending tests on steel plates reinforced by GFRP plates	63
4.4.1 Introduction.....	63
4.4.2 Specimen and bending test description.....	63
4.4.3 Test results	67
4.4.3.1 Specimens with the steel loaded in compression (BSC).....	67
4.4.3.2 Specimens with the steel loaded in tension (BST).....	86
4.5 Fatigue tests	103
4.5.1 Steel plate.....	103
4.5.1.1 Experiment description	103
4.5.1.2 Results.....	105
4.5.2 Composite plates	108
4.5.2.2 Experiment description	108
4.5.2.3 Test results	112
4.6 Creep test on FRP plate.....	119

5. MECHANICAL PROPERTIES OF GFRP LAMINATE	120
5.1 Introduction.....	120
5.2 Burn out tests.....	120
5.3 Theoretical determination of properties	121
6. FINITE ELEMENT ANALYSIS.....	139
6.1 Introduction.....	139
6.2 Creating the finite element model.....	139
6.3 FEA and experimental results comparison	143
6.4 Stress reduction factor	158
6.5 SRF improvement by material optimization	159
7. CONCLUSIONS	161

LIST OF FIGURES

Figure 1.1 Orthotropic bridge structure.....	1
Figure 1.2 Fatigue cracks in the deck plate	3
Figure 1.3 Crack propagation stages	4
Figure 1.4 Cracks in the asphalt layer, possible indicating deck plate cracks.....	5
Figure 1.5 Deck crack after the removal of the asphalt layer deck	6
Figure 1.6 Fatigue crack in the longitudinal weld between the deck plate and the trough web	7
Figure 2.1 Typical uniaxial tension stress-strain diagrams for different fibres and comparison with steel.	9
Figure 2.2 Magnified cross section of a composite material with uni-directional fibres	15
Figure 2.3 Effect of temperature on elastic modulus of polymers	16
Figure 3.1 Proposed bridged deck strengthening method using GFRP plates	27
Figure 3.2 Configuration for analytical preliminary solution	28
Figure 3.3 Single loaded trough	29
Figure 3.4 Load dispersal due to surfacing layer.....	30
Figure 3.5 Static model for a single loaded trough	30
Figure 3.6 Equivalent cross section for the composite plate	33
Figure 4.1 Tensile specimen, dimensions and geometry	37
Figure 4.2 Tensile test configuration.....	38
Figure 4.3 Specimen TP1	39
Figure 4.4 Specimen TP2	40
Figure 4.5 Specimen TP3	41
Figure 4.6 Specimen TP4	42
Figure 4.7 Specimen TP5	43
Figure 4.8 Stress – Strain diagram for specimen TP1	44
Figure 4.9 Stress – Strain diagram for specimen TP2	45
Figure 4.10 Stress – Strain diagram for specimen TP3	45
Figure 4.11 Stress – Strain diagram for specimen TP4	46
Figure 4.12 Stress – Strain diagram for specimen TP5	46
Figure 4.13 Experimental configuration -1- for the GFRP plate.....	48
Figure 4.14 Experimental configuration -2- for the GFRP plate.....	48
Figure 4.15 Four point bending configurations used.....	49
Figure 4.16 Strain gauges on the FRP plate in the mid span area	49
Figure 4.17 Failed GFRP specimen BP1 in bending.....	50

Figure 4.18 Details of failed GFRP specimen BP1 in bending	51
Figure 4.19 Details of failed GFRP specimen BP1 in bending	51
Figure 4.20 Failed GFRP specimen BP3 in bending.....	52
Figure 4.21 Details of failed GFRP specimen BP3 in bending.....	52
Figure 4.22 Failed GFRP specimen BP4 in bending.....	53
Figure 4.23 Details of failed GFRP specimen BP4 in bending.....	53
Figure 4.24 Force against vertical displacement diagram for BP1.....	55
Figure 4.25 Maximum and minimum stress against force for specimen BP1.....	56
Figure 4.26 Force against vertical displacement diagram for BP2.....	57
Figure 4.27 Force against vertical displacement diagram for BP3.....	59
Figure 4.28 Maximum and minimum stress against force for specimen BP3.....	60
Figure 4.29 Force against vertical displacement diagram for BP4.....	61
Figure 4.30 Maximum and minimum stress against force for specimen BP4.....	62
Figure 4.31 Experimental configuration -1- for the composite plate and steel in compression.....	63
Figure 4.32 Experimental configuration -2- for the composite plate and steel in compression.....	64
Figure 4.33 Experimental configuration -2- for the composite plate and steel in tension ...	64
Figure 4.34 Strain gauges on the steel plate in the mid span area.....	65
Figure 4.35 Strain gauges on the FRP plate in the mid span area.....	65
Figure 4.36 Strain gauges at the side of the steel plate on the mid span area	66
Figure 4.37 Composite plate BSC1 in bending from large deflections to failure	68
Figure 4.38 Delamination of the composite plate BSC1	69
Figure 4.39 Force against vertical displacement diagram for specimen BSC1.....	70
Figure 4.40 Minimum normal stress (located at the outer surface of the steel plate) against force diagram for specimen BSC1.....	71
Figure 4.41 Maximum normal stress (located at the outer surface of the GFRP plate) against force diagram for specimen BSC1	71
Figure 4.42 Normal stress along the side of the steel plate against force diagram for specimen BSC1	72
Figure 4.43 Normal stress distribution along the side of the steel plate for specimen BSC1	73
Figure 4.44 Failure of the composite plate BSC2	74
Figure 4.45 Force against vertical displacement diagram for specimen BSC2.....	75
Figure 4.46 Minimum normal stress (located at the outer surface of the steel plate) against force diagram for specimen BSC2.....	75
Figure 4.47 Maximum normal stress (located at the outer surface of the GFRP plate)	

against force diagram for specimen BSC2	76
Figure 4.48 Normal stress along the side of the steel plate against force diagram for specimen BSC2	77
Figure 4.49 Normal stress distribution along the side of the steel plate for specimen BSC2	77
Figure 4.50 a, b, c Failure and details of specimen BSC3.....	78
Figure 4.51 Force against vertical displacement diagram for specimen BSC3.....	79
Figure 4.52 Minimum normal stress (located at the outer surface of the steel plate) against force diagram for specimen BSC3.....	80
Figure 4.53 Maximum normal stress (located at the outer surface of the GFRP plate) against force diagram for specimen BSC3	80
Figure 4.54 Normal stress along the side of the steel plate against force diagram for specimen BSC3	81
Figure 4.55 Normal stress distribution along the side of the steel plate for specimen BSC3	81
Figure 4.56 Failure and details of specimen BSC4	82
Figure 4.57 Force against vertical displacement diagram for specimen BSC4.....	83
Figure 4.58 Maximum normal stress (located at the outer surface of the GFRP plate) against force diagram for specimen BSC4	84
Figure 4.59 Maximum normal stress (located at the outer surface of the GFRP plate) against force diagram for specimen BSC4	84
Figure 4.60 Normal stress along the side of the steel plate against force diagram for specimen BSC4	85
Figure 4.61 Normal stress distribution along the side of the steel plate for specimen BSC4	85
Figure 4.62 Composite plate BST1 in bending from large deflections to failure.	86
Figure 4.63 Failure and details of specimen BST1	87
Figure 4.64 Force against vertical displacement diagram of specimen BST1	88
Figure 4.65 Maximum normal stress (located at the outer surface of the steel plate) against force diagram of specimen BST1	88
Figure 4.66 Minimum normal stress (located at the outer surface of the GFRP plate) against force diagram for specimen BST1	89
Figure 4.67 Normal stress along the side of the steel plate against force diagram of specimen BST1.....	90
Figure 4.68 Normal stress distribution along the side of the steel plate of specimen BST1	90
Figure 4.69 Failure and details of specimen BST2	91
Figure 4.70 Force against vertical displacement diagram of specimen BST2	92

Figure 4.71 Maximum normal stress (located at the outer surface of the steel plate) against force diagram of specimen BST2	92
Figure 4.72 Minimum normal stress (located at the outer surface of the GFRP plate) against force diagram for specimen BST2.....	93
Figure 4.73 Normal stress along the side of the steel plate against force diagram of specimen BST2.....	94
Figure 4.74 Normal stress distribution along the side of the steel plate of specimen BST2	94
Figure 4.75 Failure and details of specimen BST3	95
Figure 4.76 Force against vertical displacement diagram of specimen BST3	96
Figure 4.77 Maximum normal stress (located at the outer surface of the steel plate) against force diagram of specimen BST3	96
Figure 4.78 Minimum normal stress (located at the outer surface of the GFRP plate) against force diagram for specimen BST3.....	97
Figure 4.79 Normal stress along the side of the steel plate against force diagram of specimen BST3.....	98
Figure 4.80 Normal stress distribution along the side of the steel plate of specimen BST3	98
Figure 4.81 Failure and details of specimen BST4	99
Figure 4.82 Force against vertical displacement diagram of specimen BST4	100
Figure 4.83 Maximum normal stress (located at the outer surface of the steel plate) against force diagram of specimen BST4	100
Figure 4.84 Minimum normal stress (located at the outer surface of the GFRP plate) against force diagram for specimen BST4.....	101
Figure 4.85 Normal stress along the side of the steel plate against force diagram of specimen BST4.....	102
Figure 4.86 Normal stress distribution along the side of the steel plate of specimen BST4	102
Figure 4.87 Experimental configuration for the steel plate	104
Figure 4.88 The strain gauge at the mid span area on the steel plate	105
Figure 4.89 Force range – vertical displacement at 1/4 of the supported length diagram for the steel plate	106
Figure 4.90 Maximum normal stress range $\Delta\sigma_x$ against number of cycles	107
Figure 4.91 Experimental configuration for the composite plate.....	108
Figure 4.92 Strain gauges on the steel plate in the mid span area.....	109
Figure 4.93 Strain gauges on the FRP plate in the mid span area	110
Figure 4.94 Strain gauges at the side of the steel plate on the mid span area	111
Figure 4.95 LVDT for the measurement of the displacement.....	112
Figure 4.96 Force range – vertical displacement at 1/4 of the supported length diagram for	

the composite plate (Case 1).....	113
Figure 4.97 Average minimum normal stress range $\Delta\sigma_x$ (located at the outer surface of the steel plate) against number of cycles for the composite plate (Case 1).....	113
Figure 4.98 Normal stress ranges $\Delta\sigma_x$, along the side of the steel plate, against number of cycles for the composite plate (Case 1).....	114
Figure 4.99 Average maximum normal stress range $\Delta\sigma_x$ (located at the outer surface of the GFRP plate) against number of cycles for the composite plate (Case 1).....	114
Figure 4.100 Force range – vertical displacement at 1/4 of the supported length diagram for the composite plate (Case 2).....	115
Figure 4.101 Average minimum normal stress range $\Delta\sigma_x$, located at the outer surface of the steel plate, against number of cycles for the composite plate (Case 2).....	115
Figure 4.102 Normal stress ranges $\Delta\sigma_x$, along the side of the steel plate, against number of cycles for the composite plate (Case 2).....	116
Figure 4.103 Average maximum normal stress range $\Delta\sigma_x$ (located at the outer surface of the GFRP plate) against number of cycles for the composite plate (Case 2).....	116
Figure 4.104 Stress distribution for case 1 (15.039 kN).....	117
Figure 4.105 Stress distribution for case 2 (22.5097 kN).....	118
Figure 4.106 Force and vertical displacement against time diagram for FRP plate.....	119
Figure 5.1 Reference axis for unidirectionals.....	123
Figure 5.2 Reference axis of an elementary fibre.....	124
Figure 5.3 GFRP profile for specimen BSC2.....	128
Figure 5.4 GFRP profile for specimen BSC3.....	128
Figure 5.5 GFRP profile for specimen BSC4.....	129
Figure 5.6 GFRP profile for specimen BST1.....	129
Figure 5.7 GFRP profile for specimen BST2.....	130
Figure 5.8 GFRP profile for specimen BST3.....	130
Figure 5.9 GFRP profile for specimen BST4.....	131
Figure 6.1 Solid 186 Structural solid geometry.....	140
Figure 6.2 Bilinear stress – strain diagram for steel.....	140
Figure 6.3 Finite element model.....	142
Figure 6.4 Normal stresses – force diagram for the steel plate of specimen BSC2.....	144
Figure 6.5 Normal stresses – force diagram for the GFRP plate of specimen BSC2.....	144
Figure 6.6 Error (%) – Force diagram for the minimum normal steel stresses of specimen BSC2.....	145
Figure 6.7 Error (%) – Force diagram for the maximum normal GFRP stresses of specimen BSC2.....	145
Figure 6.8 Normal stresses – force diagram for the steel plate of specimen BSC3.....	146

Figure 6.9 Normal stresses – force diagram for the GFRP plate of specimen BSC3.....	146
Figure 6.10 Error (%) – Force diagram for the minimum normal steel stresses of specimen BSC3.....	147
Figure 6.11 Error (%) – Force diagram for the maximum normal GFRP stresses of specimen BSC3	147
Figure 6.12 Normal stresses – force diagram for the steel plate of specimen BSC4	148
Figure 6.13 Normal stresses – force diagram for the GFRP plate of specimen BSC4.....	148
Figure 6.14 Error (%) – Force diagram for the minimum normal steel stresses of specimen BSC4.....	149
Figure 6.15 Error (%) – Force diagram for the maximum normal GFRP stresses of specimen BSC4	149
Figure 6.16 Normal stresses – force diagram for the steel plate of specimen BST1.....	150
Figure 6.17 Normal stresses – force diagram for the GFRP plate of specimen BST1	150
Figure 6.18 Error (%) – Force diagram for the maximum normal steel stresses of specimen BST1	151
Figure 6.19 Error (%) – Force diagram for the minimum normal GFRP stresses of specimen BST1	151
Figure 6.20 Normal stresses – force diagram for the steel plate of specimen BST2.....	152
Figure 6.21 Normal stresses – force diagram for the GFRP plate of specimen BST2.....	152
Figure 6.22 Error (%) – Force diagram for the maximum normal steel stresses of specimen BST2.....	153
Figure 6.23 Error (%) – Force diagram for the minimum normal GFRP stresses of specimen BST2.....	153
Figure 6.24 Normal stresses – force diagram for the steel plate of specimen BST3.....	154
Figure 6.25 Normal stresses – force diagram for the GFRP plate of specimen BST3.....	154
Figure 6.26 Error (%) – Force diagram for the maximum normal steel stresses of specimen BST3.....	155
Figure 6.27 Error (%) – Force diagram for the minimum normal GFRP stresses of specimen BST3.....	155
Figure 6.28 Normal stresses – force diagram for the steel plate of specimen BST4.....	156
Figure 6.29 Normal stresses – force diagram for the GFRP plate of specimen BST4.....	156
Figure 6.30 Error (%) – Force diagram for the maximum normal steel stresses of specimen BST4.....	157
Figure 6.31 Error (%) – Force diagram for the minimum normal GFRP stresses of specimen BST4.....	157

LIST OF TABLES

Table 2.1 Approximate properties of common grades of carbon fibres	10
Table 2.2 Approximate properties of common grades of glass fibres	11
Table 2.3 Approximate properties of thermosetting polymer resins	13
Table 2.4 Approximate properties of thermosetting polymer resins	17
Table 3.1 Epoxy and glass fibre properties as given by the manufacturer	28
Table 4.1 Dimensions of tensile specimens.....	37
Table 4.2 Tensile modulus of elasticity from tensile tests	46
Table 4.3 Specimen dimensions for four point bending test	50
Table 4.4 Equivalent flexural modulus of elasticity for the FRP	62
Table 4.5 Specimen dimension and configuration used.....	66
Table 5.1 Burn-out test results.....	120
Table 5.2 Volumetric fractions	121
Table 5.3 Mechanical properties of GFRP laminate of specimen TP	131
Table 5.4 Mechanical properties of GFRP laminate of specimen BP	131
Table 5.5 Mechanical properties of GFRP laminate of specimen BSC2	132
Table 5.6 Mechanical properties of GFRP laminate of specimen BSC3	133
Table 5.7 Mechanical properties of GFRP laminate of specimen BSC4	134
Table 5.8 Mechanical properties of GFRP laminate of specimen BST1	135
Table 5.9 Mechanical properties of GFRP laminate of specimen BST2	136
Table 5.10 Mechanical properties of GFRP laminate of specimen BST3.....	137
Table 5.11 Mechanical properties of GFRP laminate of specimen BST4.....	138
Table 5.12 Average Error (%)	158
Table 5.13 Stress reduction factor	159
Table 5.14 Mechanical properties of the optimized GFRP laminate	160

1. PROBLEM DESCRIPTION

1.1 Introduction

In the Netherlands there are many orthotropic steel deck bridges and most of them were built between 1960 and 1980. The design philosophy was much different then and the knowledge concerning the phenomenon of fatigue was not as extensive as it is today. This is why in this kind of bridges fatigue cracks are very commonly observed.

1.2 Orthotropic bridge deck

This type of orthotropic bridge deck is used for fixed as well as for moveable bridges and the configuration depicted in figure 1.1 is very widespread and commonly used. This type of deck is composed of four types of structural components, which are:

- The deck plate
- The longitudinal stiffener, generally closed trough profiles
- The crossbeams, also called floor beams
- The main girder

Besides those structural components a surfacing layer is applied on top of the deck plate for both corrosion protection and skid resistance purposes.

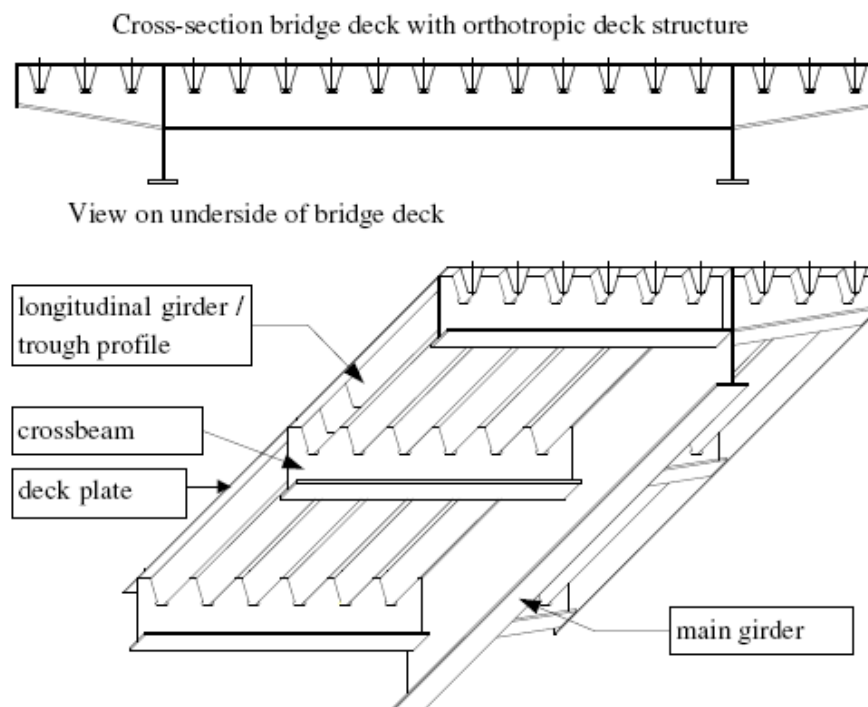


Figure 1.1 Orthotropic bridge structure

The role of the deck is to transfer the traffic loads (axle loads) directly to the longitudinal troughs. Furthermore, the deck plate acts as the top flange in the beam system of the whole deck.. A typical fixed bridge deck plate in the Netherlands has a thickness of 10 mm covered with a mastic asphaltic layer with thickness of 50 mm. On the other hand the thickness of a movable bridge deck will be 12 mm and will be covered with an epoxy layer.

In Netherlands the closed trough profile is generally used with a typical distance of 300 mm. The longitudinal troughs and the deck plate are welded together with a longitudinal weld and combined they act as a longitudinal beam system that transmits the loads to the cross beams. The deck also acts as an upper flange for the cross beams which have a typical spacing of 3 – 5 m. So, the cross beams finally transfer the deck loads the main structure of the bridge.

1.3 Fatigue cracks in orthotropic bridge decks

During the last decades fatigue cracks have appeared in the deck of bridge structures mainly due to the limited knowledge of fatigue phenomena of steel structures at the time of design and also due to the increasing traffic load. Fatigue cracks are considered to be a threat to the structure and that is why repair and renovation techniques have been used to cope with that problem. There are various methods of construction for orthotropic bridge decks and different type of details connections and therefore there are different type of fatigue cracks. More precisely they can be divided in to four categories, namely:

- Cracks in the deck plate
- Cracks in the longitudinal weld between deck plate and trough web
- Cracks in the trough splice joint
- Cracks in the connection between trough profile and crossbeam

The first two types of cracks can be observed from the cracks on the asphalt overlay, especially when the crack in the deck plate is severe and has a sufficient width. Also the first two types of cracks can endanger the safety of the bridge deck by reducing its bearing loading capacity. The mechanism of those type of cracks will be reviewed more thoroughly further on.

1.3.1 Fatigue cracks in the deck plate

In the part that the crossbeam crosses the trough girder there is a high concentration of stresses and as a result fatigue cracks are very common at that point. The troughs are continuous through the cross beam, and therefore the cross beams provide support only to the parts of the deck that is located in between the longitudinal troughs. On the other hand

the part of the deck inside of the troughs is only supported by the webs of the trough that are welded on it. Therefore the problem arises because of the concentrated loads due to the wheels of heavy vehicles which cause a local deflection of the deck plate. Thus a hogging moment appears to the connection point of the web with the deck plate and high stress concentration arises creating fatigue phenomena.

Another location that these kind of cracks appear is in the area located in between of the cross beams. Nonetheless the mechanism that causes them is actually quite different. In this case the deck plate could be modelled as a multiple span continuous beam over elastic supports and therefore there is a high stress concentration in the area of the mid span in each one of these beams causing cracks to appear.

Comparing the two aforementioned mechanisms it is easy to conclude that the stress concentration in the first one is higher than in the second one. Therefore cracks in the part that the crossbeam crosses the trough girder appear more frequently and in fact they are the most frequently observed fatigue cracks.

Both types of cracks can be seen in figure 1.2.

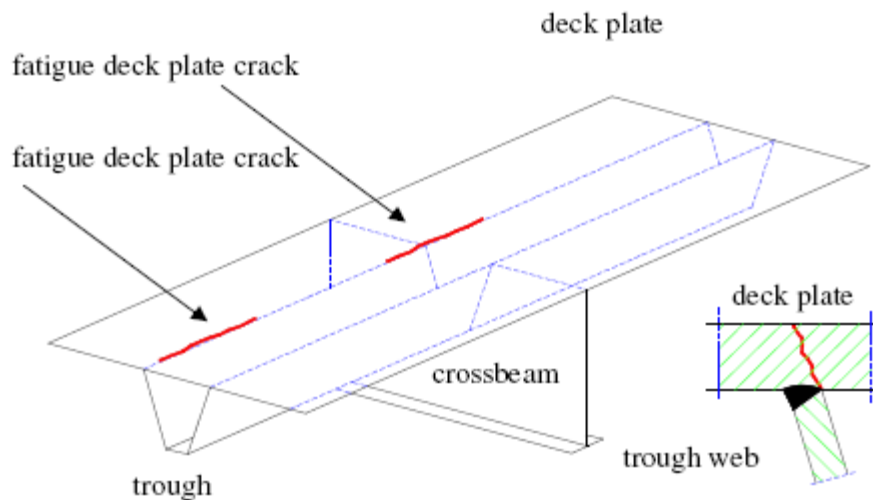


Figure 1.2 Fatigue cracks in the deck plate

Both cracks have similar propagation mechanisms. For the first type the mechanism consist of three stages:

Stage 1: The crack initiation occurs at the root of the crossbeam and the continuous close trapezoidal stiffeners.

Stage 2: The crack propagates in a vertical direction from the bottom fibres to the top of the deck.

Stage 3: After the crack has grown through the deck plate, it then grows in the longitudinal – horizontal direction.

For the second type of crack the difference consists in the fact that this is growing simultaneously in the vertical and in the horizontal direction. In other words, stage 2 and 3 happen at the same time. Both cracks have a semi-elliptical layout. Also various inspections and NDT tests (Schat, 1997-a, 1997-b, 1997-c) have shown that the length of the crack in the bottom of the deck is four times the thickness of the deck larger than the length of the crack in the top of the deck plate. The three stages described, as well as the length of the crack, can be seen in figure 1.3.

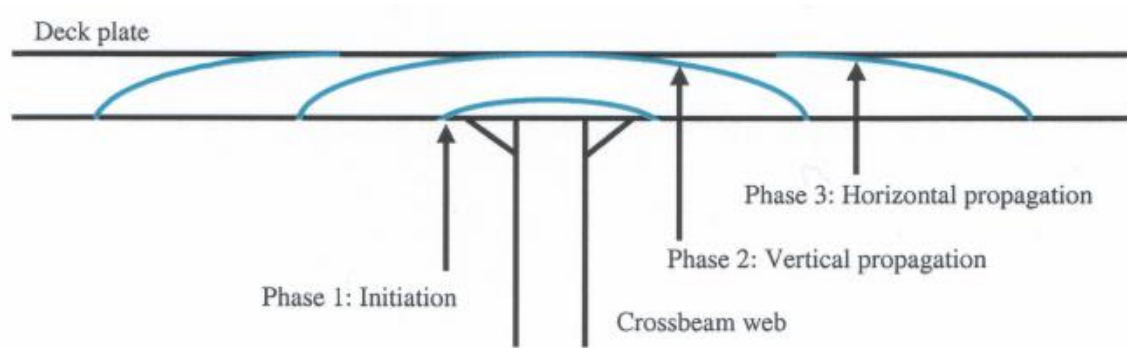


Figure 1.3 Crack propagation stages

Visual examples

Finally some visual examples of these types of cracks are presented in figures 1.4 and 1.5 and will be commented further on.



Figure 1.4 Cracks in the asphalt layer, possible indicating deck plate cracks

The crack depicted in figure 1.4 is a spider's web crack. This type of crack in combination with a relatively good condition of the rest of the asphalt layer could be an indication of fatigue crack of the deck plate. The only way to make sure is the removal of the existing asphaltic surface at the location of the cracks for a closer inspection of the deck.

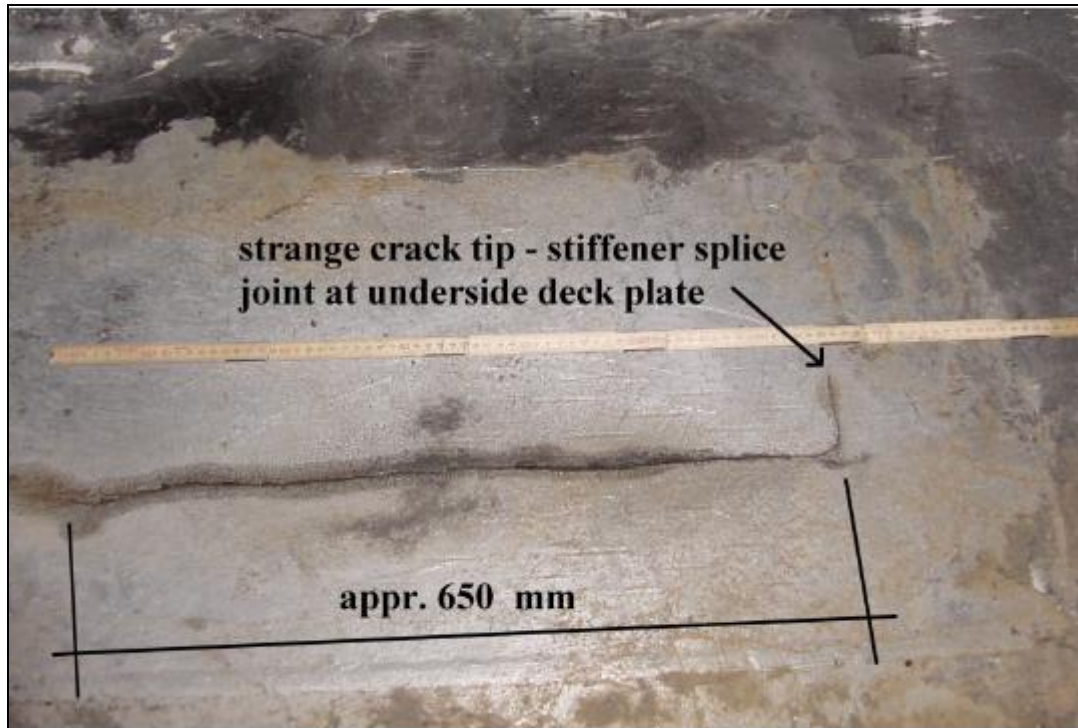


Figure 1.5 Deck crack after the removal of the asphalt layer deck

In figure 1.5 a crack in the deck plate can be seen which has been spotted after the removal of the asphalt layer in the location of a spider's web crack on the web of the Hagestein Bridge on the motorway A27 in the Netherlands. The length of the crack, as it can also be seen in the figure is of 650 mm length.

1.3.2 Fatigue cracks in the longitudinal weld between deck plate and trough web

This type of crack initiates at the root of the longitudinal weld between the trough web and the deck plate. The deck plate acts as beam with multiple supports, which are the troughs. The wheel loads applied on the part of the deck plate in between the trough webs cause a deflection of the deck plate and of the trough webs since they are welded together. That deflection causes bending moment to both the deck and the trough webs and results in high stress concentration in the longitudinal weld. The crack may initiate at any point in the longitudinal direction, except at the intersection of the crossbeam and the continuous closed trapezoidal stiffeners. The explanation for that is due to the limited bending stiffness of the trough profiles, the trough webs act as elastic supports depending on the distance from the cross beam and the point of the intersection has the minimum deformation and thus the minimum bending moment.

This type of cracks can be encountered in moveable and fixed bridges alike. The crack propagates through the weld from the inner to the outer surface of the trough web. After the crack has propagated through the web it then grows longitudinally parallel to the axis of the deck. The crack propagation rate depends on the quality and the size of the weld. Also fatigue tests have shown that the pre-weld gap between the trough web and the deck plate also affects in a negative way the fatigue behaviour. A full penetration weld shows a better fatigue behaviour than a fillet weld of 3 mm.

Visual examples

The longitudinal fatigue crack that is depicted in figure 1.6 has appeared in the deck of the Moerdijk Bridge in Netherlands.

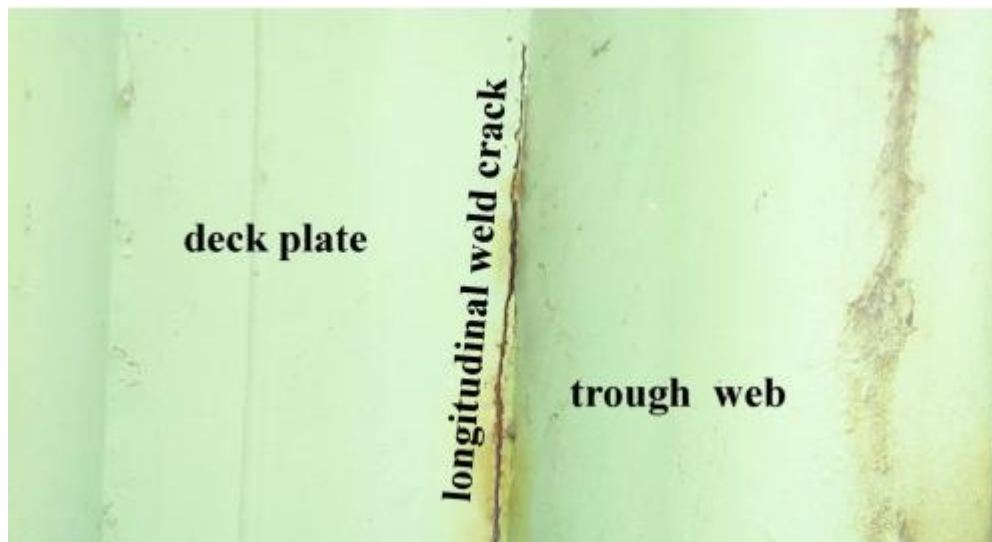


Figure 1.6 Fatigue crack in the longitudinal weld between the deck plate and the trough web

2. FRP COMPOSITES

2.1 Introduction

In much the same way that a structural engineer has knowledge of the composition of structural materials commonly used in structures such as steel, concrete, and wood, a similar working knowledge of FRP composite materials is necessary. Not only the composition, but also the method of construction is very important for the structural engineer. This includes having a qualitative knowledge of the constituent of raw materials and the processing methods used to produce the parts and how these affect the eventual mechanical and physical properties of the FRP part. The intent of this chapter is to provide with sufficient materials background to have a working knowledge of the FRP material that will be used for the strengthening of the steel bridge deck.

2.2 Materials

The main components that are used for the production of FRP composites are the fibres and the matrix. Nonetheless, when FRP are used for the strengthening of a structural system, a very important role is played by the adhesives used. Further on those three main components will be presented in detail.

2.2.1 Fibres

Fibres have a diameter in the order of 5-25 μm and constitute the primary load carrying elements (parallel to their axis) in a composite material system. Main properties of the fibres are the high tensile strength and the linear elastic behaviour to failure can be seen in figure 3.1.

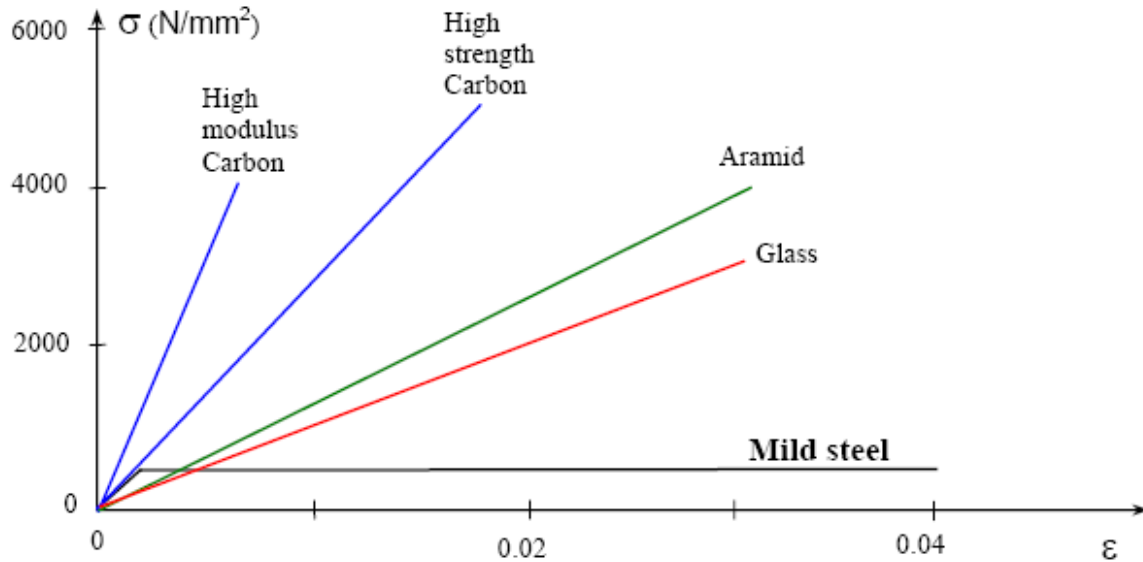


Figure 2.1 Typical uniaxial tension stress-strain diagrams for different fibres and comparison with steel.

There are three main types of fibres commonly used. Those are carbon, glass and aramid.

Carbon fibres

Carbon fibres are used in structural engineering applications today in FRP strengthening sheets and fabrics, in FRP strengthening strips and in FRP prestressing tendons. Carbon fibre is a solid semi-crystalline organic material consisting on the atomic level of planar two-dimensional arrays of carbon atoms. The two-dimensional sheet-like array is usually known as the graphitic form. Hence, the fibres are also known as graphite fibres. Carbon fibre is produced in grades known as standard modulus, intermediate modulus, high strength and ultrahigh modulus.

Carbon fibres have diameters from about 5 to 10 μm . Carbon fibre has a characteristic charcoal black colour. Due to their two-dimensional atomic structure, carbon fibres are considered to be transversely isotropic, having different properties in the longitudinal direction of the atomic array than in the transverse direction. The longitudinal axis of the fibre is parallel to the graphitic planes and gives the fibre its high longitudinal modulus and strength. Approximate properties of common grades of carbon fibers are given in table 3.1

Table 2.1 Approximate properties of common grades of carbon fibres

Grade of carbon fibre	Density (g/cm³)	Tensile modulus (GPa)	Tensile strength (MPa)	Max elongation (%)
Standard	1.7	250	3700	1.2
High strength	1.8	250	4800	1.4
High modulus	1.9	500	3000	0.5
Ultrahigh modulus	2.1	800	2400	0.2

Carbon fibre is produced at high temperatures, 1200°C to 2400°C, from three possible precursor materials: a natural cellulosic rayon textile fibre, a synthetic polyacrylonitrile (PAN) textile fibre or pitch (coal tar). Pitch-based fibres, produced as a by-product of petroleum processing, are generally lower cost than PAN- and rayon-based fibres. As the temperature of the heat treatment increases during production of the carbon fibre, the atomic structure develops more of the sheet-like planar graphitic array, giving the fibre higher longitudinal modulus.

In earlier years carbon fibres have been used primarily with epoxy resins, and suitable sizings for epoxy resin systems are readily available. Nowadays, carbon fibres are being used with vinylester and blended vinylester-polyester resins for FRP profiles and FRP strengthening strips. Sizing for carbon fibres for polyester and vinylester resins are not as common. Care must be taken when specifying a carbon fibre for use with non-epoxy resin system to ensure that the fibre is properly sized for the resin system used.

Glass fibres

Glass fibres are used in a multitude of FRP products for structural engineering, from FRP reinforcing bars for concrete, to FRP strengthening fabrics, to FRP structural profile shapes. Glass is an amorphous inorganic compound of primarily metallic oxides that is produced in fibrous form in a number of standard formulations, constituting from 50 to 70% by weight of the glass. Different grades of glass fibre are identified by letter nomenclature. A borosilicate glass known as E-glass (electrical glass) because of its high electrical resistivity is used to produce the vast majority of glass fibre used in FRP products for structural engineering. A-glass (window glass) and C-glass (corrosion resistant, also know as AR-glass of alkali-resistant glass) are used to produce specialized products for use in structural engineering. S-glass (structural or high-strength glass) is used to produce the high-performance fibres used primarily in the aerospace industry.

The diameter of an individual glass fibre of filament ranges from approximately 3 to 24 µm. For structural engineering the most commonly used fibre diameter is 17 µm. Glass fibres have a distinctive bright white colour. Glass is usually considered to be an isotropic

material. Approximate properties of commonly used grades of glass fibres are given in table 2.2. Those values are designed as a guide and should not be used in design calculations.

Table 2.2 Approximate properties of common grades of glass fibres

Grade of glass fibre	Density (g/cm ³)	Tensile modulus (GPa)	Tensile strength (MPa)	Max elongation (%)
E	2.57	72.5	3400	2.5
A	2.46	73	2760	2.5
C	2.46	74	2350	2.5
S	2.47	88	4600	3.0

Glass fibres are produced at melt temperatures of about 1400°C. Individual filaments are produced with a surface coating called a sizing that serves to protect the filaments when they are formed in a bundle or a strand. The sizing also contains coupling agents, usually silanes, that are specially formulated to enhance bonding between the glass fibre and the particular polymer resin being used when making a glass-reinforced FRP composite material. Today, most commercially available glass fibres can be obtained with sizings that are compatible with the three major thermosetting resin systems used in structural engineering: epoxy, polyester and vinylester.

Aramid fibres

Aramid fibres were first developed and patented by DuPont in 1965 under the name Kevlar and today are produced by several manufacturers under various brand names (Kevlar, Twaron, Technora). They consist of aromatic polyamide molecular chains. A combination of their relatively high price, difficulty in processing, high moisture absorption, low melting temperatures and relatively poor compressive properties have made them less attractive for FRP parts for structural engineering applications. They have a distinctive yellow colour. They are the lightest of the high performance fibres having a density of around 1.4 g/cm³. Depending on the type of aramid fibre, the fibre longitudinal tensile strength ranges from 3400 to 4100 MPa and its longitudinal tensile modulus ranges from 70 to 125 GPa.

2.2.2 Matrix

The matrix for a structural composite material is the polymer ingredient in the non-fibrous part of the FRP material that binds the fibres together and is typically a polymer resin, of thermosetting type or of thermoplastic type, with the first being the most common

one. Recent developments have resulted in matrices based on inorganic materials (e.g. cement-based). The function of the matrix is to protect the fibres against abrasion or environmental corrosion, to bind the fibres together and to distribute the load. The matrix has a strong influence on several mechanical properties of the composite, such as the transverse modulus and strength, the shear properties and the properties in compression. Physical and chemical characteristics of the matrix such as melting or curing temperature, viscosity and reactivity with fibres influence the choice of the fabrication process. Hence, proper selection of the matrix material for a composite system requires that all these factors be taken into account. Epoxy resins, polyester, vinylester and phenolics are the most common polymeric matrix materials used with high-performance reinforcing fibres. They are thermosetting polymers with good processibility and good chemical resistance. Epoxies have, in general, better mechanical properties than polyesters and vinylesters, and outstanding durability, whereas polyesters and vinylesters are cheaper. Phenolics have a better behaviour at high temperatures.

Recently, polymer-modified cement-based mortars have also become available in some applications. It is expected that these mortars will be used more and more in the near future. Also, recently polyurethane resins have been introduced to the market. A short description of the polymer resins mentioned will follow.

Epoxy resins

Epoxy resins are used in many FRP products for structural engineering applications. Most carbon fibre reinforced procured FRO strips for structural strengthening are made with epoxy resins. In addition, epoxy resin adhesives are used to bond procured FRP strips to concrete (and other materials) in the FRP strengthening process. Epoxy resins are also used extensively in FRP strengthening applications, where the epoxy resin is applied to the dry fibre sheet or fabric in the field and then cured in situ, acting as both the matrix for the FRP composite and as the adhesive to attach the FRP composite to the substrate. When applied to dry fibre sheets or fabrics, the epoxy resins are often referred to saturants. Epoxy resins have also been used to manufacture FRP tendons for prestressing concrete and FRP stay cables for bridges. They are not used extensively to produce larger FRP profiles, due to their higher costs and the difficulty entailed in processing large pultruded FRP parts

Polyester resins

Polyester resin is widely used to make pultruded FRP profiles for use in structural engineering and is also use to make some FRP rebars. They can also be used for strengthening of structures.

Vinylester resins

Developed in the last twenty years, vinylester resins have become attractive polymer resins for FRP products for structural engineering especially due to their good properties, especially their corrosion resistance and their ease of processing. Nowadays vinylester resins are used to make the majority of FRP rebars sold in the world and are also used widely in FRP pultruded profiles. They are generally replacing polyester resins in FRP products in structural engineering, due to their superior environmental durability in alkaline environments.

Phenolic resins

Phenolic resins are the oldest and most widely used thermosetting resins. However, they have only recently been used for FRP products for structural engineering, due to the difficulty of reinforcing them and curing them by condensation polymerization. They have superior fire resistance and they char and release water when burned.

Polyurethane resins

Thermosetting polyurethane resins have recently been introduced into the market as structural resins. The reason for this is that only recently have they been produced in high-density forms that can be used in resin moulding and pultrusion operations. They have high toughness and when used with glass fibres produce composites with high transverse tensile and impact strengths.

In the following table (2.3) an approximation of the properties for the thermosetting polymer resins can be found.

Table 2.3 Approximate properties of thermosetting polymer resins

Polymer resins	Density (g/cm³)	Tensile modulus (GPa)	Tensile strength (MPa)	Max elongation (%)
Polyester	1.2	4.0	65	2.5
Epoxy	1.2	3.0	90	8.0
Vinylester	1.12	3.5	82	6.0
Phenolic	1.24	2.5	40	1.8
Polyurethane	varies	2.9	71	5.9

2.2.3 Composite materials

Advanced composites as strengthening materials consist of a large number of small, continuous, directionalized, non-metallic fibres with advanced characteristics, bundled in the matrix as depicted in figure 2.2. Depending on the type of fibre they are referred to as CFRP (carbon fibre based), GFRP (glass fibre based) or AFRP (aramid fibre based). When different types of fibres are used, the material is called “hybrid”. Typically, the volume fraction of fibres in advanced composites equals about 50-70% for strips and about 25-35% for sheets. Given also that the elastic modulus of fibres is much higher than that of the matrix, it becomes clear that the fibres are the principal stress bearing components, while the matrix transfers stresses among fibres and protects them.

Basic mechanical properties of composites may be estimated if the properties of the constituent materials (fibres, matrix) and their volume fractions are known. Details about the micromechanics of composite materials are not considered here. However, for the simple, yet quite common, case of unidirectional fibres, one may apply the “rule of mixtures” simplification as follows:

For the modulus of elasticity:

$$E_{FRP} \approx E_{fib} V_{fib} + E_m V_m$$

And for the tensile strength:

$$f_{FRP} \approx f_{fib} V_{fib} + f_m V_m$$

where:

E_{FRP} = modulus of elasticity of the fibre-reinforced material in fibre direction

E_{fib} = modulus of elasticity of the fibres

E_m = modulus of elasticity of the matrix

V_{fib} = volume fraction of the fibres

V_m = volume fraction of the matrix = 1- V_{fib}

f_f = tensile strength of the fibre-reinforced material in fibre direction

f_{fib} = tensile strength of the fibres

f_m = tensile strength of the matrix

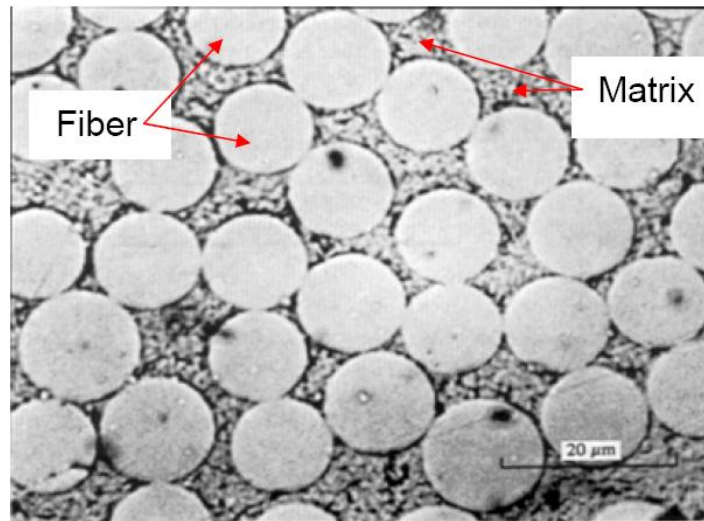


Figure 2.2 Magnified cross section of a composite material with uni-directional fibres

It should be noted that since $E_{\text{fib}}/E_m \gg 1$ and $f_{\text{fib}}/f_m \gg 1$, the above equations are approximately valid even if the second terms in the right parts are omitted. In case of prefabricated strips the material properties based on the total cross sectional area can be used in calculations and are usually supplied by the manufacturer. In case of in-situ resin impregnated systems, however, the final composite material thickness and with that the fibre volume fraction is uncertain and may vary. For this reason the properties of the total system (fibres and matrix) and the actual thickness should be provided based on experimental testing. Note that manufacturers sometimes supply the material properties for the bare fibres. In this case a property reduction factor should apply, to be provided by the supplier of the strengthening system.

2.2.4 Adhesives

The purpose of the adhesive is to provide a shear load path between the substrate (concrete or masonry) and the composite material, so that full composite action may develop. The most common type of structural adhesives is epoxy, which is the result of mixing an epoxy resin (polymer) with a hardener. Other types of adhesives may be based on inorganic materials (mainly cement-based). Depending on the application demands, the adhesive may contain fillers, softening inclusions, toughening additives and others.

When using epoxy adhesives there are two different time concepts that need to be taken into consideration. The first is the pot life and the second is the open time. Pot life represents the time one can work with the adhesive after mixing the resin and the hardener before it starts to harden in the mixture vessel. For an epoxy adhesive, it may vary between a few seconds up to several years. Open time is the time that one can have at his/her

disposal after the adhesive has been applied to the adherents and before they are joined together.

Another important parameter to consider is the glass transition temperature, T_g . Most synthetic adhesives are based on polymeric materials, and as such they exhibit properties that are characteristic for polymers. Polymers change from relatively hard, elastic, glass-like to relatively rubbery materials at a certain temperature (Fig. 2.3). This temperature level is defined as glass transition temperature, and is different for different polymers.

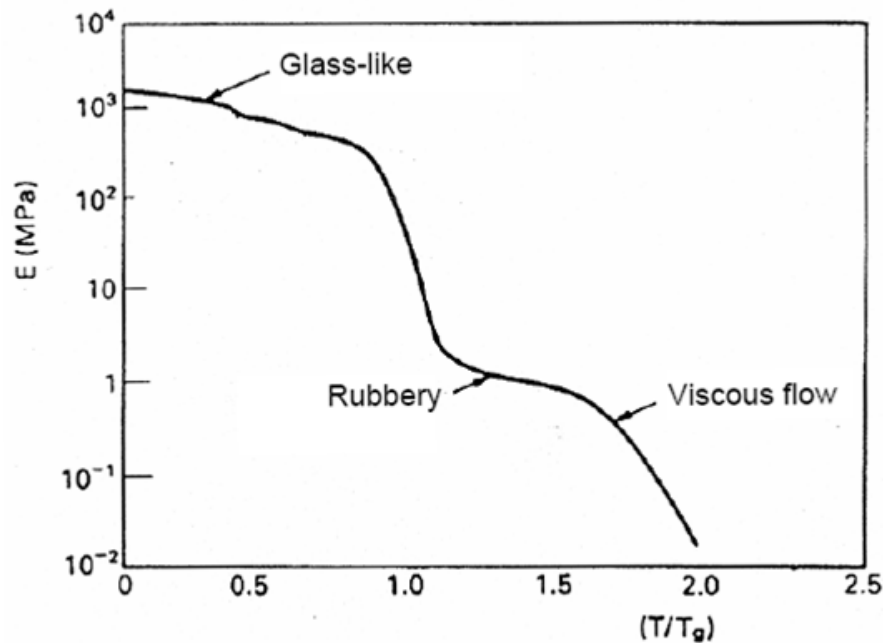


Figure 2.3 Effect of temperature on elastic modulus of polymers

Typical properties for cold cured epoxy adhesives used in civil engineering applications are given in Table 2.4 (*fib* 2001). For the sake of comparison, the same table provides information for concrete and mild steel too.

Table 2.4 Approximate properties of thermosetting polymer resins

Property (at 20°C)	Epoxy adhesive	Concrete	Mild steel
Density (kg/m ³)	1100 – 1700	2350	7800
Elastic modulus (GPa)	0.5 - 20	20 – 50	205
Shear modulus (GPa)	0.2 – 8	8 - 21	80
Poisson's ration	0.3 – 0.4	0.2	0.3
Tensile strength (MPa)	9 – 30	1 – 4	200 – 600
Shear strength (MPa)	10 – 30	2 – 5	200 – 600
Compressive strength (MPa)	55 – 110	25 – 150	200 – 600
Tensile strength at break (%)	0.5 – 5	0.015	25
Approximate fracture energy (Jm ⁻²)	200 – 1000	100	10 ⁵ – 10 ⁶
Coefficient of thermal expansion (10 ⁻⁶ /°C)	25 – 100	11 – 13	10 – 15
Water absorption: 7 days -25 °C (% w/w)	0.1 - 3	5	0
Glass transition temperature (°C)	50 – 80	-	-

Alternative materials to epoxies may be of the inorganic binder type. These materials are based on cement in combination with other binders (e.g. fly ash, silica fume, metakaolin), additives (e.g. polymers) and fine aggregates. In this case the adhesive also plays the role of the matrix in the composite material, hence it must be designed such that compatibility with the fibres will be maximized. General requirements for inorganic binders are high shear (that is tensile) strength, suitable consistency, low shrinkage and creep and good workability.

2.3 Manufacturing methods

Two main manufacturing methods are used to produce FRP composite material products for use in structural engineering. The one method is an automated industrialized process, developed in the early 1950s, called pultrusion, in which the FRP products are produced in a factory and shipped to the construction site for fabrication and installation or erection. The other method is a manual method, known as hand layup, or wet layup, in which the FRP product is manufactured in situ at the construction site at the time it is installed. It is the original method used to produce fibre-reinforced polymer composites and dates back to the development of FRP materials in the 1940s. However, as described below, the hand-layup method as it used in structural engineering is significantly different from the one used in the rest of the composites industry.

The pultrusion process is used to manufacturer FRP reinforcing bars, FRP strengthening strips, and FRP profiles and is the most cost-competitive method for producing high-quality FRP parts for use in structural engineering. The hand-layup method is used to manufacture and install dry fibre-reinforced polymer composites and dates back

to the development of FRP materials in the 1940s. However, the hand-layup method as it is used in structural engineering is significantly different from that used in the rest of the composites industry.

The pultrusion process is used to manufacture FRP reinforcing bars, FRP strengthening strips, and FRP profiles and is the most cost-competitive method for producing high quality FRP parts for use in structural engineering. The hand-layup method is used to manufacture and install dry fibre strengthening sheets and fabrics and is also very cost competitive, as it is particularly easy to use in the field. Other methods that have been used to produce specialized FRP products for use in structural engineering, such as filament winding and resin transfer moulding, will not be discussed since code based design guides for use of these products in structural engineering are either not available or are insufficiently developed at this time.

2.3.1 Pultrusion

Pultrusion is an automated and continuous process used to produce FRP parts from raw materials. When making a pultruded part, there is a great flexibility in the shape, thickness variation and size of the part cross section, but the cross section must remain constant along its length. Modifications to the common pultrusion process have been developed for non constant cross sections or for producing curved parts. It must be noted however that these are non routine variants of the pultrusion process.

To produce FRP parts for structural engineering, dry fibres impregnated with a low-viscosity liquid thermosetting polymer resin are guided into a heated chrome plated steel die, where they are cured to form the desired FRP part. The FRP is cured as the material is pulled through the die by a pulling apparatus. After exiting the die and extending past the pullers, the part is cut to length by a diamond blade cutoff saw. The rate of production of a pultruded part depends on the size of the part. Also, as the surface area of the cross section increases, a greater amount of force is needed to overcome the frictional forces to pull the part through the die.

The raw materials that are used in the pultrusion process can be broadly viewed as breaking down into two main systems which are the fibre system and the resin system. The fibre system contains all the dry reinforcements that are pulled into the resin system for wetting out prior to entering the die. The resin system refers to the mix of ingredients that is used to saturate the fibres. The resin system is typically premixed in large batches, usually 200 litres drums, in a mixing room in a pultrusion plant before it is brought to the pultrusion line and pumped or poured into the resin bath.

Fibre system for pultrusion

The fibre system used in an FRO pultruded part can consist of different types and architectures of fibre materials. The raw fibre is processed and supplied either in strand form on a spool and known as roving or tow, or in broad goods form on a roll and known as mat, fabric, veil or tissue.

Glass and carbon fibre are currently used to reinforce most FRP pultruded parts for structural engineering applications. A very small amount of aramid fibre is used in pultrusion. Glass fibre is used in pultruded profiles due to its low cost. Carbon fibre is used in FRP strengthening strips due to its high modulus.

Glass fibre rovings

Individual continuous glass filaments are bundled, generally without a twist, into multifilament strands known as rovings that are used in the pultrusion process either as is or in fabrics produced from rovings. In the pultrusion process, the rovings are aligned along the direction of the pultruded part, which is known as the machine direction. In structural design, this direction typically coincides with the longitudinal axis of the FRP bar, strips, beam, or column. Consequently, the rovings provide the pultruded part with the majority of its axial and flexural strength and stiffness. For parts requiring only high longitudinal strength and stiffness, such as FRP reinforcing bars of thin FRP strengthening strips, high percentage of rovings on the order of 50 to 60% of the total volume of the FRP composite are used. However, such parts have low transverse strength and stiffness in a pultruded part, fibre mats and fabrics are used in addition to the rovings.

Glass fibre mats - Continuous filament mat (CFM)

This is the second most widely employed glass fibre product used in the pultrusion industry. CFM is used to provide transverse strength and stiffness in platelike parts or portions of parts. CFMs consist of random, swirled, indefinitely long continuous glass fibre filaments held together by a resin soluble polymeric binder.

Glass fibre fabrics

Since unidirectional rovings give the pultruded composite reinforcement in its longitudinal direction and the continuous stand mats give reinforcement in all in plane directions equally, the range of mechanical properties of the pultruded composite consistent of only rovings and mats is limited. To obtain a greater range of properties and to “tailor” the layup of the pultruded composite to yield specific structural properties, fabric reinforcements can be used in which fibres are oriented in specific directions and at specific

volume percentages to the pultrusion axis. This design approach, in which multiaxial plies (or layers) are used, is routine in the hand layup technique. However multiaxial fabrics have been used successfully in pultrusion only in the recent years and nowadays they are only used in very special pultruded parts, as their costs can be considerably more than that of the mats.

Carbon fibre tows

Carbon fibre strands called tows can be used in the pultrusion process and have been used since the 1970s to pultruded small specialized items such as archery arrow and solid rods. However, they have not generally been used to produce pultruded profiles for structural engineering, due to their high cost relative to glass fibre roving.

Resin system for pultrusion

The three main thermosetting resins used in the pultrusion process are unsaturated polyesters, unsaturated vinylesters and epoxies. To each of these base resins supplementary constituents are added to cause the polymerization to occur, to modify the processing variables, and to tailor the properties of the final FRP pultruded part. The additional constituents that are added can be broadly grouped into three main categories:

Polymerization agents, which are known as either catalysts or curing agents, or even hardeners, depending on the resin type being used.

Fillers, which are sometimes called extenders.

Additives are also known as modifiers or process aids.

Polymerisation agents

Unsaturated polyester and vinylester resins that react with a styrene monomer are catalyzed with organic peroxides. The peroxide is used to “kick-off” or initiate the curing reaction and is heat-activated by the die so that the resin does not begin to gel and cure in the resin bath.

Fillers

Inorganic particulate fillers are used to fill or extend the base polymer resin used for pultrusion for three primary reasons, and these are to improve processing dynamics, to reduce cost, and to alter cured part properties.

Additives

The third group of constituents that are added to the resin mix are those used to assist in the processing or to modify the properties of the cured FRP part. There are many reasons to use the various types of additives and these are:

Prevent the FRP part from sticking to the die interior.

Remove entrained air from the resin mix

Give different colours to the finished parts of FRP

Protect the resin in the cured part from the effects of sunlight

Retard flame spread in the cured FRP part.

Prevent shrinkage cracking in the interior of thick parts and at the surface of thin parts.

Improve the bond between the fibres and the resin.

It must be noted however that all of these additives can influence both the physical and mechanical properties of the FRP part since they all affect the resin chemistry.

2.3.2 Hand layup

Hand layup is the term given to the manual method of constructing an FRP composite part by laying up, or rather, putting down, successive layers of fibres and impregnating them with a liquid polymer resin which then cures to form a solid FRP composite element. The solid part takes the form and shape of the mould or surface to which it is applied. The method is also known as laminating or wet layup or simply layup and is used to make laminates or panels of FRP composites. The hand layup method is probably the oldest method of producing FRO parts and is used to make a variety of FRP products. The method is deceptively simple, and producing a high quality FRP part using the method requires a significant degree of skill and good quality control.

It is important that the FRP composite that it is applied by hand layup onto the surface of an existing structural element needs to be firmly adhered to, or be firmly in contact with, the surface in order to perform its strengthening function. Herein lies the difficulty in using the hand layup method in structural engineering. Not only is the method being used to produce the FRP strengthening element, but it is being used to create the interface between the FRP element and the existing structural element. This interface is in and of itself a vital part of the FRP strengthening system.

In the hand layup system it is crucial to select the fibre and resin systems very carefully, such that both the adhesive function and the wetting-out function of the resin are present. Since the adhesive properties of the resin system will depend on the surface to which it is being bonded and the method of application, well tested combination of fibres

and resins and application method should be used only in structural engineering applications.

When used in structural engineering, the hand layup method is typically used in its most elementary form, with the resin impregnated fibres being cured at ambient temperatures without the use of externally applied pressure or high temperature. In this case, the FRP composite laminate is formed directly on the structural element to be strengthened, such as a beam or a column, and cured in place, in much the same way that reinforced concrete is cured in place.

Fibre system for hand layup

Two primary types of fibre systems are used when the hand layup method is used for FRP strengthening: unidirectional tow sheets and uni- or multidirectional woven or stitched fabrics. Carbon and E-glass are the most commonly used fibre types. However, some manufacturers do supply aramid fibre fabrics and also hybrid fibre fabrics. AR-glass fibre fabrics can be obtained for corrosive environments.

Carbon fibre tow sheets

The term tow sheet is used to describe a wide, dry carbon fibre product in which individual carbon tows, usually 12K tows, are aligned parallel to each other and held in place by an open weave glass fiber scrim cloth and epoxy soluble adhesive. The scrim cloth is oriented at a $\pm 45^\circ$ angle to the tow fibre. It is called a sheet, to differentiate it from a fabric, because it is very thin and is not woven or stitched.

Carbon and glass fiber fabrics

The other large family of fibre products used for FRP strengthening applications are of the woven or stitched fabric type. These fabrics are similar to those used in pultrusion applications. However, they are typically supplied with a predominantly 0° or a unidirectional fibre system. Bidirectional fabrics with fibres that are usually balanced in 0° and 90° orientations are also available and can be used in cases in which bidirectional strengthening is desired, such as walls or two way slabs.

Resin system for hand layup

Epoxy resins are used almost exclusively for structural hand layup for FRP strengthening applications. This is due largely to their superior adhesive properties and their low shrinkage when cured relative to polyester and vinylester resins that are used extensively in the industrial hand-layup method. Epoxy resins are reasonably easy to mix in

the field, typically requiring the mixing of one large amount, the epoxy resin, together with another large amount, the curing agent. This is very different from polyester and vinylester resins, which require very small percentages (often less than 1%) of catalysts and processing aids to be added at the time of mixing to process the resin. In addition, the properties of the epoxy are not as highly dependent on the mix ratios as polyester and vinylester resins, which can be affected significantly by small amounts of additive or catalyst.

As already mentioned, the condition of the surface to which the FRP strengthening system is applied in the hand layup method is very important. When the FRP strengthening system is applied to a reinforced concrete member, for example, the surface of the concrete needs to be smoothed to a specific profile, sandblasted, and cleaned. If the concrete is damaged, for instance due to corrosion, it must first be repaired. Protrusions must be ground down. The surface must be dried and a primer must be applied to seal the concrete. Thereafter, a putty is used to fill holes and cracks. After the FRP layers have been applied, a protective coating is usually applied as the last coat. An architectural finish can also be applied over the strengthening system if desired. These details must be specified by the structural engineer in the project specifications and should not be left to the FRP system installed as a performance item.

2.4 Durability

2.4.1 General

This chapter provides a brief overview of the durability of FRP-based strengthening systems with regard to a number of factors, namely:

- Temperature effects
- Moisture
- Ultraviolet light exposure
- Alkalinity and acidity
- Galvanic corrosion
- Creep, stress rupture, stress corrosion
- Fatigue
- Impact

2.4.2 Temperature effects

High temperatures, in the order of 60-80 °C, cause a dramatic degradation of properties in resins (matrix material in FRPs, adhesive at the FRP-substrate interface). Much higher temperatures, such as those developed during fire, result in complete resin

decomposition; hence FRPs during fire cannot carry any stresses. The decomposition of glass, carbon and aramid fibres starts at about 1000 oC, 650 oC and 200 oC, respectively. Experimental results have shown that CFRP jackets suffer substantial strength reduction at temperatures exceeding approximately 260 oC. Hence, an FRP strengthening system without special fire protection measures should be considered as ineffective during (and after) fire. Fire protection may be provided using either standard mortar plastering (with a minimum thickness of at least 40 mm, according to the JSCE 2001 guidelines), or special mortars or gypsum-based boards.

2.4.3 Moisture

FRP materials are, in general, highly resistant to moisture. Occasionally, extremely prolonged exposure to water (either fresh or salt) may cause problems with some fibre/resin combinations. The resin matrix absorbs water, which causes a slight reduction in strength and the glass transition temperature. However, most structural adhesives (high quality epoxy resins) are extremely resistant to moisture (Blaschko et al. 1998). As far as the fibres are concerned, the high susceptibility of aramid to moisture deserves special attention; carbon fibres are practically unaffected, whereas glass fibres have an intermediate behaviour.

At this point it is worth pointing out that full jacketing with FRP provides a moisture/vapor/air barrier which increases the longevity of members by protecting them from harsh conditions (e.g. chlorides, chemicals). On the hand, in case of poor concrete conditions, the encapsulation is at risk if the member is exposed to extreme climate cycling and/or excessive moisture. Applications of FRP to a structural member that is at risk of water pooling should not involve fully encapsulating the concrete. Good internal and surface concrete conditions, proper surface preparation, adequate concrete substrate exposure and proper application of an adequate FRP system may substantially reduce this risk.

2.4.4 UV light exposure

UV light affects the chemical bonds in polymers and causes surface discoloration and surface micro-cracking. Such degradation may affect only the matrix near the surface exposed to UV, as well as some types of fibres, such as aramid (Ahmad and Plecnik 1989); carbon and glass fibres are practically unaffected by UV. Anti-UV protection may be provided by surface coatings or special acrylic or polyurethane – based paints.

2.4.5 Alkalinity and acidity

The performance of the FRP strengthening over time in an alkaline or acidic environment will depend on both matrix and the reinforcing fibre. Carbon fibres are resistant to alkali and acid environment, glass fibres can degrade and aramid displays an intermediate behaviour. However, a properly applied resin matrix will isolate and protect the fibres and postpone the deterioration. Nevertheless RC structures located in high alkalinity combined with high moisture or relative humidity environments should be strengthened using carbon fibres.

2.4.6 Galvanic corrosion

The contact of carbon fibres with steel may lead to galvanic corrosion, a problem which is not of concern in the case of glass or aramid fibres.

2.4.7 Creep, stress rupture, stress corrosion

In general, creep strains in composite materials loaded parallel to the fibres are very low. CFRP does not creep, the creep of GFRP is negligible, but that of AFRP cannot be neglected. Hence, the creep behaviour of CFRP - or GFRP - plated RC members is governed primarily by the compressive creep of concrete. As AFRP creeps itself, long-term deformations increase considerably in the case of AFRP-strengthened elements. However, it should be born in mind that in (the very common) case when FRP strengthening systems are designed for additional loads (beyond the permanent ones), creep is not of concern.

Another important issue regarding time-effects is the poor behaviour of GFRP under sustained loading. Glass fibres exhibit premature tensile rupture under sustained stress, a phenomenon called stress rupture. Hence the tensile strength of GFRP drops to very low values (as low as 20%) when the material carries permanent tension.

Stress occurs when the atmosphere or ambient environment is of a corrosive nature but not sufficiently so that corrosion would occur without the addition of stress. This phenomenon is time, stress level, environment, matrix and fibre related. Failure is deemed to be premature since the FRP fails at a stress level below its ultimate. Carbon fibre are relatively unaffected by stress corrosion at stress levels up to 80% of ultimate. Glass and aramid fibres are susceptible to stress corrosion. The quality of the resin has a significant effect on time to failure and the sustainable stress levels. In general, the following order of fibres and resins gives increasing vulnerability either to stress rupture or to stress corrosion: carbon-epoxy, aramid-vinylester, glass-polyester. We may also state that, in general, given the stress rupture of GFRP and the relatively poor creep behaviour of AFRP, it is

recommended that when the externally bonded reinforcement is to carry considerable sustained load, composites with carbon fibres should be the designer's first choice.

2.4.8 Fatigue

In general, the fatigue behaviour of unidirectional fibre composites is excellent, especially when carbon fibres are used, in which case the fatigue strength of FRP is even higher than that of the steel rebars (e.g. Kaiser 1989, During 1993, Barnes and Mays 1999).

2.4.9 Impact

The strength of composites under impact loading is highest when aramid fibres are used (hence the use of these materials in bridge columns that may suffer impact loading due to vehicle collision) and lowest in the case of carbon fibres. Glass gives intermediate results.

3. PROPOSED STRENGTHENING METHOD

3.1 Introduction

As it has already been mentioned before, the solution that it is proposed to alleviate the steel stresses is the application of a GFRP plate. In this chapter the GFRP will be treated as a linear elastic isotropic material. A steel plate will be reinforced with a GFRP plate and a preliminary linearly elastic solution will take place in order to obtain an estimation of the stress reduction factor (SRF) of the steel stresses.

3.2 Configuration of proposed solution

The proposed solution for strengthening steel bridge decks is by applying a layer of FRP with glass fibres on the steel deck. The GFRP layer will be applied using the hand lay-up method which is described in section 2.3.2. This is a solution that has never been used before. Many materials have been used such as steel, high performance concrete and even timber, but never GFRP. The reason for that is that GFRP has a rather low modulus of elasticity when compared to the modulus of elasticity of steel. Also another factor is that only recently these kinds of materials have started being used in the field of civil engineering, thus the experience is limited.

The configuration that is going to be used is depicted in figure 3.1

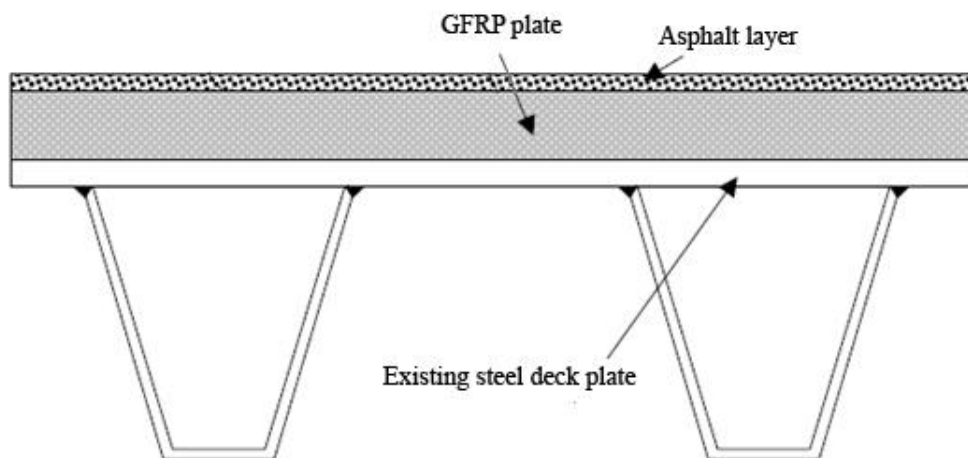


Figure 3.1 Proposed bridged deck strengthening method using GFRP plates

As it can be seen in figure 3.1 on top of the GFRP layer an asphalt layer will be applied. The problem with that is that the asphalt layer will have a very high temperature at the time that it is poured on the GFRP layer and it could damage it. Nevertheless, the

producer of the material reassured that this is not an issue. Finally the information for the GFRP straight from the manufacturing company is:

HSK300 Laminate

The laminate is build up with Woven Roving 300 g/m². For a better wetting of the laminate each layer is separated with a CSM mat of approximately 300 g/m². The matrix used is a standard Bisphenol A epoxy resin with an aliphatic amine curing agent including some additives.

The properties of the matrix (epoxy) and the glass fibres that are going to be needed for the analysis are the modulus of elasticity (E), Poisson's ratio (ν) and the density (ρ). All these properties were provided by the manufacturer and can be found in the following table.

Table 3.1 Epoxy and glass fibre properties as given by the manufacturer

	E (GPa)	ρ (g/cm³)	ν
Glass fibres	73	2.5	0.23
Epoxy	3.4	1.15	0.36

3.3 Preliminary analytical solution

At this point a linear elastic solution will take place. In order for this to be done, three things must be determined:

The static model that is going to be used

The load that will be applied

The mechanical properties of the materials used

The dimensions and properties of the FRP layer

Static model

The static model that is going to be used will be a simply supported beam loaded by two point loads as depicted in figure 3.2. The reason for choosing this model is due to the fact that the same configuration is going to be used for the four point bending test.

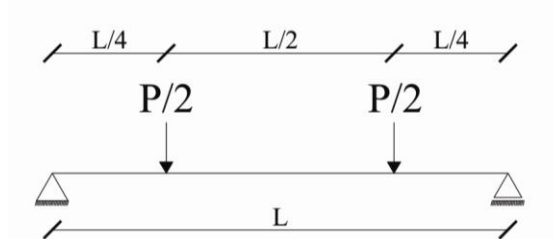


Figure 3.2 Configuration for analytical preliminary solution

Therefore the chosen length of the steel plate will be 400 mm while the cross section will have a thickness of 12 mm and a width of 100 mm.

Load

Since we are interested in strengthening the deck for the case of fatigue loads, the corresponding load models from the Eurocode will be used. There are five fatigue load models in the Eurocode. However, the most commonly used model is fatigue model 3 and this is what we are going to use as well. Nonetheless, the model is not a bridge deck, but just a specimen with dimensions much smaller than a bridge deck. Therefore the idea is to apply a load that will generate the same moment on the specimen as the moment that will be generated from the fatigue load model 3 of the Eurocode.

The strengthening of the deck refers to a trough bridge deck. The typical dimensions of a trough can be seen in figure 3.3.

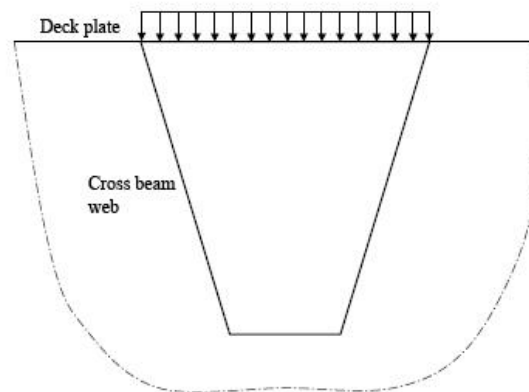


Figure 3.3 Single loaded trough

For this case, the load that is going to be used is from one tyre of the vehicle of fatigue load model 3. The dimensions of the tyre are 400mm x 400mm. The axle load is 120 kN and therefore the load on each tyre is 60 kN. Thus, corresponding uniform distributed load per metre of the tyre is:

$$q = \frac{60 \text{ kN}}{0.4 \text{ m}} = 150 \text{ kN / m}$$

However there is also one parameter that has to be taken into consideration and this is the load dispersal due to the surfacing layer of the deck. On fixed bridges it is usually

used a 50 mm thick mastic asphalt surfacing layer. On moveable bridges common practice is a thin epoxy layer of 8 mm of thickness. The worst case scenario is the moveable bridge which has the thinnest surfacing layer and therefore the lowest load dispersal. Also, although a typical steel deck has a thickness of 10mm, a thickness of 12 mm will be chosen in order to be in agreement with the test specimens.

The load due to the load dispersal (fig 3.4) will be:

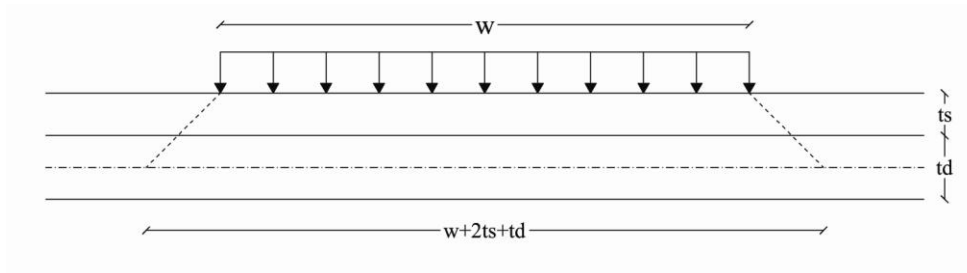


Figure 3.4 Load dispersal due to surfacing layer

$$q' = \frac{w}{w + 2t_s + t_d} q = \frac{400}{400 + 2 \times 8 + 12} \times 150 \text{ kN/m} = 140.19 \text{ kN/m} \approx 140 \text{ kN/m}$$

The legs of a typical trough (3.3) are welded on the deck at distance between each led of 300 mm. The area of the deck located in between the trough's legs, can be modelled as a double fixed beam (fig 3.5).

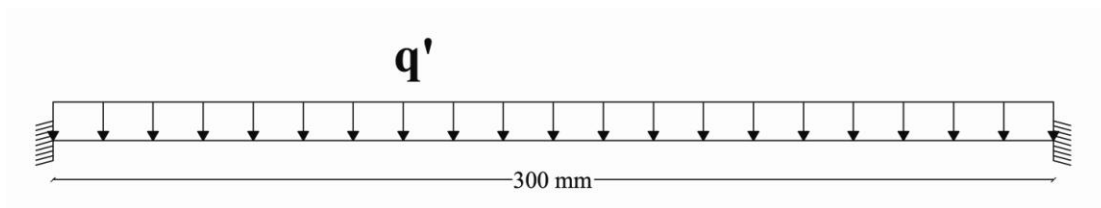


Figure 3.5 Static model for a single loaded trough

The maximum hogging moment is located at the supports of the beam and it is:

$$M_{hog} = \frac{q'l^2}{12} = \frac{140 \times 0.3^2}{12} = 1.05 \text{ kNm}$$

The maximum sagging moment is located at the mid span:

$$M_{sag} = \frac{q'l^2}{24} = \frac{140 \times 0.3^2}{24} = 0.525 \text{ kNm}$$

At this point, the load P is not necessary to be evaluated, since what we are interested in are the stresses that develop in the steel cross section. For that purpose the moment is all that is necessary.

Mechanical properties

The only mechanical property that is needed for the static, linear elastic solution is the modulus of elasticity. That is of course of both materials are going to be considered as linear elastic isotropic. This is true for the steel, but not for the FRP. However since is just a preliminary solution, it is safe to assume that FRP is isotropic as well. Later, for the FEM analysis, the FRP layer will be considered as orthotropic and its properties will be evaluated more accurately. For the time being, the modulus of elasticity of the laminate can be evaluated by the simple law of mixtures. For that the volumetric percentage must be known.

It is known that the FRP laminate is fabricated using the hand layup method. More details such as the additives used and the exact method are not known since it is the privacy of the company not to reveal more information that necessary. Nonetheless knowing the manufacturing method, it is safe to assume a fibre volumetric percentage of 30%. Thus the modulus of elasticity based on the law of mixtures is:

$$E_c = E_f \cdot V_f + E_m \cdot V_m = 0.3/2 \cdot 73 + 0.7 \cdot 3.4 = 15.05 \text{ GPa}$$

The reason for taking only 15% of the fibres in consideration, is due to the fact that the direction of the fibres of the woven layers have a 0° /90° direction and therefore at the longitudinal direction only 50% of the fibres are activated.

For the steel the modulus of elasticity is known and it is $E_s = 200 \text{ GPa}$.

Now that all the elements that are needed for the analysis are known, we can precede. Firstly the stresses that develop in the un-strengthened steel plate must be evaluated. Secondly, the stresses in the steel plate that is strengthened with the use of the GFRP layer, first loaded with the point loads in a way that a sagging moment develops and then in a way that a hogging moment develops.

3.3.1 Case 1: Steel plate without FRP plate

This is the case that corresponds to the un-strengthened steel deck. The length of the steel plate is 400 mm, while the cross section is of 100 mm width and has a thickness of 12mm.

$$\text{Therefore, the moment of inertia is: } I_s = \frac{t_s^3 \times b_s}{12} = \frac{12^3 \times 100}{12} = 14400 \text{ mm}^4$$

Normal stresses in the mid span area (l/2) due to maximum sagging moment

The maximum and the minimum normal stresses have the same absolute value due to symmetry. Therefore the normal stresses due to the maximum sagging moment are:

$$\sigma_{x.\max} = \frac{M_{\text{sag}} y}{I_s} = \frac{525000 \text{ Nmm} \times 6 \text{ mm}}{14400 \text{ mm}^4} = 218.75 \text{ MPa} = -\sigma_{x.\min}$$

Normal stresses in the mid span area (l/2) due to maximum hogging moment

Same as before the normal stresses due to the maximum hogging moment are:

$$\sigma_{x.\min} = \frac{M_{\text{hog}} y}{I_s} = \frac{-1050000 \text{ Nmm} \times 6 \text{ mm}}{14400 \text{ mm}^4} = -437.5 \text{ MPa} = -\sigma_{x.\max}$$

The stress found with absolute value of 437.5 MPa is not a realistic value, since the yielding stress value is 355 MPa. However just for this analysis and with the purpose of finding the stress reduction factor, this value will be accepted.

3.3.2 Case 2: Steel plate with FRP plate

In this case the steel plate is reinforced by a GFRP plate. The modulus of elasticity has been already determined and it is $E_c=15.05 \text{ GPa}$. The only thing that needs to be determined is the cross section of the FRP plate. The width and the length are the same as for the steel plate. However the thickness steel needs to be determined. Assuming that each layer has a thickness of 0.4 mm, which is a typical value, and 39 layers, then the thickness of the entire GFRP laminate would be 15.6 mm thick.

In order to perform the calculations 100% composite behaviour was assumed. The two plates are glued together due to the epoxy and previous experience has shown that this is a very accurate assumption. Furthermore it is expected that the neutral axis is located in

the steel plate due to the fact that the steel plate is much stiffer than the GFRP laminate and all the calculations to follow will take place having that in mind. The stresses in the steel will be calculated with the method of the equivalent cross section (fig. 3.6).

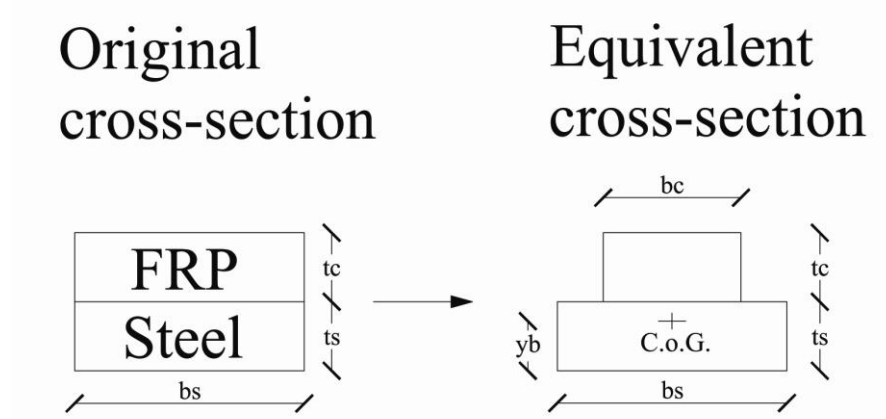


Figure 3.6 Equivalent cross section for the composite plate

The modulus of elasticity is E_s for the steel and E_c for the FRP

The modified width of the FRP plate will be:

$$b_c = \frac{E_c}{E_s} b_s = \frac{15.05}{200} 100 = 7.525 \text{ mm} \approx 7.53 \text{ mm}$$

The moment of inertia for the steel (I_s) and the GFRP cross section (I_c) are:

$$I_s = 14400 \text{ mm}^3 \text{ and } I_c = \frac{b_c \cdot t_c^3}{12} = \frac{7.53 \times 15.6^3}{12} = 2382.25 \text{ mm}^3$$

Then, the centre of gravity for the equivalent cross section is:

$$\begin{aligned} \bar{y}_b &= \frac{A_s \bar{y}_{s,b} + A_c \bar{y}_{c,b}}{A_s + A_c} = \frac{b_s \cdot t_s \cdot (t_s / 2) + b_c \cdot t_c \cdot (t_s + t_c / 2)}{b_s \cdot t_s + b_c \cdot t_c} \Rightarrow \\ \bar{y}_b &= \frac{100 \times 12 \times (12 / 2) + 7.53 \times 15.6 \times (12 + 15.6 / 2)}{100 \times 12 + 7.53 \times 15.6} = 7.23 \text{ mm} \end{aligned}$$

The moment of inertia of the equivalent cross section based on Steiner's rule is:

$$\begin{aligned} I &= I_s + A_s a_s^2 + I_c + A_c a_c^2 = I_s + b_s \cdot t_s \cdot \bar{y}_b - t_s / 2^2 + I_c + b_c \cdot t_c \cdot t_s + t_c / 2 - \bar{y}_b^2 \Rightarrow \\ I &= 14400 + 100 \cdot 12 \cdot 7.23 - 12 / 2^2 + 2382.25 + 7.53 \cdot 15.6 \cdot 12 + 15.6 / 2 - 7.23^2 \Rightarrow \\ I &= 37158.25 \text{ mm}^4 \end{aligned}$$

Normal stresses in the mid span area (l/2) due to maximum sagging moment

The maximum and the minimum normal stresses have the same absolute value due to symmetry. Therefore the normal stresses due to the maximum sagging moment are:

$$\sigma_{x,\max} = \frac{M_{\text{sag}} \cdot y}{I} = \frac{525000 \text{ Nmm} \times 7.23 \text{ mm}}{37158.25 \text{ mm}^4} = 102.15 \text{ MPa}$$

Normal stresses in the mid span area (l/2) due to maximum hogging moment

Same as before the normal stresses due to the maximum hogging moment are:

$$\sigma_{x,\min} = \frac{M_{\text{hog}} \cdot y}{I_s} = \frac{-1050000 \text{ Nmm} \times 7.23 \text{ mm}}{37158.25 \text{ mm}^4} = -204.30 \text{ MPa}$$

3.3.3 Expected stress reduction factor (SRF)

The stress reduction factor based on the stresses evaluated in paragraphs 3.3.1 and 3.3.2 is going to be evaluated:

$$SRF = \frac{\sigma_x \text{ in steel plate (un-strengthened steel plate)}}{\sigma_x \text{ in steel plate (strengthened plate)}}$$

Since the material is assumed to be linear elastic and isotropic the SRF is going to be the same in the case of hogging and sagging moment alike. Thus:

$$SRF = \frac{218.75}{102.15} = 2.14$$

or

$$SRF = \frac{218.75 - 102.15}{218.75} \cdot 100 = 53.3\%$$

This value of the SRF is actually not very impressive. However, according to the company that manufactures the material the cost is very low compared to the current solutions. Besides that GFRP has excellent fatigue properties and other qualities that will be discussed later on this thesis. Furthermore if the stress reduction factor that this solution has to offer is

sufficient, then the fact that it is a cheap solution and has excellent fatigue properties might be enough to be consider a good alternative.

In the following chapters the experiments that were made will be presented in order to see the actual behaviour of the material and evaluate the actual SRF.

4. EXPERIMENTS AND RESULTS

4.1 Introduction

FRP in general is a very unique type of material and one that is very difficult to determine its exact properties accurately. Their properties are determined not only by the materials used, but also greatly on the manufacturing process that will be chosen. Having that in mind and taking also into consideration the fact that the applications of this type of material is very limited in the field of civil engineering, it becomes apparent that thorough testing must be performed prior to actual application on steel bridge decks. There were

- Tensile tests on GFRP specimens
- Bending tests on GFRP plates
- Bending tests on steel plates reinforced by GFRP plates
- Fatigue tests on steel plates reinforced by GFRP plates
- Creep test on GFRP plate

The description of each test performed along with the results will be presented in the following paragraphs.

4.2 Tensile tests on GFRP specimens

The tensile test is probably the most fundamental test. Through the results obtained from this type of test, the behaviour of the material will be determined. If it is linear elastic, at least for the first part of the loading process, then the modulus of elasticity for tension, which is the same for compression, will be determined and later on it will be compared against the theoretical value that will be determined in the fourth chapter.

4.2.1 Specimen and tensile test description

Five specimens were tested in tension in order to specify the modulus of elasticity with accuracy. The specimens were made based on the ASTM standards. The dimensions and the geometry of the specimen can be seen in figure 4.1. As it can be seen the specimen consists of the main plate and four tabs, two at each side. The purpose of the tabs is to reinforce the area at which the specimen is going to be clamped. Furthermore, the tabs help to avoid stress concentration on the main part of the specimen due to clamping. Also their have tapered edges for smooth transition to the gage.

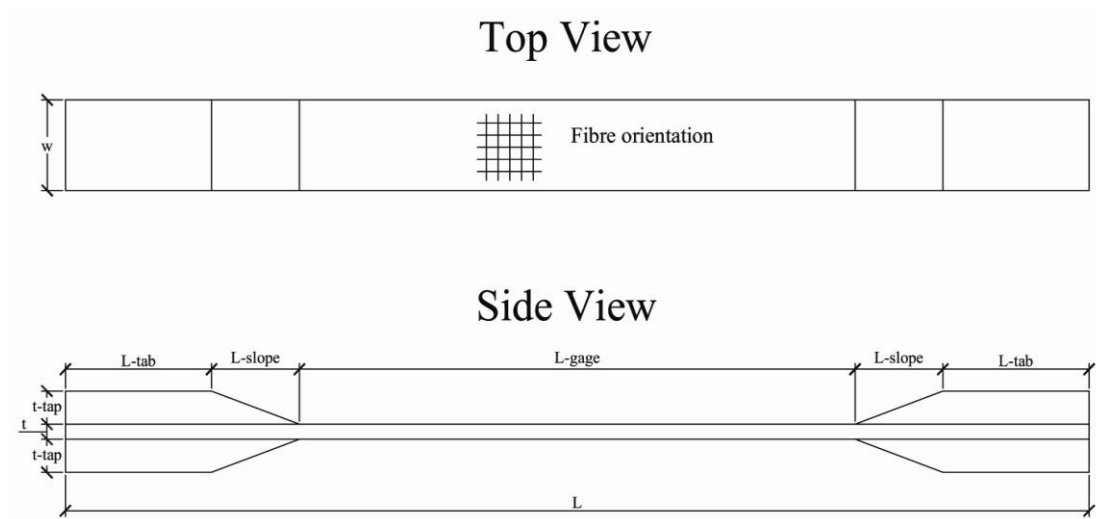


Figure 4.1 Tensile specimen, dimensions and geometry

All the tensile specimens, except for the tabs, originate from the same GFRP plate. This means that the thickness of all the specimens is somehow constant. Nonetheless, the exact dimensions of all the specimens can be found in table 4.1. The dimensions of tabs are not mentioned due to the fact that the edges of the specimens ($2t_{\text{tab}}+t$) were grinded down to a total of 27 mm in order to fit in the clamps. Also it was made sure that the top and the bottom tab of an edge (fig 4.1) had the same thickness after the grinding process. Furthermore in all the specimens the tapered portion of the tabs had an angle of approximately 20° .

Table 4.1 Dimensions of tensile specimens

Specimen	L (cm)	L_{gage} (cm)	Strain gauges area		Minimum area	
			Width (mm)	Thickness (mm)	Width (mm)	Thickness (mm)
TP1	35	18.7	30.12	5.77	29.32	5.69
TP2	35	18.6	29.99	5.88	29.67	5.74
TP3	33.5	18.7	31.30	5.93	30.45	5.84
TP4	34.85	18.65	28.72	6.06	28.24	6.05
TP5	35	19.1	31.30	5.82	31.20	5.82

The loading was parallel to the fibre plane. Two strain gauges were placed on the specimen parallel to the fibre plain. The specimen was clamped at the upper and lower edge. To avoid fibre cracks in the clamped area of the specimen, aluminium plates were attached on the tabs of the specimen. The aluminium plates had a thickness of 0.5 mm and

TP1

Specimen TP1 was the first one tested in the series of five specimens. As it can be seen in figure 4.3 a, the failure took place at the point where the tapered portion of the tab ends and the gage starts. Although one might think that there was a stress concentration at this point, this is not the case. This exact spot is the one at which the specimen has its smallest cross-section (table 4.1) and the failure at that point was predicted even before the actual testing.

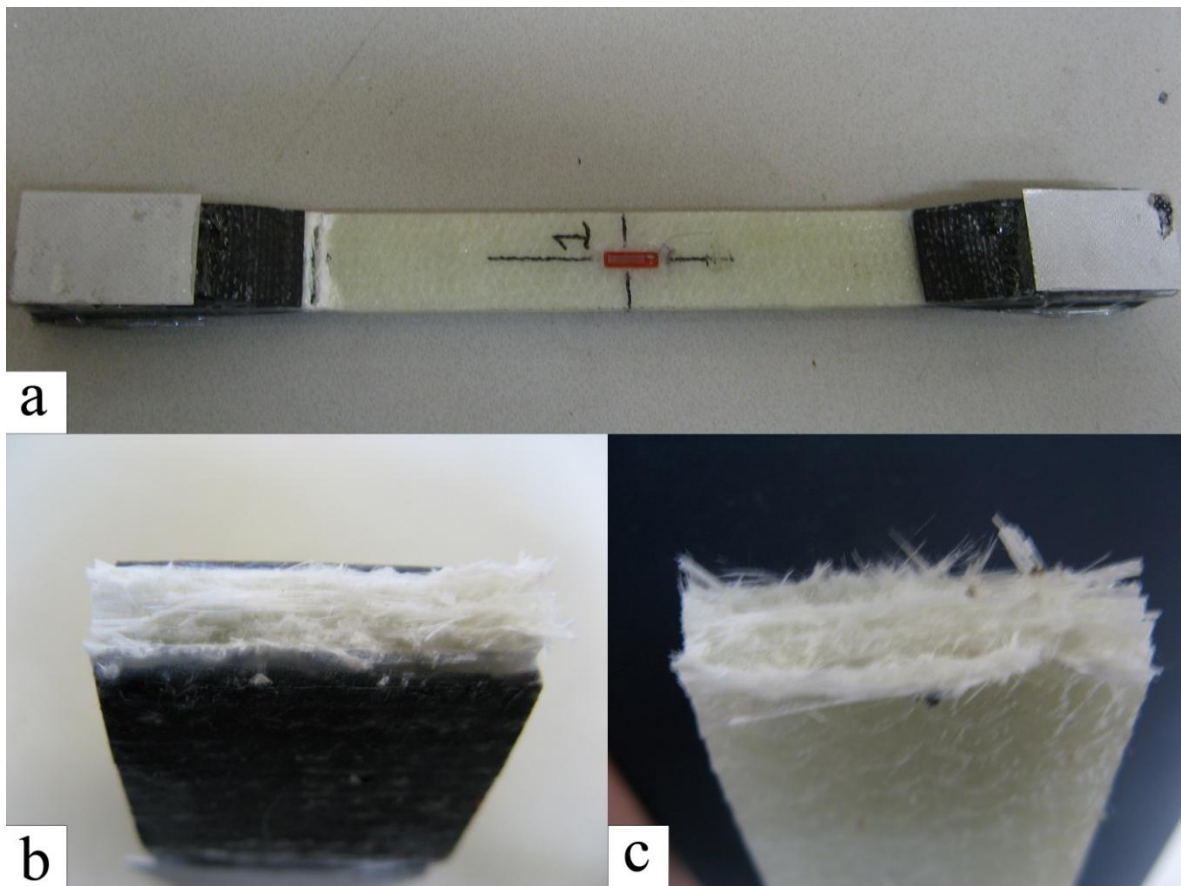


Figure 4.3 Specimen TP1

TP2

In figure 4.4 the cracked specimen is depicted. It failed at about the same position as the TP1 specimen, but as before that was the position of the minimum cross section (table 4.1) and therefore the failure was not due to stress concentration because of the tabs. However it must be noted it was observed that the tabs at the transition point from the taper to the gage weren't firmly attached.

Furthermore the main part of the specimen was somehow warped round the longitudinal axis. However it didn't seem to affect the measuring obtained

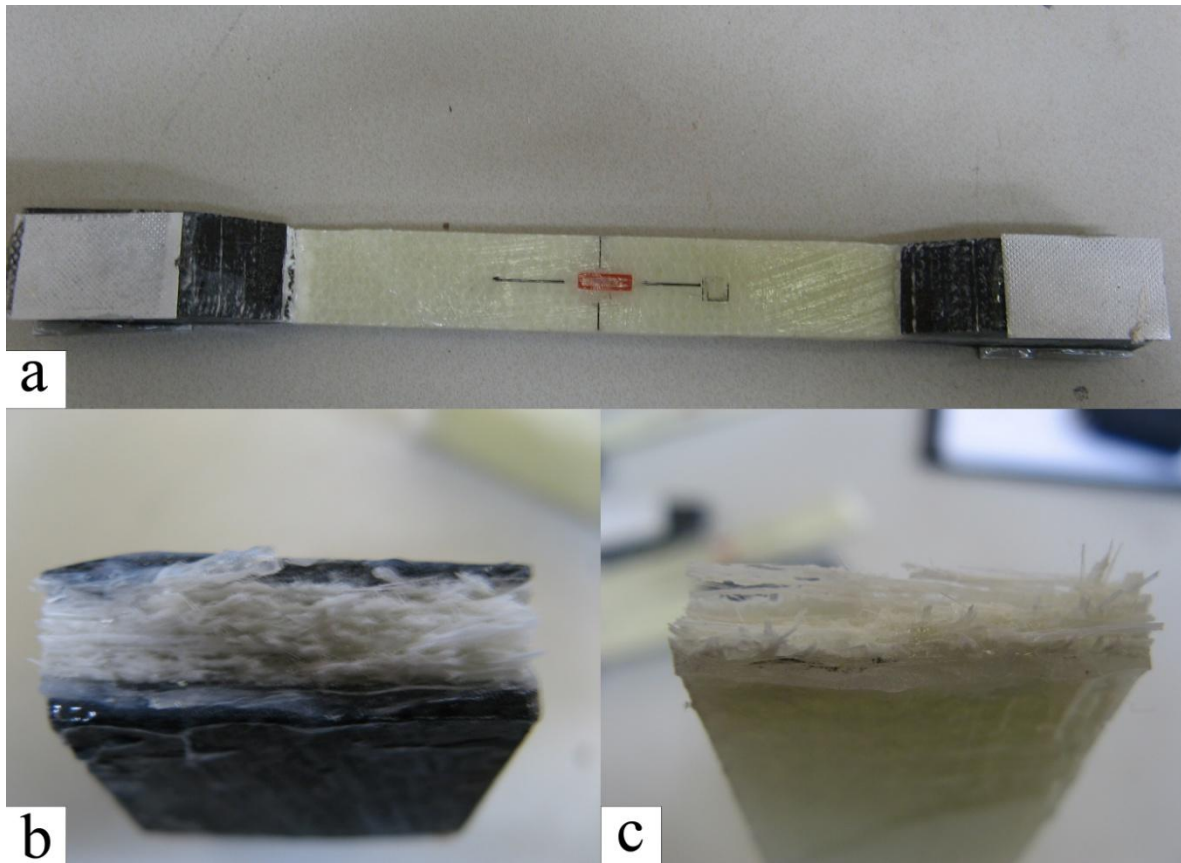


Figure 4.4 Specimen TP2

TP3

The TP3 specimen developed an initial curvature during clamping that was neutralized during loading. Fortunately the strain gauges were reset before the clamping process and the measuring were in agreement between the two strain gauges.

The failed specimen can be seen in figure 4.5. Again the crack is near the transition point from the tapered tabs to the gage. Once again the minimum cross section is located at the same point (table 4.1).

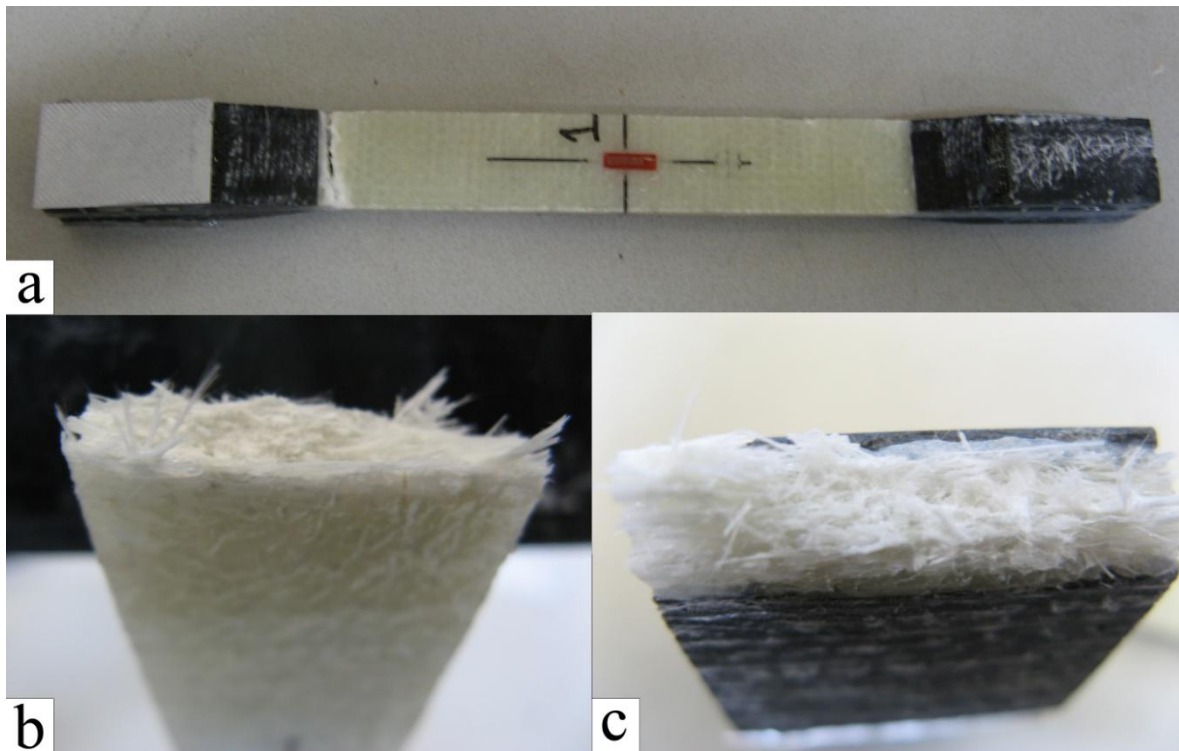


Figure 4.5 Specimen TP3

TP4

Specimen TP4 didn't seem to have any initial faults. As the previous specimen before it, the specimen broke close to the transition point where the minimum cross section was located. It must be also noted that all the previous specimens failed towards the upper clamp. Just to make sure that this was not a rule and just odds, we chose to place the specimen with the minimum cross section facing the lower clamp, where it failed. The failed specimen is depicted in figure 4.6.

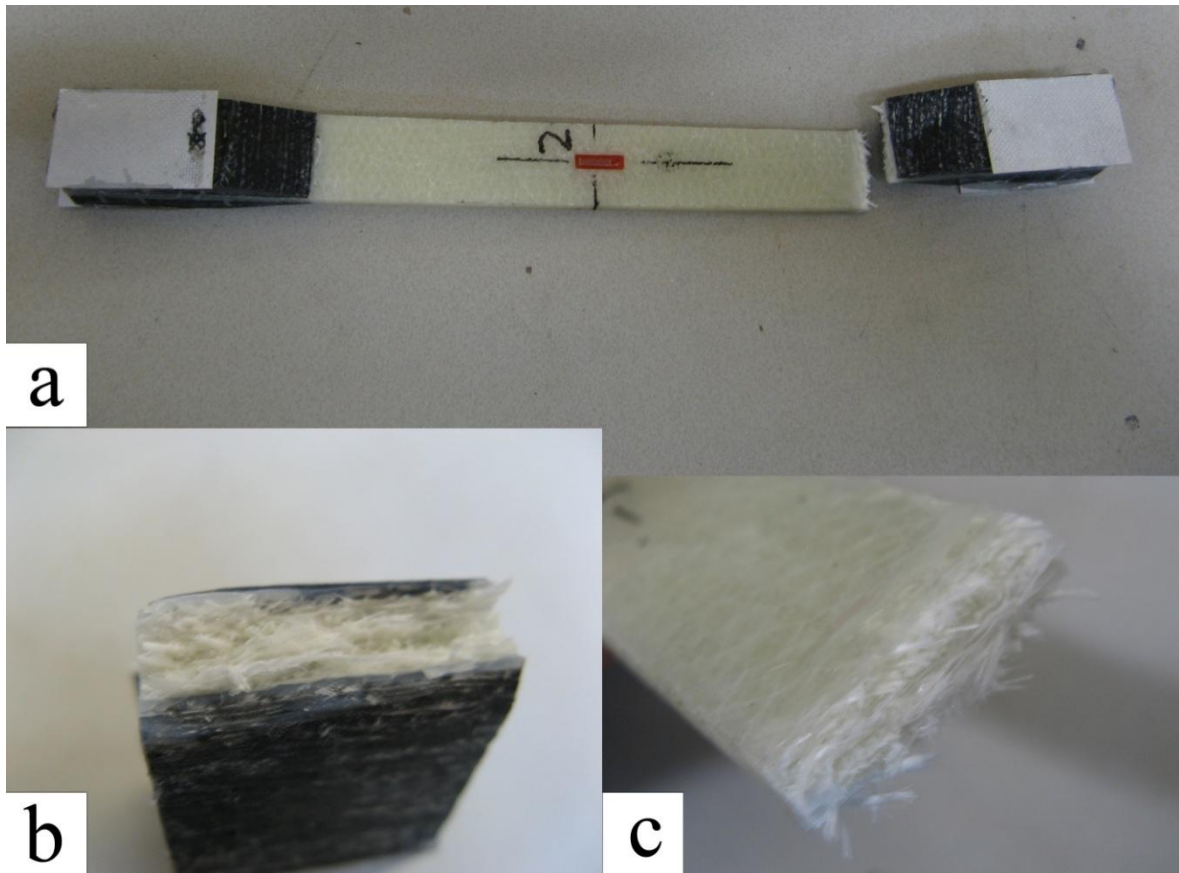


Figure 4.6 Specimen TP4

TP5

Specimen TP5 had the same imperfection, as far as the tabs are concerned, as the TP2 specimen. The tabs were not firmly attached close to the transition point and that flaw was more evident than in TP2. This would explain why the failure of the specimen occurred between the tabs (fig 4.7 c). This and the fact that, that position was the one with the smallest cross section.

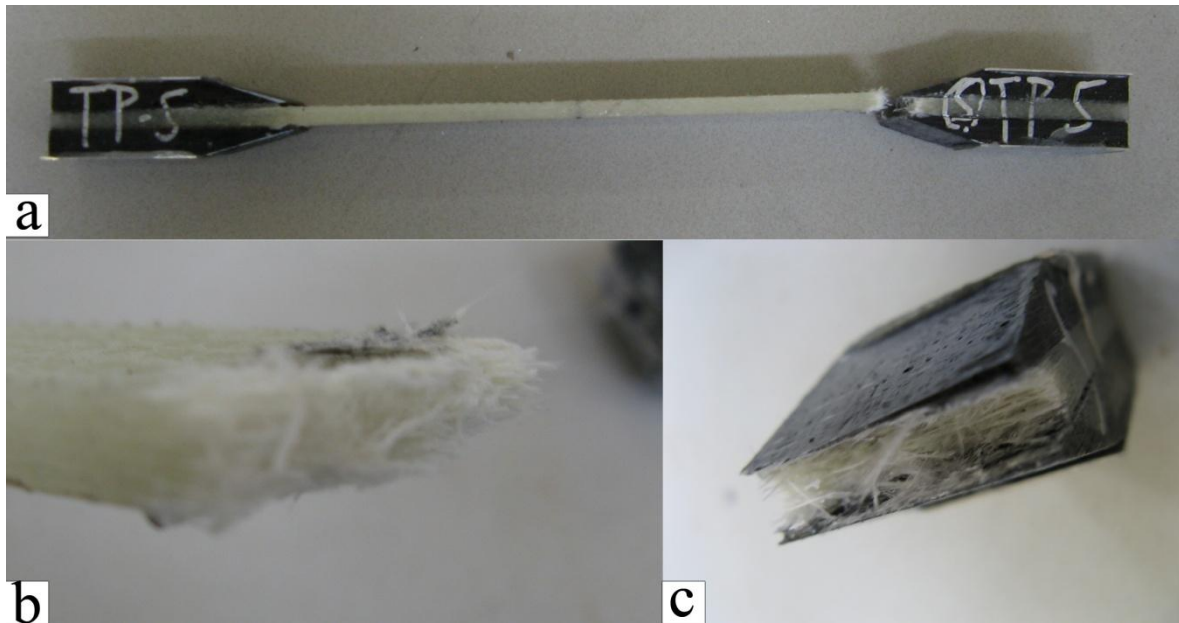


Figure 4.7 Specimen TP5

4.2.3 Tensile test results

In this paragraph the experimental results from the five tensile tests will be presented. In order to find the modulus of elasticity the stress strain diagrams have been drawn. The strain was obtained by the measurements of the strain gauges and the stress was found by the applied force divided by the cross-sectional area of each specimen at the position where the strain gauges were applied. It must be noted that the stressed uses is the average of the values measured for the strain from the two strain gauges. The stress strain diagrams for each specimen are depicted in figures 4.8 to 4.12.

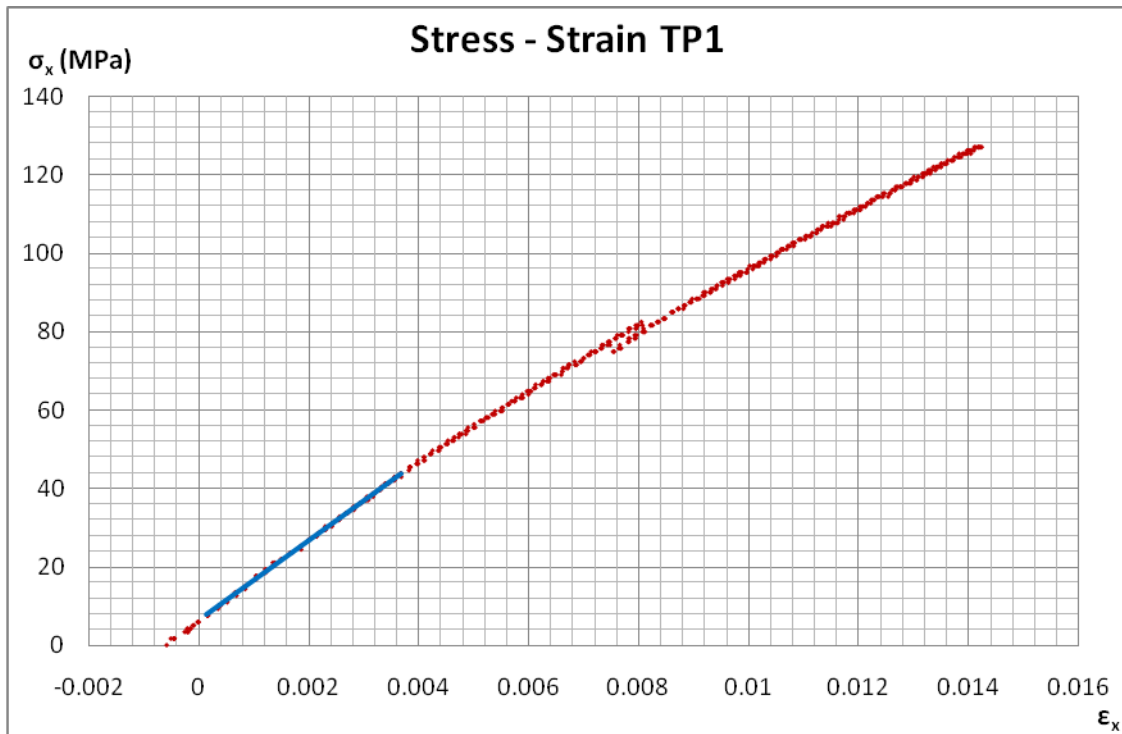


Figure 4.8 Stress – Strain diagram for specimen TP1

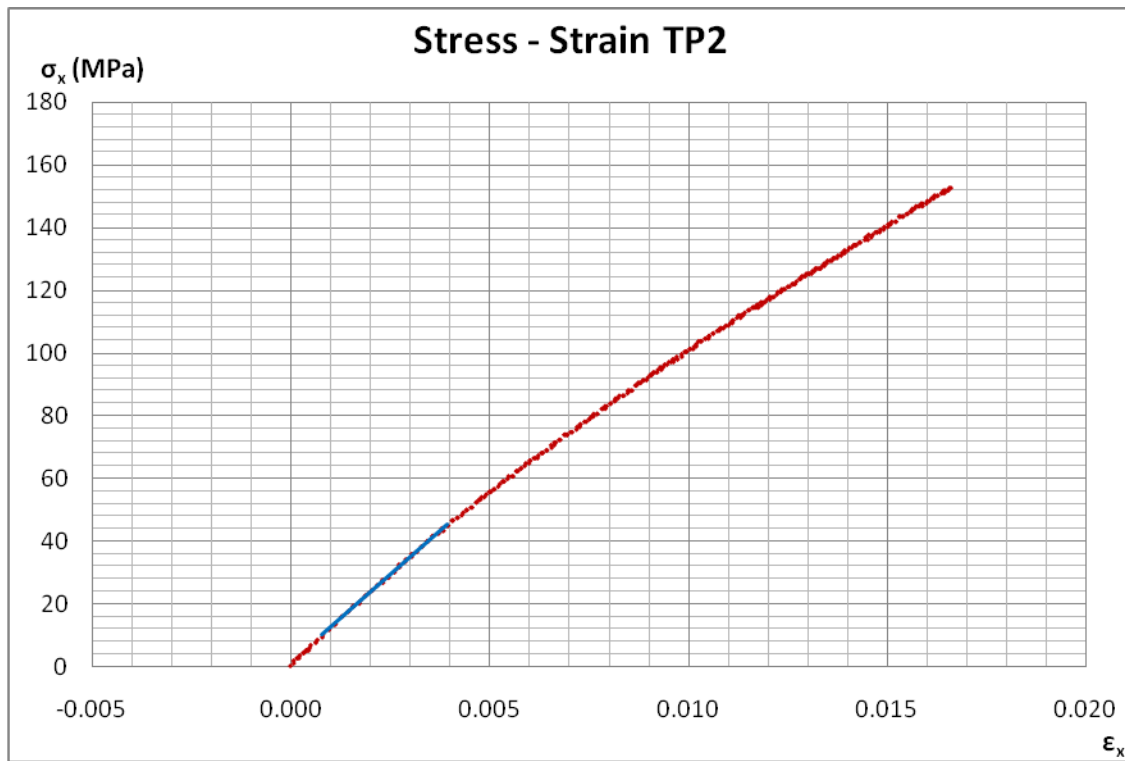


Figure 4.9 Stress – Strain diagram for specimen TP2

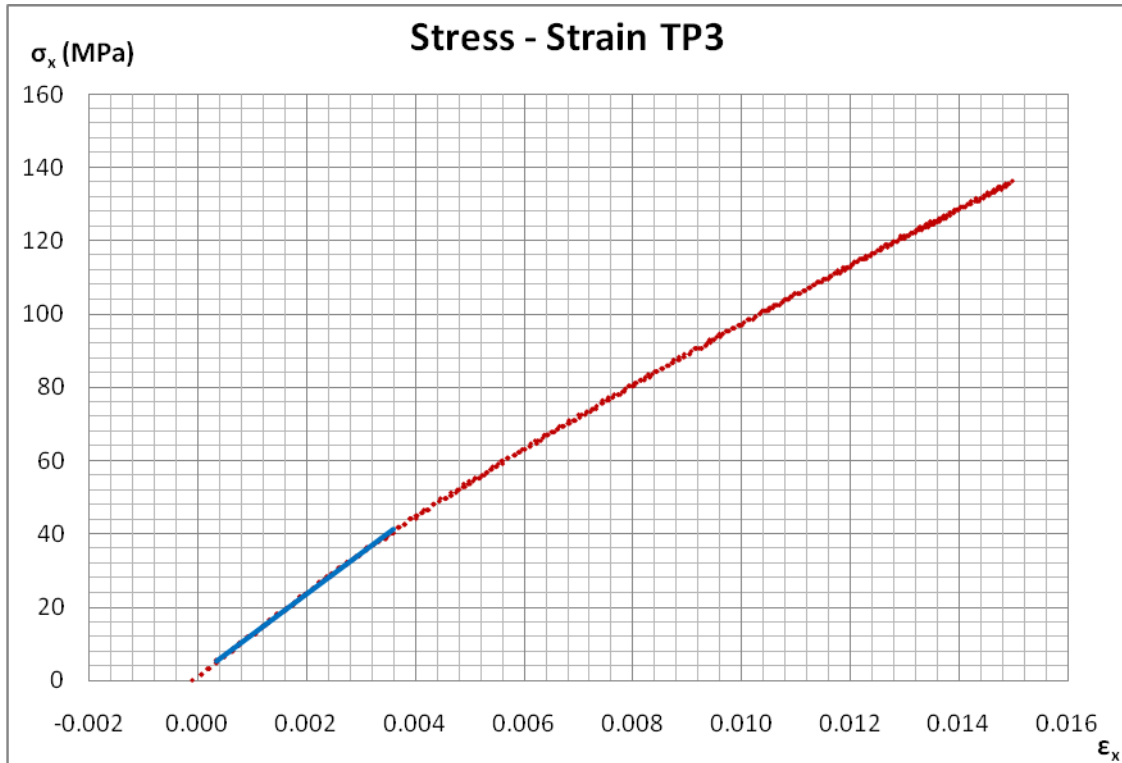


Figure 4.10 Stress – Strain diagram for specimen TP3

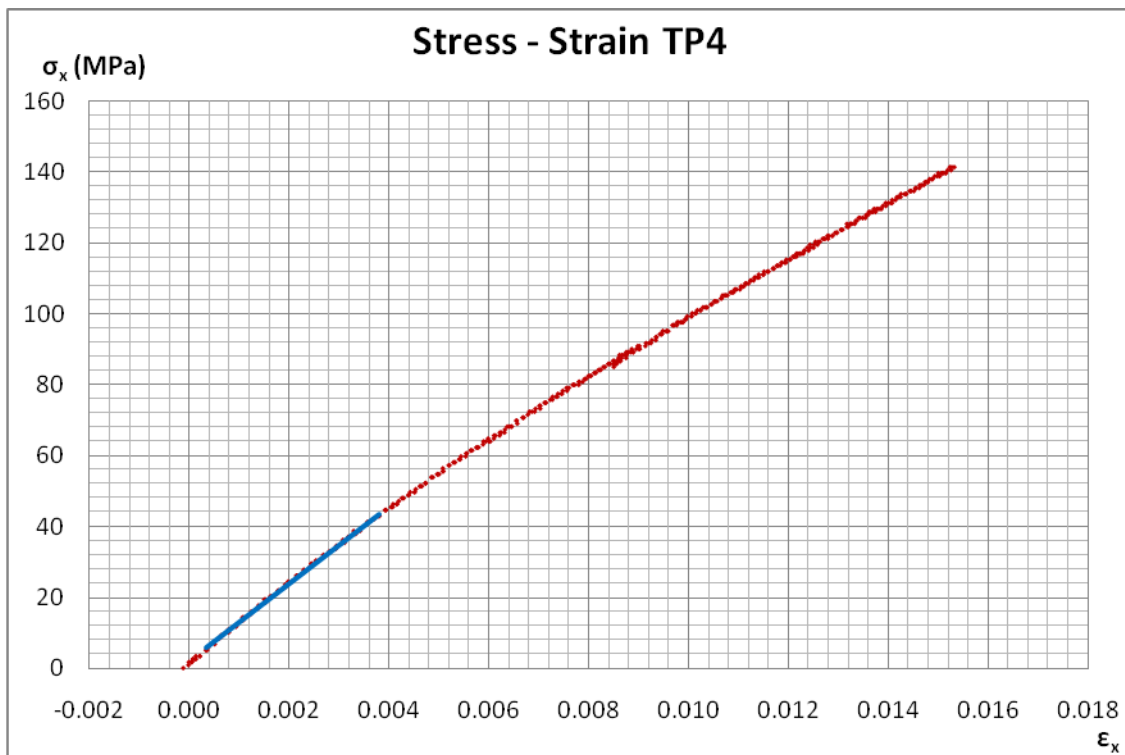


Figure 4.11 Stress – Strain diagram for specimen TP4

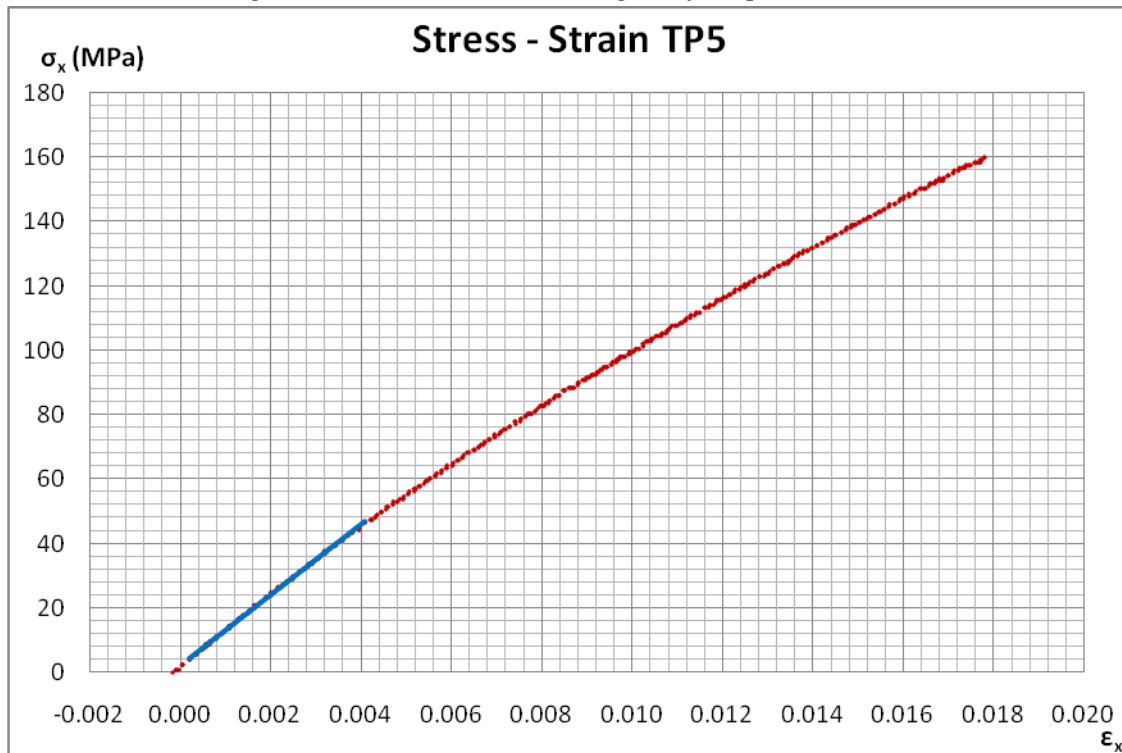


Figure 4.12 Stress – Strain diagram for specimen TP5

The diagram that derived from the measurements of specimen TP1 (figure 4.8) will be discarded due to the fact that one of the strain gauges malfunctioned and the measurement was based on the results of only one strain gauge that also malfunctioned after a stress value of approximately 80 MPa.

The blue line on each of the diagrams is the line that was fitted on each curve using the linear regression method. The line was fitted only near the “early” parts of the curve that the behaviour is linear. The tensile moduli of elasticity that were evaluated for each specimen are presented in the following table.

Table 4.2 Tensile modulus of elasticity from tensile tests

Specimen	TP1	TP2	TP3	TP4	TP5
E (GPa)	10.14	11.16	11.01	10.95	10.92
Average E-modulus without TP1 (GPa)				11.01	
Average E-modulus with TP1 (GPa)				10.84	

The values found for the moduli of elasticity for specimens TP2-TP5 are very consistent, in contradiction to the modulus of elasticity found for specimen TP1 which is little lower. Although the found value is not that inconsistent, since the measurement was based only on the measurements of one strain gauge, it cannot be trusted. Nonetheless in table 4.2 except for the average tensile modulus of elasticity without TP1, also the average tensile E-modulus taking into account TP1 can be found. In chapter 5, where the theoretical mechanical properties of the GFRP laminate will be determined, a comparison between the theoretical tensile E-modulus and the one found based on the test results.

4.3. Bending tests on GFRP plates

The bending test is the next test that we did on the GFRP plates. The purpose of the testing is to find out the behaviour of the GFRP laminate in bending, since this will be the loading situation in a deck bridge.

4.3.1 Specimen and bending test description

There were four specimens tested in total. All the specimens originated from the same GFRP plate and this is why a consistency between the results is expected. The test was a four point bending test. That means that there were two supports and two point loads. To have the smallest contact area as possible between the specimen and the supports/loads without damaging the specimen, steel cylinders were used (fig 4.13). The supported length was 400 mm. As far as the loading is concerned two configurations were used. For the first configuration, the loads were applied with a 100 mm offset from the edge of the supported length. For the second configuration, the loads were applied with an offset of 150 mm from the edge of the supported length. A simplified drawing of the two configurations can be seen in figure 4.15, while the two actual configurations -1- and -2- in figures 4.13 and 4.14 respectively.

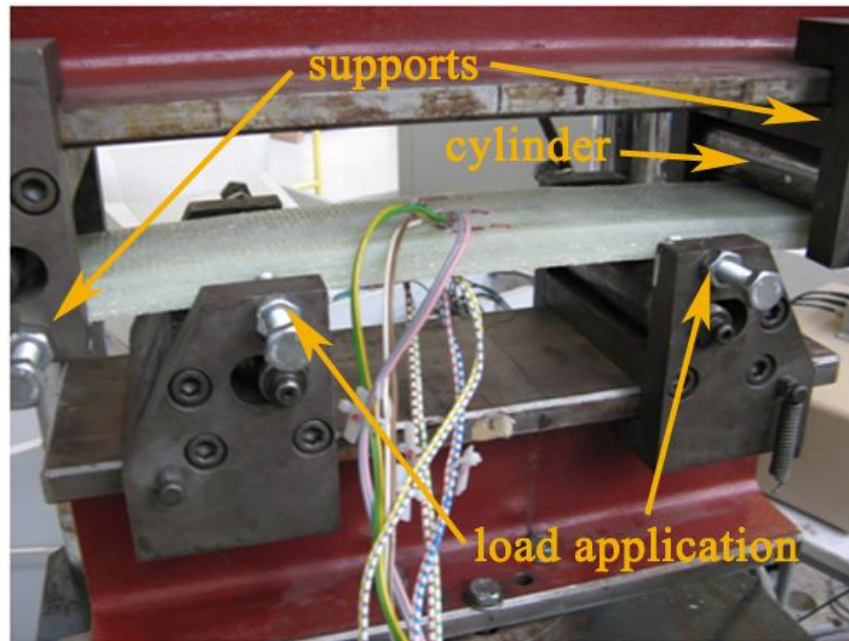


Figure 4.13 Experimental configuration -1- for the GFRP plate

In the second configuration (fig 3.37) the supported length of the plate was again 400 mm as in the previous one but this time the load were applied at 150 mm ($3/8$ length) from the supports.



Figure 4.14 Experimental configuration -2- for the GFRP plate

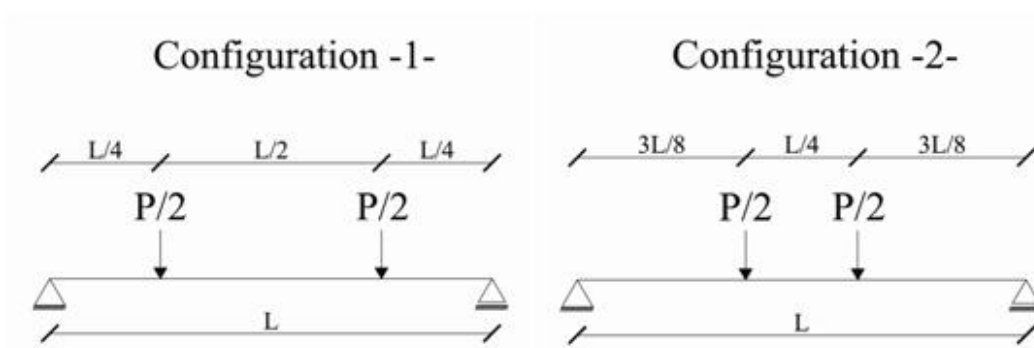


Figure 4.15 Four point bending configurations used

Three of the specimens were tested using configuration -1- and only one with -2-. The specimen was very flexible and during the bending test using configuration -2-, before failure the mid area of the specimen came in contact with the upper I-beam (fig 4.13, 4.14) forcing the premature end of the test. This problem was solved using configuration -1-.

Three strain gauges were used at the mid span area (fig 4.15), at the top and bottom surface of the FRP plate.

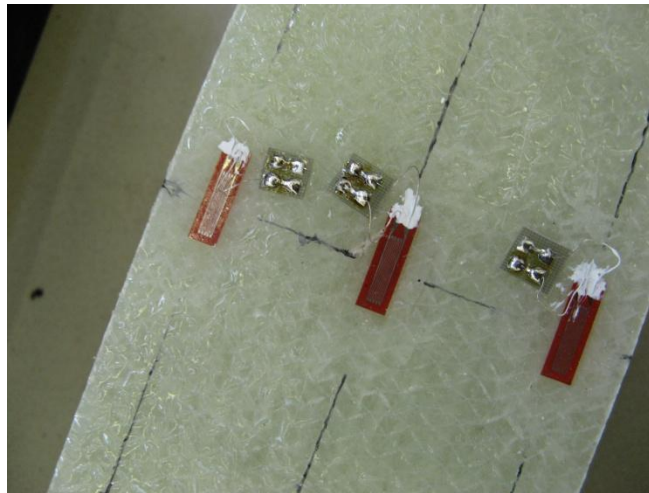


Figure 4.16 Strain gauges on the FRP plate in the mid span area

The dimensions of the specimens were the same for all four since they originated from the same plate and the cutting was performed by a very skilled person with excellent accuracy.

Table 4.3 Specimen dimensions for four point bending test

Specimen	Supported Length (mm)	Width (mm)	FRP thickness (mm)
BP1-4	400	80.04	18.36

4.3.2 Specimen failure pattern

As already mentioned, all the specimens originated from the same FRP plate. Based on that fact a similar failure pattern is to be expected. It must be noted here that no pictures of the failed specimen BP2 exist, since this specimen didn't reach failure due to the configuration used.

BP1

The failed specimen can be seen in figure 4.17. As it can be seen crack initiated from the point where the load was applied. The cracks appear to be initiated from shear forces. After the first cracks appear in the position where the loads were applied, they propagated towards the mid area of the plate quite easily due the lack of fibres in the thickness direction. The lack of fibres in the thickness direction means that the element that resists the stresses is only the matrix which has significant lower strength in comparison to the glass fibres. It also must be mentioned that after the first cracks, the local curvature at that point increased rapidly and this is another reason for the type of failure of the specimen.



Figure 4.17 Failed GFRP specimen BP1 in bending

In figure 4.18 a and b the crack parallel to the longitudinal axis of the plane can be seen in more detail. The fibres that can be seen in the crack were not initially in the thickness direction and this is noted so as the reader won't be confused since it is already mentioned that there are no fibres in that direction.



Figure 4.18 Details of failed GFRP specimen BP1 in bending

In figure 4.19 a, the crack can be seen in more detail. It can be observed that some fibres stayed attached to the epoxy during the cracking. However this wasn't the case in figure 4.19 b where there are hardly any fibres visible in the cracked area. In figure 4.19 c the cracked area of the layer that was in tension can be seen while in figure 4.19 d the one in compression. In figure 4.19 d, it can be seen that after the crack was, in a way, folded.

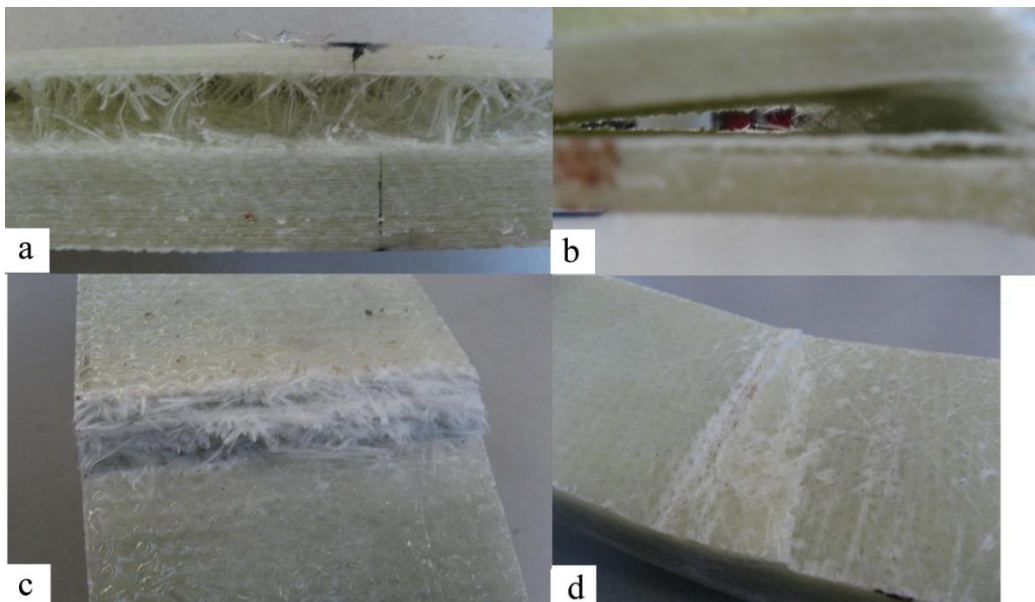


Figure 4.19 Details of failed GFRP specimen BP1 in bending

BP3

The failed specimen can be seen in figure 4.20. The failure pattern is the same as the one for BP1. The first difference that can be noted is that there is a double crack in the area where the load was applied. The reason for that is that after the failure, the specimen was crashed against the top beam. The second difference is that the cracking didn't propagate till the mid area of the specimen.



Figure 4.20 Failed GFRP specimen BP3 in bending

In figure 4.21 a,b,c and d details of the failed specimen can be seen and it can easily be seen that the cracking is very similar to the cracking of BP1.

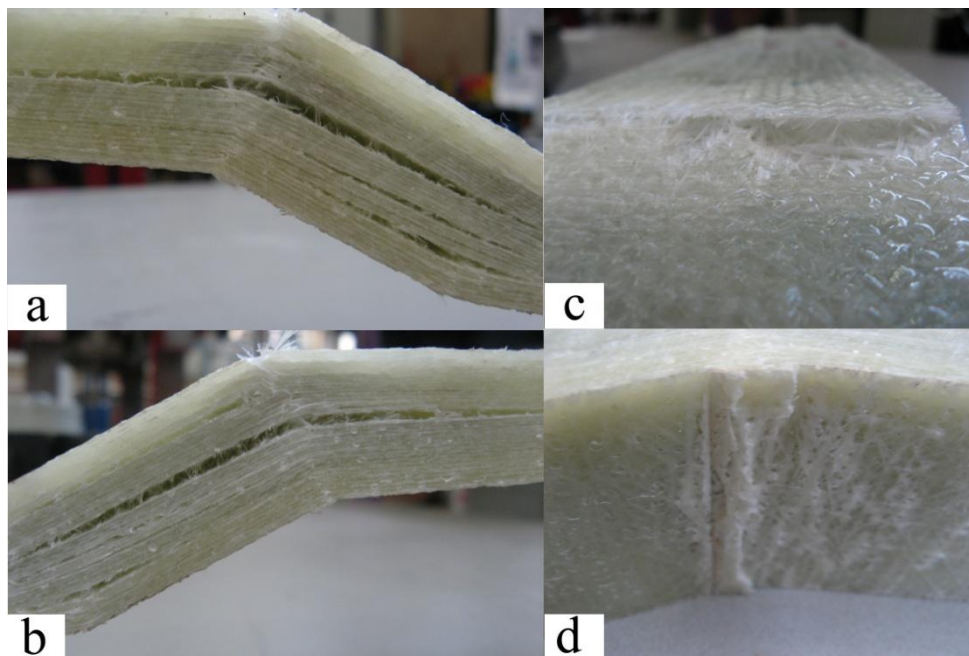


Figure 4.21 Details of failed GFRP specimen BP3 in bending

BP4

The failed specimen can be seen in figure 4.22. The failure pattern is the same as the one for BP1 and BP3. Actually it is more similar to BP3 in the aspect that the crack didn't propagate till the mid area of the specimen



Figure 4.22 Failed GFRP specimen BP4 in bending

In figure 4.23 a,b,c and d details of the failed specimen can be seen and it can easily be seen that the cracking is very similar to the cracking of BP1 and BP3.

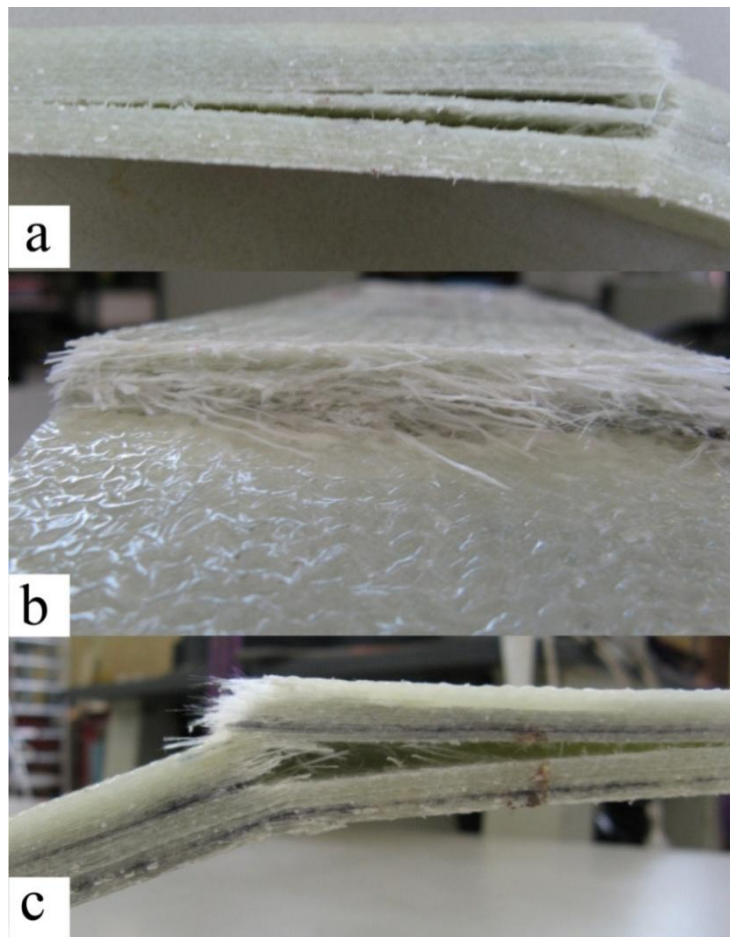


Figure 4.23 Details of failed GFRP specimen BP4 in bending

4.3.3 Bending test results

In this paragraph the experimental results will be presented. The force – vertical displacement diagram can be drawn straight from the measurements obtained, without any data processing. However, this is not the case for the normal stress against vertical displacement diagram. The first difficulty is that we assumed that FRP is linear elastic anisotropic material. However in the present case another more simplifying assumption will be made. FRP will be assumed to be isotropic and Hooke's law for the evaluation of stresses will be used. It is also safe to use Hooke's law for the one dimensional case, and therefore the stresses will be directly determined from the measured strains utilizing the modulus of elasticity found paragraph 4.2.3. By using the same modulus of elasticity we assume that the volumetric fractions between the two kinds of specimens, TP and BP, are the same or at least similar.

Based on the force – vertical displacement diagram, it is possible to determine an equivalent flexural modulus of elasticity. This doesn't have a real physical meaning, but it helps us realise the degree of anisotropy of the material. Nonetheless this equivalent flexural modulus of elasticity can by no means used for the calculation of stresses.

It is useful to know that the displacement is measured at the point where the load is applied. That means that in configuration -1- the vertical displacement is measured at the points located 100 mm from the support and in configuration -2- at the points located at 150 mm from the support.

Another point that must be stressed is that the force that will be plotted in the diagrams is the one applied from the actuator and therefore if we call it P then due to symmetry each cylinder applies a force of $P/2$ on the composite plate.

BPI

The force against vertical displacement graph can be seen in figure 3.46. From this figure a linear elastic behaviour can be observed till the value of 15 kN at which point the inclination of the curve changes. This was noticed also at the time that the experiment was taking place. At the moment when the load reached the value of the 15 kN minor cracking sounds were audible. However the specimen didn't failed at this load value, but carried on until an ultimate load value of 32 kN.

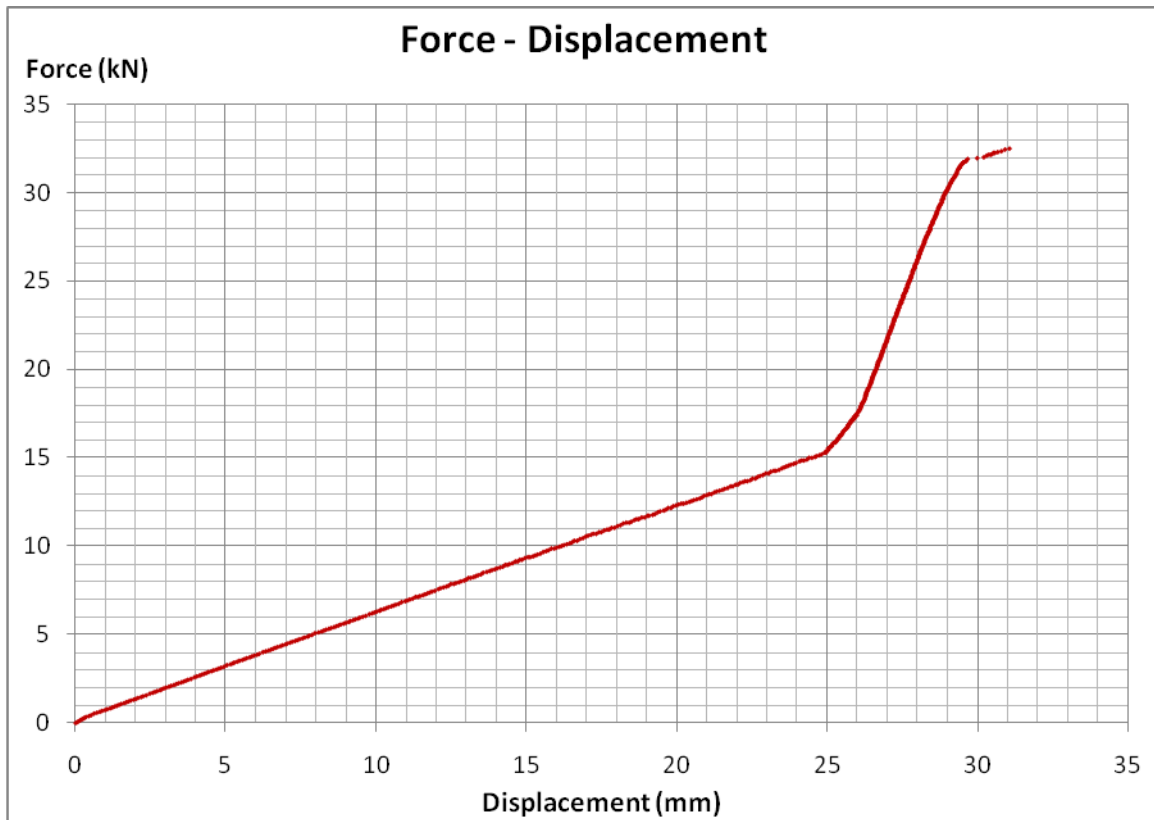


Figure 4.24 Force against vertical displacement diagram for BP1

This is really strange since both the epoxy and the glass fibres are brittle materials. A possible explanation for this phenomenon can be found by resembling the behaviour of the FRP plate to a reinforced concrete one. In that case the epoxy plays the role of the concrete and the glass fibres the role of the steel rebars. So the assumed mechanism could be as follows: At the value of 15 kN the epoxy starts to fail. However the bond between the glass fibres and the epoxy still exists. That is certain at least for the free length of the plate left and right of the supports. So, the remaining strength is due to the existence of the fibres. Finally at the load value of 32 kN there is either a failure at the bond between the epoxy and the fibres or a failure of the fibres themselves. That has as result the abrupt failure that was observed in the lab. This pseudo elasto-plastic behaviour was observed in all the specimens as it was of course expected.

From figure 4.24 the equivalent flexural modulus of elasticity can be evaluated. The theoretical deflection of the plate for the current configuration was found to be:

$$d = \frac{Pl^3}{96EI},$$

Where P is the force applied by the actuator, d the displacement at the point where the load is applied, E the equivalent flexural modulus of elasticity and $I = bh^3/12$ the moment of inertia of the plate.

The slope of the linear part of the curve in figure 3.44 is:

$$k = \frac{P}{d} = 613 \text{ N/mm}$$

Equating these two relations the equivalent flexural modulus of elasticity can be found:

$$E = \frac{kl^3}{96I} = \frac{613 \cdot 400^3 \cdot 12}{96 \cdot 80 \cdot 18.36^3} = 9.90 \text{ GPa}$$

The next diagram is that of the maximum and minimum normal stress against force.

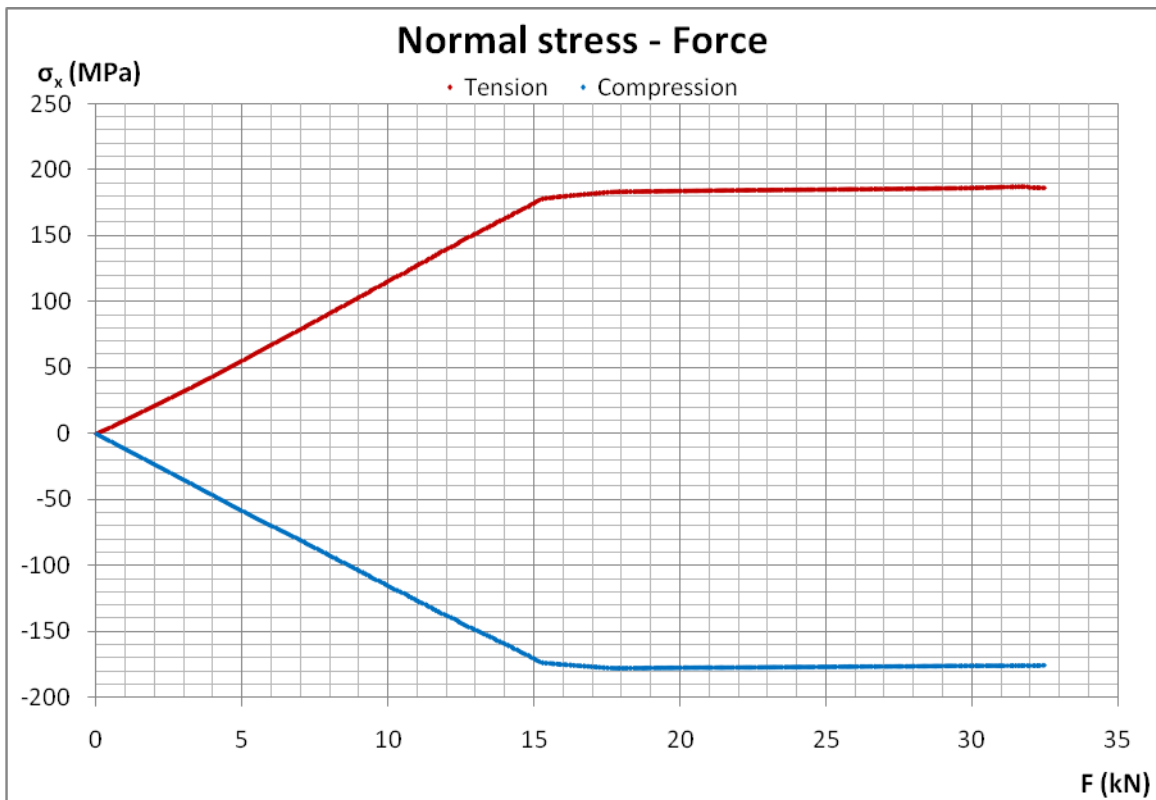


Figure 4.25 Maximum and minimum stress against force for specimen BP1

Both the compressive and tensile stresses have been drawn in the same diagram in order to show that they have almost the same value and to be easier to visualize the location of the neutral axis which is approximately in the middle. That of course means that the modulus of elasticity in tension and compression is the same.

BP2

This is the only specimen tested with the second configuration and didn't reached failure. However the linear part could still be obtained and used to evaluate the equivalent flexural modulus of elasticity. Furthermore no strain measurements are available for this specimen as well due to a malfunction of the equipment. The force – displacement curve can be seen in figure 4.26.



Figure 4.26 Force against vertical displacement diagram for BP2

The equivalent modulus of elasticity will be evaluated as before, but this time the configuration is different. So, for the current configuration the theoretical displacement at the point where the load is applied is found to be:

$$d = \frac{31Pl^3}{1536EI},$$

Where P is the force applied by the actuator, d the displacement at the point where the load is applied, E the equivalent flexural modulus of elasticity and $I = bh^3/12$ the moment of inertia of the plate.

The slope of the linear part of the curve in figure 4.26 is:

$$k = \frac{P}{d} = 341 \text{ N/mm}$$

Equating these two relations the equivalent flexural modulus of elasticity can be found:

$$E = \frac{31kl^3}{1536I} = \frac{31 \cdot 346 \cdot 400^3 \cdot 12}{1536 \cdot 80 \cdot 18.36^3} = 10.68 \text{ GPa}$$

BP3

The force against vertical displacement graph can be seen in figure 4.27. From this figure a linear elastic behaviour can be observed till the value of 16 kN at which point the inclination of the curve changes. The specimen finally failed at the ultimate load value of 31.8 kN.



Figure 4.27 Force against vertical displacement diagram for BP3

Same as before the equivalent modulus of elasticity is found equal to:

$$E = \frac{kl^3}{96I} = \frac{644 \cdot 400^3 \cdot 12}{96 \cdot 80 \cdot 18.36^3} = 10.41 \text{ GPa}$$

Again from the maximum and normal stress diagram fig 4.28 it can be verified that the behaviour of the material in tension and compression is almost identical.

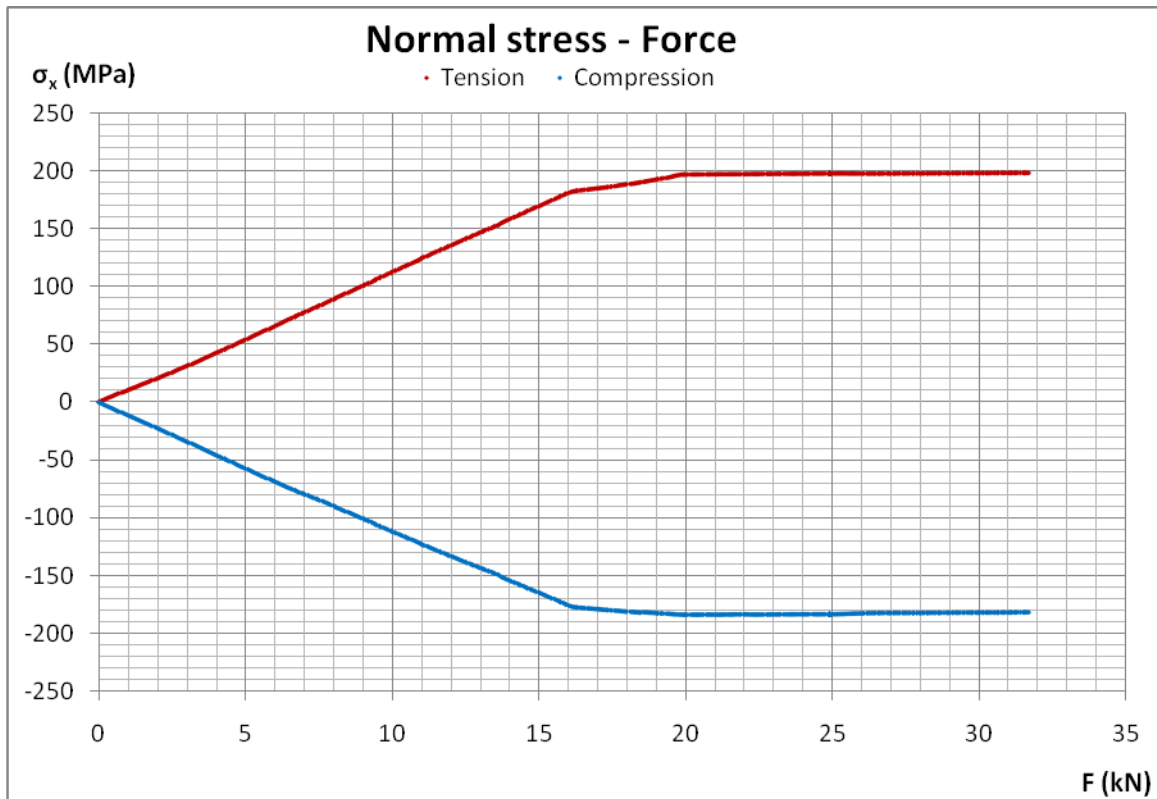


Figure 4.28 Maximum and minimum stress against force for specimen BP3

BP4

The force against vertical displacement graph can be seen in figure 4.29. From this figure a linear elastic behaviour can be observed till the value of 14.8 kN at which point the inclination of the curve changes. The failure finally was reached at the ultimate load value of 29 kN.



Figure 4.29 Force against vertical displacement diagram for BP4

Same as before the equivalent modulus of elasticity is found equal to:

$$E = \frac{kl^3}{96I} = \frac{597 \cdot 400^3 \cdot 12}{96 \cdot 80 \cdot 18.36^3} = 9.65 \text{ GPa}$$

And the maximum, minimum stress against force diagram.



Figure 4.30 Maximum and minimum stress against force for specimen BP4

Finally the moduli of elasticity found along with the average value can be seen in the following table:

Table 4.4 Equivalent flexural modulus of elasticity for the FRP

Specimen	BP1	BP2	BP3	BP4
E (GPa)	9.90	10.68	10.41	9.65
Average E (GPa)	10.16			

The flexural modulus of elasticity found from the bending test is smaller than the tensile modulus of elasticity found from the tensile tests. This confirms the already known fact, that FRP is not isotropic. However the difference is only 7.72%, which means that it could be assumed as an isotropic material with a small loss in accuracy.

4.4 Bending tests on steel plates reinforced by GFRP plates

4.4.1 Introduction

The purpose of the experiments done is to estimate the stress reduction factor of the steel plate. For that purpose eight specimens were tested. Four of them were tested with the GFRP being in tension and four with the GFRP in compression. Further on the experimental configuration used will be described and the test results will be reviewed.

4.4.2 Specimen and bending test description

All the experiments were four point bending tests. Two configurations were used, same as in the bending test on the GFRP plates (fig.4.15).. Configuration -1- was used for testing three specimens with the steel in compression and the GFRP in tension (fig 4.31). Configuration -2- was used for the testing of one specimen with the steel in compression and for all the specimens with the steel in tension (fig.4.32, 3.33).

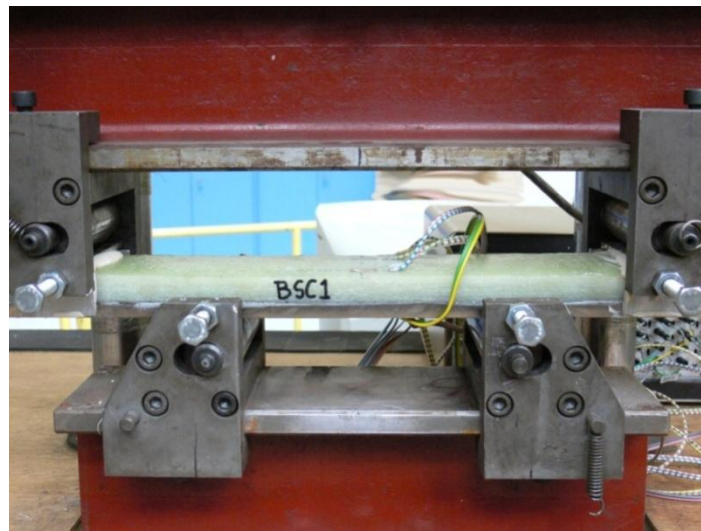


Figure 4.31 Experimental configuration -1- for the composite plate and steel in compression.

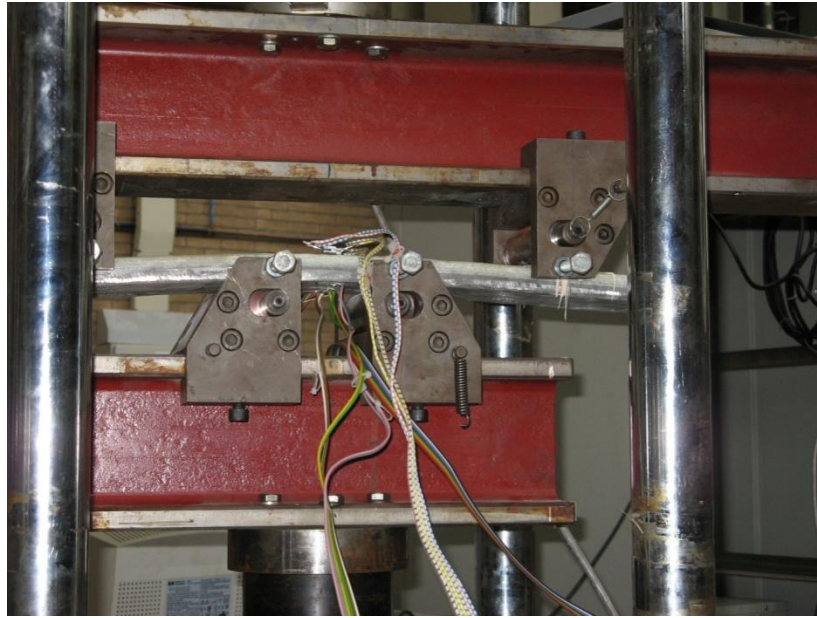


Figure 4.32 Experimental configuration -2- for the composite plate and steel in compression

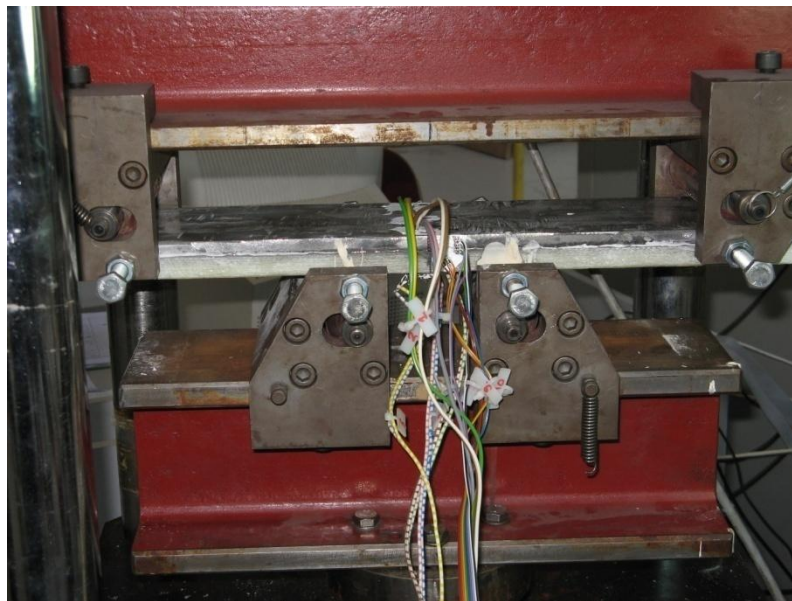


Figure 4.33 Experimental configuration -2- for the composite plate and steel in tension

Three strain gauges were used at the mid span area, at the top and bottom surface of the composite plate, which means three on the steel plate and three on the FRP plate which can be seen in figure 3.56 and 3.57 respectively.



Figure 4.34 Strain gauges on the steel plate in the mid span area

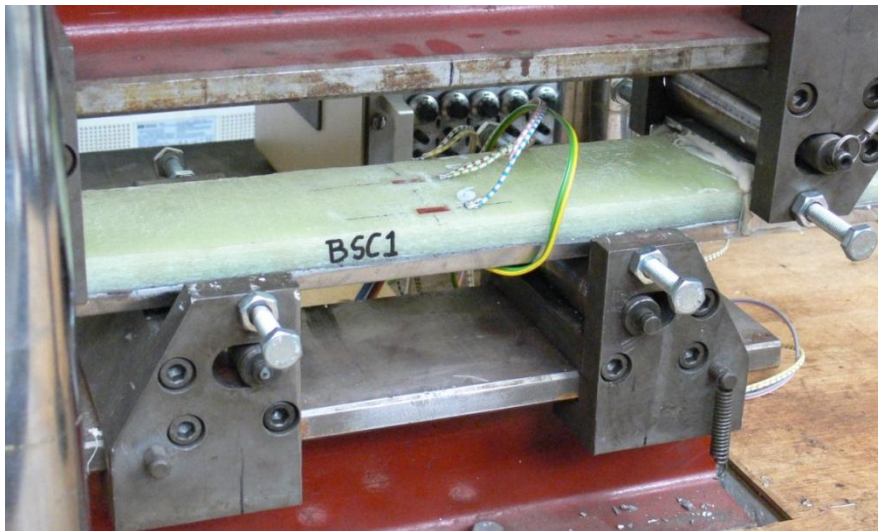


Figure 4.35 Strain gauges on the FRP plate in the mid span area

Also 5 strain gauges were used at the side of the steel plate again in the mid span area (fig 4.36).

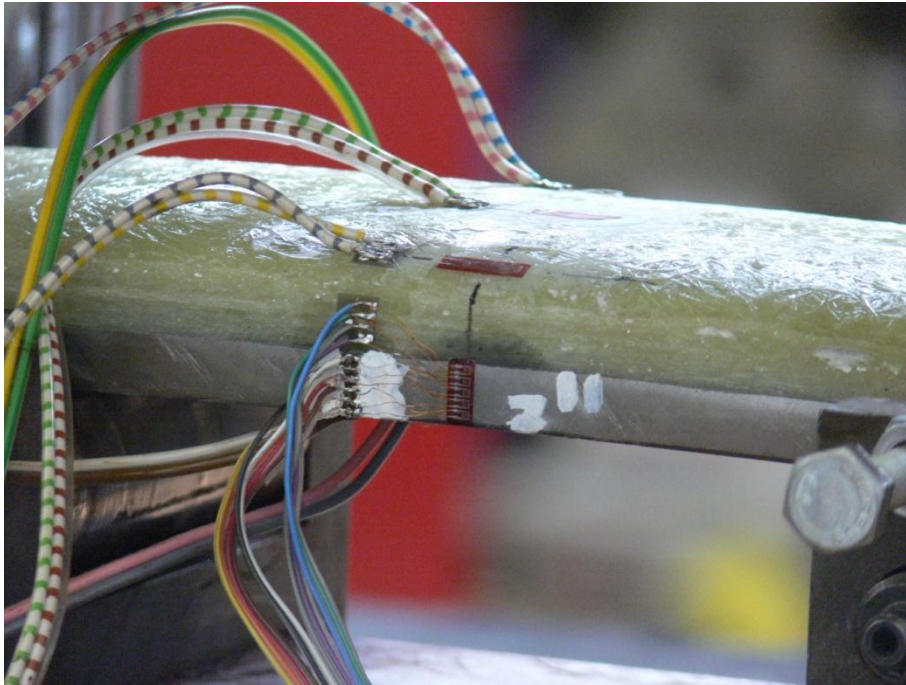


Figure 4.36 Strain gauges at the side of the steel plate on the mid span area

Specimens

As already mentioned, eight specimens were tested in total. The thickness of the GFRP plate was variable from specimen to specimen. Therefore the dimensions of the specimens will be easier to be presented in a table form. In table 3.6 the dimensions of each specimen can be seen and also the configuration used. The thickness of the steel plate is the same in all the specimens and it is equal to 12 mm. The specimens that were tested with the GFRP being in tension are the ones with the name BSC, while the ones with the GFRP being in compression are the ones with the name BST.

Table 4.5 Specimen dimension and configuration used

Specimen	Supported Length (mm)	Width (mm)	FRP thickness (mm)	Overall thickness (mm)	Configuration used
BSC1	400	99.24	16.5	28.50	1
BSC2	400	99.39	15.5	27.50	1
BSC3	400	99.73	13.5	25.50	1
BSC4	400	99.86	13.00	25.00	2
BST1	400	99.76	17.00	29.00	2
BST2	400	99.49	14.20	26.20	2
BST3	400	99.54	15.85	27.85	2
BST4	400	99.79	18.00	30.00	2

4.4.3 Test results

In this section the test results of each individual specimen will be presented. The FRP plate in each specimen has different thickness and probably different number of layers, and since the mechanical properties of the FRP haven't been determined with accuracy yet it is really difficult to group the results. Also it must be noted that the displacement is measured at the point that the load is applied. That means that in configuration -1- the vertical displacement is measured at the points located 100 mm from the support and in configuration -2- at the points located at 150 mm from the support.

Another point that must be stressed is that the force that will be plotted in the diagrams is the one applied from the actuator and therefore if we call it P then due to symmetry each cylinder applies a force of $P/2$ on the composite plate.

First the specimens with the GRP loaded in tension will be presented and afterwards the specimens with the GFRP loaded in compression.

4.4.3.1 Specimens with the steel loaded in compression (BSC)

BSCI

The specimen failed at a force of 76.8 kN. The displacement, as it can be seen in figure 4.37 a through e, was large and certainly not feasible in the case of a bridge deck. However it was a good opportunity to find out how exactly the composite plate reaches failure. So, when the load reached the value of 76.8 kN the FRP plate completely delaminated from the steel plate which was already in the plastic area. Therefore it can be assumed that the interface layer reached its shear capacity although, since the deflection was so large and there was also a tensile force applied in the interface layer. However it is a fact that the interface layer was able to endure past the plasticization of the steel plate which is really positive because it proves that the material used for the interface layer is really effective.

In figure 4.37 a,b,c,d,e,f the way to failure of the specimen can be seen. It starts with a mild deflection and finally after the steel plate has entered the plastic area it fails by fully delaminating.

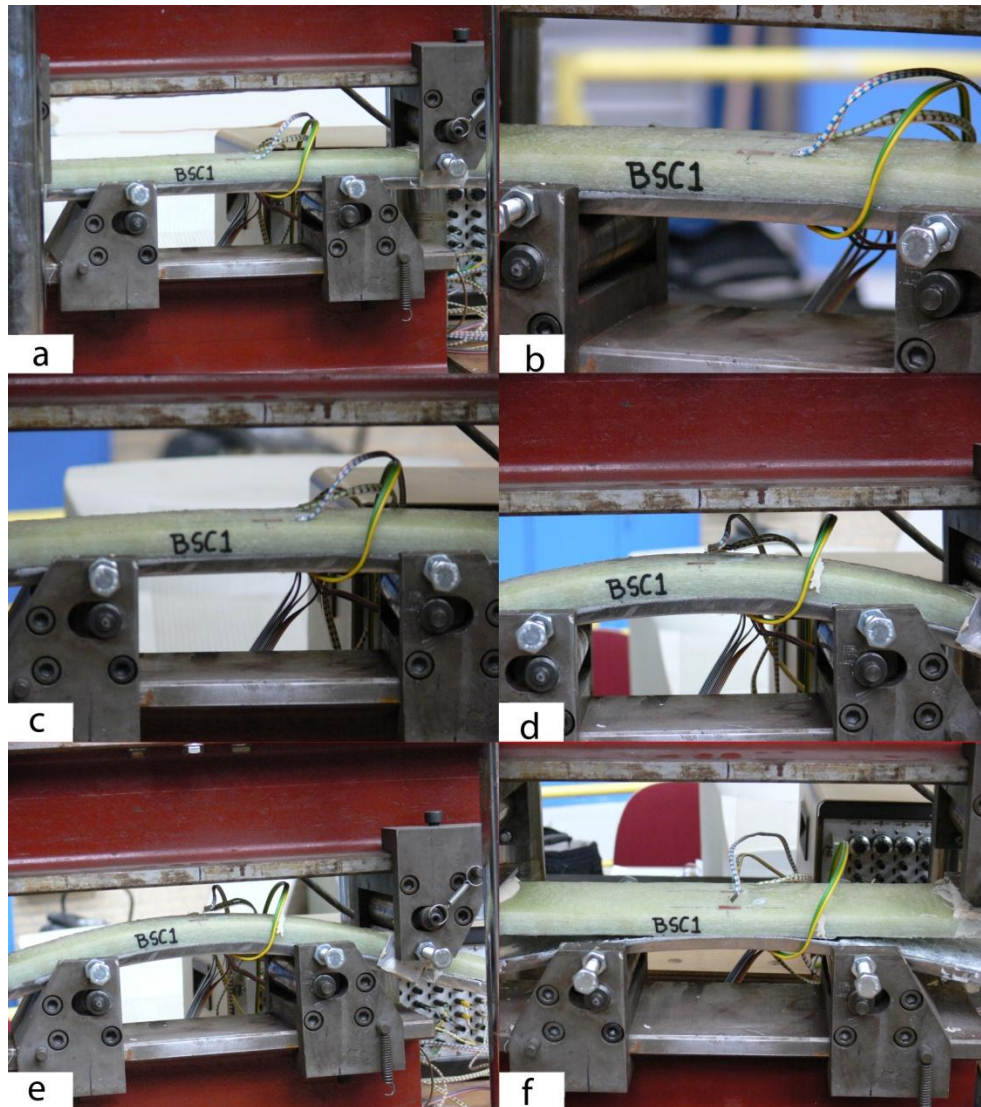


Figure 4.37 Composite plate BSC1 in bending from large deflections to failure

In the next figures some more detail pictures of the delaminated area are depicted.

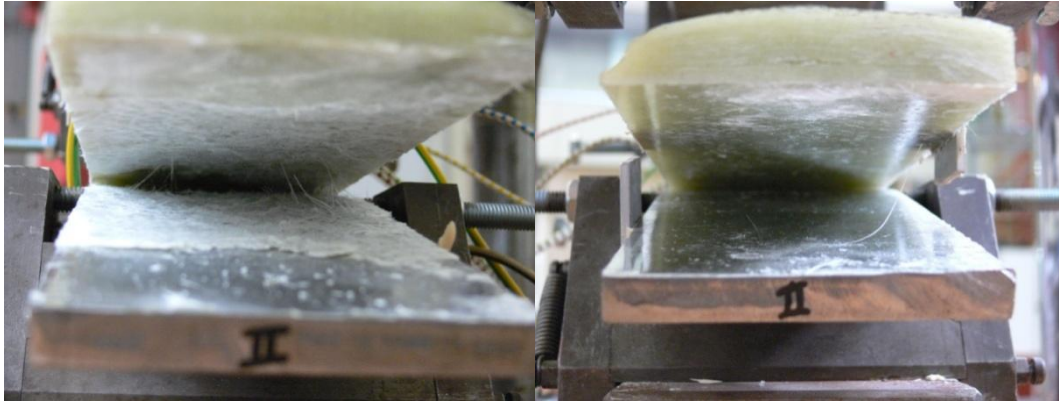


Figure 4.38 Delamination of the composite plate BSC1

In figure 4.38 a it can be seen that at the moment of failure the glue was able to hold on to the FRP forcing it to rip. On the other hand in figure 438 b it can be seen that the delamination was caused due to failure of the glue to keep the two plates together. Nonetheless the behaviour of the adhesive is excellent since the failure came under an extremely high load which is impossible to encounter in steel bridge decks.

Now that the failure has been reviewed the evaluation of the results will follow. Starting with the first diagram which is depicted in figure 4.39 one can see that the relation between the force and the vertical displacement is linear. Also in the same figure one might observe that there is a little leap close to the 50 kN area. The reason for this is that at that point the bending experiment was paused for a few seconds. The specimen failed at 76.8 kN and at that moment the FRP plate completely delaminated from the steel plate which was already in the plastic area. Finally it can be said that from the point of 44 kN the curvature is changing but the change is very small. That is due to the fact that the steel has begun to yield and to enter in the plastic area (fig 4.39). The little leap at the point that the force reaches 50 kN appear in every figure for this specimen and that is why it will not be mentioned again.



Figure 4.39 Force against vertical displacement diagram for specimen BSC1

In the following figure the stress on the outer surface of the steel plate can be seen. The stresses were evaluated from the strains measured by the strain gauges via Hooke's law for the one dimensional case. Even though it is a three dimensional case the error is insignificant. The modulus of elasticity used for the steel is 200 GPa. Although there is no specific purpose to be presented the diagram for the GFRP stresses, it will be included for the sake of completeness. The E modulus that is going to be used for the stress evaluation of the GFRP laminate, is the one found in 4.2.3.

For the steel a linear relation between the stress and the force can be observed until the load reaches the value of 44 kN at which point the steel cross section begin to yield. The strain gauges failed at the stress value of 625 MPa. However the moment of failure is not of big concern to us since the purpose of this experiment is mainly to estimate the stress reduction factor and secondarily to witness the failure mechanism, find out the load capacity and comprehend the behaviour of the composite plate while it is still behaving linearly.



Figure 4.40 Minimum normal stress (located at the outer surface of the steel plate) against force diagram for specimen BSC1

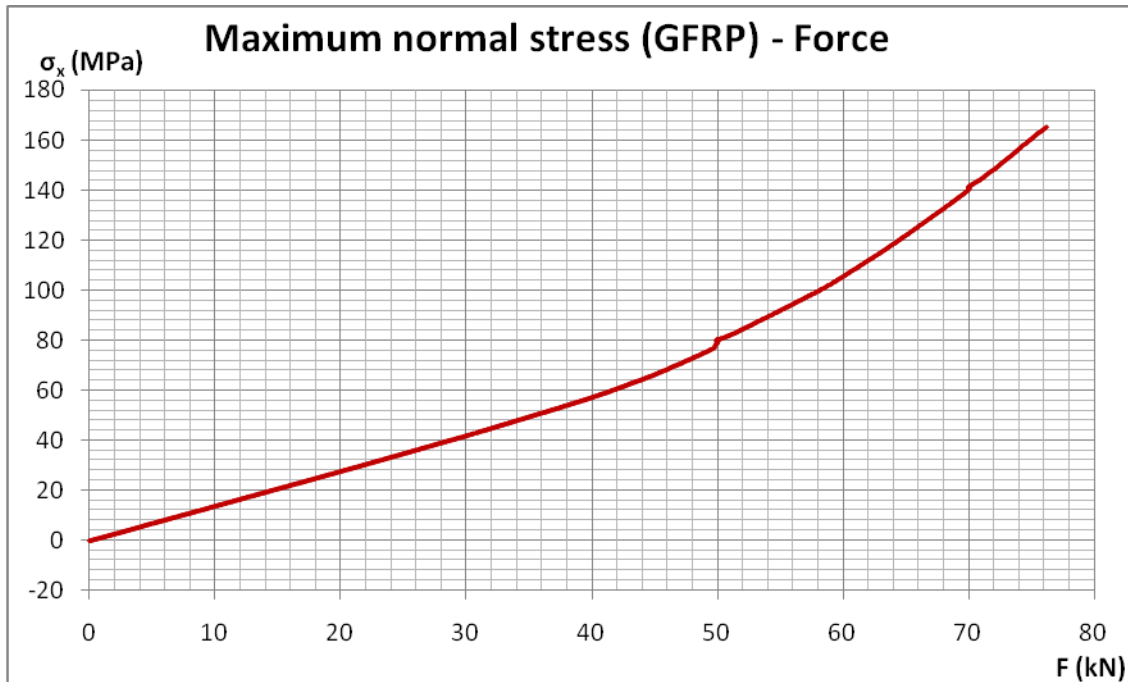


Figure 4.41 Maximum normal stress (located at the outer surface of the GFRP plate) against force diagram for specimen BSC1

Further on, there are the stresses along the side of the steel plate are depicted (fig 4.42). The stress was evaluated utilizing Hooke's law and since the strain gauges were attached on the steel plate, the strain was multiplied by 200 GPa which is the modulus of elasticity for the steel. It can be observed that the red line that corresponds to strain gauge 8 crosses the blue line which corresponds to strain gauge 7. So, for a short period a layer of steel closer to the neutral axis has higher stress value than a layer that is closer to the outer surface. That is due to the phenomenon called steel hardening. This will come up again in similar diagrams to follow and it is an expected behaviour and not a malfunction of a strain gauge.

The same behaviour pattern as in figure 4.40 can be observed. This is why we pick a lower value such as 20 kN in order to have linear behaviour, and to be able to plot the stress distribution along at the side of the steel plate and this way to determine the position of the neutral axis as it is depicted in figure 4.42.

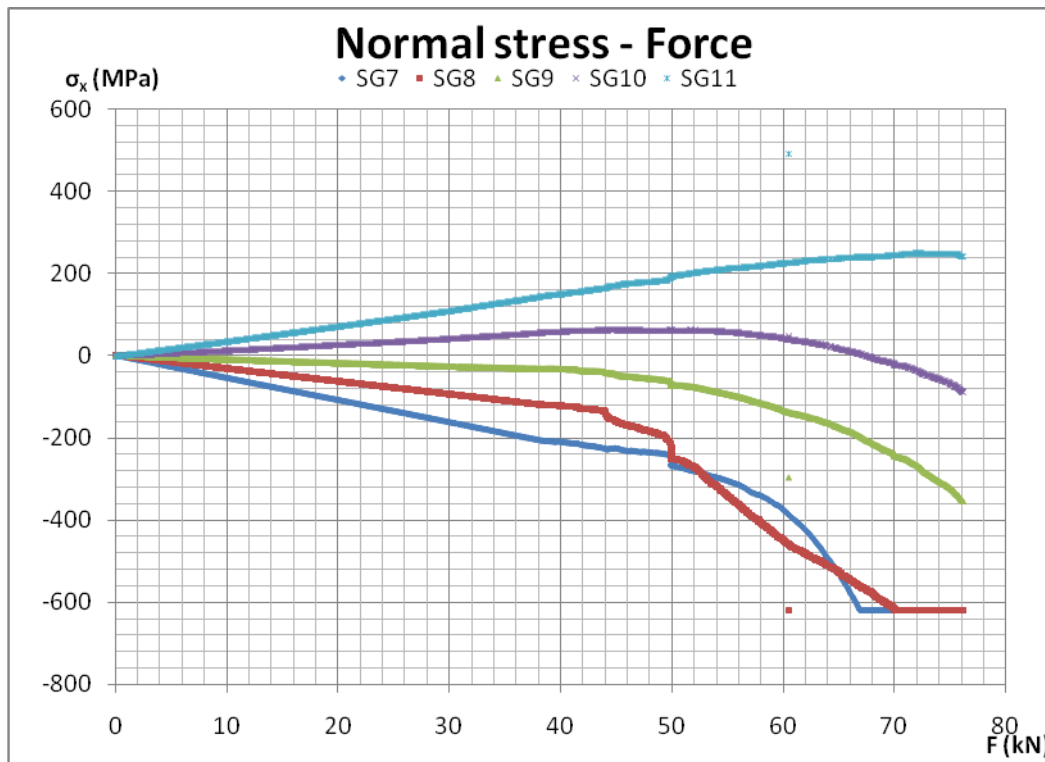


Figure 4.42 Normal stress along the side of the steel plate against force diagram for specimen BSC1

It is rather important at this point to note that the exact position of the strain gauges on the side of the steel plate can be determined with the utmost accuracy since they are very small (fig 4.36). Henceforth, the assumption that has been made is that the strain gauges are

evenly distributed on the side of the steel plate. This assumption is used throughout this report.

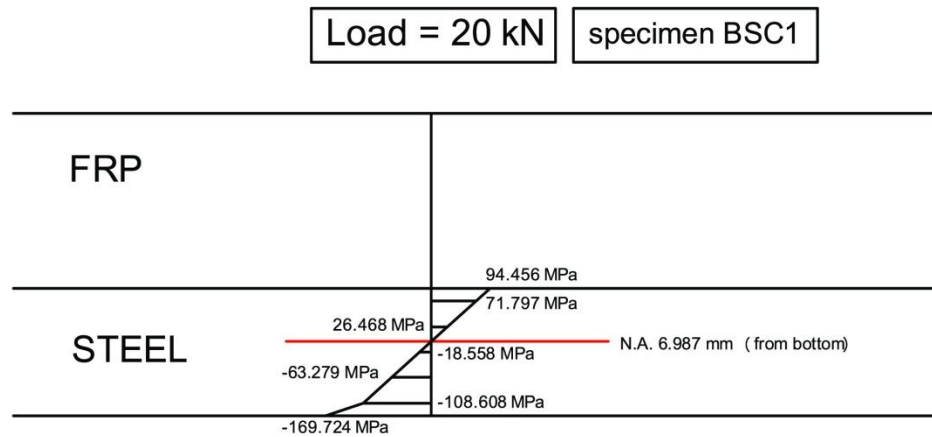


Figure 4.43 Normal stress distribution along the side of the steel plate for specimen BSC1

BSC2

The specimen failed at a force of 73.1 kN. However there was a problem with the calibration of the strain gauges that they were attached to the outer surface of the steel and the GFRP plate and this is why the corresponding graph of the stresses at the outer surface of the steel plate will be just for the elastic area. The way to failure will not be presented this time since it is the same as for the BSC1. In fact, it is the same for all the specimens and this is why it will not be presented for none else as well.

The failed specimen can be seen in figure 4.44 a along with two detailed pictures of the failed area (fig 4.44 b,c). This time there was no delamination observed. The steel plate obviously yielded and entered in the plastic area. That caused the neutral axis to be transposed towards the FRP and most probably to assume a new position in the FRP plate. That has as a result a more abrupt increase of the normal stresses from zero in the inner surface of the FRP plate to a maximum value to the outer. The lack of fibres in the vertical plane (parallel to the loading plane) contributed finally to the form of failure depicted in figure 4.44. The positive fact is that the interface layer proved to be really resilient in this case.

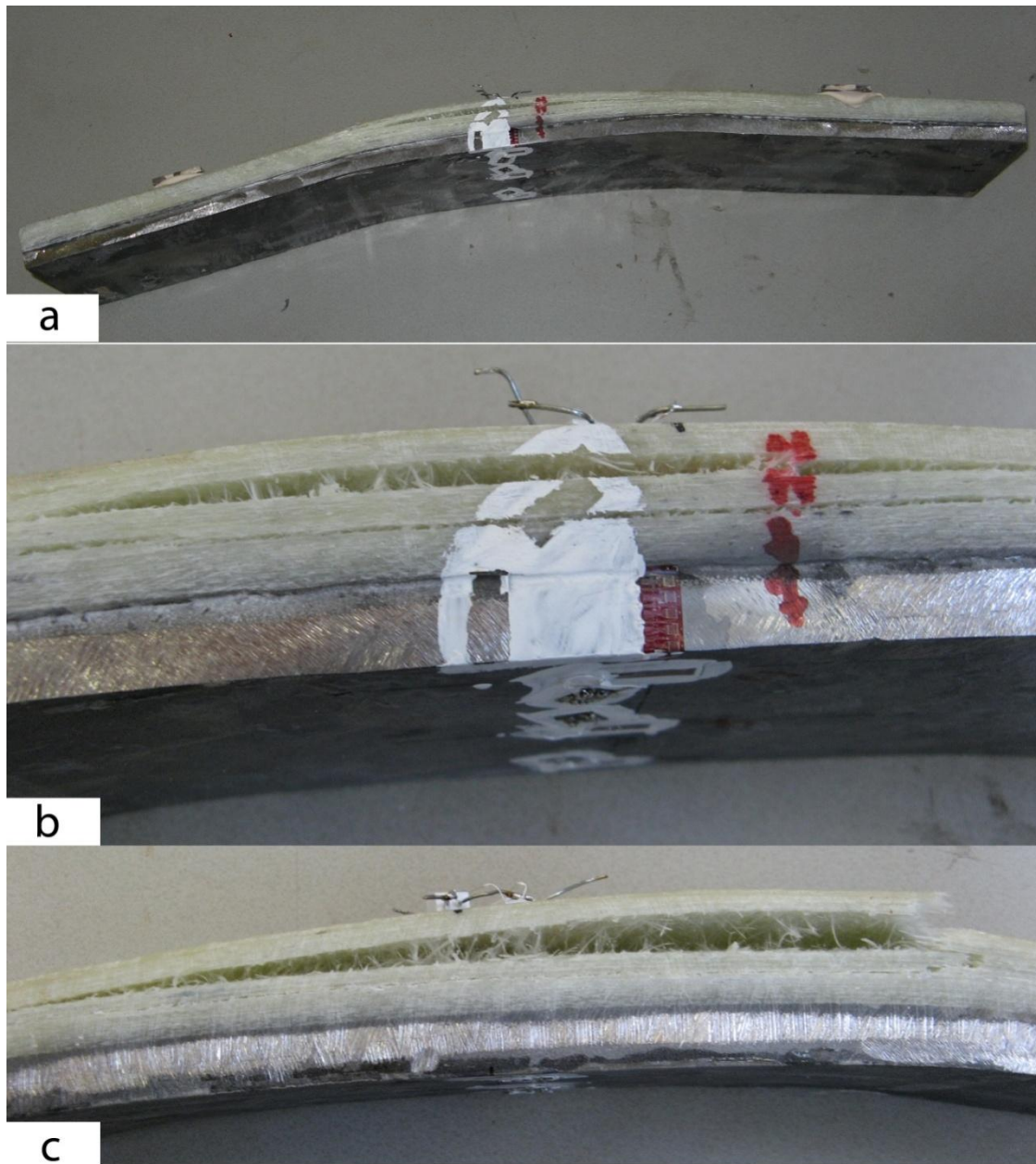


Figure 4.44 Failure of the composite plate BSC2

Now that the failure has been reviewed the evaluation of the results will follow. Starting with the force – vertical displacement diagram it can be seen that the relation between the force and the vertical displacement is linear till the force of 36 kN (yielding of the steel), at which point the curvature slightly changes.

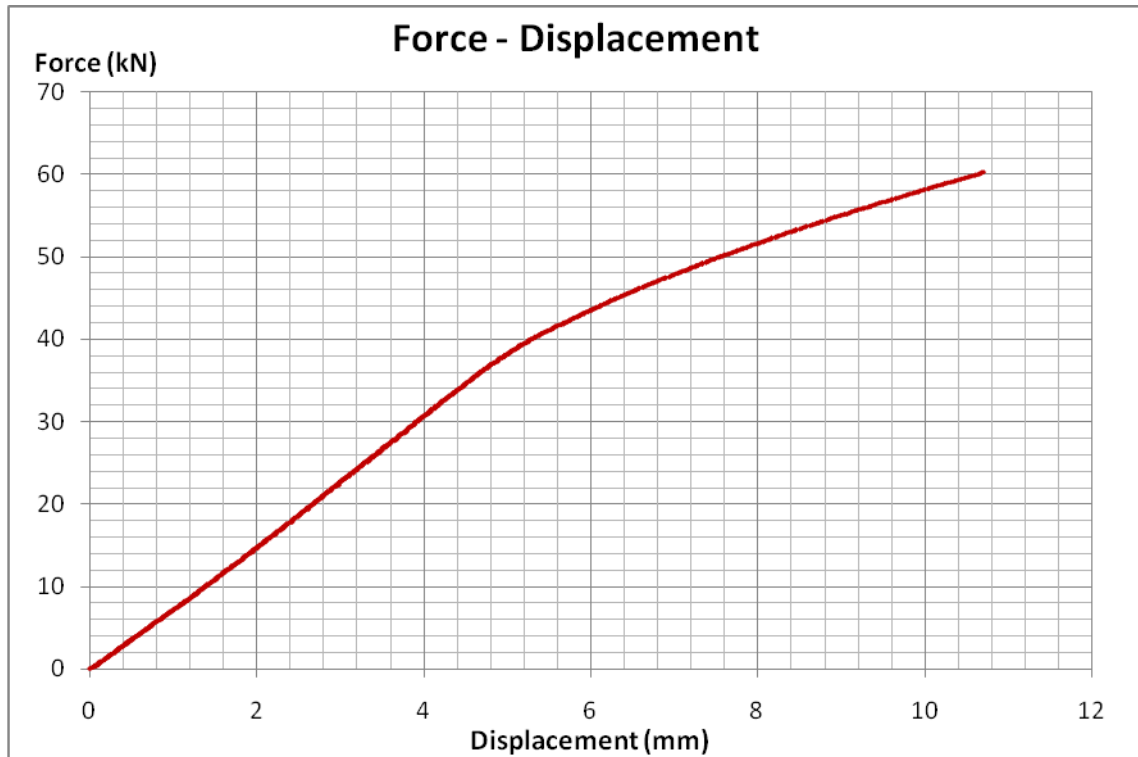


Figure 4.45 Force against vertical displacement diagram for specimen BSC2



Figure 4.46 Minimum normal stress (located at the outer surface of the steel plate) against force diagram for specimen BSC2

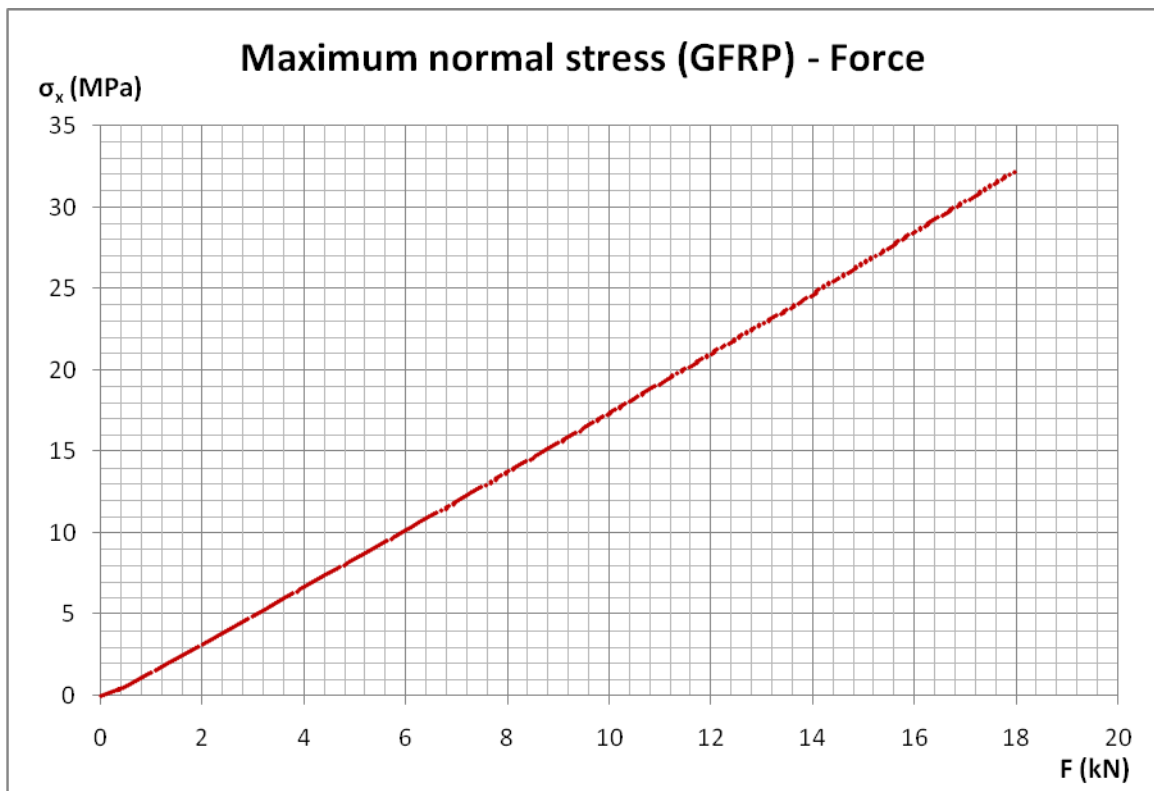


Figure 4.47 Maximum normal stress (located at the outer surface of the GFRP plate) against force diagram for specimen BSC2

Further on there are the stresses along the side of the steel plate are depicted. The stress was evaluated utilizing Hooke's law and since the strain gauges were attached on the steel plate, the strain was multiplied by 200 GPa which is the modulus of elasticity for the steel. From the stress distribution at the side of the steel plate (fig. 4.48) the position of the neutral axis can be evaluated (fig. 4.49).

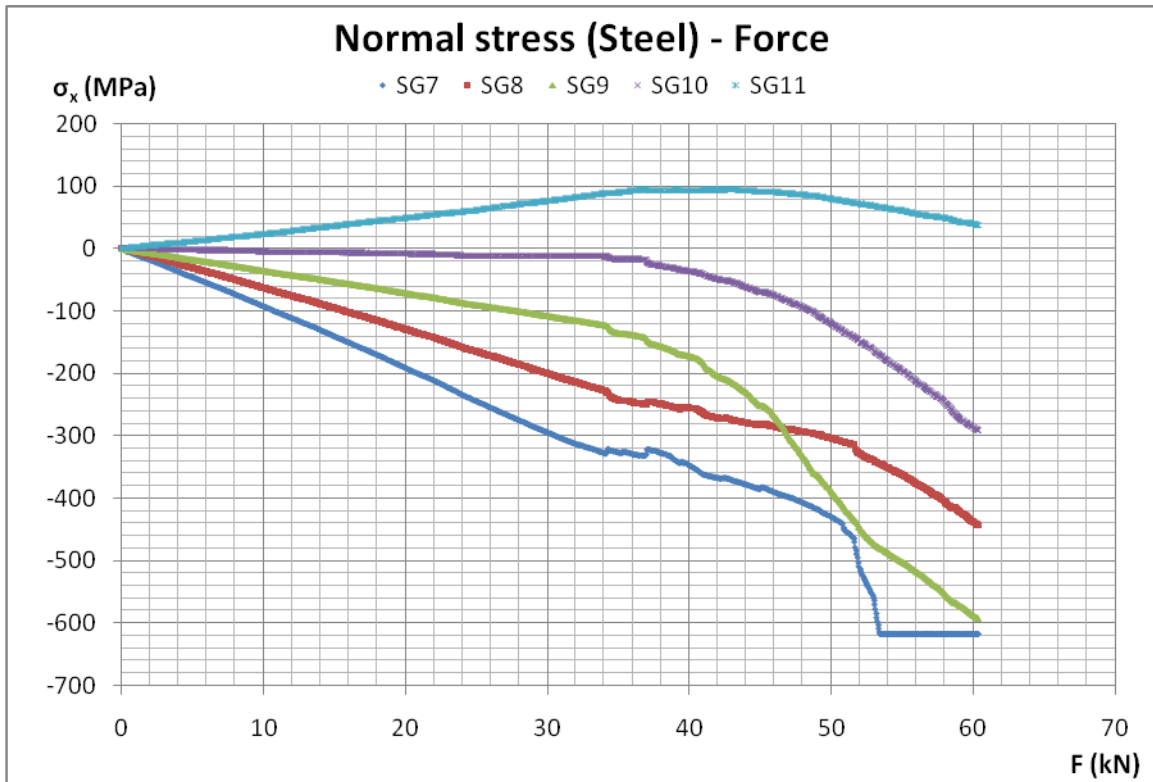


Figure 4.48 Normal stress along the side of the steel plate against force diagram for specimen BSC2

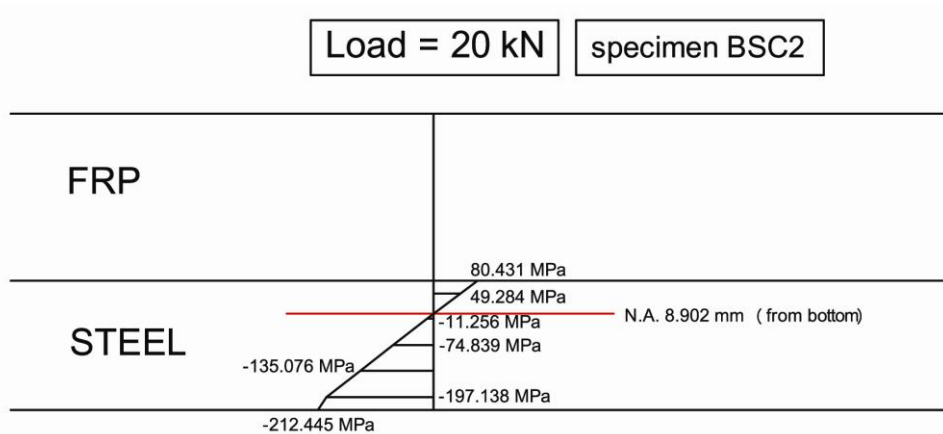


Figure 4.49 Normal stress distribution along the side of the steel plate for specimen BSC2

BSC3

Specimen BSC3 failed at a load of 63.037. In figure 4.50 the failed specimen can be seen as well as two more detailed photos of the failed area. The failure pattern seems to be very similar to the failure pattern of BSC2. The steel plate has again crossed to the plastic area and the FRP plate has developed shear cracks. In figures 4.50 b, c the weaving of the fibres can be seen. The plane of the fibres is vertical to the loading plane. No fibres exist in the height direction and in that direction the stress capacity of the plate is the capacity of the matrix, meaning the epoxy. That has as a consequence a rather low shear capacity of the FRP plate in comparison with the other properties of the material. The bonding between the two materials was retained throughout the entire experiment.

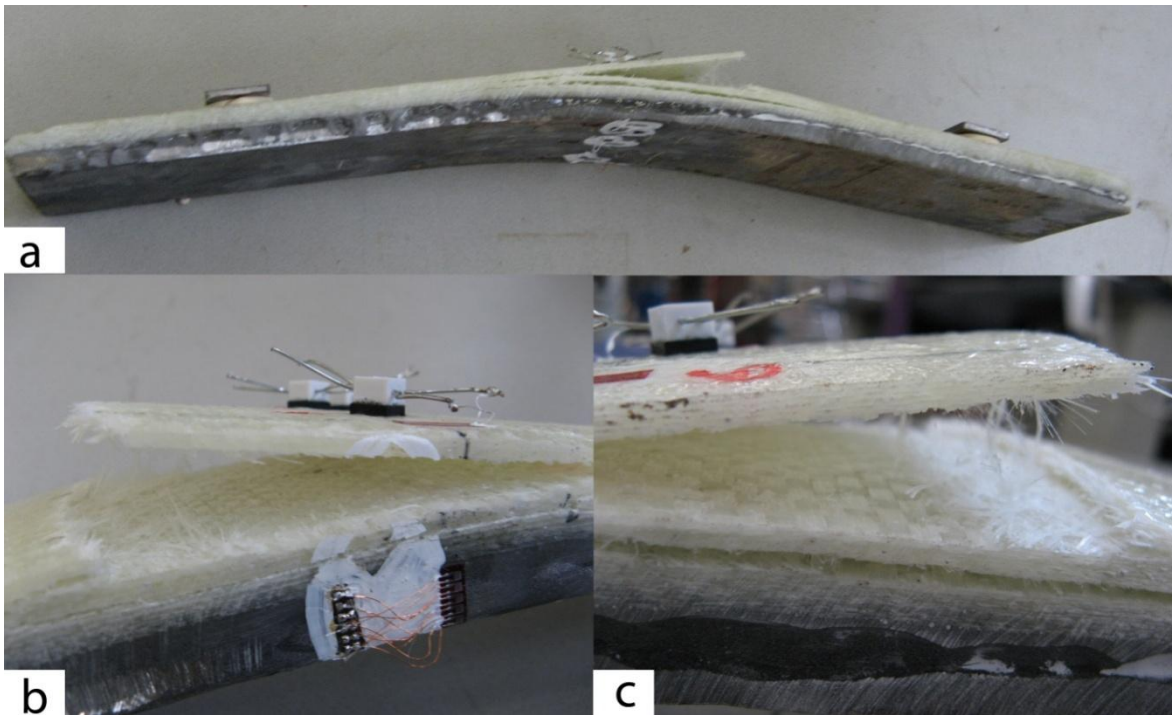


Figure 4.50 a, b, c Failure and details of specimen BSC3

Now that the failure pattern has been reviewed, the actual tests results will be presented. Starting from figure 4.51, a linear behaviour can be observed till a load value of 30 kN. After that point the curvature slightly change and stays approximately constant until failure.



Figure 4.51 Force against vertical displacement diagram for specimen BSC3

The stresses at the outer surface of the steel are depicted in figure 4.52. As expected the same linear behaviour is observed until the load of 30 kN has been reached. After that the steel starts to yield. The yielding stress seems to be close to 390 MPa, and higher than the one expected from a steel of Fe510 quality, which is 355 MPa, but it is still feasible. In figure 4.54 the stresses at the outer layer of the GFRP plate are depicted.



Figure 4.52 Minimum normal stress (located at the outer surface of the steel plate) against force diagram for specimen BSC3

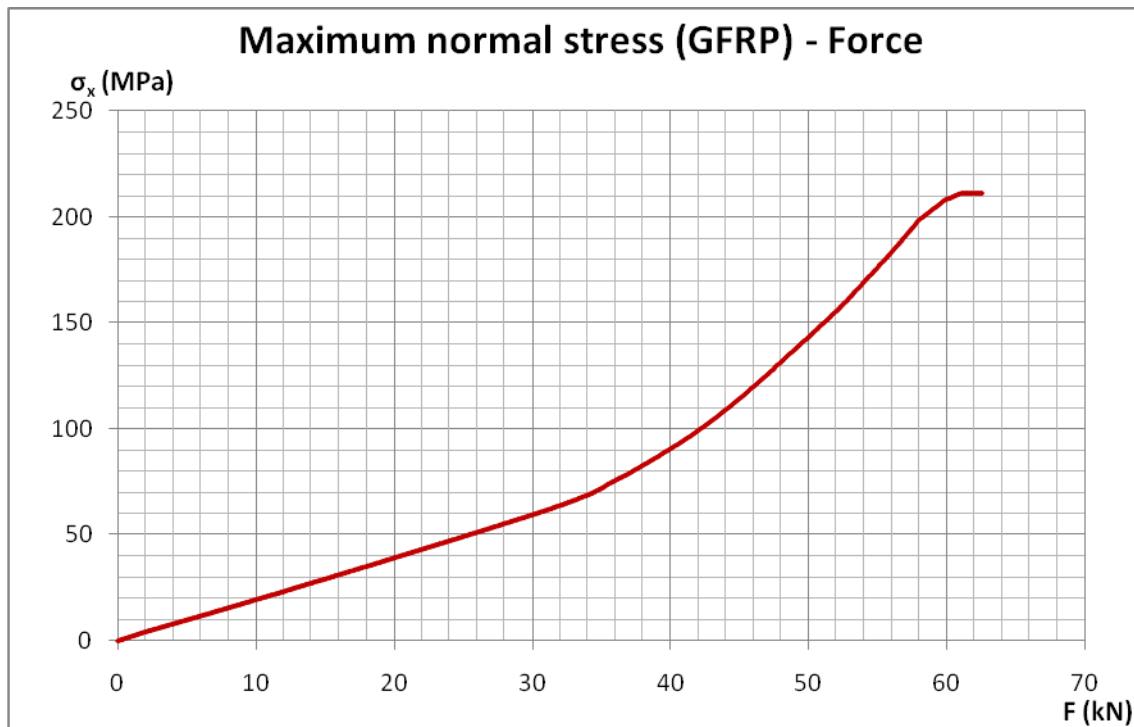


Figure 4.53 Maximum normal stress (located at the outer surface of the GFRP plate) against force diagram for specimen BSC3

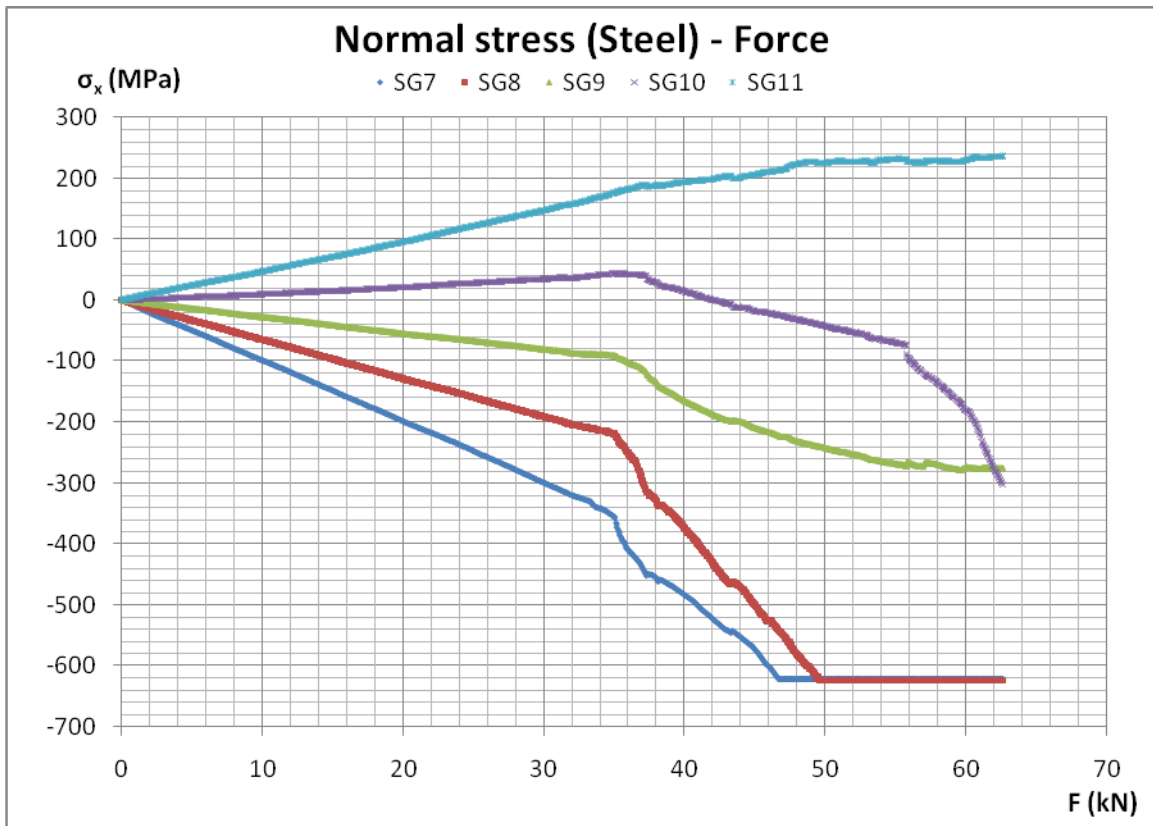


Figure 4.54 Normal stress along the side of the steel plate against force diagram for specimen BSC3

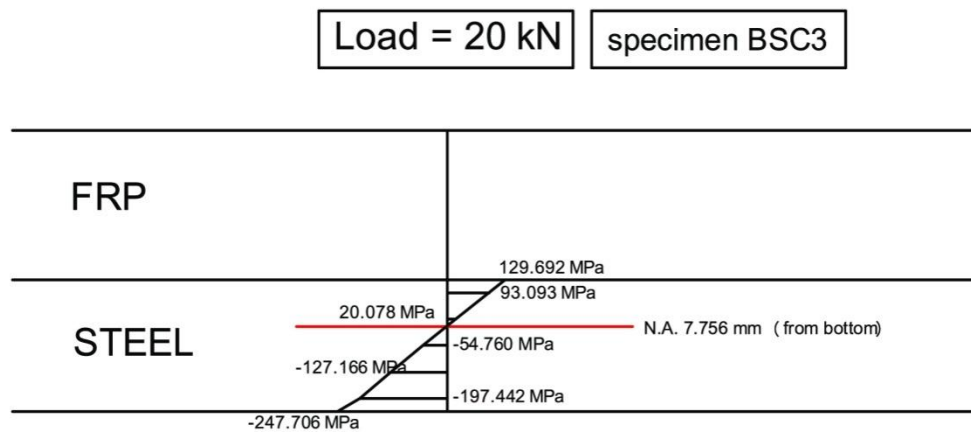


Figure 4.55 Normal stress distribution along the side of the steel plate for specimen BSC3

BSC4

Specimen BSC4 is the first specimen tested with configuration -2-. The reason for this configuration is that since the load would be located closer to the mid area of the specimen, there will be a larger area in which shear forces would develop. The difference regarding the failure pattern in comparison with the previous specimens is that the curvature is much higher which is caused by the fact that the loads were applied closer to the mid of the specimen causing the failure that can be seen in figure 4.56.



Figure 4.56 Failure and details of specimen BSC4

As expected the load failed in a much lower load value since because of the configuration used the moment was much higher. The same linear behaviour as before is observed till a value of 18.5 kN (yielding of the steel). The specimen finally fails at a load value of 37 kN. That kind of load is again really high, because it must be reminded that this high a load with the configuration used is highly unlikely if not impossible to occur in a bridge deck

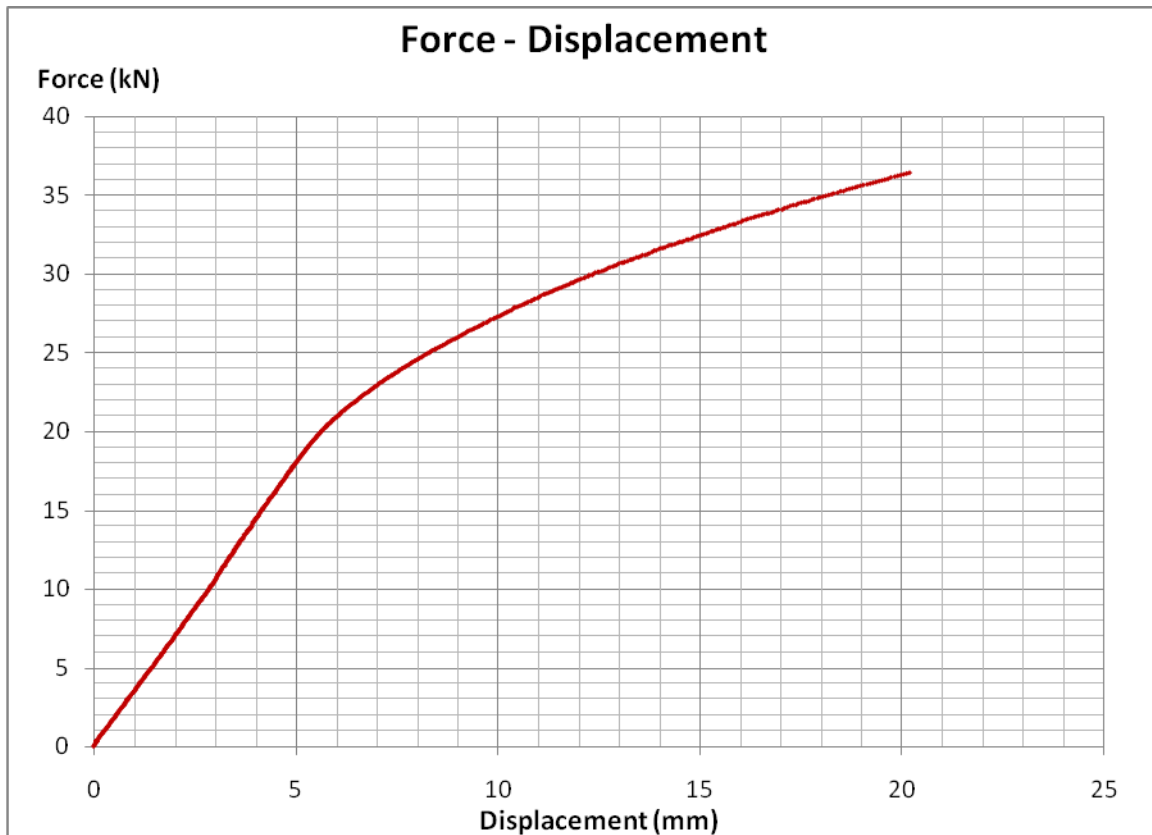


Figure 4.57 Force against vertical displacement diagram for specimen BSC4

The minimum steel stresses (fig 4.57) show the same linear behaviour as this is observed at the force – vertical displacement graph. The yielding is reached for a steel stress value of about 380 MPa which is consistent with the stress value estimated for BSC1 and really close to the theoretical value of 355 MPa.



Figure 4.58 Maximum normal stress (located at the outer surface of the GFRP plate) against force diagram for specimen BSC4

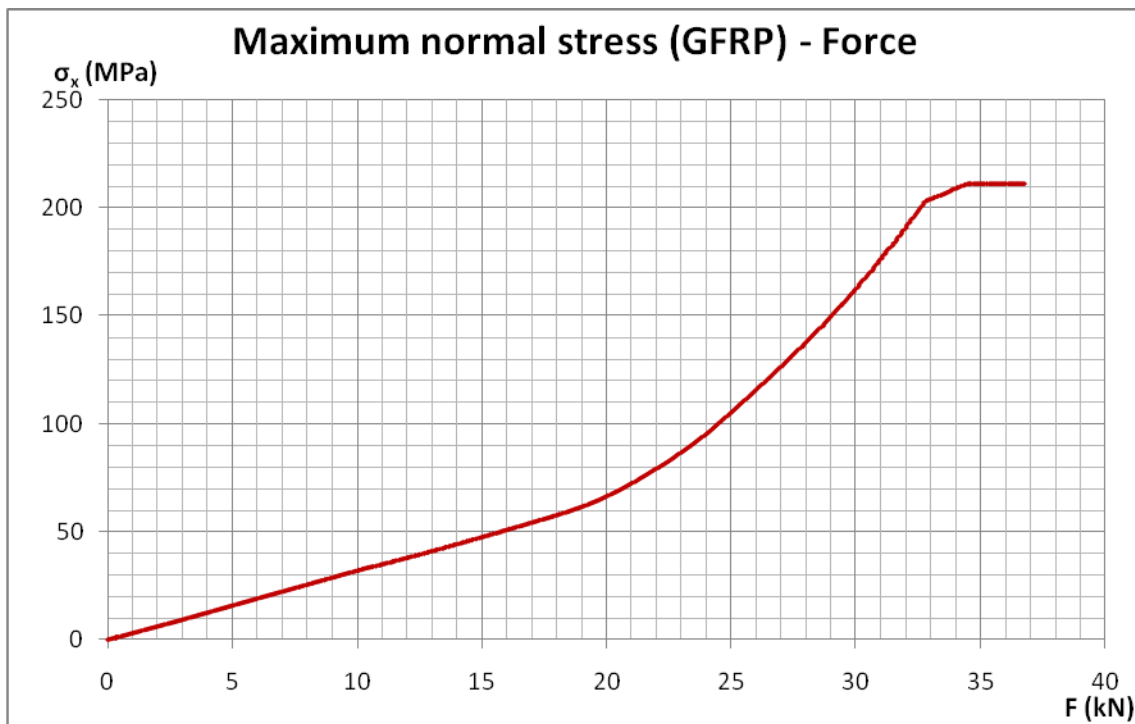


Figure 4.59 Maximum normal stress (located at the outer surface of the GFRP plate) against force diagram for specimen BSC4

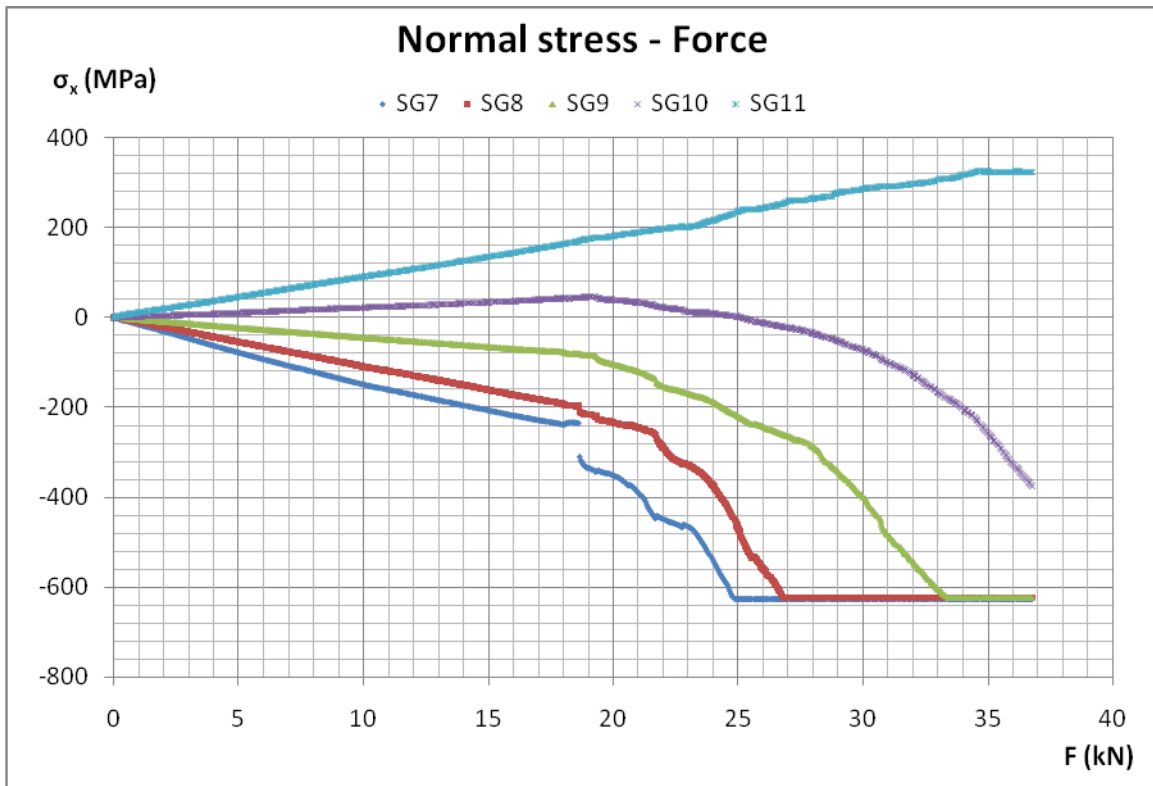


Figure 4.60 Normal stress along the side of the steel plate against force diagram for specimen BSC4

Finally, since the steel stresses at the side of the steel are known (fig 4.60) the position of the neutral axis can be determined and that is 7.610 mm from the outermost surface of the steel plate (fig 4.61).

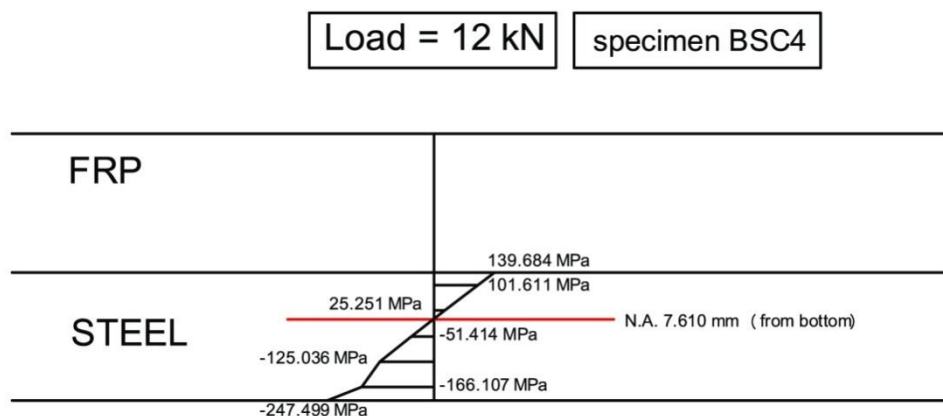


Figure 4.61 Normal stress distribution along the side of the steel plate for specimen BSC4

4.4.3.2 Specimens with the steel loaded in tension (BST)

BST1

BST1 is the first specimen that was used in a line of four specimens with the steel being loaded in tension. This is why the loading procedure till failure will be presented for this specimen. This will not be necessary for the following specimens, since it identical and the only difference is in the failure pattern and of course the actual tests results.

In figure 4.62 a the experimental configuration can be seen and also the point where the load is close to 0. The deflections start to increase (fig 4.62 b, c) and finally the failure of the specimen at a load of 50.390 kN.

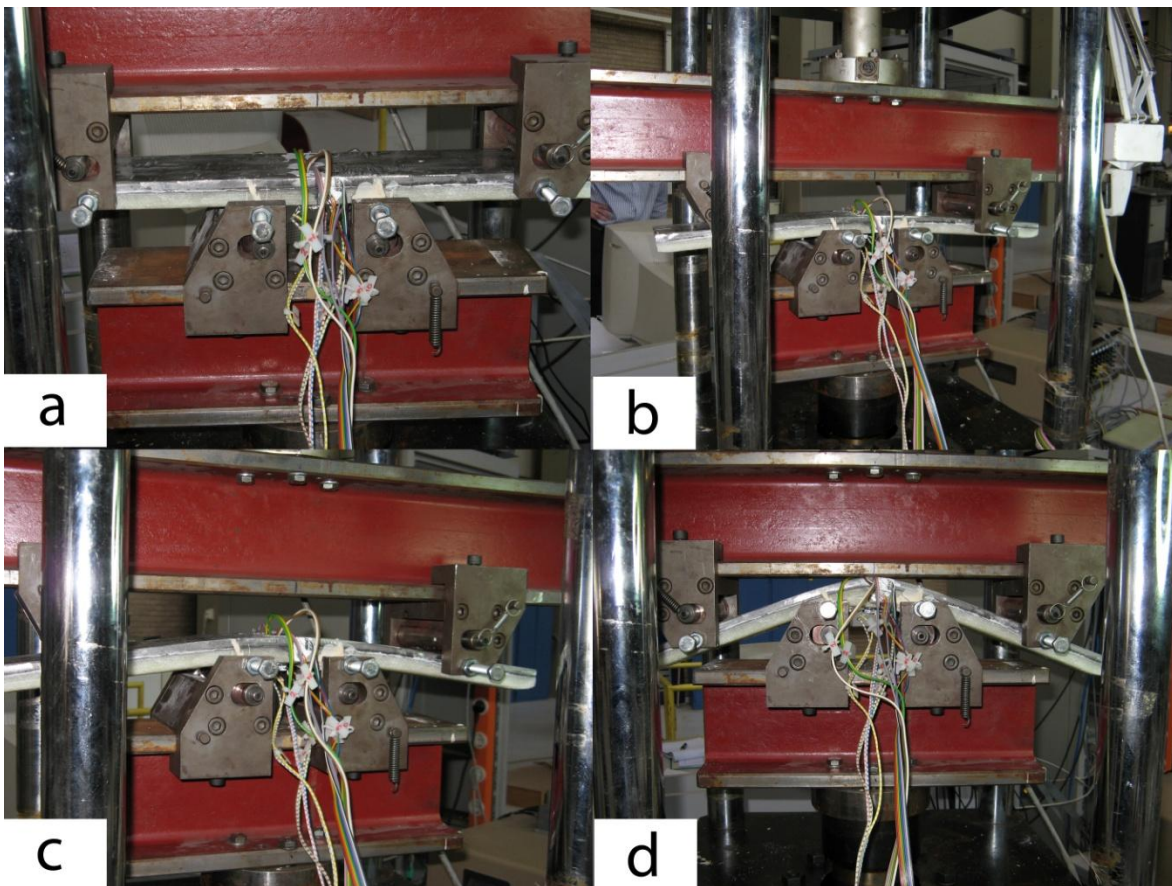


Figure 4.62 Composite plate BST1 in bending from large deflections to failure.

The failed specimen is depicted in figure 4.63 a. As in the BSC specimens the steel has entered in the plastic area and the FRP plate has failed. The failure was abrupt. Due to the fact that the steel entered the plastic area, the neutral axis transposed towards the FRP plate and the stresses transcend from zero to a maximum more abruptly causing the initial

crack to the outer surface of the FRP plate and due to the lack of fibres in the vertical plane cracks parallel to the plate appeared (fig 4.63 b,c).



Figure 4.63 Failure and details of specimen BST1

In the force against vertical displacement graph (fig. 4.64) a linear behaviour is observed until a value of approximately 25 kN which is due to the fact that the steel reaches its yield limit at which point the cross section starts to enter the plastic area. That is validated by the normal stress - force graph (fig. 4.65)

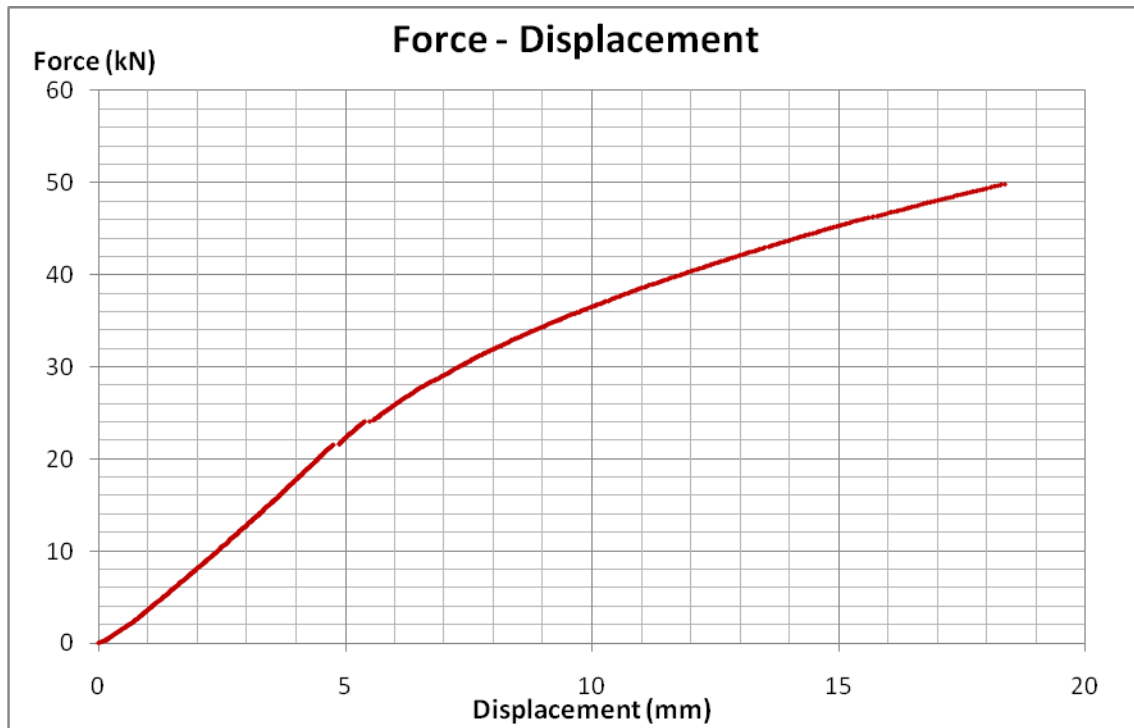


Figure 4.64 Force against vertical displacement diagram of specimen BST1



Figure 4.65 Maximum normal stress (located at the outer surface of the steel plate) against force diagram of specimen BST1



Figure 4.66 Minimum normal stress (located at the outer surface of the GFRP plate) against force diagram for specimen BST1

The stresses at the side of the steel are depicted in figure 4.67. As before choosing a value of 12 kN in which the behaviour is still linear the stress distribution can be plotted (fig. 4.68).

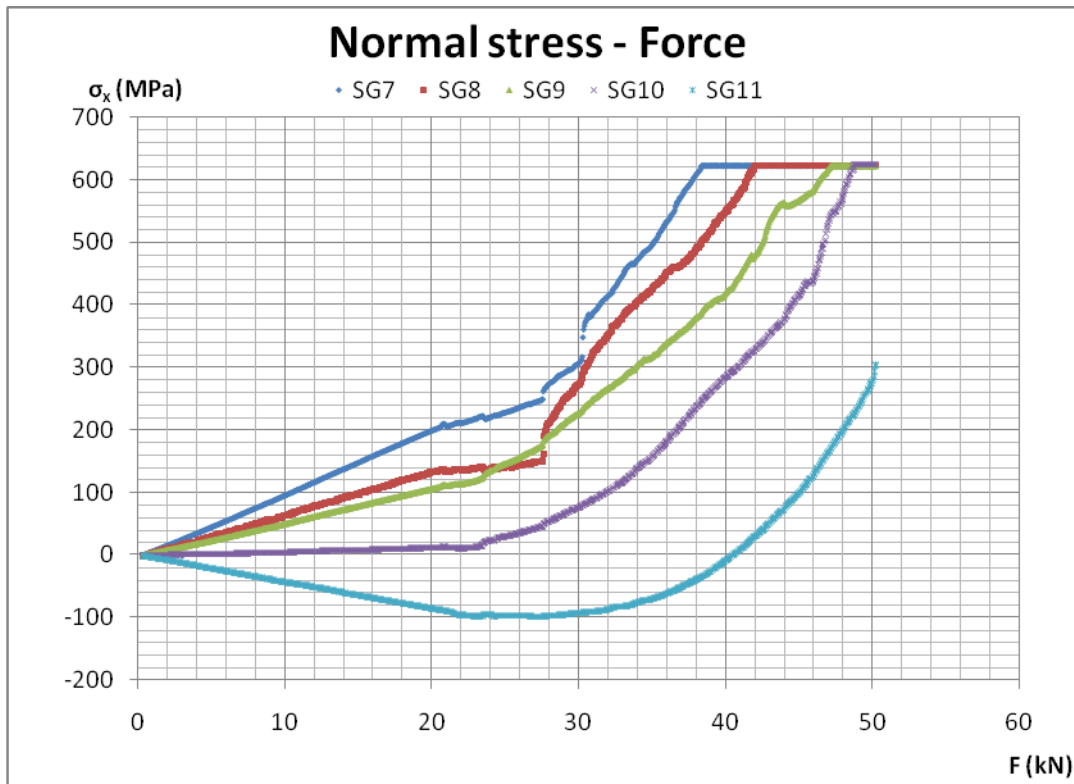


Figure 4.67 Normal stress along the side of the steel plate against force diagram of specimen BST1

From the plotting of the stresses the position of the neutral axis is at 8.622 mm from the outer surface of the steel plate.

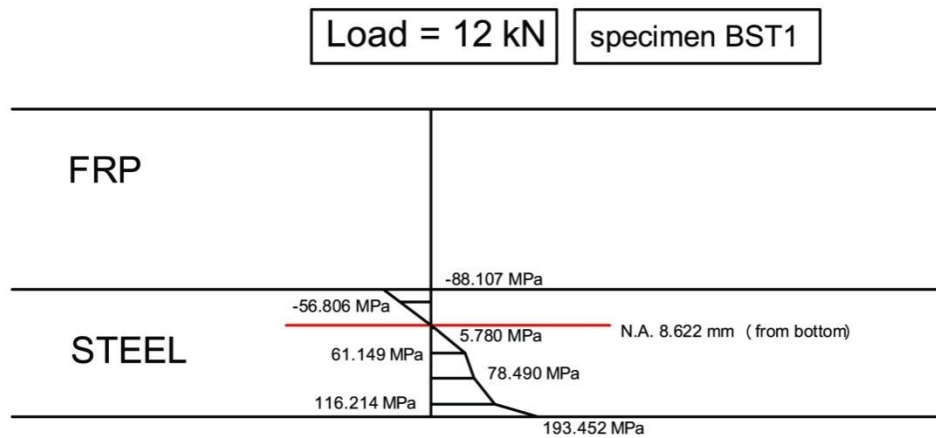


Figure 4.68 Normal stress distribution along the side of the steel plate of specimen BST1

BST2

The specimen failed at 45.1 kN. The failed specimen is depicted in figure 4.69 a. The steel has entered in the plastic area and the FRP plate has failed. The failure was abrupt. Due to the fact that the steel entered the plastic area, the neutral axis transposed towards the FRP plate and the stresses transcend from zero to a maximum value more abruptly causing the initial crack due to compression to the outer surface of the FRP plate and due to the lack of fibres in the vertical plane cracks parallel to the plate to appear (fig 4.69 b,c).

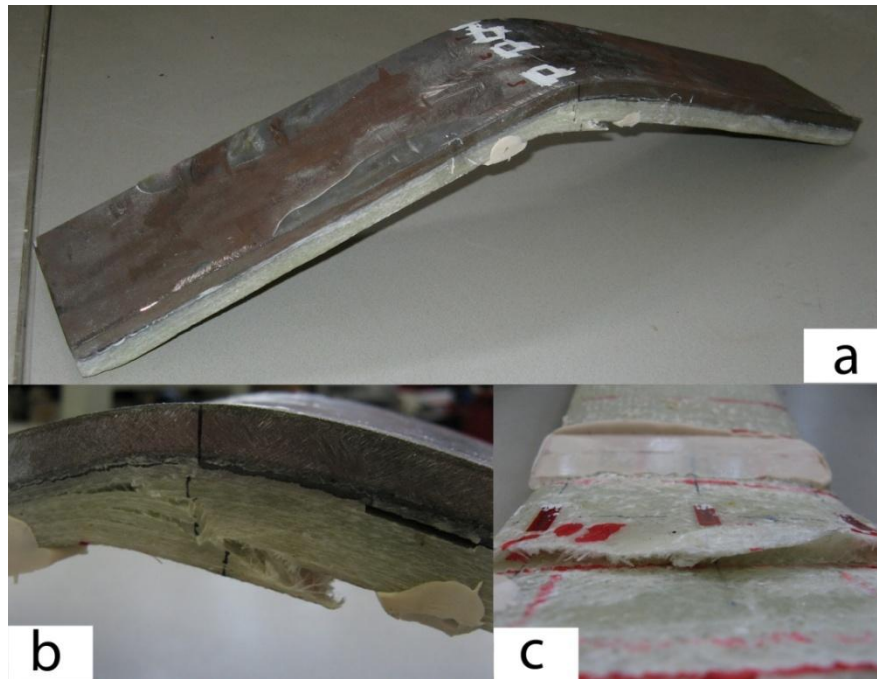


Figure 4.69 Failure and details of specimen BST2

In the force against vertical displacement graph (fig. 4.70) a linear behaviour is observed until a value of approximately 23 kN which is due to the fact that the steel reaches its yield limit at which point the cross section starts to enter the plastic area. That is validated by the normal stress - force graph (fig. 4.70)

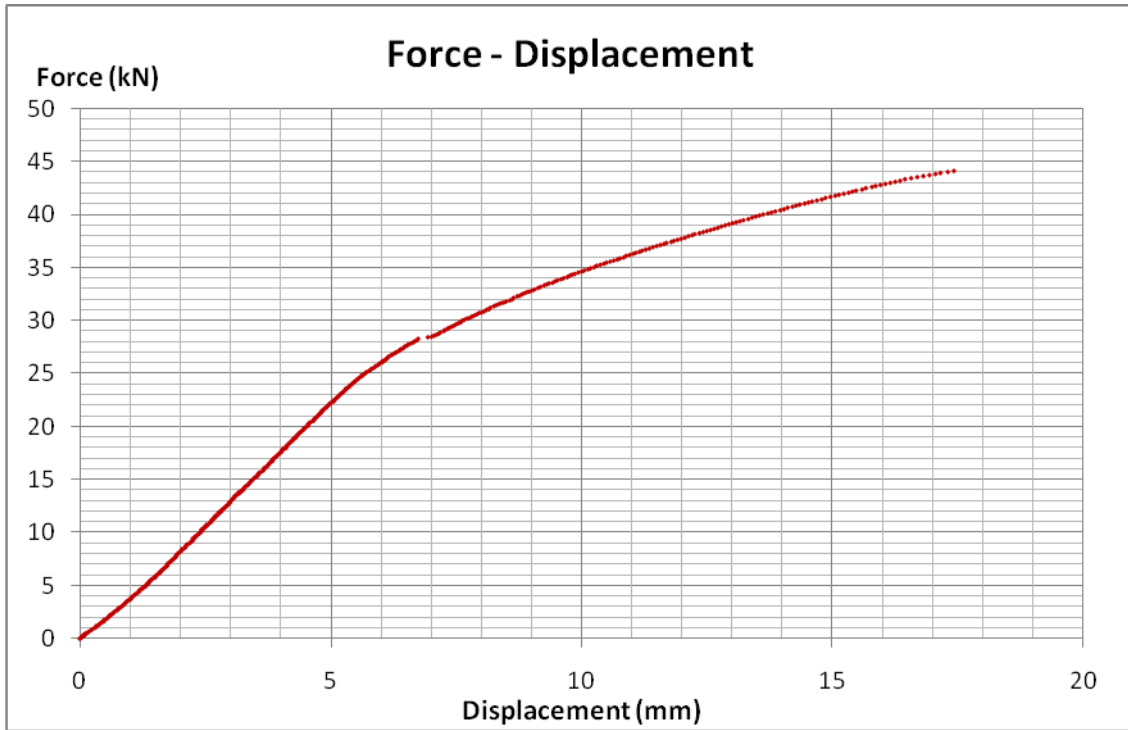


Figure 4.70 Force against vertical displacement diagram of specimen BST2



Figure 4.71 Maximum normal stress (located at the outer surface of the steel plate) against force diagram of specimen BST2

The stresses at the side of the steel are depicted in figure 4.73. As before choosing a value of 12 kN in which the behaviour is still linear the stress distribution can be plotted (fig. 4.74).

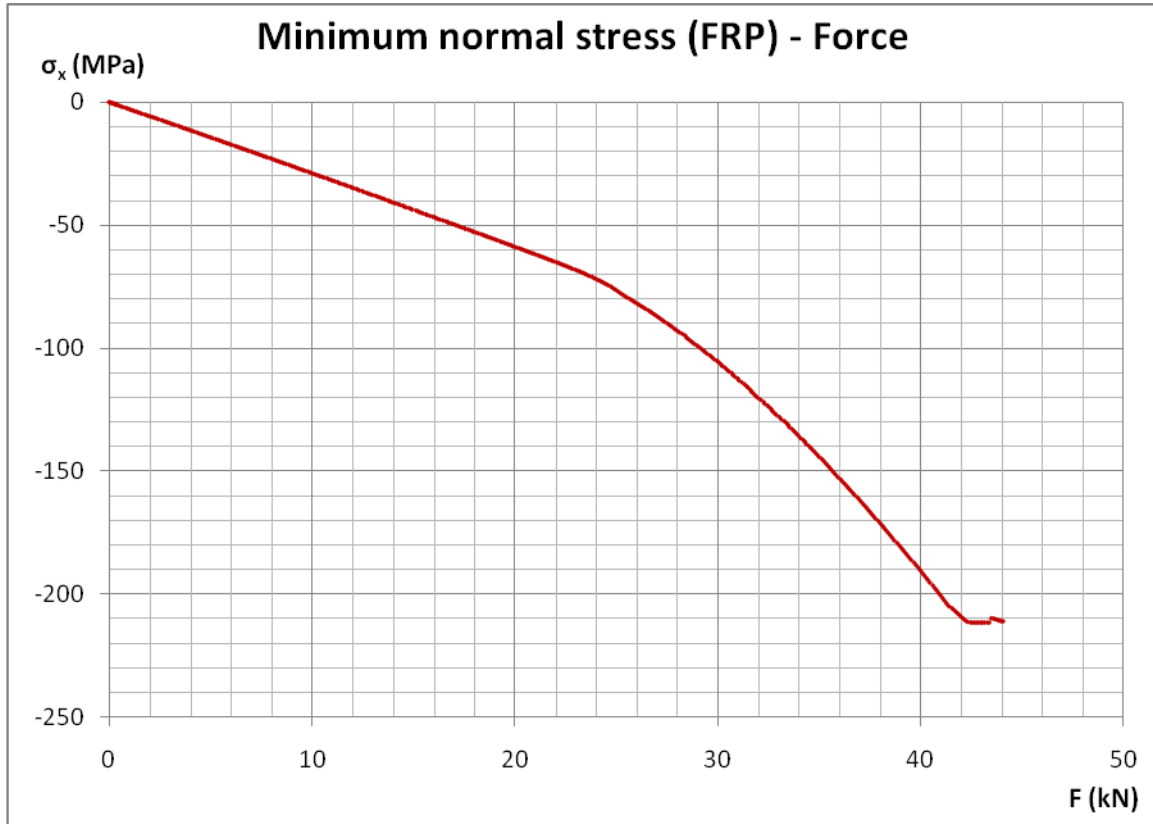


Figure 4.72 Minimum normal stress (located at the outer surface of the GFRP plate) against force diagram for specimen BST2

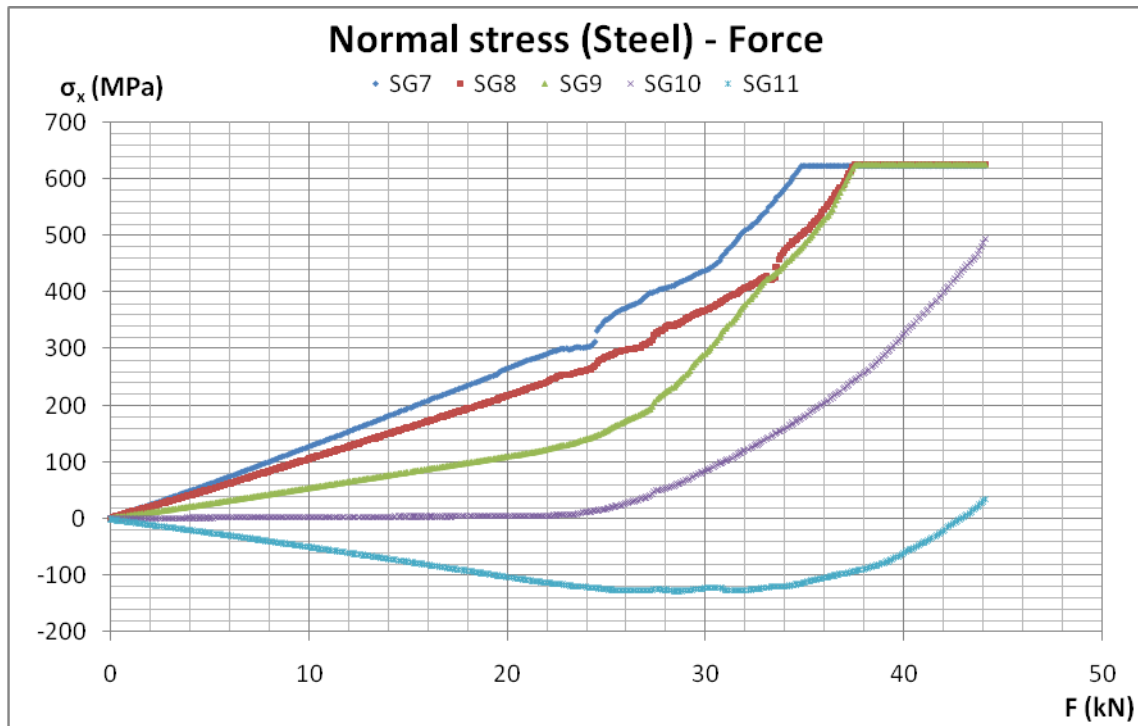


Figure 4.73 Normal stress along the side of the steel plate against force diagram of specimen BST2

From the plotting of the stresses the position of the neutral axis is at 8.573 mm from the outer surface of the steel plate.

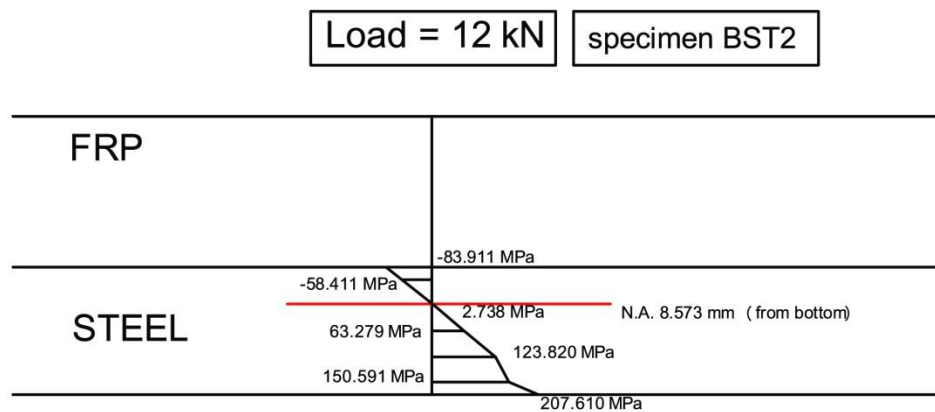


Figure 4.74 Normal stress distribution along the side of the steel plate of specimen BST2

BST3

This specimen reached a load value of 44.4 kN. At that value the actuator malfunctioned and it wasn't able to increase the load any more. Therefore the last value in the graphs is not failure. We were forced to unload the specimen and then increasing the loads with a much higher rate, the specimen cracked with a very similar pattern (fig. 4.75) to the previous specimens that is not necessary to be described again.

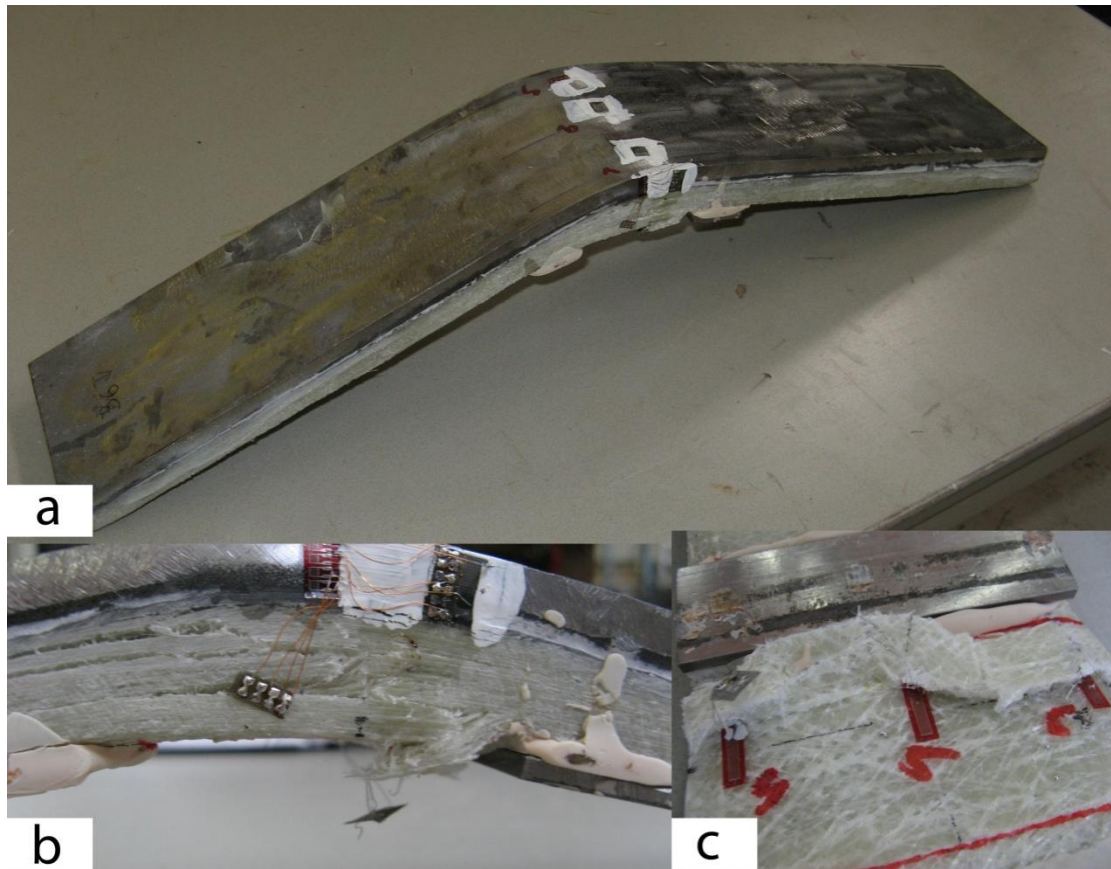


Figure 4.75 Failure and details of specimen BST3

In the force against vertical displacement graph (fig 4.76) a linear behaviour is observed until a value of approximately 23 kN which is due to the fact that the steel reaches its yield limit at which point the cross section starts to enter the plastic area. That is consistent with the normal stress - force graph (fig. 4.77)

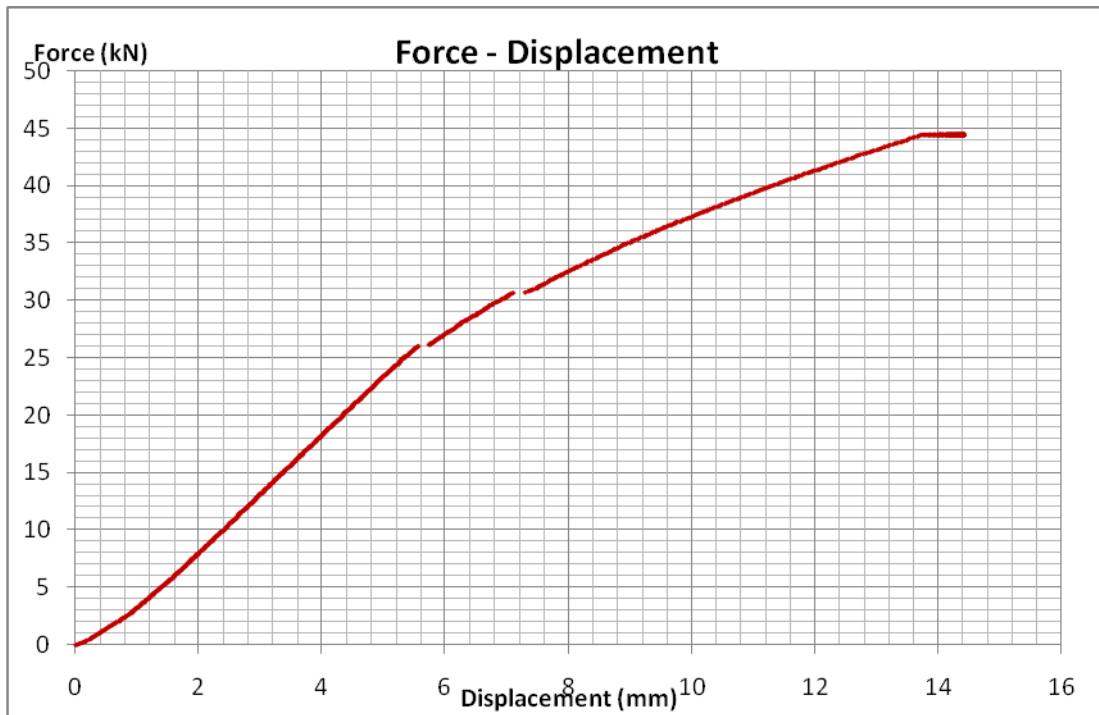


Figure 4.76 Force against vertical displacement diagram of specimen BST3

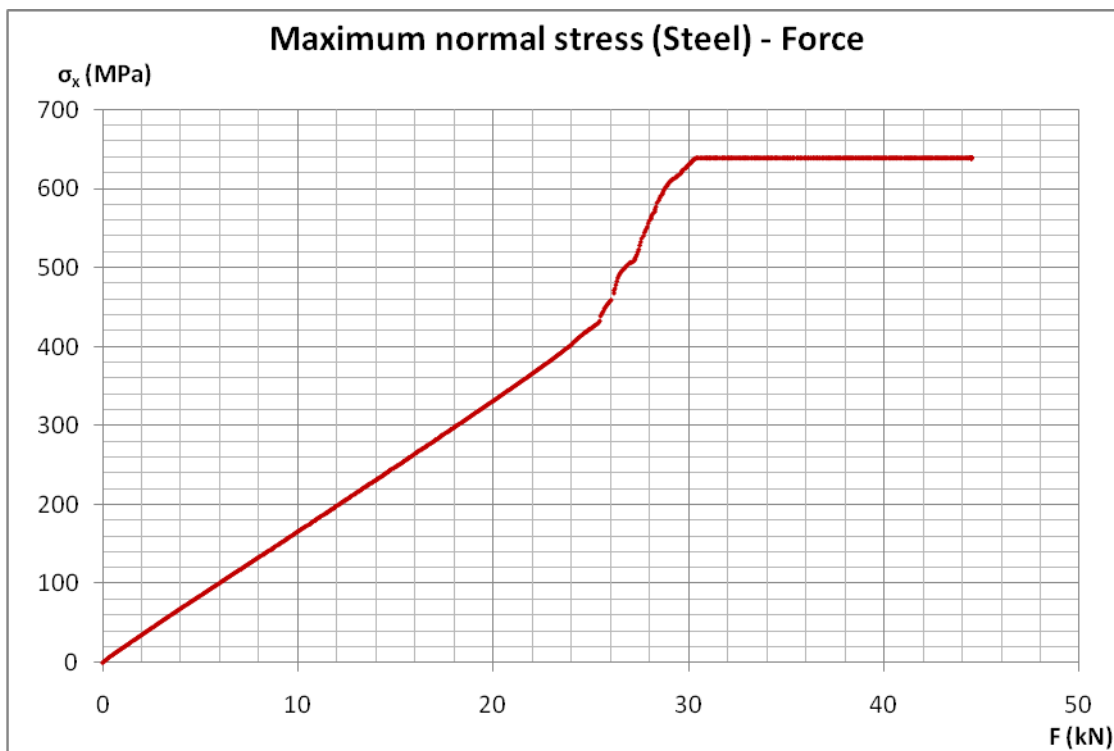


Figure 4.77 Maximum normal stress (located at the outer surface of the steel plate) against force diagram of specimen BST3

The stresses at the side of the steel are depicted in figure 4.79. As before choosing a value of 12 kN in which the behaviour is still linear the stress distribution can be plotted (fig. 4.80).



Figure 4.78 Minimum normal stress (located at the outer surface of the GFRP plate) against force diagram for specimen BST3

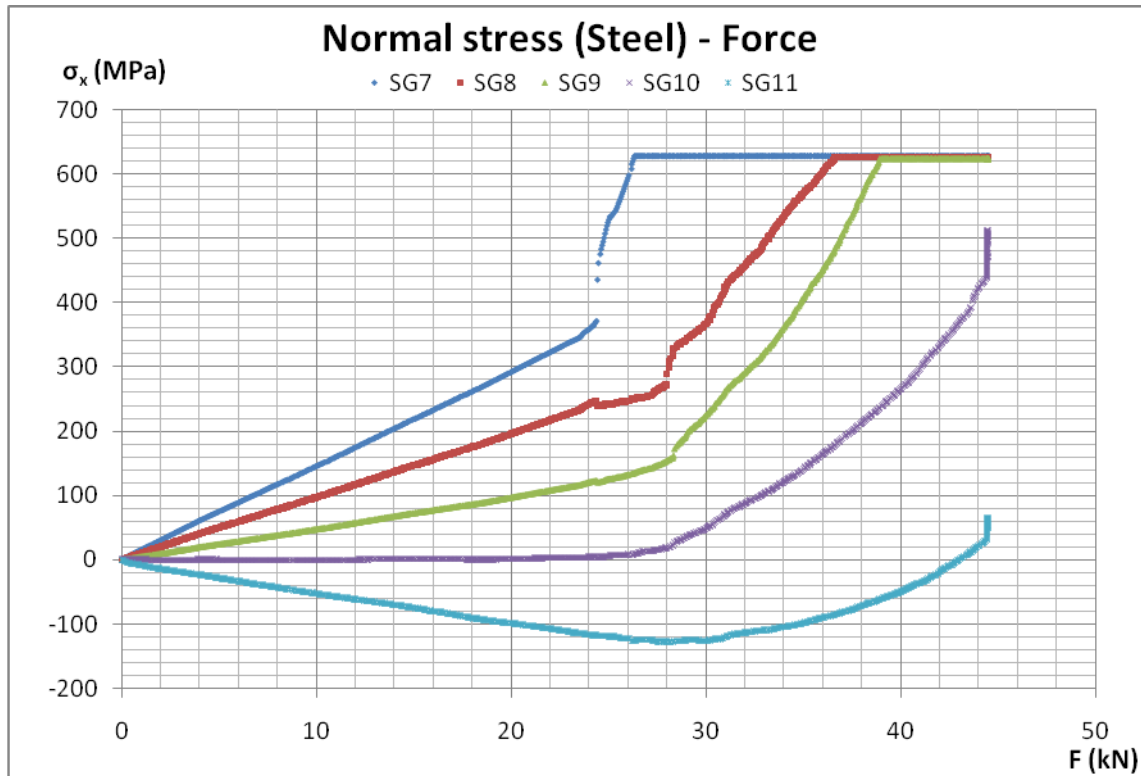


Figure 4.79 Normal stress along the side of the steel plate against force diagram of specimen BST3

From the plotting of the stresses the position of the neutral axis is at 8.374 mm from the outer surface of the steel plate (fig.4.80).

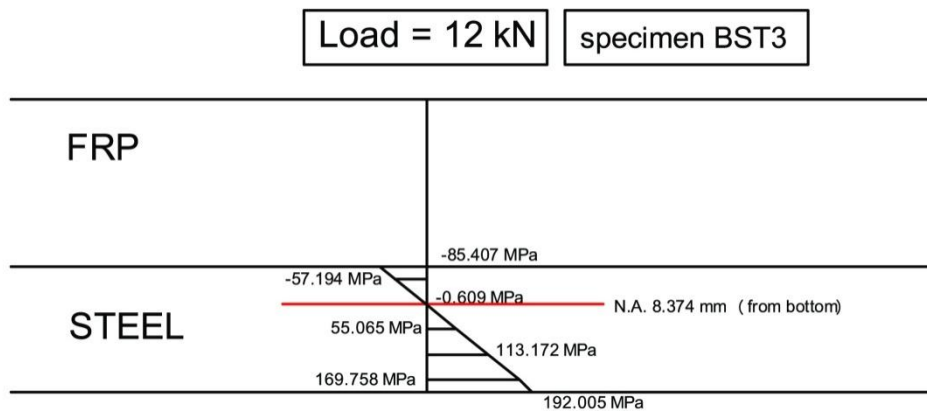


Figure 4.80 Normal stress distribution along the side of the steel plate of specimen BST3

BST4

This specimen failed at a load value of 61.0. The failed specimen is fairly similar with the previous three; therefore nothing else can be added to the description of the failure pattern (fig. 4.81).

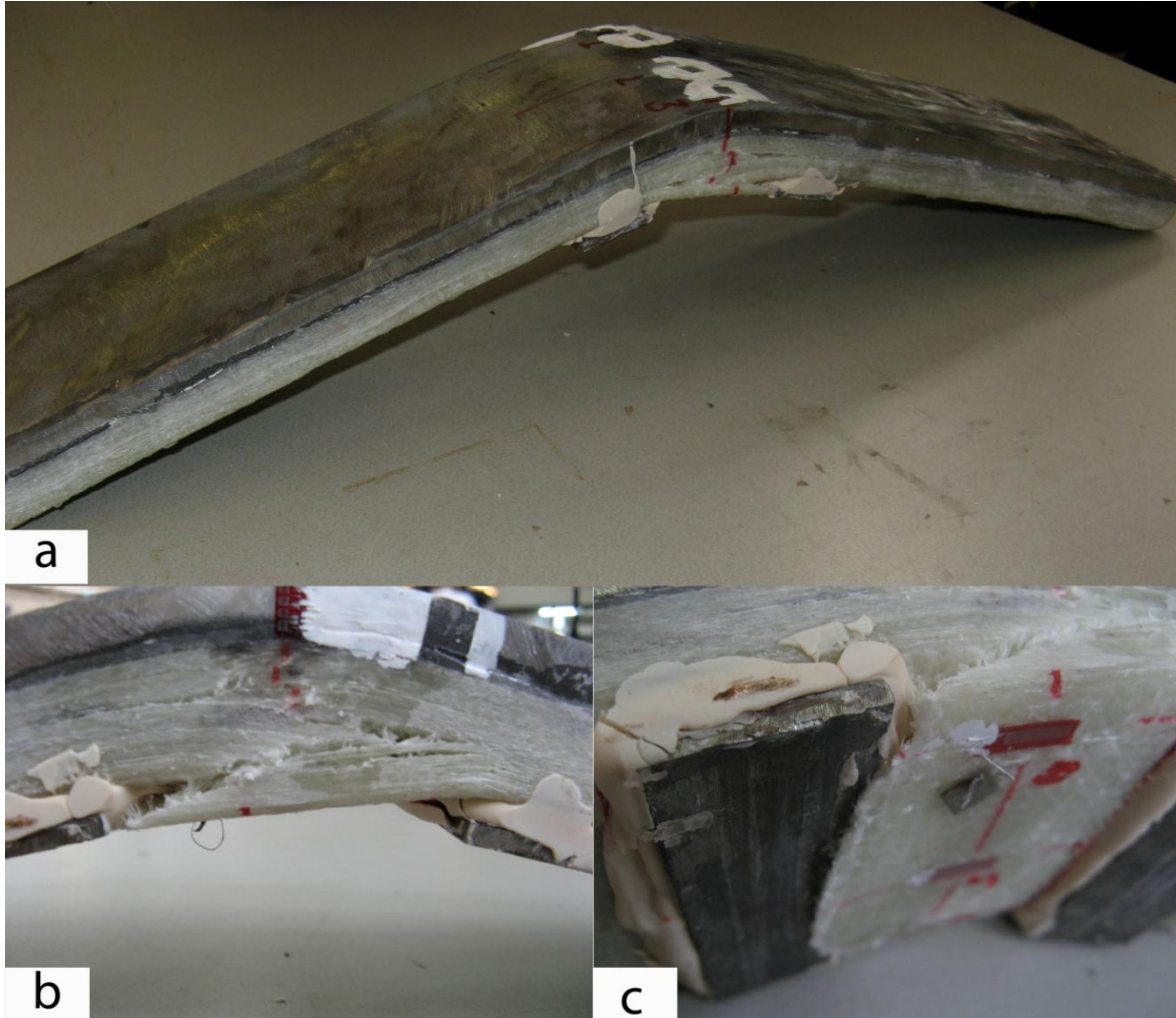


Figure 4.81 Failure and details of specimen BST4

In the force against vertical displacement graph (fig 4.82) a linear behaviour is observed until a value of approximately 30 kN which is due to the fact that the steel reaches its yield limit at which point the cross section starts to enter the plastic area. That is consistent with the normal stress - force graph (fig. 4.83).



Figure 4.82 Force against vertical displacement diagram of specimen BST4



Figure 4.83 Maximum normal stress (located at the outer surface of the steel plate) against force diagram of specimen BST4

The stresses at the side of the steel are depicted in figure 4.85. As before choosing a value of 12 kN in which the behaviour is still linear the stress distribution can be plotted (fig. 4.86).



Figure 4.84 Minimum normal stress (located at the outer surface of the GFRP plate) against force diagram for specimen BST4

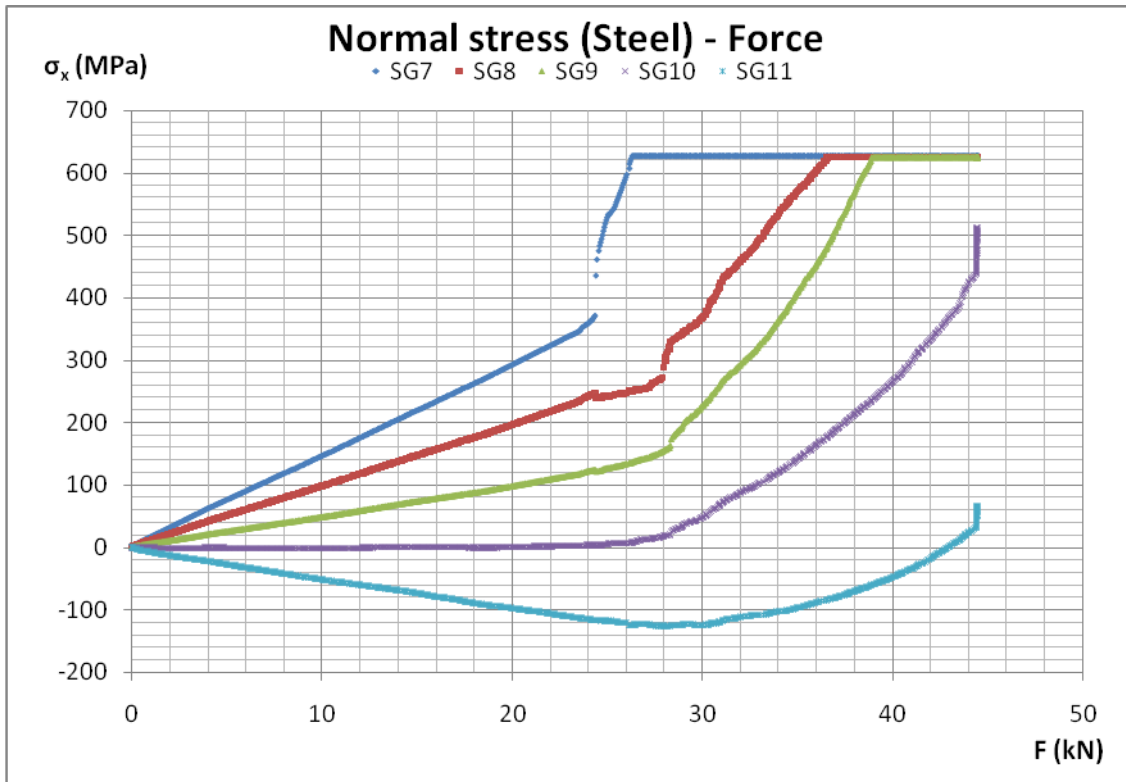


Figure 4.85 Normal stress along the side of the steel plate against force diagram of specimen BST4

From the plotting of the stresses the position of the neutral axis is at 8.716 mm from the outer surface of the steel plate.

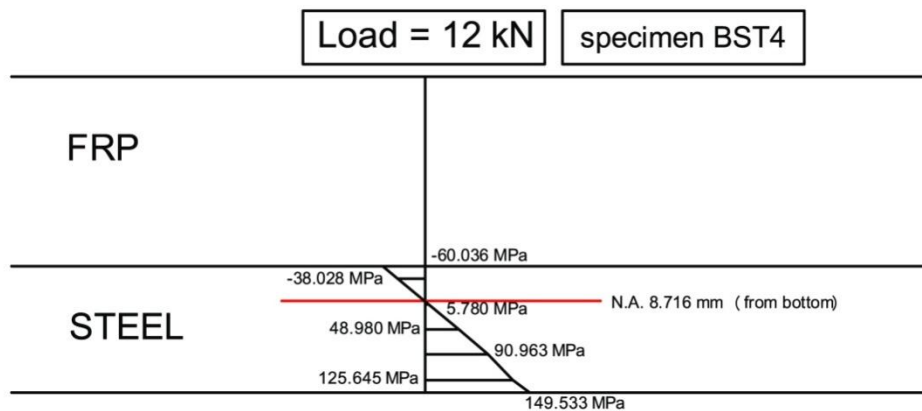


Figure 4.86 Normal stress distribution along the side of the steel plate of specimen BST4

4.5 Fatigue tests

Three fatigue tests have taken place. One experiment was on a steel plate and two on composite plates of G FRP and steel. Further on the experiments will be described and the results will be presented. The reason that only two fatigue tests were performed is, as it will be shown in the following paragraphs, that there was no failure or significant deterioration of the GFRP reinforced specimen. In general GFRP materials behave very well under fatigue loads due to the fact that they are not susceptible to micro-cracking which is one of the main problems when having to do with fatigue loading.

4.5.1 Steel plate

4.5.1.1 Experiment description

The steel plate used had dimensions of 600 mm x 99.40 mm x 12 mm. The plate was simply supported and the length that was finally tested was $l = 400$ mm. The load was applied via cylinders at the $l/4$ (100 mm) and $3 l/4$ (300 mm) of the supported length. The total cyclic load had an average range of 4.25 kN and had a frequency of 4 Hz. As already mentioned the load was applied via two cylinders which means that each cylinder, due to symmetry transfers a load of $4.25 \text{ kN}/2 = 2.125 \text{ kN}$. The configuration can be seen in the following figure. This actually is configuration -1- that was used in the previous experiments (fig.4.15).



Figure 4.87 Experimental configuration for the steel plate

Because of symmetry there was only one strain gauge (for measurement of the strains) used in the mid span area (fig 4.88) and no LVDT (for measurement of the displacement).



Figure 4.88 The strain gauge at the mid span area on the steel plate

4.5.1.2 Results

The results that will be presented for this experiment are the force and the vertical displacement at $1/4$ and $3/4$ of the supported length (that is because the displacement was measured by the displacement of the piston that applied the force) against the number of cycles as well as the normal stresses at $1/2$ in the longitudinal direction against the number of cycles. In figure 4.89 the applied force range versus displacement are depicted while in figure 4.90 the normal stress.

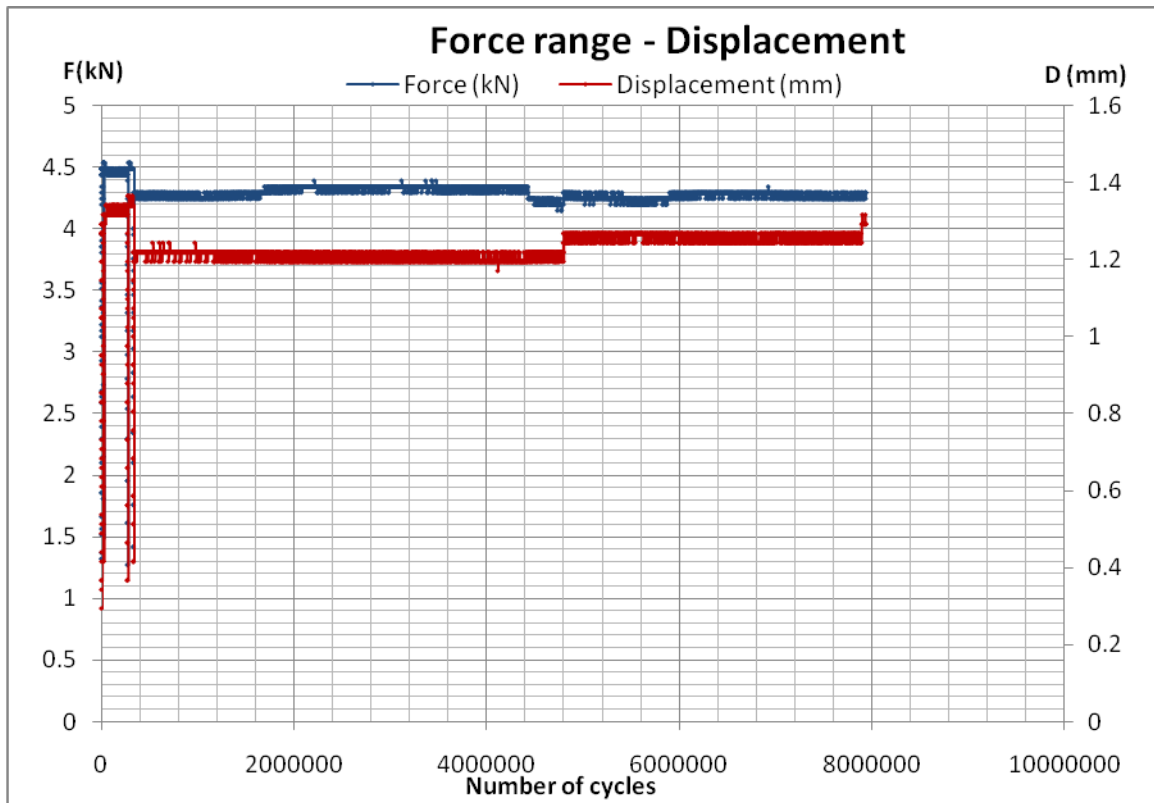


Figure 4.89 Force range – vertical displacement at 1/4 of the supported length diagram for the steel plate

It should be noted that the measurements taken from the strain gauges are in μ -strain. To convert them into stress the strain measurements were multiplied according to Hooke's law by the modulus of elasticity of the material to which they were attached. Although this is the Hooke's law for the one dimensional stress strain case, it is safe to assume that the stress results by the use of Hooke's law will be sufficiently correct and the error will be insignificant. The modulus of elasticity for the steel plate is known and it is 200 GPa.

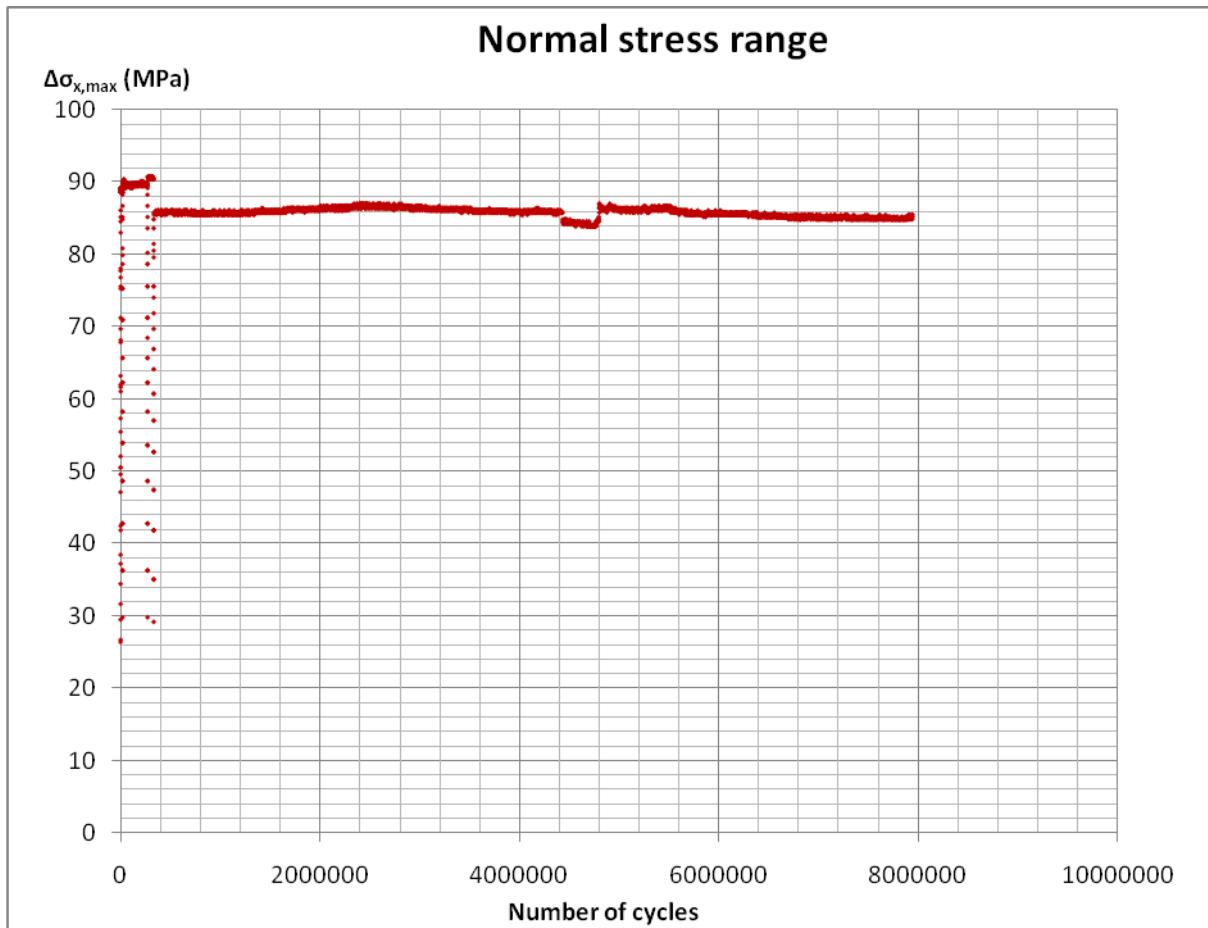


Figure 4.90 Maximum normal stress range $\Delta\sigma_x$ against number of cycles

At this point it must be mentioned that the stresses were found by the corresponding strains measured by the strain gauges by multiplying with the modulus of elasticity. Although it is a three-dimensional structure, the error of using the Hooke's law for one-dimensional conditions will be insignificant. The results will be verified in the following chapter by hand calculations. Nonetheless according to the EC, a minimum level of detail category of $\Delta\sigma_x = 125$ MPa, can be used and depending to the quality of the cutting planes a higher value up to 160 MPa can be used. The cut off limit for lowest category is

$$\Delta\sigma_x = \frac{2}{5}^{1/5} \times 120 \text{ kN} = 100 \text{ kN} \text{ and therefore no fatigue cracks are expected to appear.}$$

4.5.2 Composite plates

4.5.2.2 Experiment description

As already mentioned there were two experiments made for the case of the composite plates. In both cases the FRP plate was in tension and the steel plate was in compression. The configuration used was exactly the same as the one used for the test of the steel plate (fig 4.91).

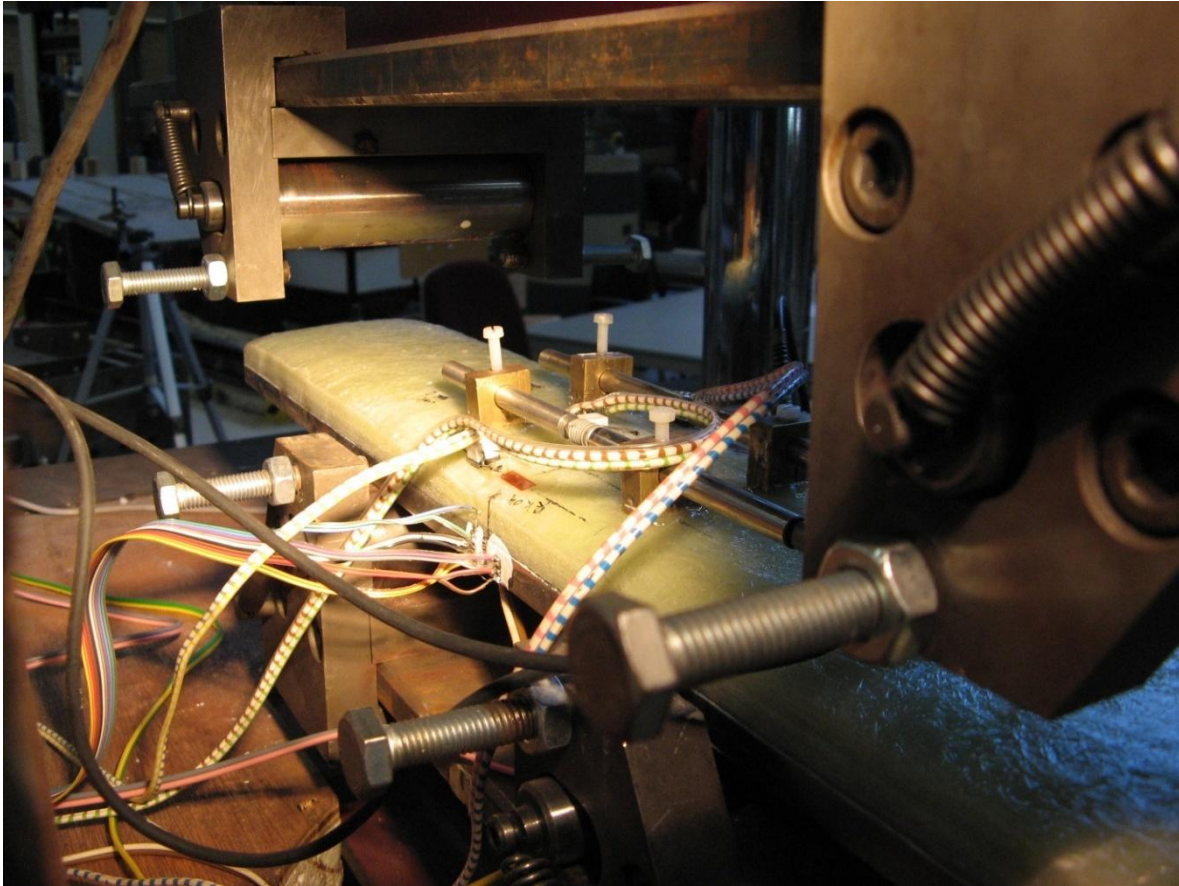


Figure 4.91 Experimental configuration for the composite plate

Three strain gauges were used at the mid span area, at the top and bottom surface of the composite plate, which means three on the steel plate and three on the FRP plate which can be seen in figure 4.92 and 4.93 respectively.

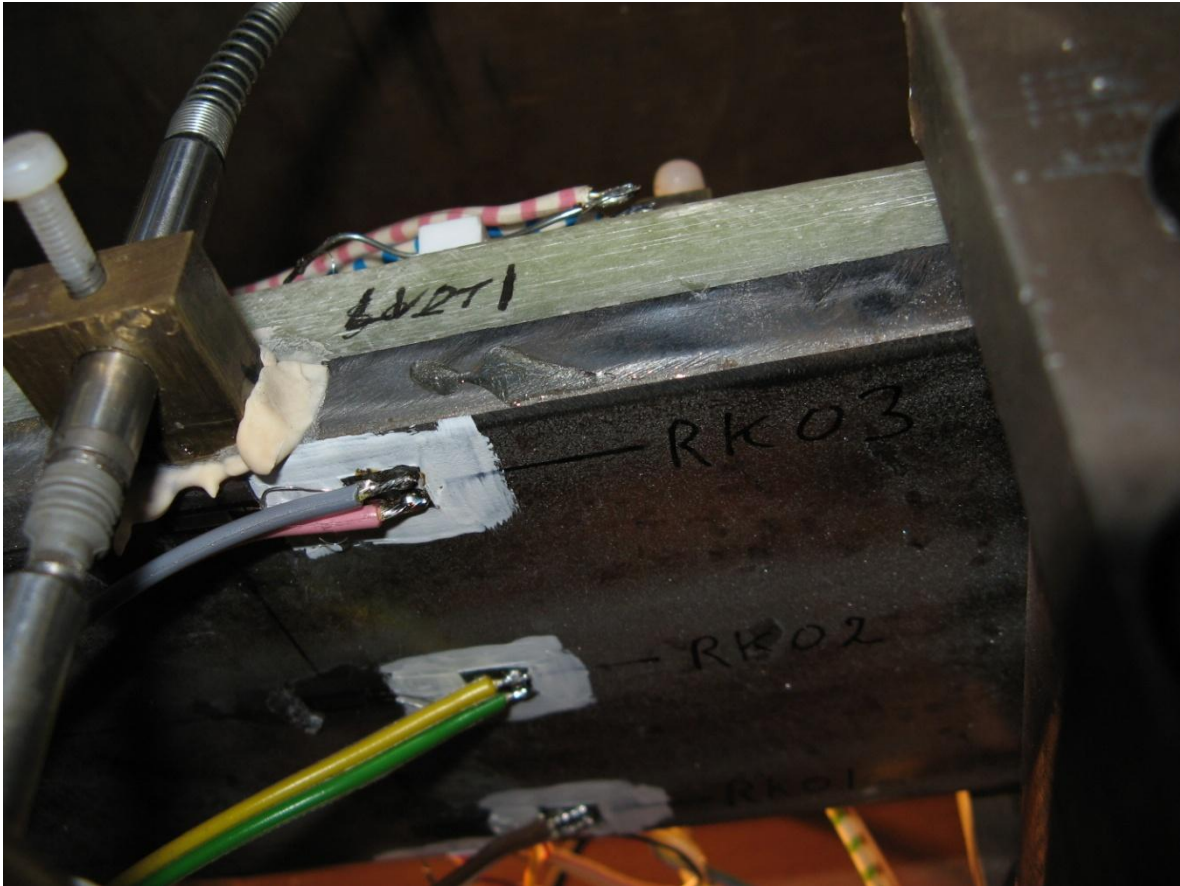


Figure 4.92 Strain gauges on the steel plate in the mid span area



Figure 4.93 Strain gauges on the FRP plate in the mid span area

Also 5 strain gauges were used at the side of the steel plate again in the mid span area (fig 4.94).

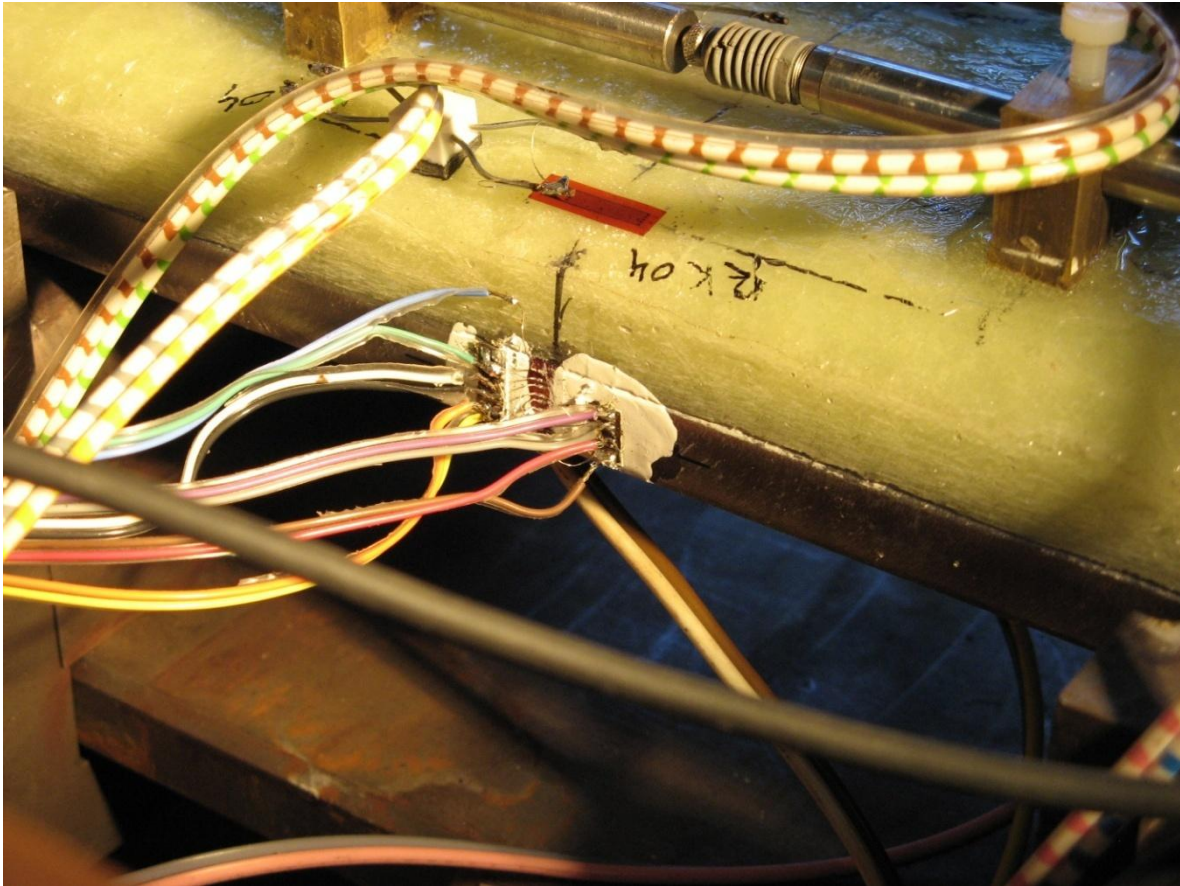


Figure 4.94 Strain gauges at the side of the steel plate on the mid span area

Finally, for the measurement of the displacements there were three LVDT placed. Two on top of the FRP plate, measuring displacement in the longitudinal direction and one on the steel plate measuring vertical displacement (fig 4.95).

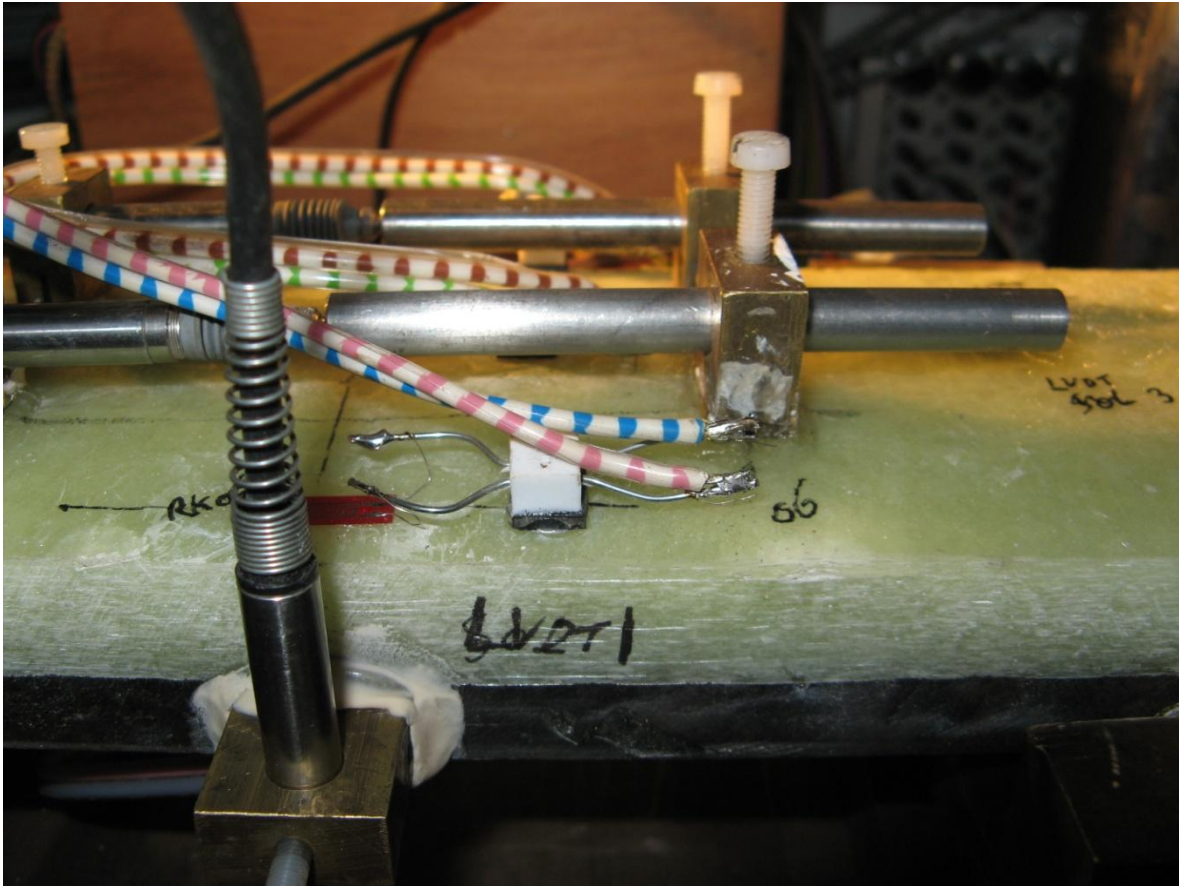


Figure 4.95 LVDT for the measurement of the displacement

4.5.2.3 Test results

In the following figures the force range and the vertical displacement of the plate at $1/4$ and $3/4$ of the supported length against the number of cycles as well as the normal stress range in the longitudinal direction against number of cycles will be presented. Also the stress ranges along the side of the steel plate against the number of cycles. The maximum and minimum stress range is an average of the three strain gauges on the top of the FRP plate and on the bottom of the steel plate respectively. For the following figures case 1 will be the first experiment on composite plate with an average load range of 15 kN and a frequency of 1 Hz, while case 2 the second load with an average load range of 23 kN and a frequency of 1.2 Hz.

As already mentioned for the evaluation of the stress, Hooke's law for the one dimensional case is used.

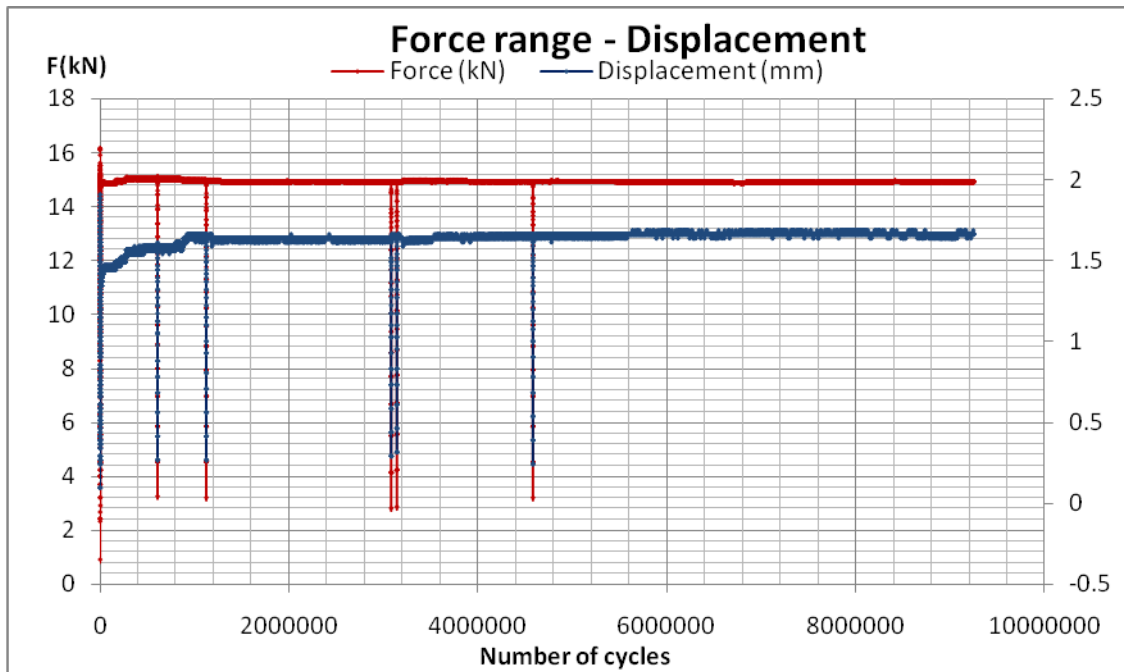


Figure 4.96 Force range – vertical displacement at 1/4 of the supported length diagram for the composite plate (Case 1)

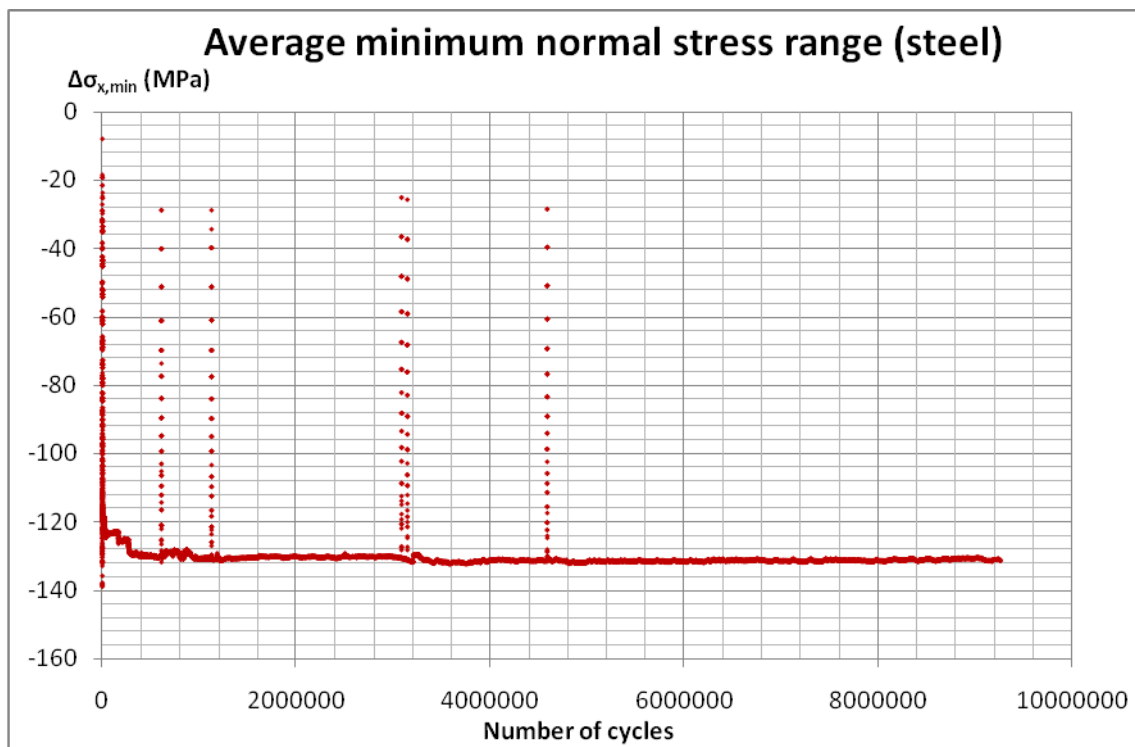


Figure 4.97 Average minimum normal stress range $\Delta\sigma_x$ (located at the outer surface of the steel plate) against number of cycles for the composite plate (Case 1)

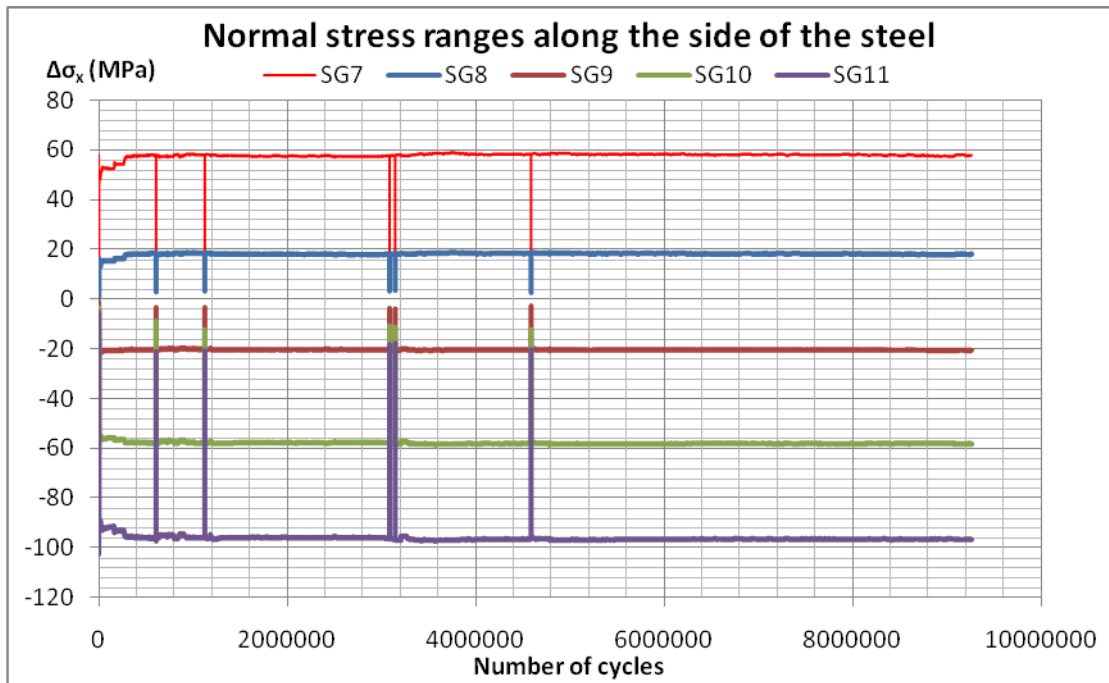


Figure 4.98 Normal stress ranges $\Delta\sigma_x$ along the side of the steel plate, against number of cycles for the composite plate (Case 1)

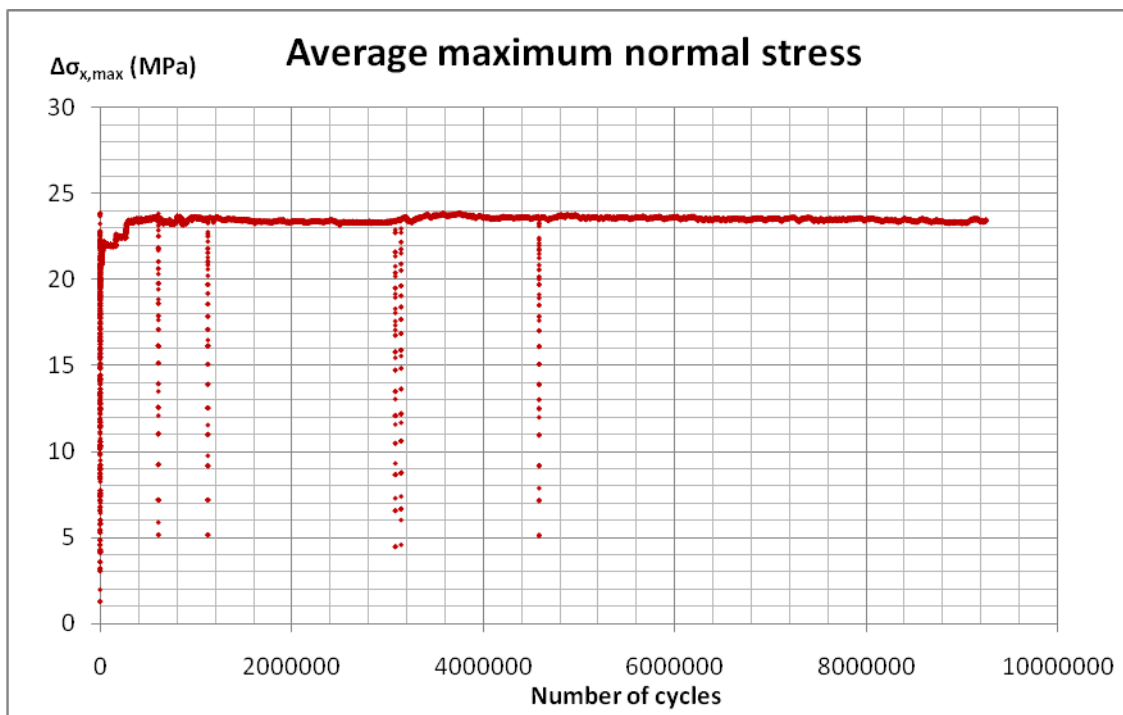


Figure 4.99 Average maximum normal stress range $\Delta\sigma_x$ (located at the outer surface of the GFRP plate) against number of cycles for the composite plate (Case 1)

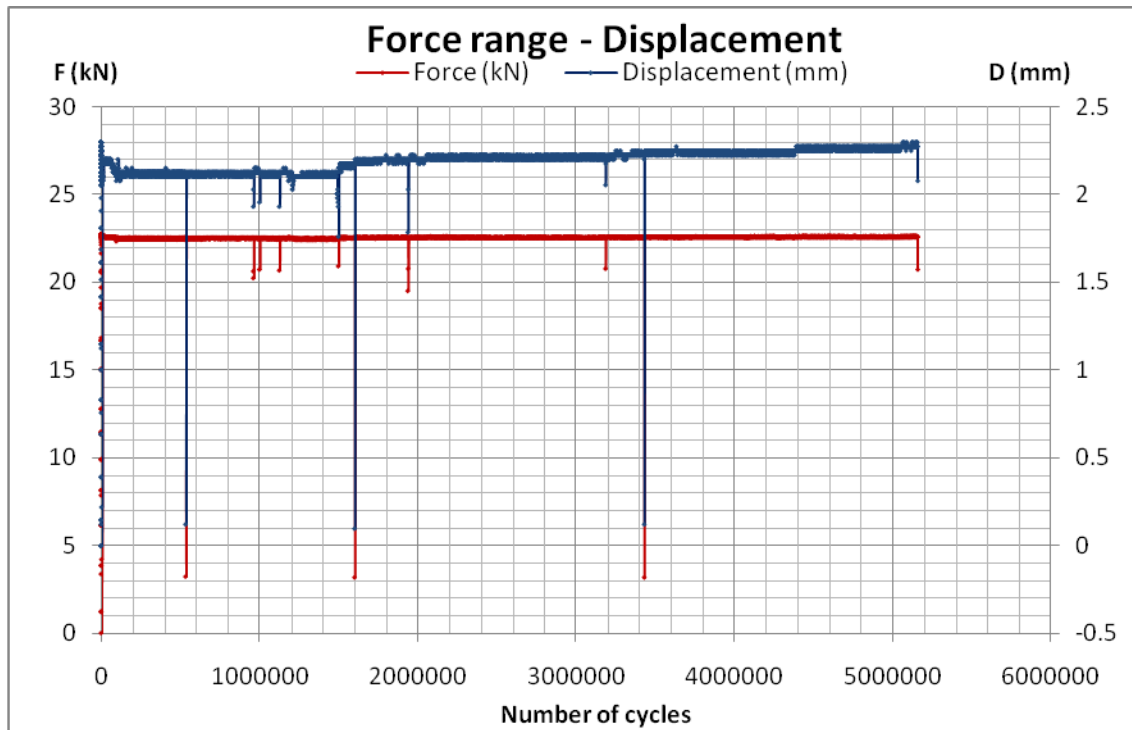


Figure 4.100 Force range – vertical displacement at 1/4 of the supported length diagram for the composite plate (Case 2)

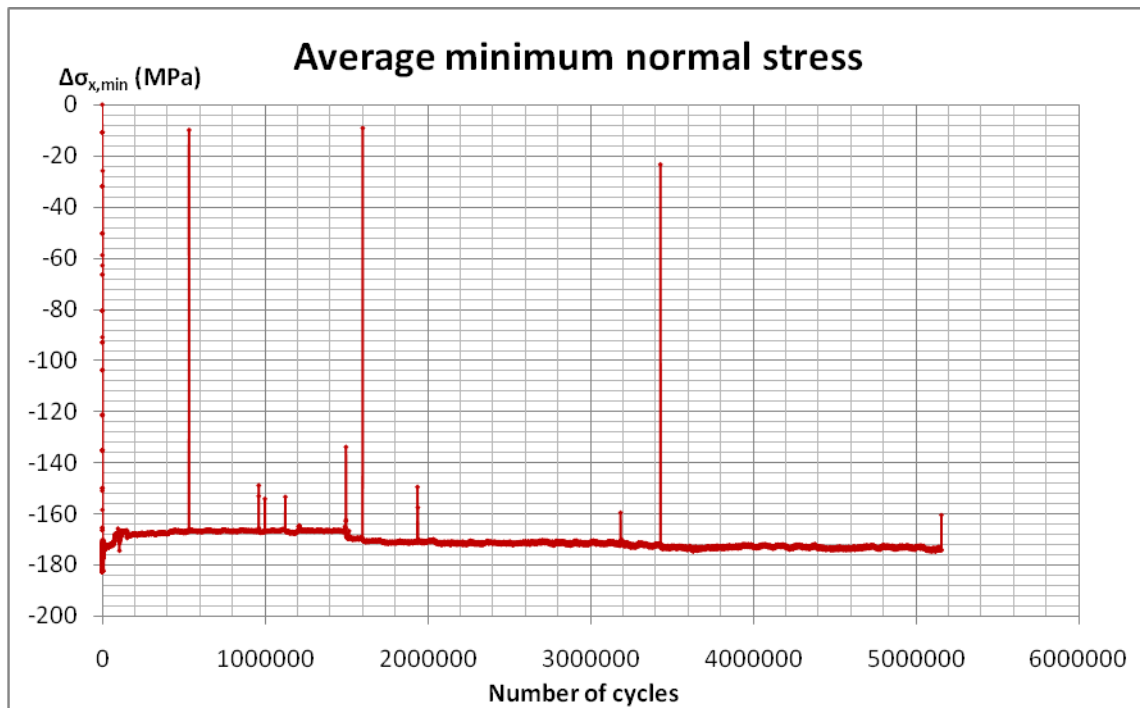


Figure 4.101 Average minimum normal stress range $\Delta\sigma_x$, located at the outer surface of the steel plate, against number of cycles for the composite plate (Case 2)

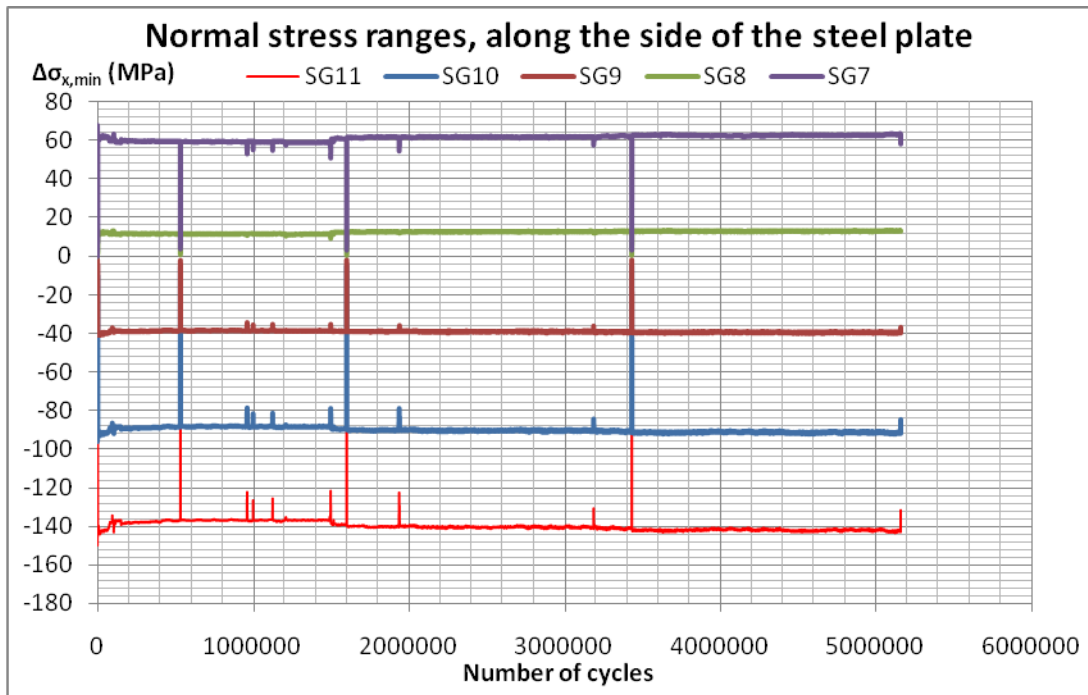


Figure 4.102 Normal stress ranges $\Delta\sigma_x$, along the side of the steel plate, against number of cycles for the composite plate (Case 2)

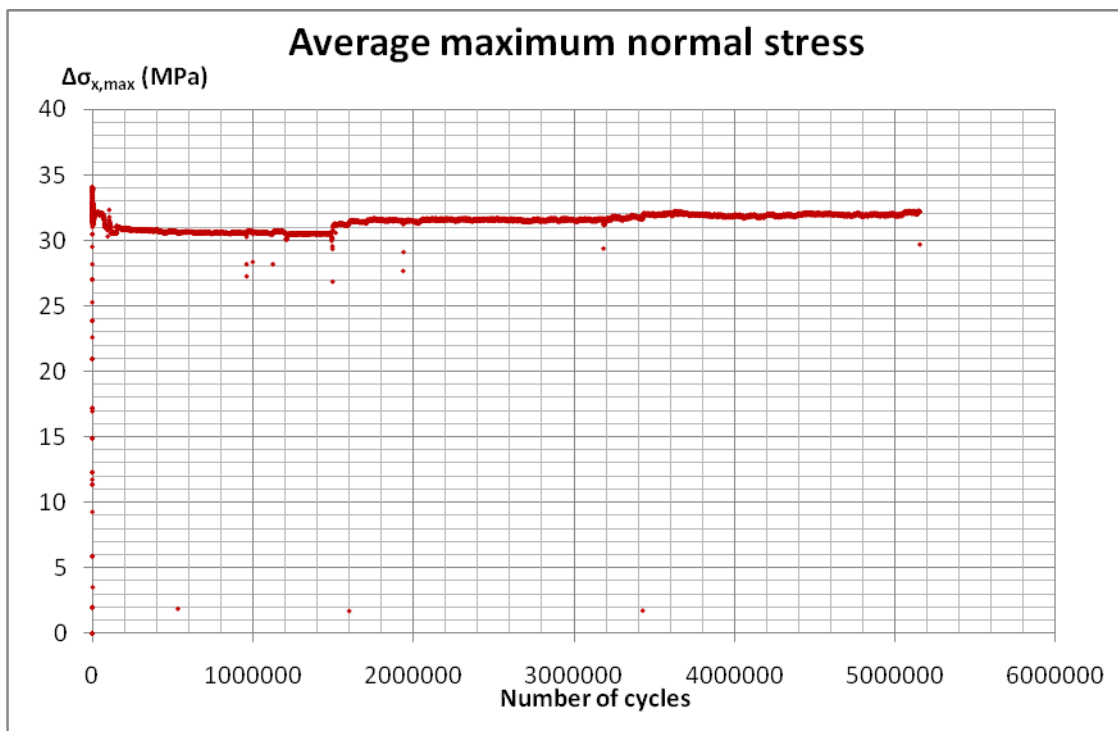


Figure 4.103 Average maximum normal stress range $\Delta\sigma_x$ (located at the outer surface of the GFRP plate) against number of cycles for the composite plate (Case 2)

As mentioned earlier, according to the EC, a minimum level of detail category of $\Delta\sigma_x = 125$ MPa, can be used and depending to the quality of the cutting planes a higher value up to 160 MPa can be used. The cut off limit for lowest category is $\Delta\sigma_x = \frac{2}{5}^{\frac{1}{5}} \times 120 \text{ kN} = 100 \text{ kN}$ and therefore more detailed fatigue analysis will be needed to determine whether or not fatigue cracks are going to appear.

Furthermore from figure 4.96 for case 1 and from figure 4.102 for case 2, the location of the neutral axis can be evaluated. However there it should be noted for the measurements of the strain gauges along the side of the steel plate that the exact location of the strain gauges cannot be determined with accuracy. Therefore the assumption that was made was that the strain gauges were equally distributed along the 12 mm of the thickness of the steel plate. So, each strain gauge covers an area of $12 \text{ mm}/5 = 2.4 \text{ mm}$ and the measurement is in the middle of each area. Finally the stress distribution for the two cases as well as the neutral axis location can be seen in the following two figures. For case 1 the load that corresponds to the stress distribution that will be presented is 15.039 kN while for case 2 it is 22.5097 kN.

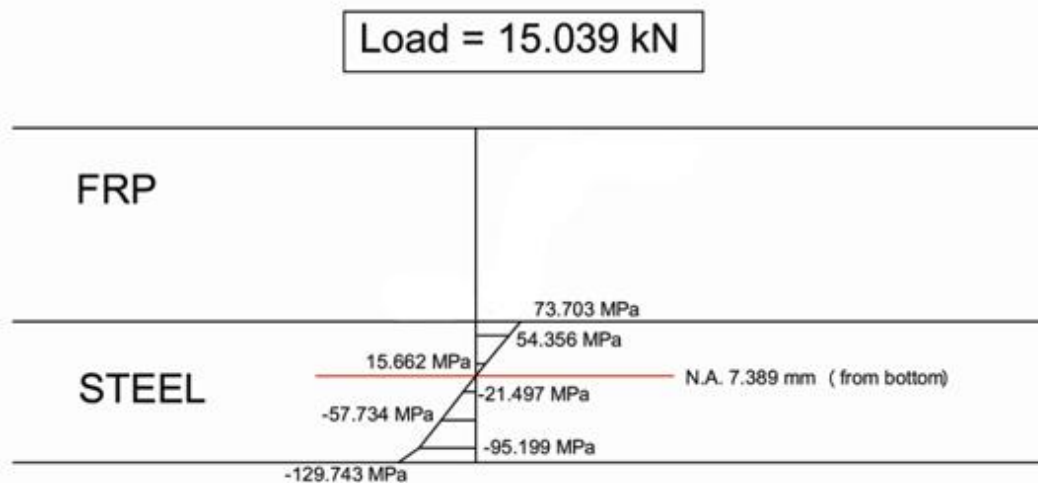


Figure 4.104 Stress distribution for case 1 (15.039 kN)

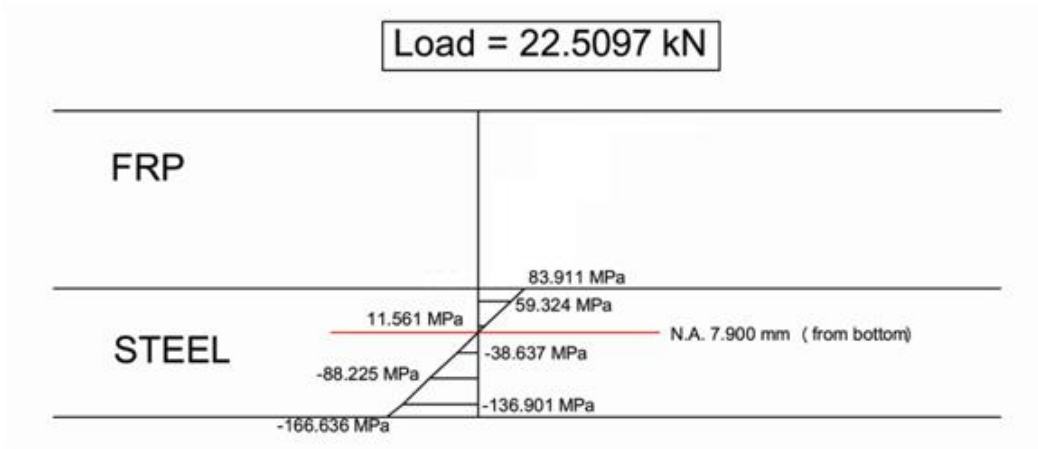


Figure 4.105 Stress distribution for case 2 (22.5097 kN)

So, in case 1 the neutral axis is located at 7.389 mm from the outer surface of the steel plate and in case 2 at 7.900 mm. The location of the neutral axis in those two cases is close and the small difference could be attributed to the fact that the precise position of the strain gauges is not known and also due to the fact that the outer surface of the FRP is not flat but curved and this is why the 16.5 mm selected as height is actually an equivalent height.

4.6 Creep test on FRP plate

The final test that was made on an FRP plate and it was a creep test. The configuration used was the same as configuration -1- for the bending of the FRP tests. The applied load was 11.82 kN which is the 77.4% of the “yielding” load. That means it is a really high load, but it had to be since the time that we had was limited. The experiment lasted approximately two weeks. In figure 4.106 the applied load and resulting displacement at the loading position against time are plotted. From this figure it can be seen that the creep is actually a significant phenomenon for this type of material. Under a constant load the displacements grew from 18.7 mm to 24.9 mm which is an increase of 31%. Therefore the designer should be aware that creep is not insignificant. However more testing should be done with lower and perhaps higher loads, but this is out of the scope at the time being.

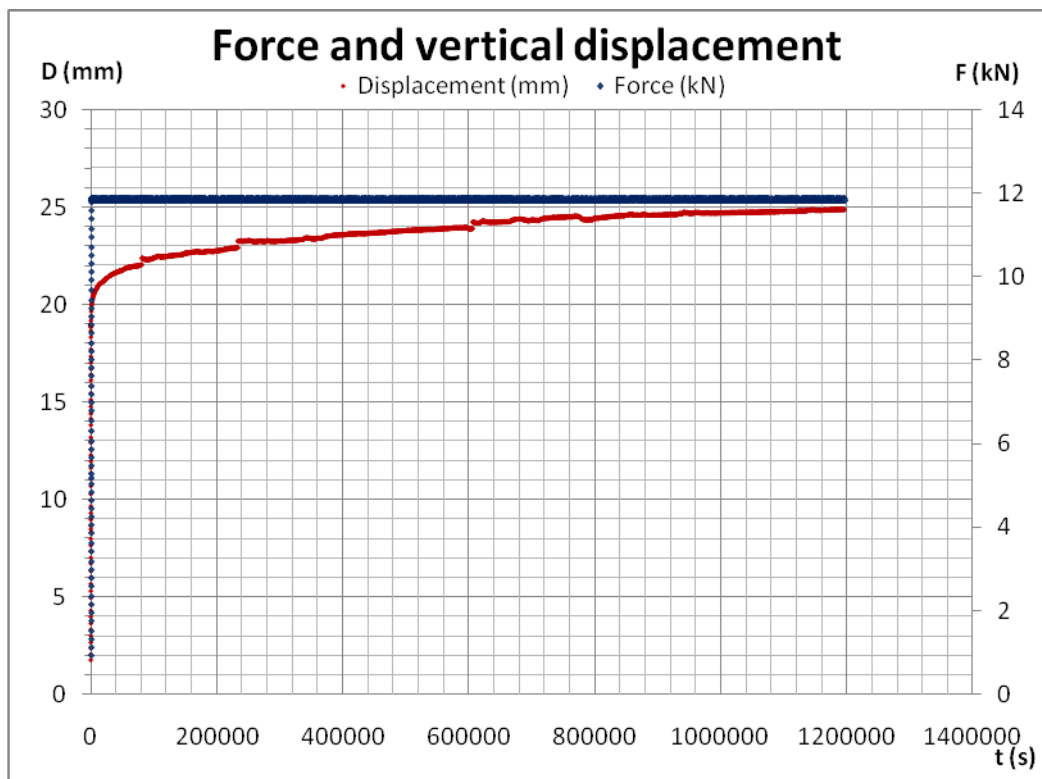


Figure 4.106 Force and vertical displacement against time diagram for FRP plate

5. MECHANICAL PROPERTIES OF GFRP LAMINATE

5.1 Introduction

In this chapter the material properties of the GFRP laminate are going to be determined. In order to do that burn-out test has been performed on the BP, TP, BSC and BST specimens. The purpose of the test was to determine the volumetric fractions as well as the number of layers in each laminate. After that using a method proposed from Bureau of Veritas (B.V.) the mechanical properties of each layer was determined and afterwards the entire laminate was composed. Finally the properties of each GFRP plate have been determined.

5.2 Burn out tests

The burn-out tests are the only tests that weren't performed in the faculty of civil engineering. For those the furnace of the aerospace faculty was utilized. The idea is to burn out the epoxy and leave behind the glass fibres. The temperature used was 560° for 90 minutes. The specimens were weighed before and after, thus the entire laminate mass, the fibre mass as well as the mass of the epoxy were obtained. The results of the burn out test can be reviewed in table 5.1.

Table 5.1 Burn-out test results

Specimen	m_f (g)	m_m (g)	t (mm)	A (mm ²)	Number of layers	
					Woven	CSM
TP	2.24	3.34	5.87	690.28	5	6
BP	4.96	7.41	18.36	483.10	16	17
BSC1	6.47	8.36	20.06	519.35	15	26
BSC2	3.94	5.73	17.19	410.00	14	15
BSC3	3.14	6.67	14.77	482.72	9	11
BSC4	2.96	5.32	12.00	485.05	8	10
BST1	3.63	6.20	15.98	447.24	11	14
BST2	3.38	6.32	14.51	484.33	10	13
BST3	3.80	6.28	16.02	461.37	13	14
BST4	4.16	7.24	20.02	413.58	16	18

The extra data needed were provided by the company, Pakor, and can be found in table 3.1. In table 5.2 the volumetric fractions were determined based the test results (table

5.1) and the material properties (table 3.1). The procedure will not be presented here but rather in the next section where the B.V. method will be analytically presented.

Table 5.2 Volumetric fractions

Specimen	V_f (%)	V_m (%)
TP	24	76
BP	23	77
BSC1	26	74
BSC2	24	76
BSC3	18	82
BSC4	20	80
BST1	21	79
BST2	20	80
BST3	22	78
BST4	21	79

Now that everything that is needed is known the mechanical properties of the GFRP laminate can be determined. However this will not include specimen BSC1. When the layers of this specimen were counted, the CSM layers weren't distinct enough for us to be certain for the exact number.

5.3 Theoretical determination of properties

As mentioned before the method that was used for the theoretical determination of properties of each individual layer was from the Bureau of Veritas. The method is going to be presented as follows:

First all the symbols that are going to be used in the following formulas are:

C_{eq} : Woven balance coefficient for woven rovings.

e : Individual layer thickness, in mm

E_{f0° : Longitudinal Young's modulus of fibre, in MPa

E_{f90° : Transversal Young's modulus of fibre, in MPa

E_m : Young's modulus of resin, in MPa

G_f : Shear modulus of fibre, in MPa

G_m : Shear modulus of resin, in MPa

m : Total mass per square meter of individual layer, in gr/m^2

M_f : Content in mass of fibre in an individual layer, in %

M_m : Content in mass of resin in an individual layer, in %

P_f : Total mass per square meter of dry reinforcement fabric, in g/m²

V_f : Content in volume of fibre in an individual layer, in %

V_m : Content in volume of resin in an individual layer, in %

ν_f : Poisson's coefficient of fibre

ν_m : Poisson's coefficient of resin

ρ : Density of an individual layer

ρ_f : Density of fibre

ρ_m : Density of resin

First the volumetric fractions are:

$$V_f = \frac{(M_f / \rho_f)}{(M_f / \rho_f) + ((1 - M_f) / \rho_m)}$$

$$V_m = 1 - V_f$$

The individual layer thickness in mm is:

$$e = (P_f \cdot (\frac{1}{\rho_f} + \frac{1 - M_f}{M_f \rho_m}))$$

Unidirectionals

The reference axis system for a unidirectional is as follows see fig 5.1 :

- 1 : axis parallel to the fibre's direction
- 2 : axis perpendicular to the fibre's direction
- 3 : axis normal to plane containing axis 1 and 2, leading to direct reference axis system.

The reference axis for an elementary fibre is defined as follows (fig 5.2):

- 0° : Longitudinal axis of the fibre
- 90° : Transverse axis of the fibre.

The longitudinal modulus of elasticity of an individual unidirectional layer is:

$$E_{UD1} = C_{UD1} \cdot (E_{f90^\circ} \cdot V_f + E_m \cdot (1 - V_f))$$

The transverse modulus of elasticity of an individual unidirectional layer is:

$$E_{UD2} = E_{UD3} = C_{UD2} \cdot \left(\left(\frac{E_m}{1 - \nu_m^2} \right) \cdot \frac{1 + 0.85 \cdot V_f^2}{(1 - V_f)^{1.25} + \frac{E_m}{E_{f90^\circ}} \cdot \frac{V_f}{1 - \nu_m^2}} \right)$$

The shear moduli of an unidirectional layer:

$$G_{UD12} = G_{UD31} = C_{UD12} \cdot G_m \times \frac{1 + \eta \cdot V_f}{1 - \eta \cdot V_f}$$

with

$$\eta = \frac{\frac{G_f}{G_m} - 1}{\frac{G_f}{G_m} + 1}$$

and

$$G_{UD23} = 0.7 \cdot G_{UD12}$$

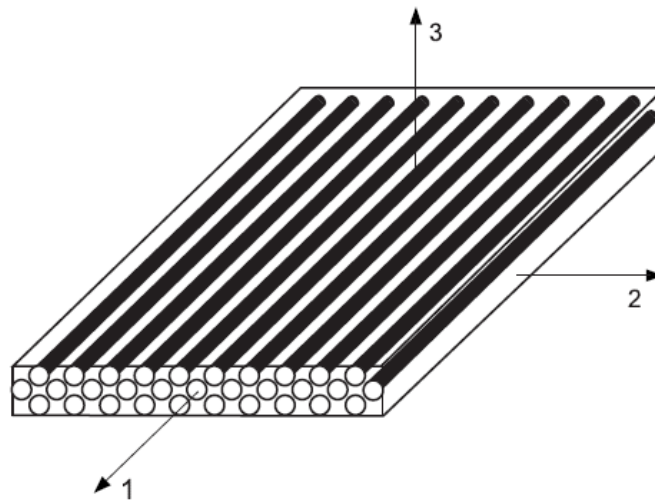


Figure 5.1 Reference axis for unidirectionals

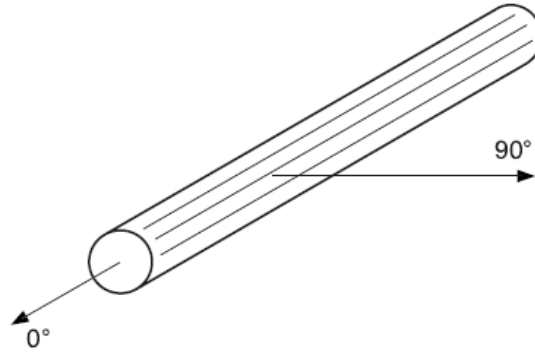


Figure 5.2 Reference axis of an elementary fibre

Poisson's coefficients:

$$v_{UD13} = v_{UD12} = C_{UDv} \cdot (v_f \cdot V_f + v_m \cdot (1 - V_f))$$

$$v_{UD21} = v_{UD31} = v_{UD12} \cdot \frac{E_{UD2}}{E_{UD1}}$$

$$v_{UD23} = v_{UD32} = C_{UDv} \cdot (v_f' \cdot V_f + v_m \cdot (1 - V_f))$$

with

$$v_f' = v_f \cdot \frac{E_{f90^\circ}}{E_{f0^\circ}}$$

The coefficients C_{UD1} , C_{UD2} , C_{UD12} and C_{UDv} are experimental coefficients taking into account the specific characteristics of fibre's type. For E-glass it is:

$$C_{UD1} = 1$$

$$C_{UD2} = 0.8$$

$$C_{UD12} = 0.9$$

$$C_{UDv} = 0.9$$

Woven rovings

For the woven rovings the reference axis are the same than for unidirectionals with the following denomination:

- 1 : axis parallel to warp direction
- 2 : axis parallel to weft direction
- 3 : axis normal to plane containing axis 1 and 2, leading to direct reference axis system.

The elastic coefficients of woven rovings as individual layers are estimated as follow:

$$E_{T1} = \frac{1}{e} \cdot \left(A_{11} - \frac{A_{12}^2}{A_{22}} \right)$$

Young's modulus in warp direction in MPa:

$$E_{T2} = \frac{1}{e} \cdot \left(A_{22} - \frac{A_{12}^2}{A_{11}} \right)$$

Young's modulus in weft direction in MPa:

$$E_{T3} = E_{UD3}$$

Out-of-plane Young's modulus in MPa:

$$E_{T3} = E_{UD3}$$

Shear moduli in MPa:

$$G_{T12} = \frac{1}{e} \cdot A_{33}$$

and

$$G_{T23} = G_{T31} = 0.9 \cdot G_{T12}$$

Poisson's coefficients:

$$\nu_{T12} = \frac{A_{12}}{A_{22}}$$

$$\nu_{T21} = \nu_{T12} \cdot \frac{E_{T2}}{E_{T1}}$$

$$\nu_{T32} = \nu_{T31} = (\nu_{UD32} + \nu_{UD31}) / 2$$

$$\nu_{T13} = (\nu_{UD23} + \nu_{UD13}) / 2$$

where:

$$A_{11} = e \cdot (C_{eq} \cdot Q_{11} + (1 - C_{eq}) \cdot Q_{22})$$

$$A_{22} = e \cdot (C_{eq} \cdot Q_{22} + (1 - C_{eq}) \cdot Q_{11})$$

$$A_{12} = e \cdot Q_{12}$$

$$A_{33} = e \cdot Q_{33}$$

with:

$$Q_{11} = E_{UD1} / (1 - (v_{UD12} \cdot v_{UD21}))$$

$$Q_{22} = E_{UD2} / (1 - (v_{UD12} \cdot v_{UD21}))$$

$$Q_{12} = (v_{UD21} \cdot E_{UD1}) / (1 - (v_{UD12} \cdot v_{UD21}))$$

$$Q_{33} = G_{UD12}$$

Chopped Strand Mats (CSM)

As CSM is made of cut fibres, random arranged and supposedly uniformly distributed in space, it is assumed as isotropic material. Isotropic assumption makes possible to define only three elastic coefficients:

Young's moduli, in MPa:

$$E_{mat1} = E_{mat2} = \frac{3}{8} \cdot E_{UD1} + \frac{5}{8} \cdot E_{UD2}$$

$$E_{mat3} = E_{UD3}$$

Poisson's coefficient is as all isotropic materials:

$$v_{mat12} = v_{mat21} = v_{mat32} = v_{mat13} = 0.3$$

Shear moduli, in MPa:

$$G_{mat12} = E_{mat1} / (2 \cdot (1 + v_{mat21}))$$

$$G_{mat23} = G_{mat31} = 0.7 \cdot G_{UD12}$$

At this stage the Young's moduli, the shear moduli and the Poisson's ratios have been evaluated for each layer; the woven rovings and the CSM. To determine the mechanical properties of the entire laminate, the compliance matrix must be composed. The stiffness matrix for the three dimensional case is $[K]$ and the inverse is the compliance matrix:

$$[K]^{-1} = \begin{pmatrix} \frac{1}{E_1} & -\frac{\nu_{12}}{E_1} & -\frac{\nu_{13}}{E_1} & 0 & 0 & 0 \\ -\frac{\nu_{12}}{E_1} & \frac{1}{E_2} & -\frac{\nu_{23}}{E_2} & 0 & 0 & 0 \\ -\frac{\nu_{13}}{E_1} & -\frac{\nu_{23}}{E_2} & \frac{1}{E_3} & 0 & 0 & 0 \\ 0 & 0 & 0 & \frac{1}{G_{23}} & 0 & 0 \\ 0 & 0 & 0 & 0 & \frac{1}{G_{31}} & 0 \\ 0 & 0 & 0 & 0 & 0 & \frac{1}{G_{12}} \end{pmatrix}$$

In order to compose the entire laminate the following formula is going to be used:

$$[K_{lam}] = \frac{1}{N_{woven} + N_{csm}} N_{woven} \cdot [K_{woven}] + N_{CSM} \cdot [K_{CSM}]$$

where,

$[K_{lam}]$ is the stiffness matrix of the laminate

$[K_{woven}]$ is the stiffness matrix of the woven rovings

$[K_{CSM}]$ is the stiffness matrix of the CSM

Then the mechanical properties of the entire laminate can be extracted from the compliance matrix $[K_{lam}]$ of the laminate. Following this procedure the mechanical properties of all the GFRP laminates of the aforementioned specimens were determined. The only problem that was encountered was the fact that the group of specimens BSC and BST didn't have a flat GFRP plate. The thickness was varying along the width direction. Assuming that the number of layers is constant in the entire GFRP laminate of each specimen, the parameter that is affected from the thickness variation is the volume of the epoxy and thus the volumetric fractions. The solution to this was to measure the thickness every 5 mm and to determine the mechanical properties for each section and finally obtain the average values. The GFRP profiles that were measured are depicted in figures 5.3 – 5.9. Specimen BSC1 is not included for the aforementioned reason.

All the mathematical calculations were performed with the use of the software Mathematica.

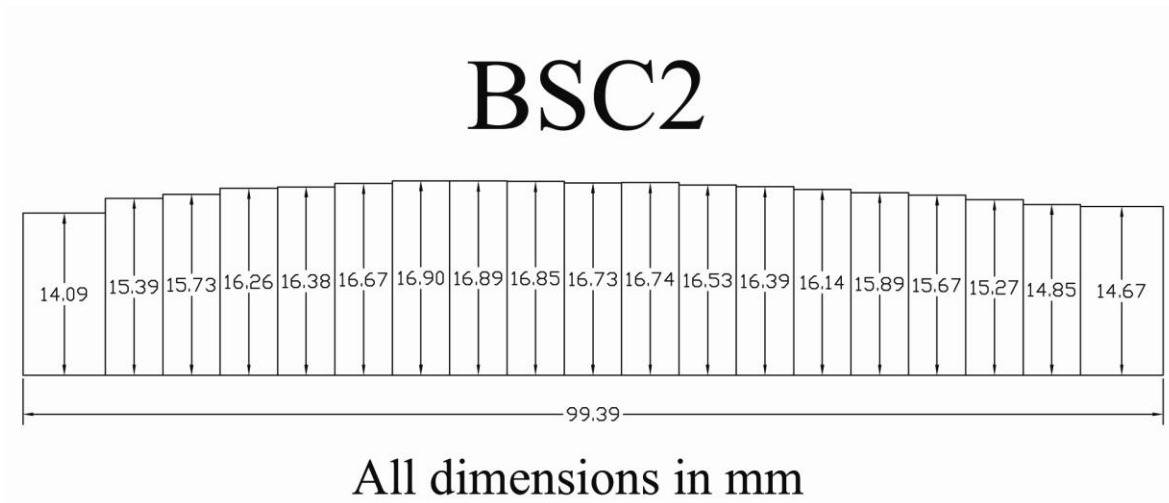


Figure 5.3 GFRP profile for specimen BSC2

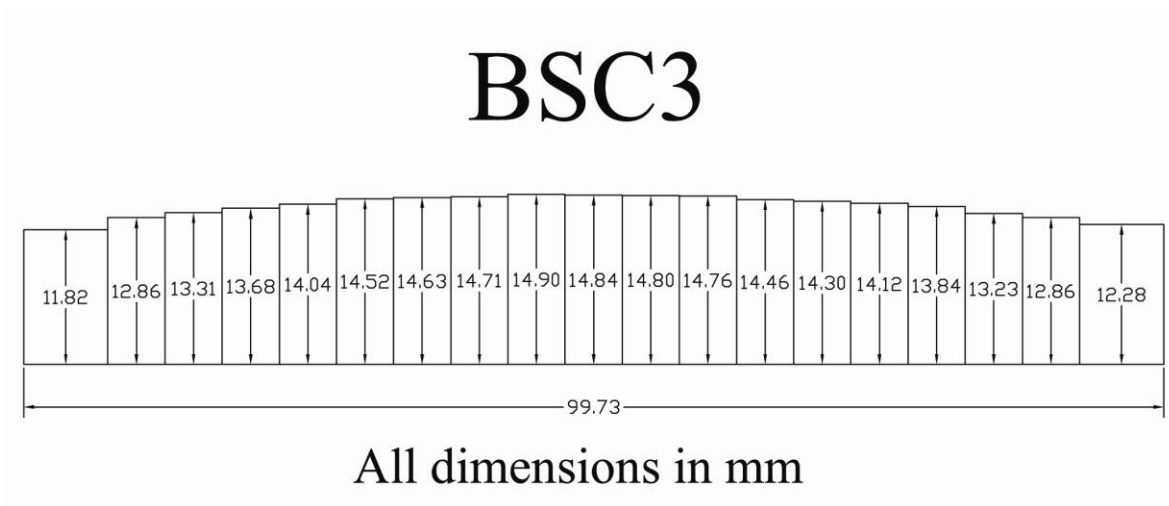
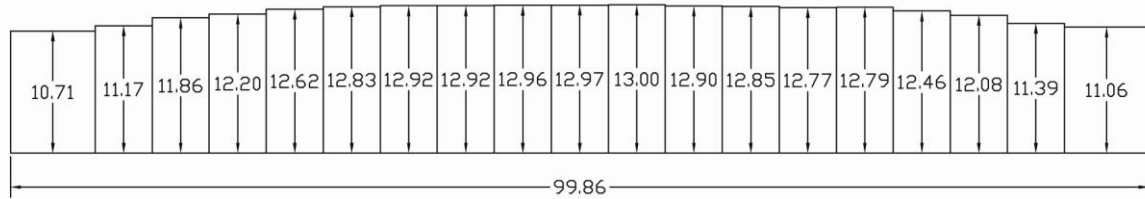


Figure 5.4 GFRP profile for specimen BSC3

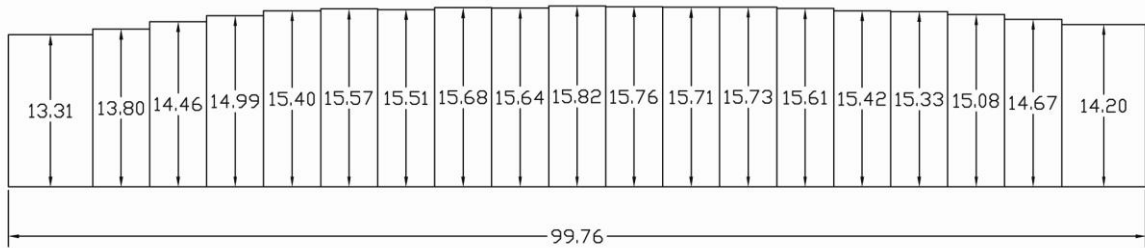
BSC4



All dimensions in mm

Figure 5.5 GFRP profile for specimen BSC4

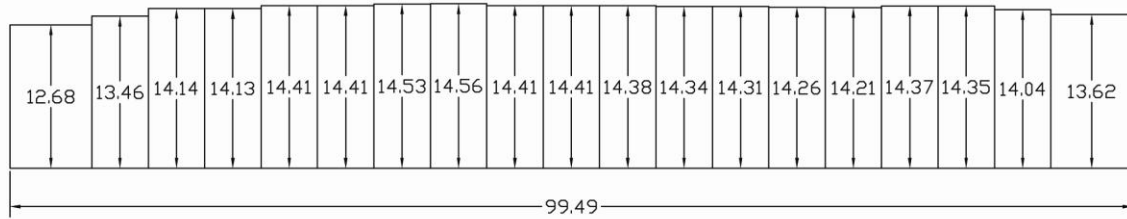
BST1



All dimensions in mm

Figure 5.6 GFRP profile for specimen BST1

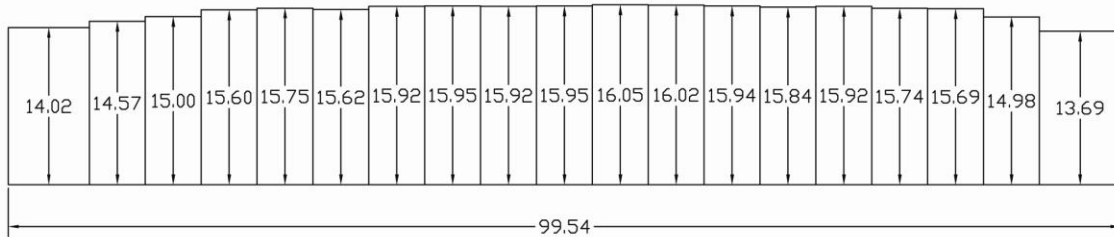
BST2



All dimensions in mm

Figure 5.7 GFRP profile for specimen BST2

BST3



All dimensions in mm

Figure 5.8 GFRP profile for specimen BST3

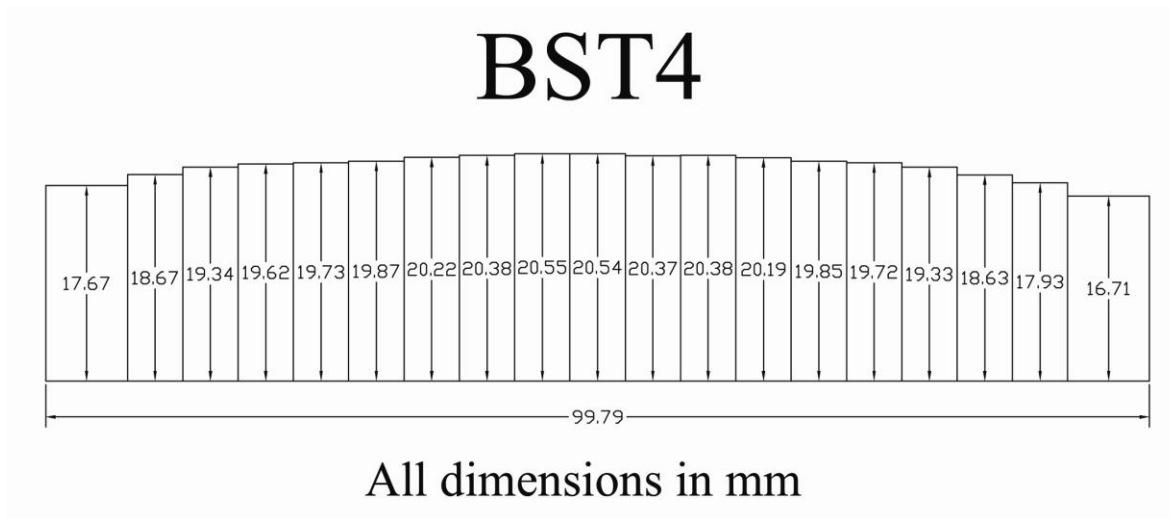


Figure 5.9 GFRP profile for specimen BST4

The mechanical properties of TP, BP, BSC and BST are presented in the following tables. Specifically for specimen group BSC and BST, the mechanical properties of each specimen are included.

Table 5.3 Mechanical properties of GFRP laminate of specimen TP

E_1, E_2 (Gpa)	E_3 (Gpa)	G_{12} (Gpa)	G_{23}, G_{31} (Gpa)	ν_{12}	ν_{23}, ν_{13}
11.269	4.505	2.859	1.382	0.201	0.305

The modulus of elasticity in the longitudinal direction is very close to the one found from the tensile test in paragraph 4.2.3 which was 11.010 GPa. That is a very good indication that the method works well and can be trusted.

Table 5.4 Mechanical properties of GFRP laminate of specimen BP

E_1, E_2 (Gpa)	E_3 (Gpa)	G_{12} (Gpa)	G_{23}, G_{31} (Gpa)	ν_{12}	ν_{23}, ν_{13}
11.249	4.485	2.859	1.387	0.204	0.305

Table 5.5 Mechanical properties of GFRP laminate of specimen BSC2

Section	E_1, E_2 (Gpa)	E_3 (Gpa)	G_{12} (Gpa)	G_{23}, G_{31} (Gpa)	ν_{12}	ν_{23}, ν_{13}
1	12.669	4.848	3.179	1.496	0.201	0.304
2	11.835	4.630	2.993	1.431	0.203	0.305
3	11.641	4.581	2.950	1.416	0.203	0.305
4	11.354	4.511	2.887	1.394	0.204	0.305
5	11.288	4.495	2.873	1.389	0.204	0.305
6	11.138	4.460	2.840	1.378	0.205	0.305
7	11.025	4.433	2.815	1.370	0.205	0.305
8	11.035	4.435	2.817	1.370	0.205	0.305
9	11.055	4.440	2.821	1.372	0.205	0.305
10	11.107	4.452	2.833	1.376	0.205	0.305
11	11.107	4.452	2.833	1.376	0.205	0.305
12	11.213	4.477	2.856	1.383	0.205	0.305
13	11.277	4.493	2.870	1.388	0.204	0.305
14	11.410	4.525	2.899	1.398	0.204	0.305
15	11.547	4.558	2.930	1.409	0.204	0.305
16	11.665	4.587	2.956	1.417	0.203	0.305
17	11.898	4.646	3.007	1.435	0.203	0.305
18	12.158	4.713	3.065	1.456	0.202	0.304
19	12.281	4.745	3.092	1.465	0.202	0.304
Average	11.511	4.552	2.922	1.406	0.204	0.305

Table 5.6 Mechanical properties of GFRP laminate of specimen BSC3

Section	E_1, E_2 (Gpa)	E_3 (Gpa)	G_{12} (Gpa)	G_{23}, G_{31} (Gpa)	ν_{12}	ν_{23}, ν_{13}
1	10.702	4.372	2.825	1.339	0.212	0.306
2	10.083	4.233	2.684	1.295	0.214	0.306
3	9.843	4.181	2.630	1.278	0.215	0.306
4	9.654	4.141	2.588	1.265	0.216	0.307
5	9.484	4.106	2.549	1.254	0.216	0.307
6	9.269	4.062	2.501	1.239	0.217	0.307
7	9.223	4.052	2.491	1.236	0.217	0.307
8	9.192	4.046	2.484	1.234	0.218	0.307
9	9.111	4.030	2.466	1.228	0.218	0.307
10	9.140	4.036	2.472	1.230	0.218	0.307
11	9.155	4.039	2.476	1.231	0.218	0.307
12	9.170	4.042	2.479	1.232	0.218	0.307
13	9.300	4.068	2.508	1.241	0.217	0.307
14	9.371	4.082	2.524	1.246	0.217	0.307
15	9.451	4.099	2.542	1.251	0.216	0.307
16	9.577	4.125	2.570	1.260	0.216	0.307
17	9.880	4.189	2.639	1.281	0.215	0.306
18	10.083	4.233	2.684	1.295	0.214	0.306
19	10.417	4.307	2.760	1.319	0.213	0.306
Average	9.585	4.129	2.572	1.261	0.216	0.307

Table 5.7 Mechanical properties of GFRP laminate of specimen BSC4

Section	E_1, E_2 (Gpa)	E_3 (Gpa)	G_{12} (Gpa)	G_{23}, G_{31} (Gpa)	ν_{12}	ν_{23}, ν_{13}
1	10.973	4.438	2.901	1.358	0.212	0.305
2	10.637	4.360	2.824	1.334	0.213	0.306
3	10.195	4.260	2.723	1.302	0.215	0.306
4	9.994	4.216	2.677	1.288	0.215	0.306
5	9.756	4.165	2.623	1.271	0.216	0.307
6	9.643	4.141	2.597	1.263	0.217	0.307
7	9.597	4.131	2.587	1.260	0.217	0.307
8	9.597	4.131	2.587	1.260	0.217	0.307
9	9.579	4.127	2.583	1.259	0.217	0.307
10	9.579	4.127	2.583	1.259	0.217	0.307
11	9.560	4.124	2.578	1.258	0.217	0.307
12	9.615	4.135	2.591	1.261	0.217	0.307
13	9.633	4.139	2.595	1.263	0.217	0.307
14	9.680	4.149	2.606	1.266	0.217	0.307
15	9.670	4.147	2.603	1.265	0.217	0.307
16	9.843	4.183	2.643	1.277	0.216	0.306
17	10.056	4.230	2.691	1.292	0.215	0.306
18	10.492	4.327	2.791	1.323	0.214	0.306
19	10.712	4.377	2.841	1.339	0.213	0.306
Average	9.937	4.206	2.664	1.284	0.216	0.306

Table 5.8 Mechanical properties of GFRP laminate of specimen BST1

Section	E_1, E_2 (Gpa)	E_3 (Gpa)	G_{12} (Gpa)	G_{23}, G_{31} (Gpa)	ν_{12}	ν_{23}, ν_{13}
1	11.524	4.575	3.041	1.398	0.212	0.305
2	11.219	4.500	2.970	1.375	0.213	0.305
3	10.838	4.409	2.882	1.347	0.214	0.306
4	10.561	4.344	2.818	1.327	0.214	0.306
5	10.359	4.298	2.771	1.313	0.215	0.306
6	10.276	4.280	2.752	1.307	0.215	0.306
7	10.303	4.286	2.758	1.309	0.215	0.306
8	10.231	4.270	2.741	1.304	0.215	0.306
9	10.249	4.274	2.746	1.305	0.215	0.306
10	10.159	4.254	2.725	1.298	0.216	0.306
11	10.186	4.260	2.731	1.300	0.215	0.306
12	10.213	4.266	2.737	1.302	0.215	0.306
13	10.204	4.264	2.735	1.302	0.215	0.306
14	10.258	4.276	2.748	1.305	0.215	0.306
15	10.350	4.296	2.769	1.312	0.215	0.306
16	10.397	4.307	2.780	1.315	0.215	0.306
17	10.512	4.333	2.806	1.324	0.214	0.306
18	10.723	4.382	2.855	1.339	0.214	0.306
19	10.990	4.445	2.917	1.359	0.213	0.305
Average	10.503	4.332	2.804	1.323	0.215	0.306

Table 5.9 Mechanical properties of GFRP laminate of specimen BST2

Section	E_1, E_2 (Gpa)	E_3 (Gpa)	G_{12} (Gpa)	G_{23}, G_{31} (Gpa)	ν_{12}	ν_{23}, ν_{13}
1	10.674	4.373	2.857	1.334	0.215	0.306
2	10.231	4.272	2.754	1.303	0.216	0.306
3	9.881	4.195	2.673	1.278	0.217	0.306
4	9.881	4.195	2.673	1.278	0.217	0.306
5	9.752	4.168	2.643	1.269	0.218	0.306
6	9.752	4.168	2.643	1.269	0.218	0.306
7	9.694	4.155	2.630	1.265	0.218	0.307
8	9.686	4.153	2.628	1.264	0.218	0.307
9	9.752	4.168	2.643	1.269	0.218	0.306
10	9.752	4.168	2.643	1.269	0.218	0.306
11	9.769	4.171	2.647	1.270	0.218	0.306
12	9.786	4.175	2.651	1.271	0.218	0.306
13	9.795	4.177	2.653	1.272	0.218	0.306
14	9.820	4.182	2.659	1.274	0.218	0.306
15	9.846	4.188	2.665	1.275	0.218	0.306
16	9.769	4.171	2.647	1.270	0.218	0.306
17	9.778	4.173	2.649	1.271	0.218	0.306
18	9.925	4.205	2.683	1.281	0.217	0.306
19	10.144	4.253	2.734	1.296	0.217	0.306
Average	9.878	4.195	2.672	1.278	0.218	0.306

Table 5.10 Mechanical properties of GFRP laminate of specimen BST3

Section	E_1, E_2 (Gpa)	E_3 (Gpa)	G_{12} (Gpa)	G_{23}, G_{31} (Gpa)	ν_{12}	ν_{23}, ν_{13}
1	11.297	4.498	2.878	1.389	0.205	0.305
2	10.981	4.423	2.808	1.366	0.206	0.305
3	10.748	4.369	2.757	1.349	0.206	0.306
4	10.447	4.301	2.692	1.327	0.207	0.306
5	10.375	4.285	2.676	1.322	0.207	0.306
6	10.438	4.299	2.690	1.327	0.207	0.306
7	10.296	4.268	2.659	1.317	0.208	0.306
8	10.288	4.266	2.657	1.316	0.208	0.306
9	10.296	4.268	2.659	1.317	0.208	0.306
10	10.288	4.266	2.657	1.316	0.208	0.306
11	10.236	4.255	2.646	1.312	0.208	0.306
12	10.253	4.258	2.650	1.314	0.208	0.306
13	10.288	4.266	2.657	1.316	0.208	0.306
14	10.331	4.275	2.666	1.319	0.208	0.306
15	10.296	4.268	2.659	1.317	0.208	0.306
16	10.384	4.287	2.678	1.323	0.207	0.306
17	10.402	4.291	2.682	1.324	0.207	0.306
18	10.758	4.372	2.760	1.350	0.206	0.306
19	11.494	4.546	2.921	1.404	0.204	0.305
Average	10.521	4.319	2.708	1.333	0.207	0.306

Table 5.11 Mechanical properties of GFRP laminate of specimen BST4

Section	E_1, E_2 (Gpa)	E_3 (Gpa)	G_{12} (Gpa)	G_{23}, G_{31} (Gpa)	ν_{12}	ν_{23}, ν_{13}
1	11.014	4.436	2.844	1.366	0.207	0.305
2	10.577	4.335	2.746	1.334	0.209	0.306
3	10.320	4.277	2.690	1.316	0.210	0.306
4	10.210	4.253	2.665	1.308	0.210	0.306
5	10.172	4.245	2.657	1.306	0.210	0.306
6	10.118	4.233	2.645	1.302	0.210	0.306
7	10.000	4.207	2.619	1.293	0.211	0.306
8	9.942	4.195	2.606	1.289	0.211	0.306
9	9.885	4.183	2.594	1.286	0.211	0.307
10	9.885	4.183	2.594	1.286	0.211	0.307
11	9.949	4.196	2.608	1.290	0.211	0.306
12	9.942	4.195	2.606	1.289	0.211	0.306
13	10.007	4.209	2.621	1.294	0.211	0.306
14	10.126	4.235	2.647	1.302	0.210	0.306
15	10.172	4.245	2.657	1.306	0.210	0.306
16	10.320	4.277	2.690	1.316	0.210	0.306
17	10.594	4.339	2.750	1.336	0.209	0.306
18	10.900	4.409	2.818	1.358	0.208	0.306
19	11.486	4.549	2.949	1.402	0.206	0.305
Average	10.296	4.274	2.684	1.315	0.210	0.306

6. FINITE ELEMENT ANALYSIS

6.1 Introduction

In this chapter, a finite element analysis is going to be performed using finite element analysis software Ansys. The results are going to be compared to the experimental in order to determine how accurate the modeling that was chosen is. The specimens that were modeled were the GFRP strengthened steel plates except for the BSC1 specimen due to the fact the reason that the number of layers haven't been determined correctly as already mentioned in paragraph 5.2. Furthermore, in order to determine the stress reduction factor, the corresponding steel plates for all the specimens without the GFRP layer were analyzed.

6.2 Creating the finite element model

For the modeling procedure there are five main components:

- Element type
- Material models
- Meshing
- Restraints and applied loads
- Type of analysis

Element type

The element type that was used for all the performed analysis is called Solid186 (fig.6.1) Solid186 is a higher order 3-D 20-node solid element that exhibits quadratic displacement behaviour. The element is defined by 20 nodes having three degrees of freedom per node: translations in the nodal x, y, and z directions. The element supports plasticity, hyperelasticity, creep, stress stiffening, large deflection, and large strain capabilities. It also has mixed formulation capability for simulating deformations of nearly incompressible elastoplastic materials, and fully incompressible hyperelastic materials.

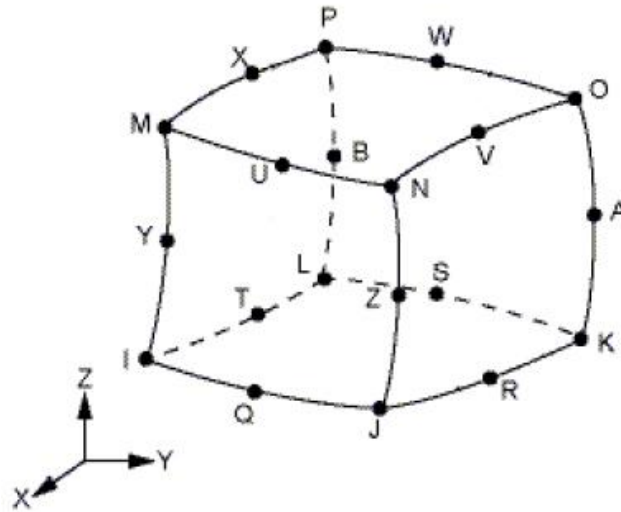


Figure 6.1 Solid 186 Structural solid geometry

Material models

There are two materials that were used; steel and GFRP. For all the analysis the GFRP laminate was modelled as a linear elastic orthotropic material using the material data that were determined in chapter 5. For the steel there were two material models used. For the linear analysis where steel stresses didn't reach the yielding point, steel was modelled as a linear elastic isotropic material with a Young modulus of $E = 200 \text{ GPa}$ and a Poisson's ratio $\nu = 0.3$. For the non linear analysis a bilinear graph for the steel was used as seen in figure 6.2.



Figure 6.2 Bilinear stress – strain diagram for steel

Meshing

For the meshing of the models a rather dense meshing was chosen. The number of elements in the longitudinal direction (x) was 80 elements for all the models. Also the number of elements in the width (y) direction was the same for all the models and it was 20 elements. Thus the only difference was in the thickness direction. Specifically the only difference was the number of elements in the thickness (z) direction of the GFRP plate. The steel plates had 4 elements in the thickness directions. The GFRP plate had 5 elements for specimens BSC2, BSC3, BST1, BST2 and BST3, 4 elements for specimen BSC4 and 6 elements for specimen BST4.

The reason for such a dense meshing was due to the fact that a sufficient number of elements were needed for the thickness direction. The number of elements in the x and y direction were depending on the number of elements in the z direction due to the fact that the ratio of 2:1 for the element dimensions shouldn't be violated. The density of the meshing didn't affect the time needed for the analysis since it was linear.

As mentioned eight more models were analyzed; the corresponding un-strengthened steel plates. The meshing was obviously the same as for the steel plates of the strengthened specimens.

The total number of elements and nodes used were: 14400 elements and 65319 nodes for specimens BSC2, BSC3, BST1, BST2 and BST3, 12800 elements and 58617 nodes for specimen BSC4 and 16000 elements and 72021 nodes for specimen BST4. For the un-strengthened steel plates the number of elements was 6400 and the number of nodes 31809.

In figure 6.3 the meshing of specimen BSC2 is depicted for reference. The light blue is the steel plate, while the purple is the GFRP plate

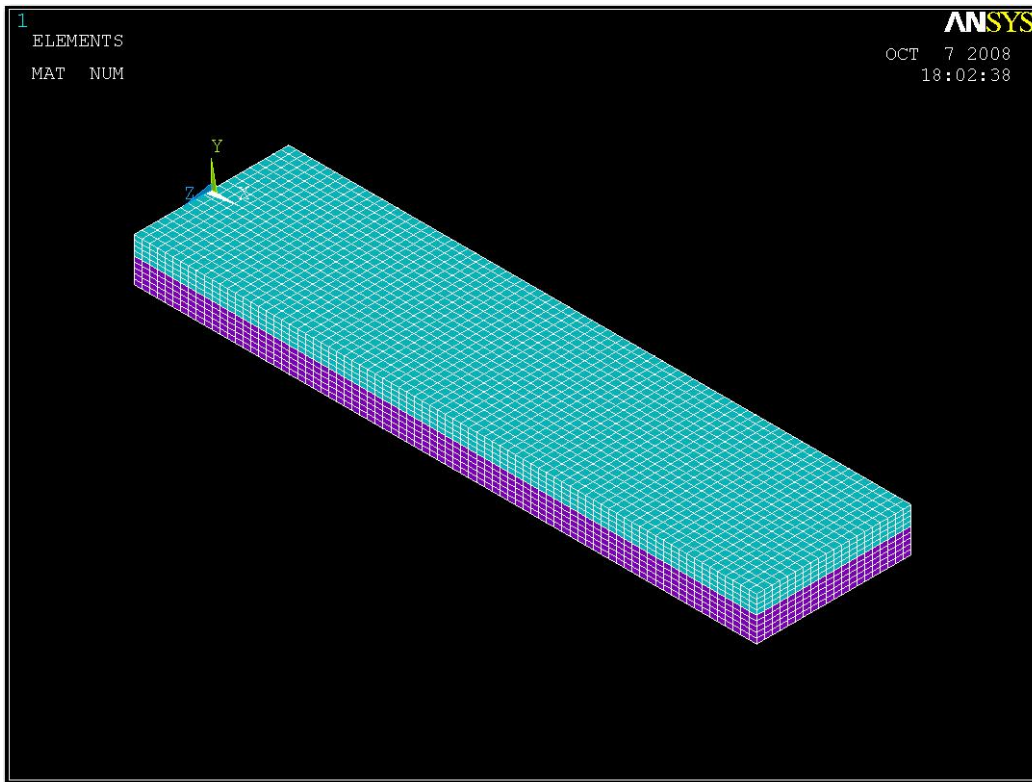


Figure 6.3 Finite element model

Restraints and applied loads

The loads and configuration used have already been described in paragraph 3.3. The only difference is that the loads are a little higher. That is due to the fact that in this case it is assumed that the load is applied directly on the upper surface of steel plate of the deck and not on the neutral axis of the steel. Therefore the load dispersal produces a uniformly distributed load per meter:

$$q' = \frac{w}{w + 2t_s} q = \frac{400}{400 + 2 \times 8} \times 150 \text{ kN/m} = 144.23 \text{ kN/m} \approx 144 \text{ kN/m}$$

The corresponding loads are $P = 20.6 \text{ kN}$ for specimens BSC2 and BSC3, $P = 14.4 \text{ kN}$ for specimen BSC4 and $P = 7.2 \text{ kN}$ for specimens BST1, BST2, BST3 and BST4. These loads were according to the configuration used following the exact same method of paragraph 3.3. The loads were applied on the nodes along the y direction.

As far as the restraints are concerned, the bottom two edges parallel to the y axis were restrained in the y and z direction. Also one of the two was also restrained in the x direction so as for the model to be statically determined.

Type of analysis

All the analysis were linear, except for the analysis of the un-strengthened steel plates that correspond to specimens BSC2, BSC3 and BSC4 that was non-linear. However the non-linear part of the analysis is of no interested in the particular thesis, since the purpose of the thesis is to determine the stress reduction factor and not sufficiency of the un strengthened steel deck. Therefore only the linear part will be used for that cause.

6.3 FEA and experimental results comparison

The results that are going to be presented are the normal stresses in the x direction (parallel to the longitudinal axis), since they are the only results that can be compared against the experimental ones. The normal stress – force diagrams that were presented in 4.4.3 are going to be reviewed again, but this time with the corresponding analysis results. Although the steel stresses are of immediate interest to us, the GFRP stresses are going to be presented as well as the error between the experimental data and the FEM analysis results both for the GFRP and the steel plate.

BSC2



Figure 6.4 Normal stresses – force diagram for the steel plate of specimen BSC2

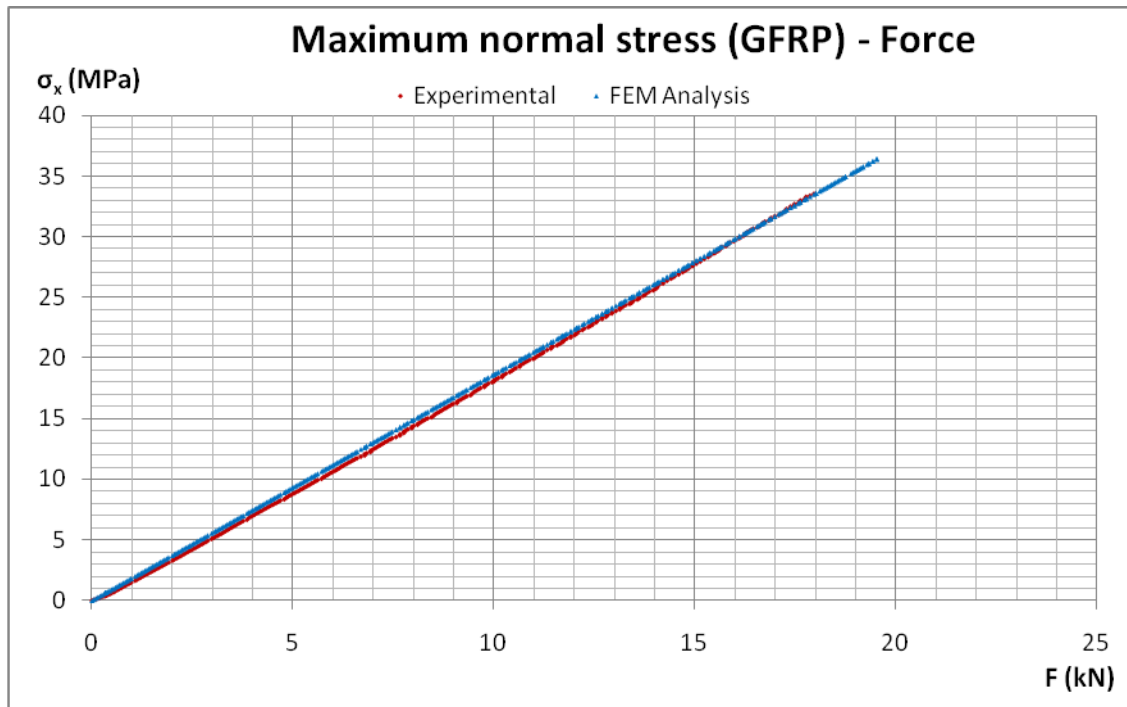


Figure 6.5 Normal stresses – force diagram for the GFRP plate of specimen BSC2

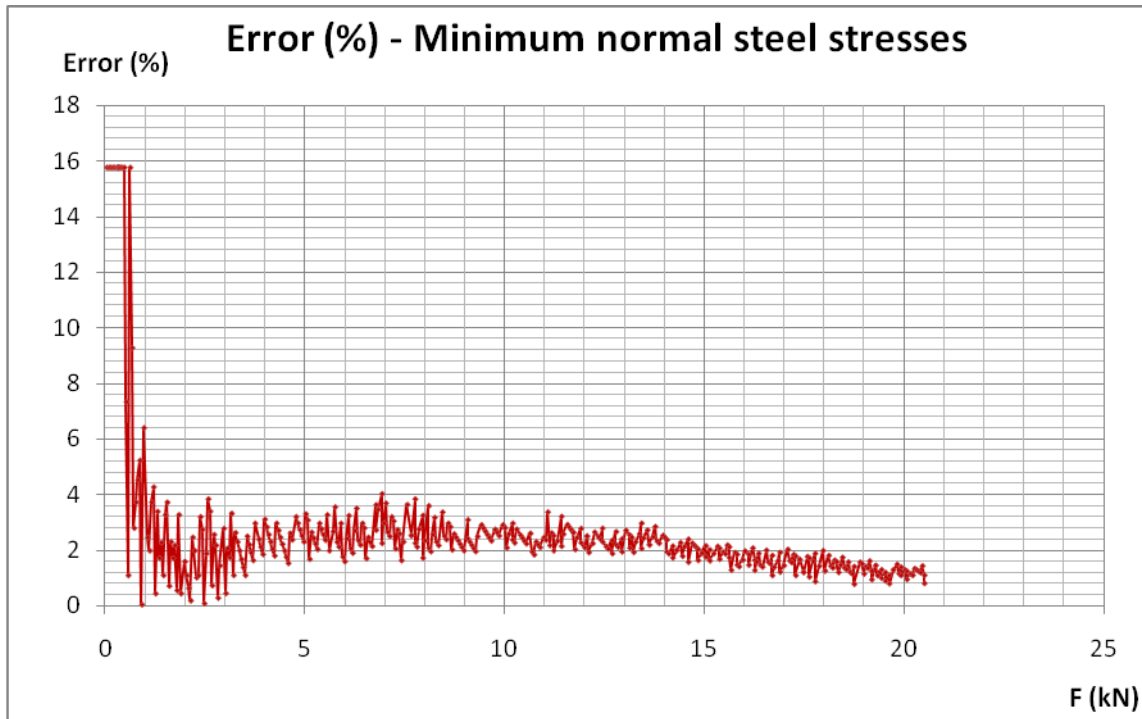


Figure 6.6 Error (%) – Force diagram for the minimum normal steel stresses of specimen BSC2

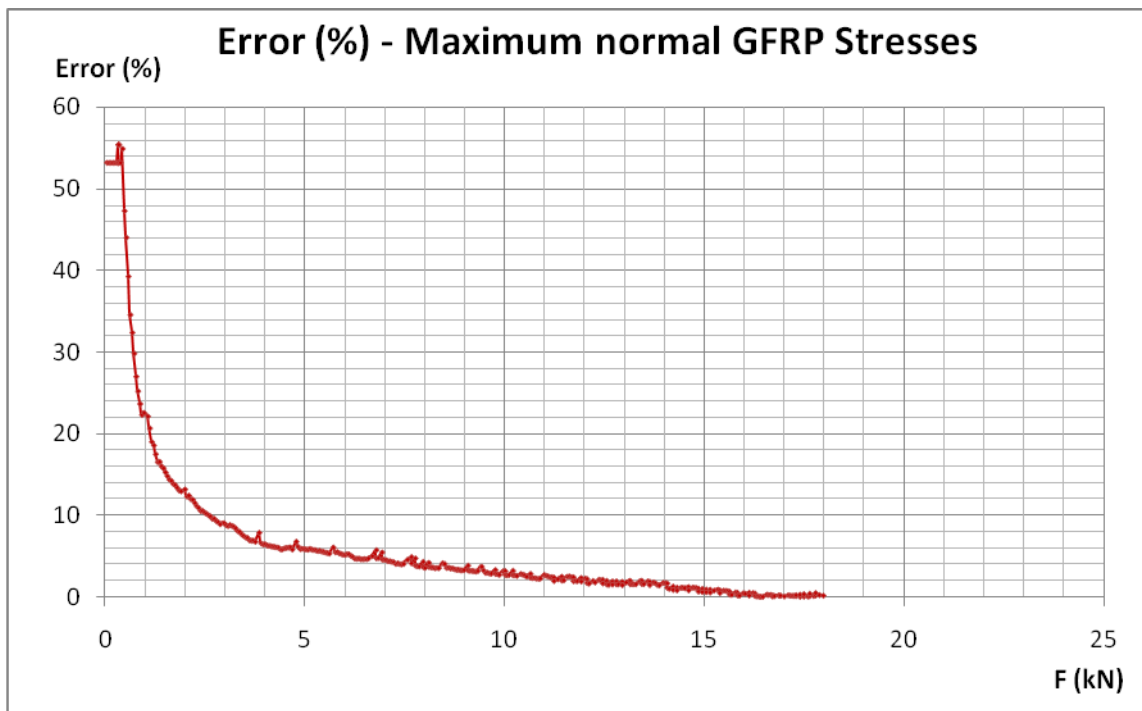


Figure 6.7 Error (%) – Force diagram for the maximum normal GFRP stresses of specimen BSC2

BSC3

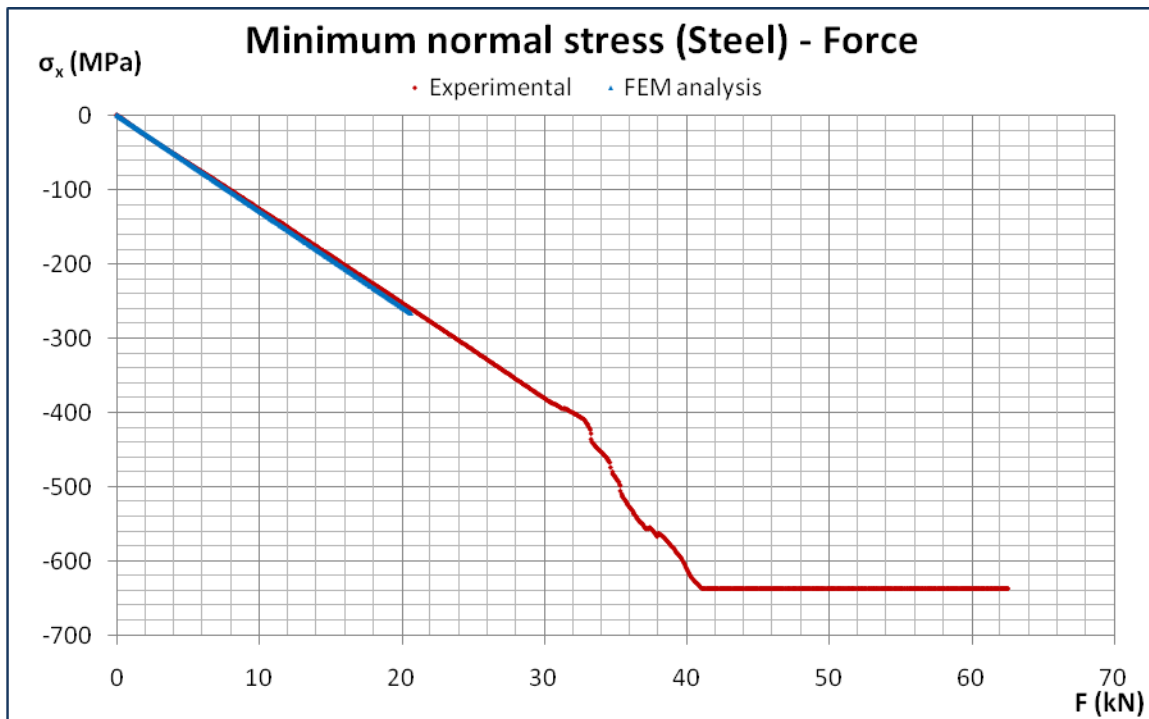


Figure 6.8 Normal stresses – force diagram for the steel plate of specimen BSC3

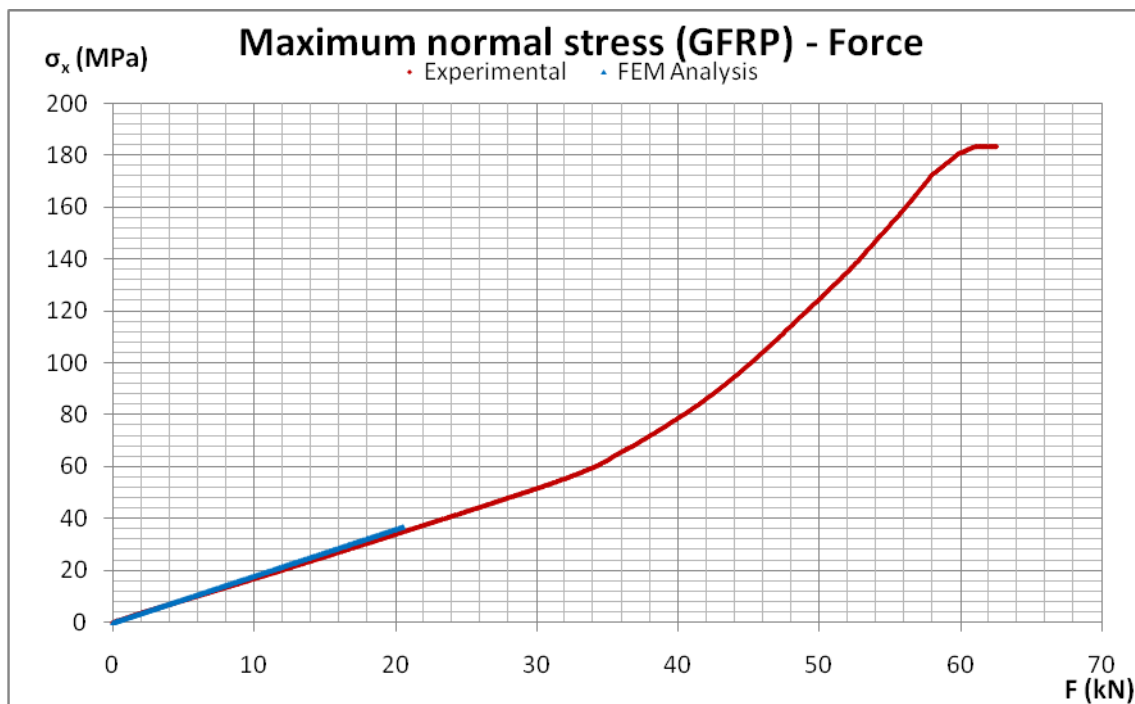


Figure 6.9 Normal stresses – force diagram for the GFRP plate of specimen BSC3

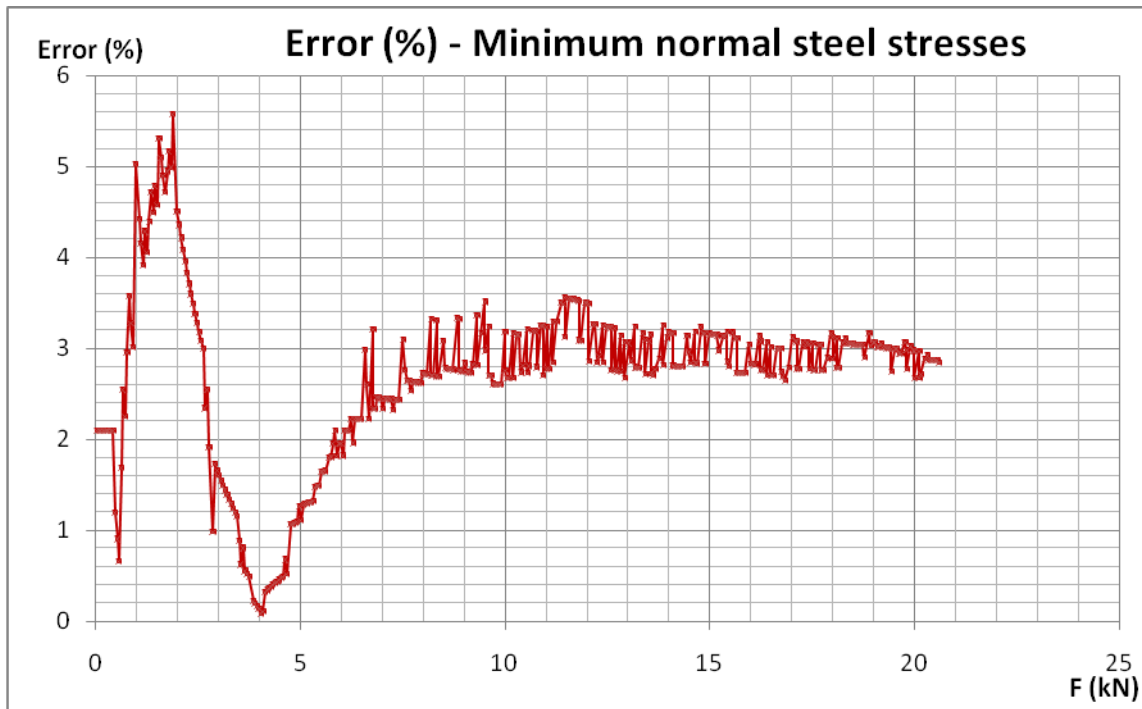


Figure 6.10 Error (%) – Force diagram for the minimum normal steel stresses of specimen BSC3

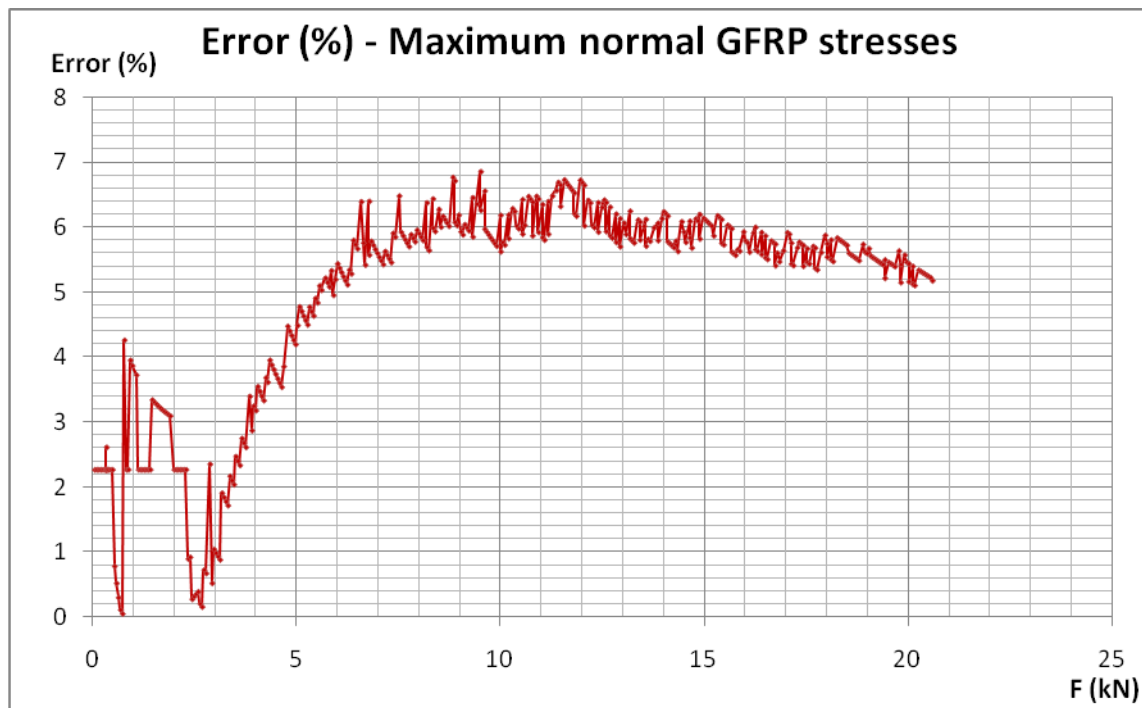


Figure 6.11 Error (%) – Force diagram for the maximum normal GFRP stresses of specimen BSC3

BSC4



Figure 6.12 Normal stresses – force diagram for the steel plate of specimen BSC4

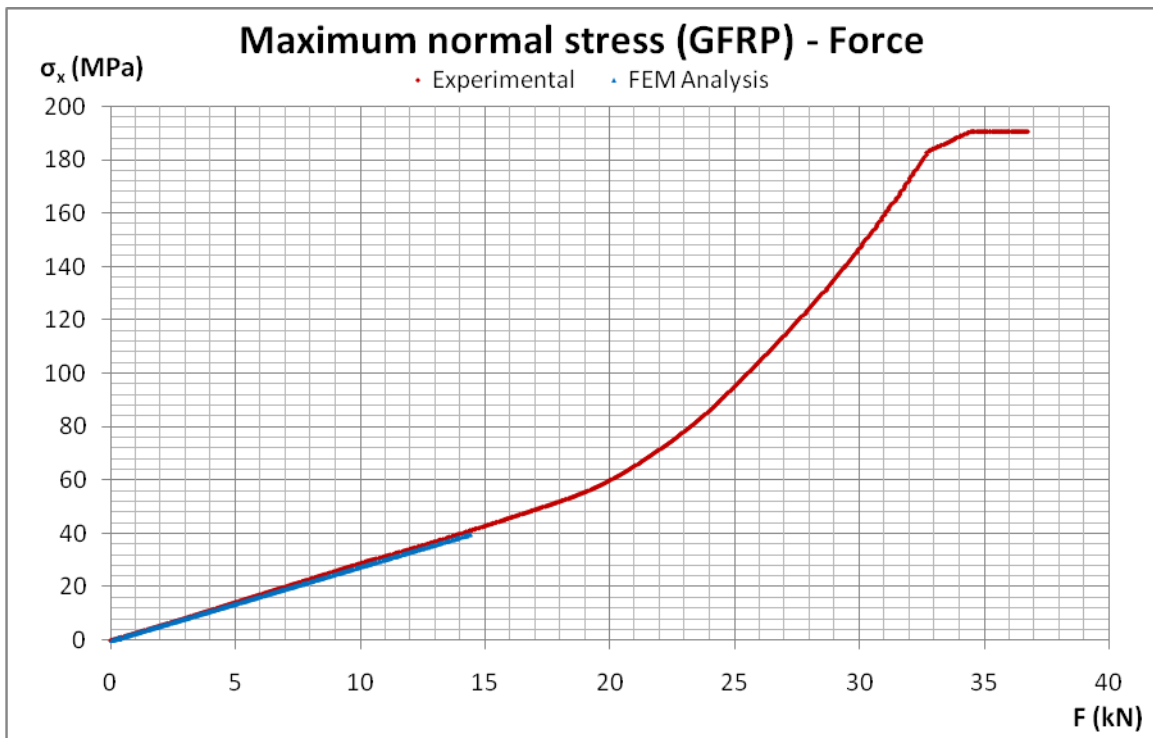


Figure 6.13 Normal stresses – force diagram for the GFRP plate of specimen BSC4

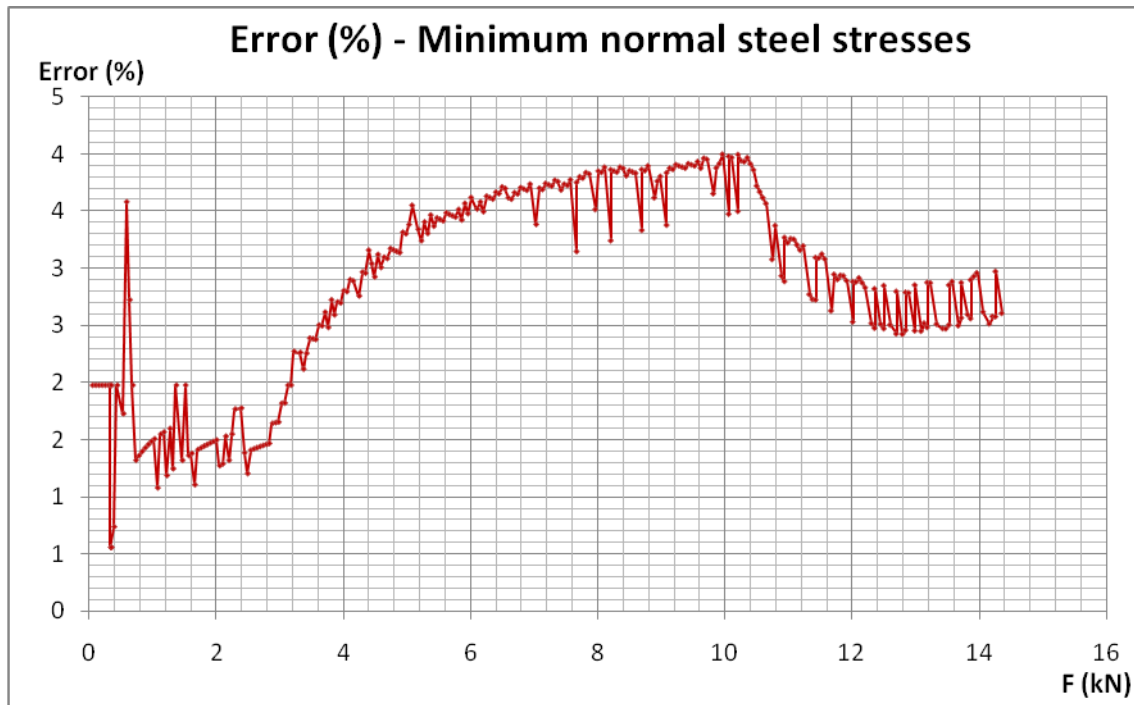


Figure 6.14 Error (%) – Force diagram for the minimum normal steel stresses of specimen BSC4

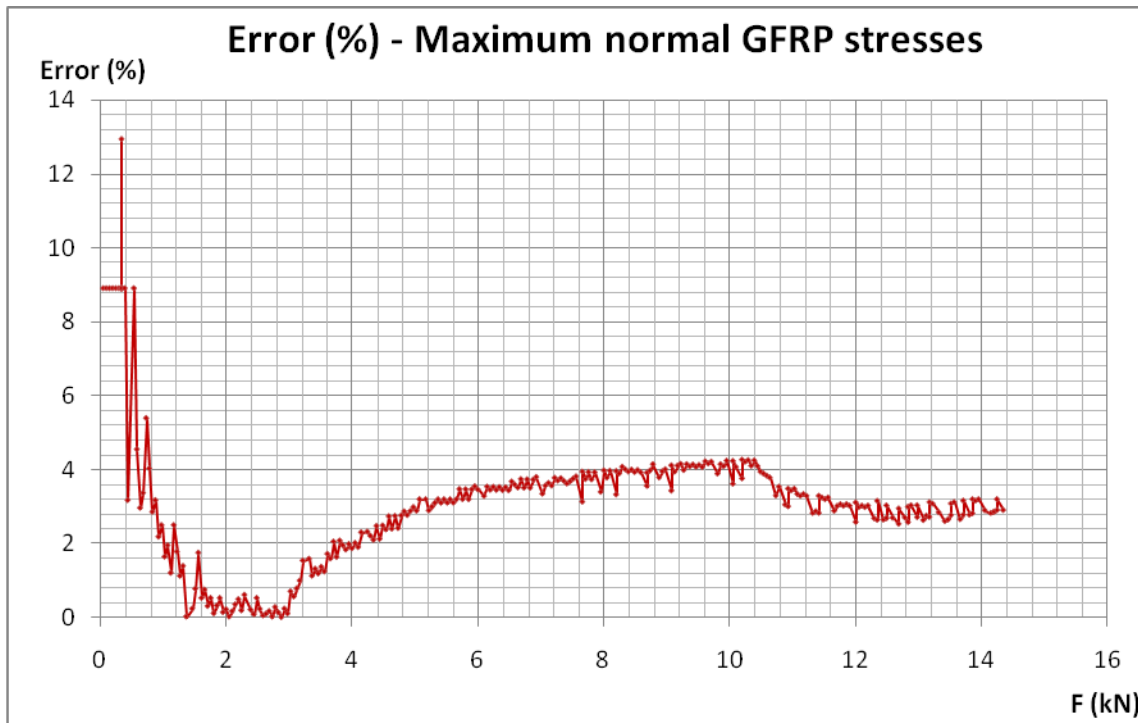


Figure 6.15 Error (%) – Force diagram for the maximum normal GFRP stresses of specimen BSC4

BST1

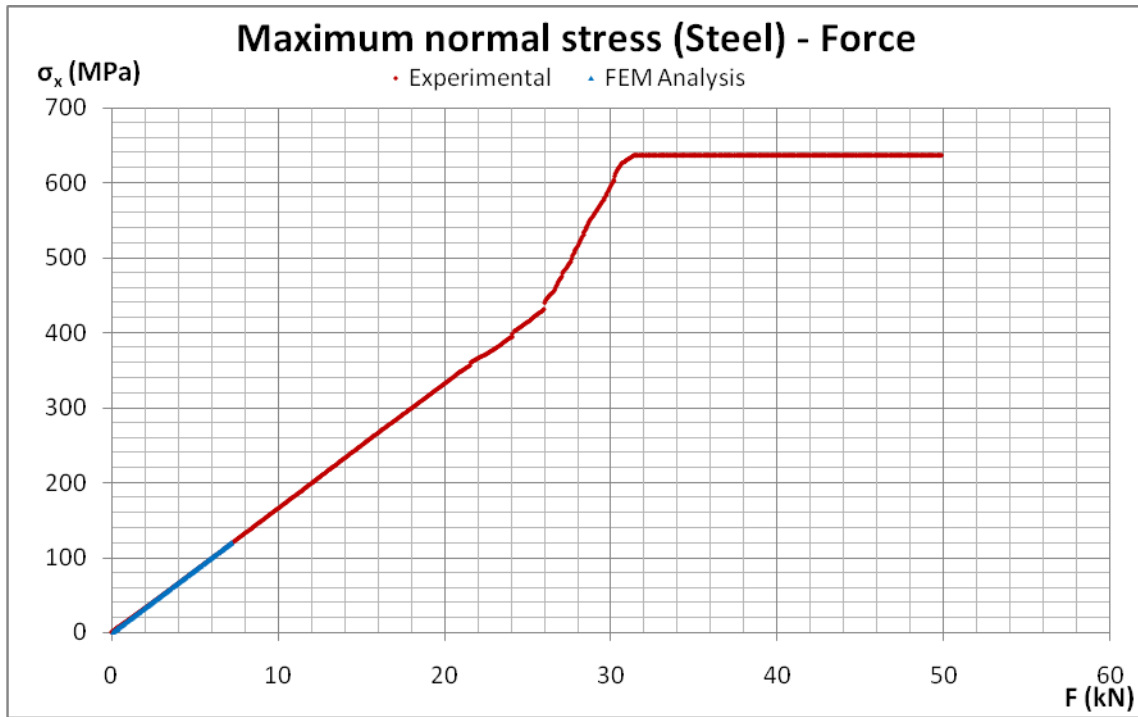


Figure 6.16 Normal stresses – force diagram for the steel plate of specimen BST1

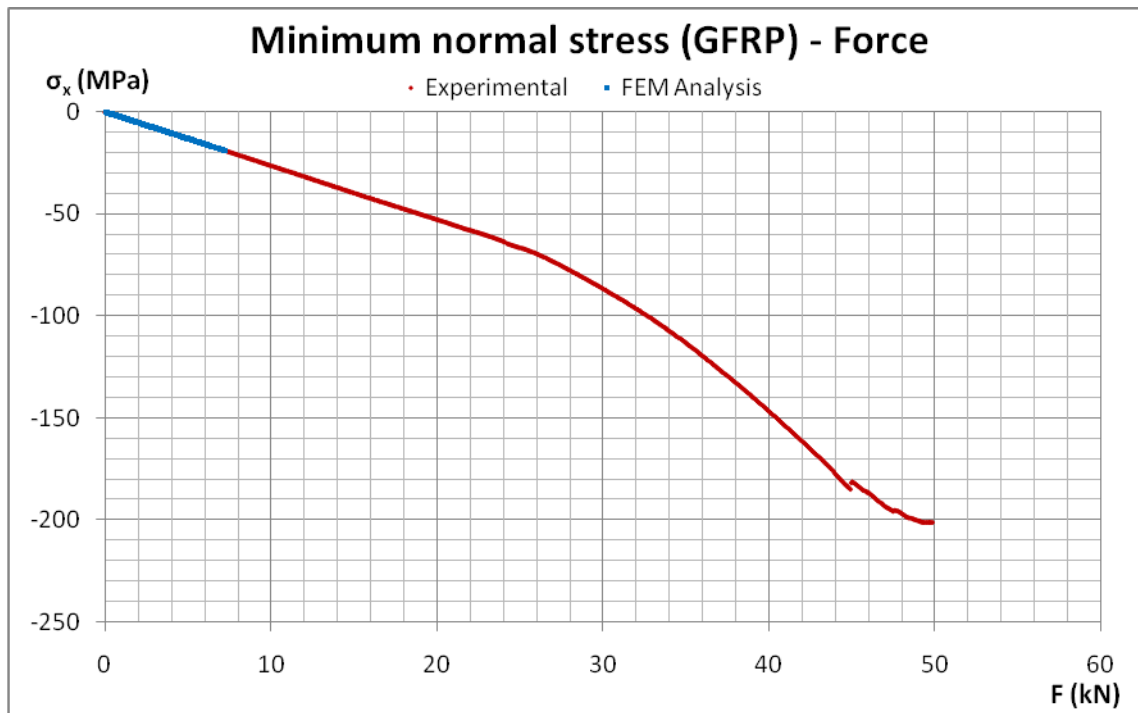


Figure 6.17 Normal stresses – force diagram for the GFRP plate of specimen BST1

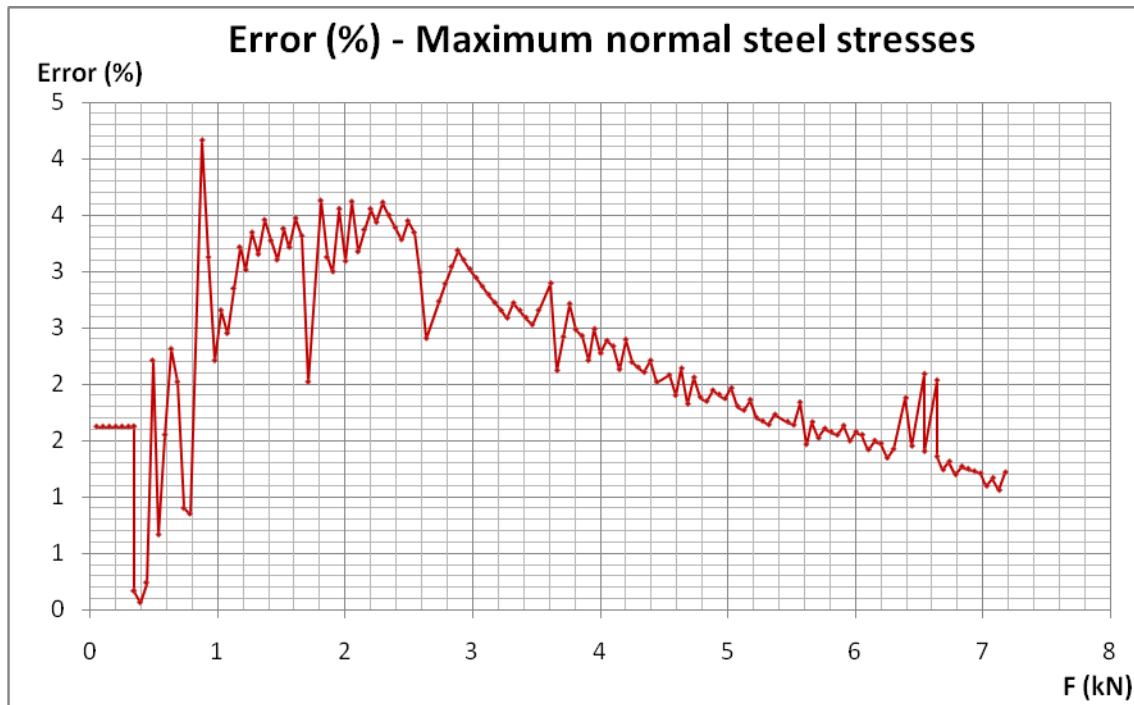


Figure 6.18 Error (%) – Force diagram for the maximum normal steel stresses of specimen BST1

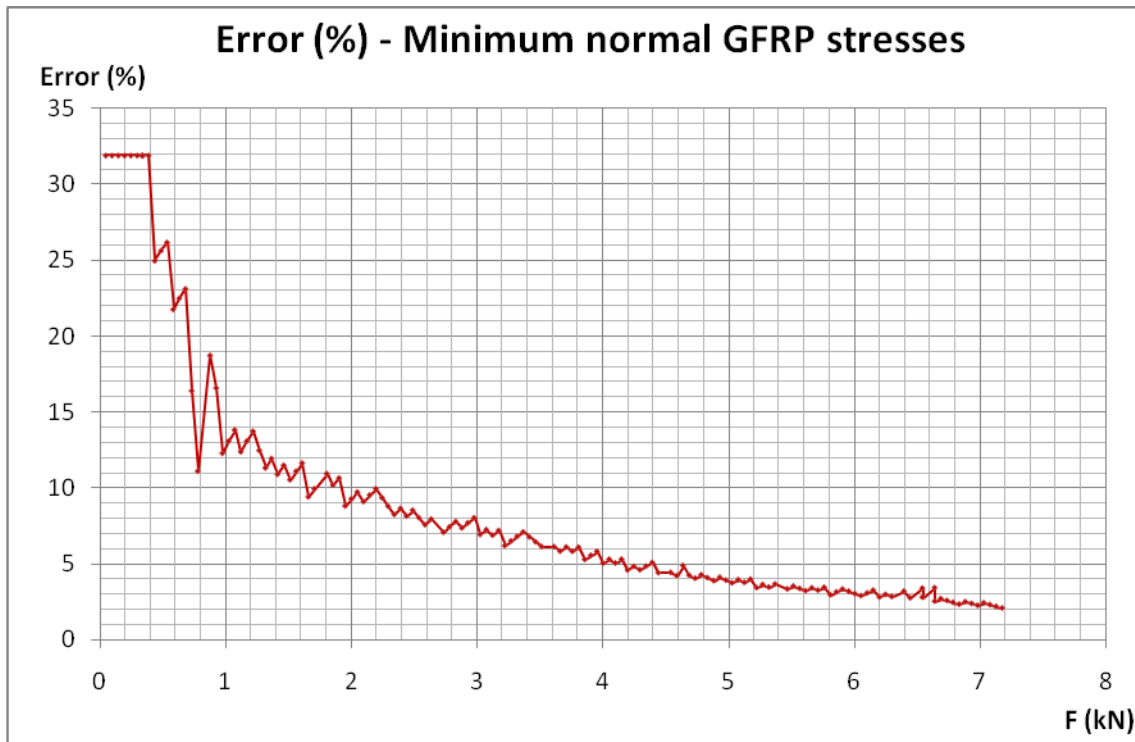


Figure 6.19 Error (%) – Force diagram for the minimum normal GFRP stresses of specimen BST1

BST2

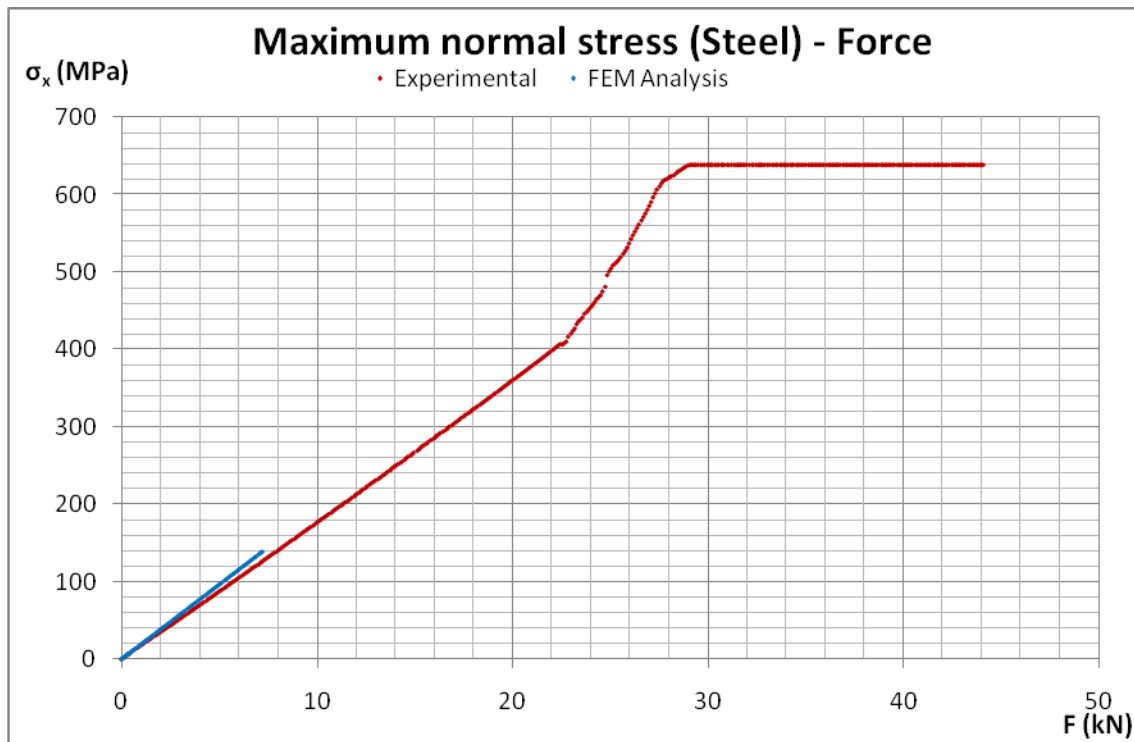


Figure 6.20 Normal stresses – force diagram for the steel plate of specimen BST2

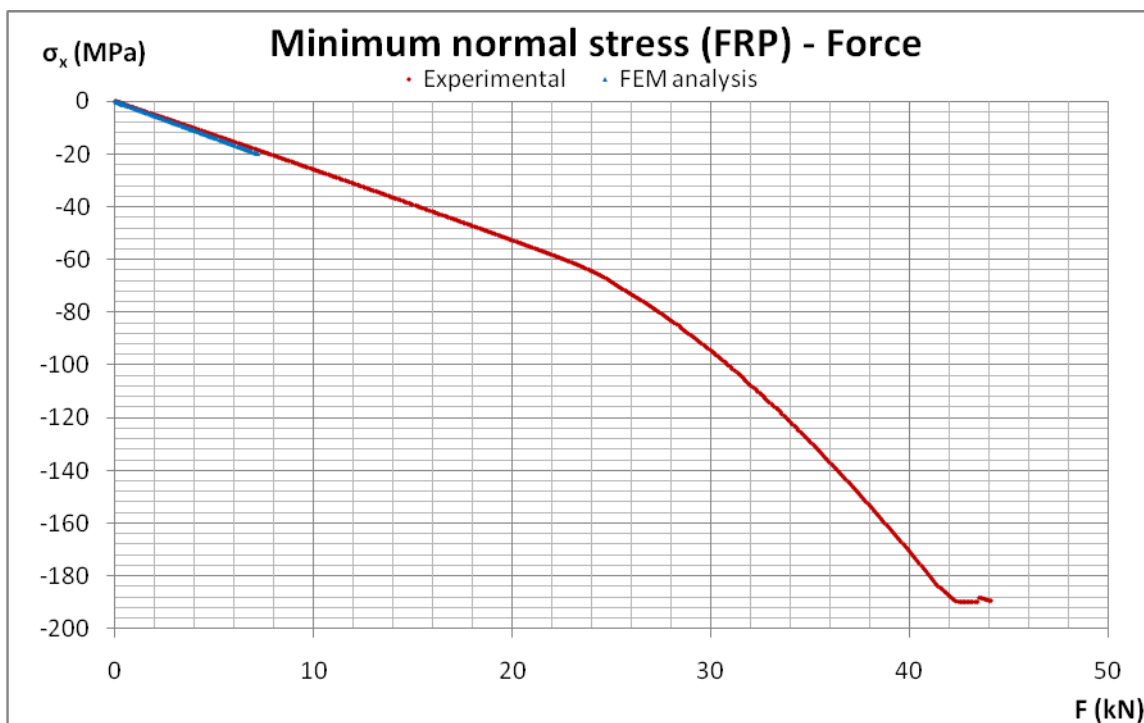


Figure 6.21 Normal stresses – force diagram for the GFRP plate of specimen BST2

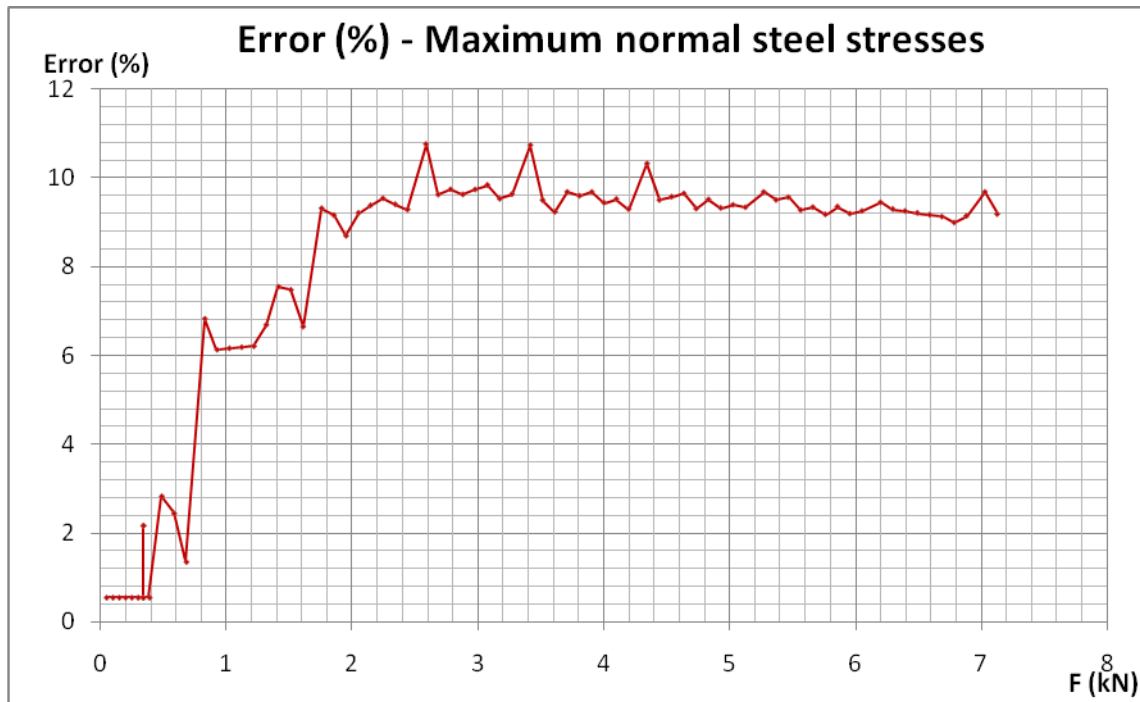


Figure 6.22 Error (%) – Force diagram for the maximum normal steel stresses of specimen BST2

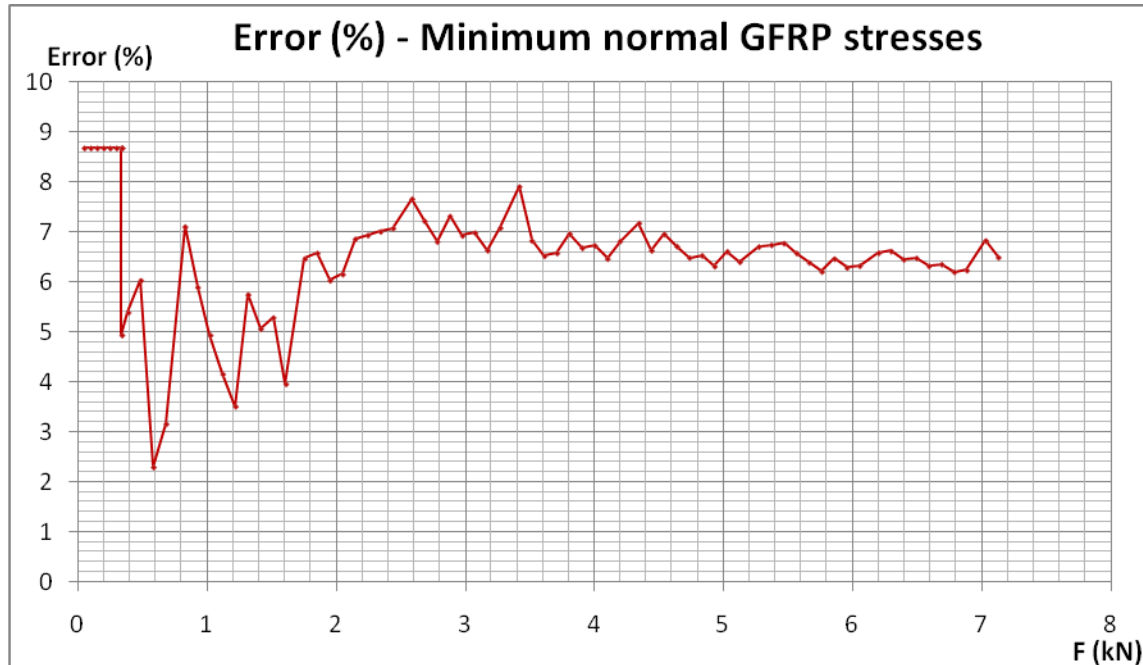


Figure 6.23 Error (%) – Force diagram for the minimum normal GFRP stresses of specimen BST2

BST3



Figure 6.24 Normal stresses – force diagram for the steel plate of specimen BST3

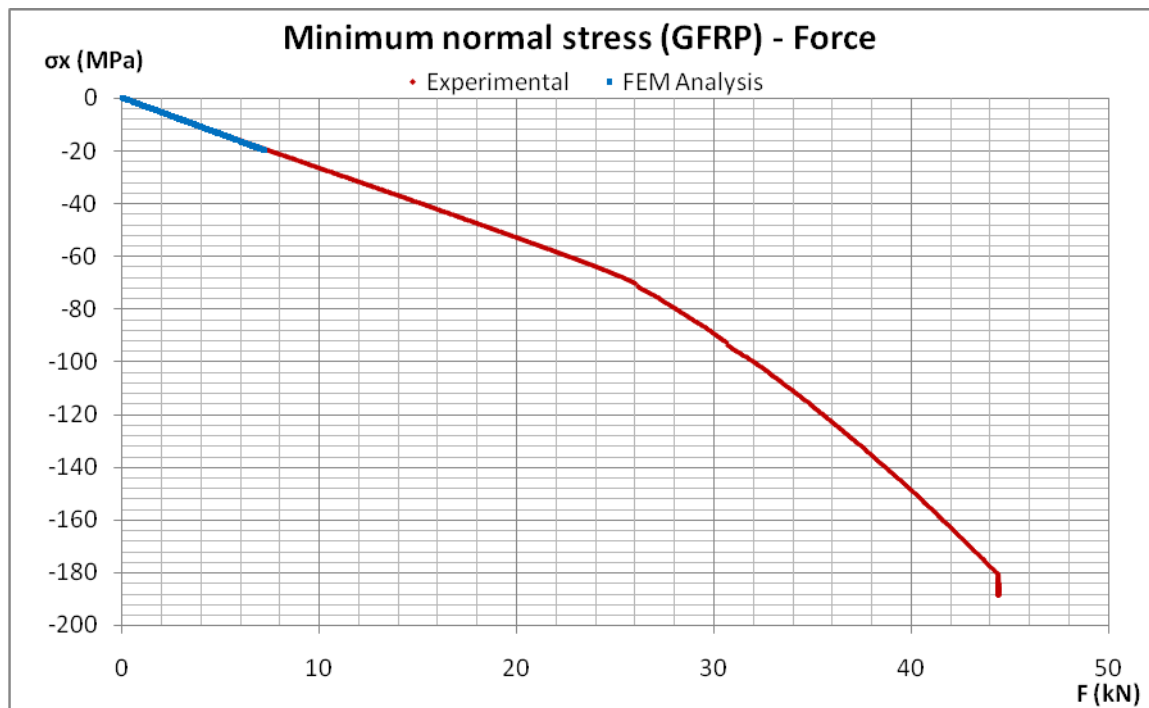


Figure 6.25 Normal stresses – force diagram for the GFRP plate of specimen BST3

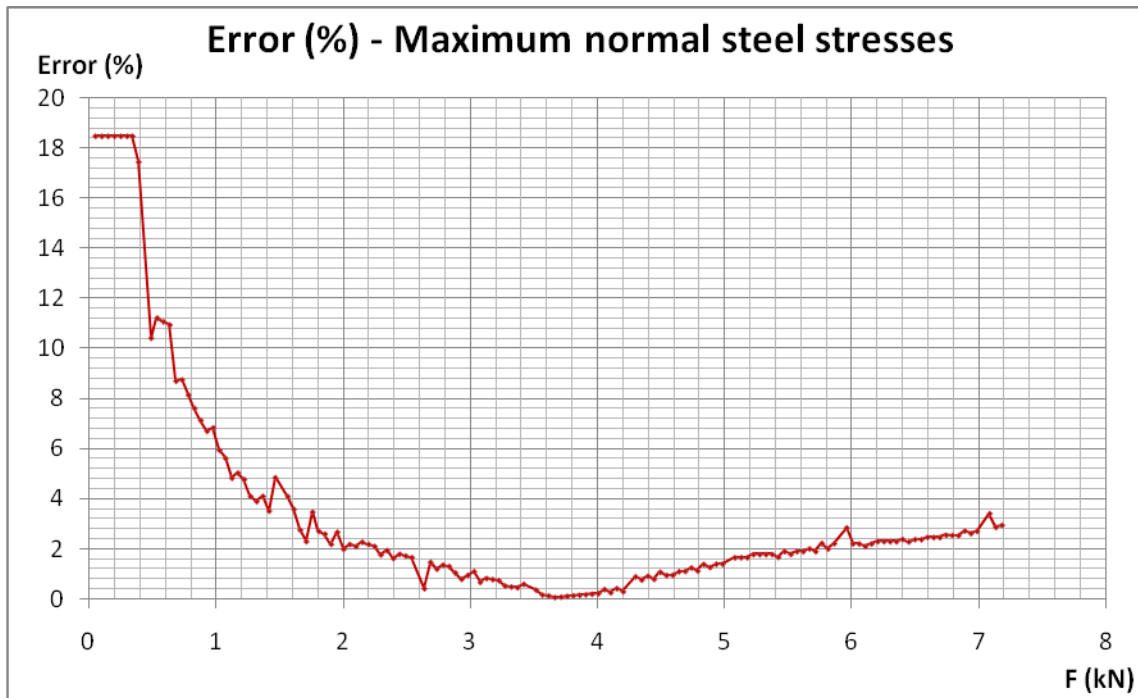


Figure 6.26 Error (%) – Force diagram for the maximum normal steel stresses of specimen BST3

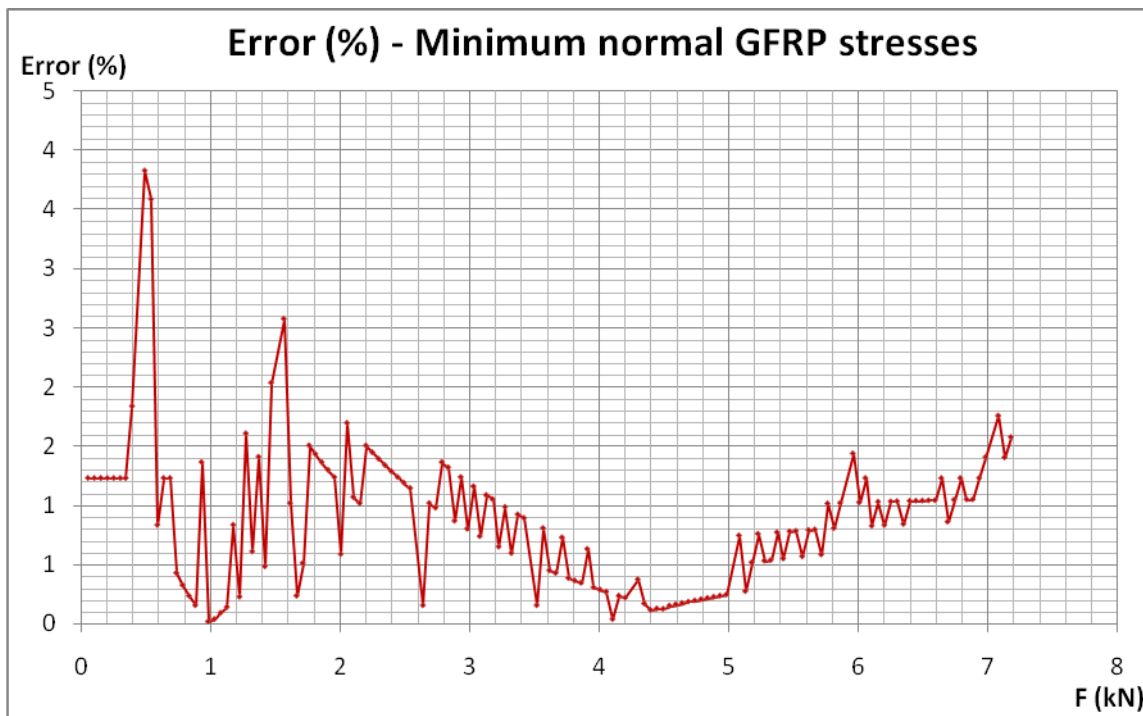


Figure 6.27 Error (%) – Force diagram for the minimum normal GFRP stresses of specimen BST3

BST4

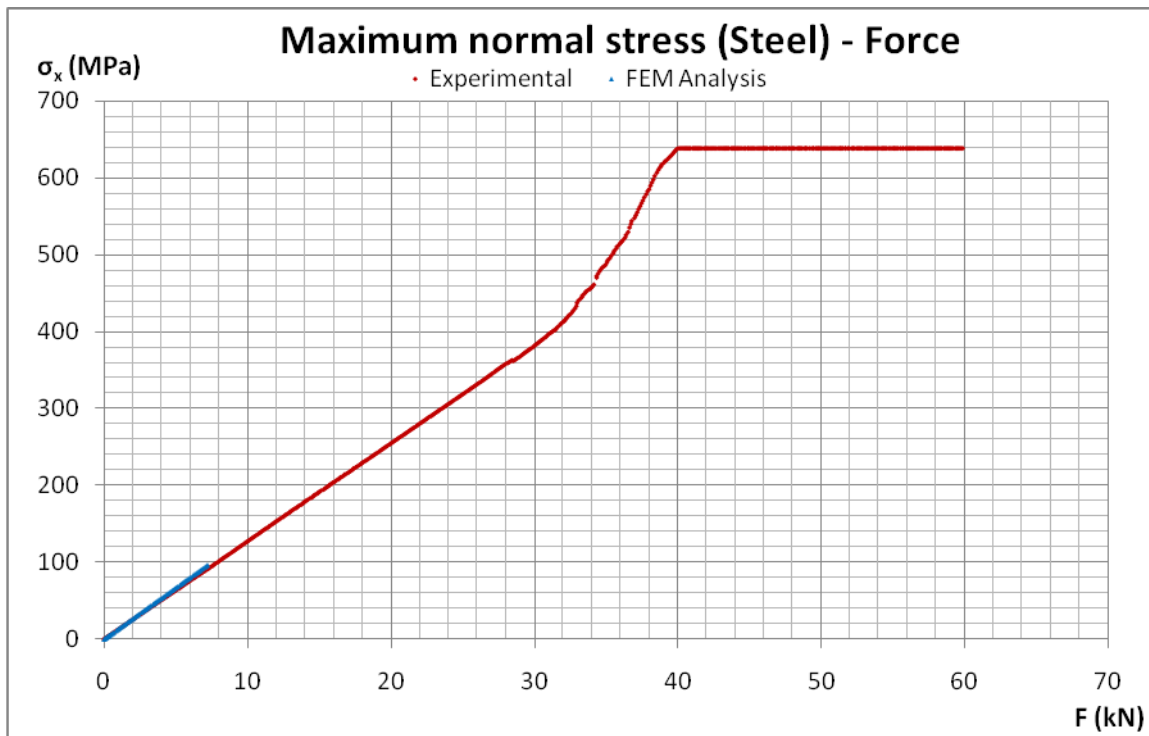


Figure 6.28 Normal stresses – force diagram for the steel plate of specimen BST4

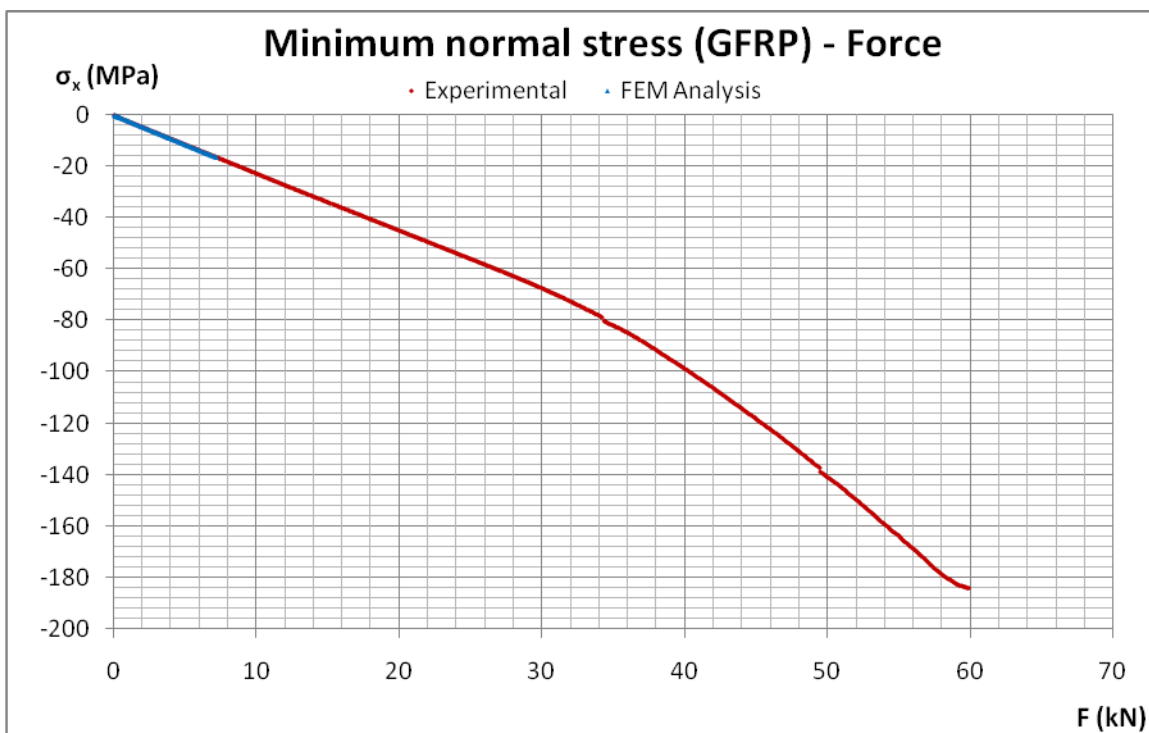


Figure 6.29 Normal stresses – force diagram for the GFRP plate of specimen BST4

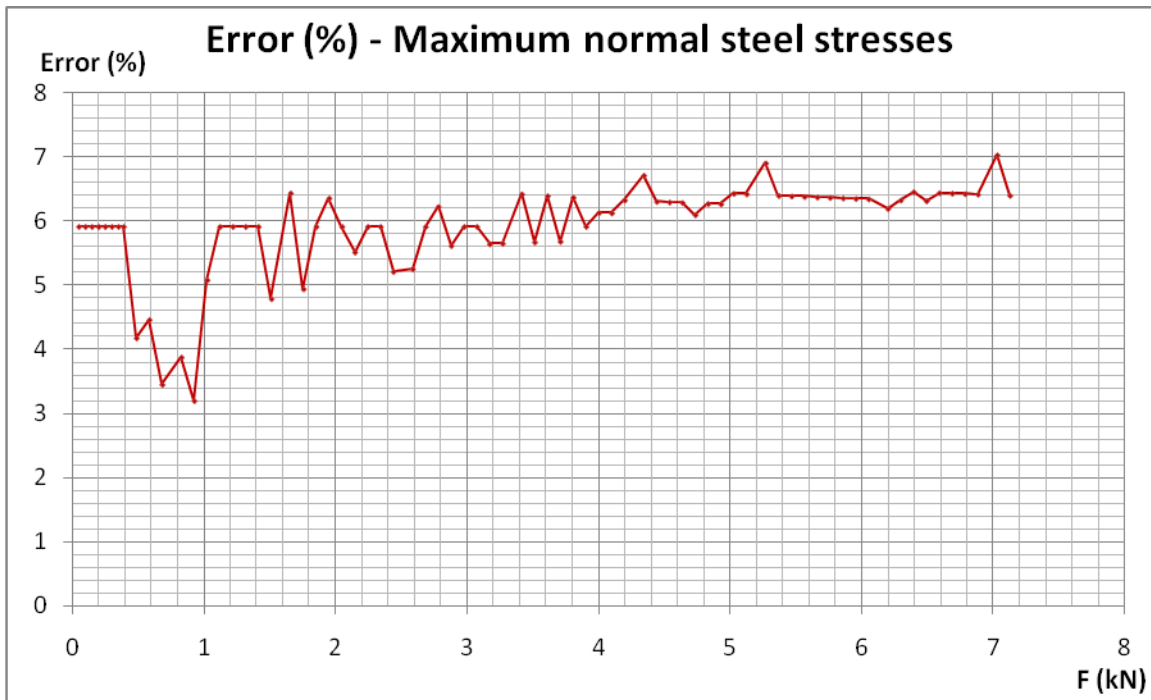


Figure 6.30 Error (%) – Force diagram for the maximum normal steel stresses of specimen BST4

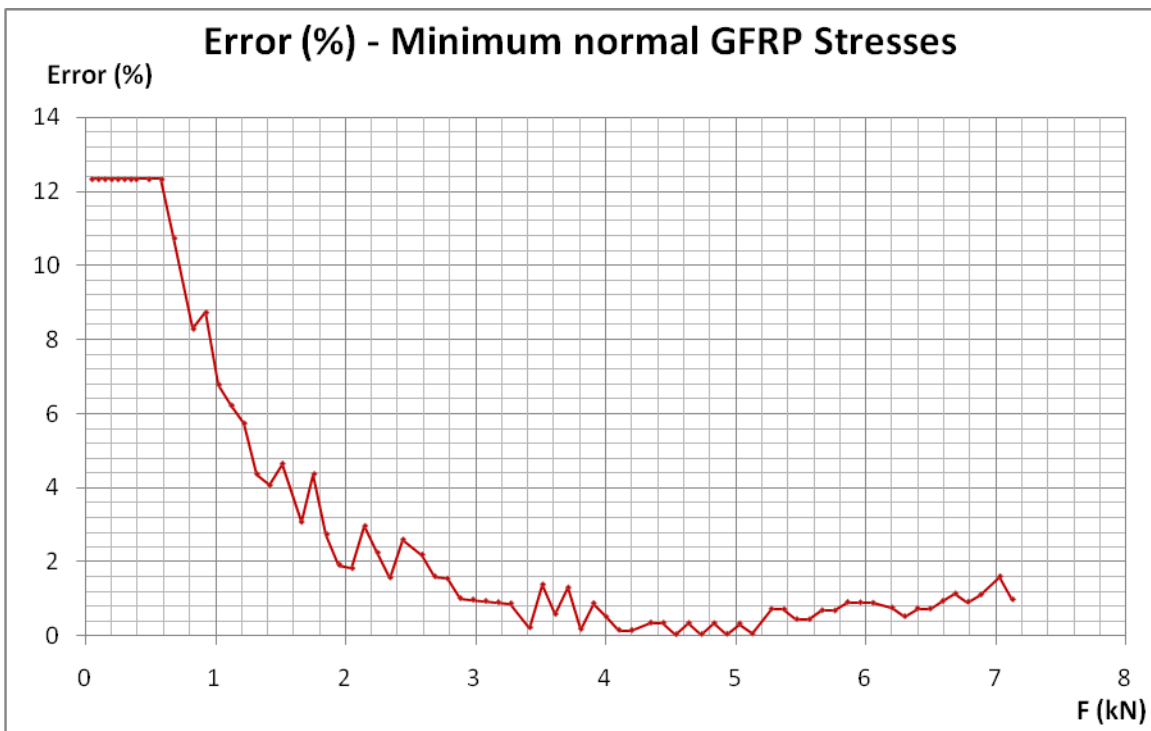


Figure 6.31 Error (%) – Force diagram for the minimum normal GFRP stresses of specimen BST4

Error (%)

As it can be seen, the analysis produced results very close the experimental. That means that the modelling was successful. The average error for each specimen can be found in the following table.

Table 5.12 Average Error (%)

Specimen	Error (%)	
	Steel stresses	GFRP stresses
BSC2	2.70	7.07
BSC3	2.68	4.94
BSC4	2.83	3.18
BST1	2.19	9.23
BST2	7.52	6.60
BST3	3.37	0.88
BST4	5.87	3.47

Now that the average error has been determined, the stress reduction factor (SRF) can be evaluated based on the experimental and the analysis data.

6.4 Stress reduction factor

The stress reduction factor is the ratio between the steel stresses of the un-strengthened steel plate and the strengthened steel plate.

$$SRF = \frac{\sigma_x \text{ in steel plate (un-strengthened steel plate)}}{\sigma_x \text{ in steel plate (strengthened plate)}}$$

The first were found from the FEM analysis, while the latter from both the experiments and the FEM analysis. The results are presented in the following table.

Table 5.13 Stress reduction factor

Specimen	SRF - Experimental	SRF - FEM
BSC2	2.05	2.00
BSC3	1.69	1.63
BSC4	1.45	1.50
BST1	1.92	1.90
BST2	1.83	1.68
BST3	1.92	1.86
BST4	2.47	2.32

Comments

The stress reduction is as low as expected (see 3.3.3) and in some cases even lower. However the material is not fully optimized. There are many parameters that can be altered in order to make it more efficient. For instance in the particular case, if the fibres of the woven rovings layer didn't have a 50%/50% distribution in the x, y direction but rather a 85%/15% in the x, y direction, then the efficiency of the material in that direction would be improved. The modulus of elasticity would become higher in the x direction with a subsequent fall in the y direction.

Furthermore another factor that would contribute to the improvement of the properties is the rise of the fibre volumetric fraction. To achieve this, the manufacturing method must be enhanced. A way is the vacuum assisted resin transfer moulding that can be applied with the hand lay-up method. With this method fibre volumetric fractions till 60% can be achieved. However a more realistic achievable value would be 40%. Combining these two the SRF would probably rise sufficiently. This is what it will be found in the next paragraph.

6.5 SRF improvement by material optimization

For the new configuration of the GFRP laminate, it has been assumed in the last paragraph that:

$$V_f = 0.40$$

$$V_m = 0.60$$

Assuming 50 woven roving layers with fibre orientation 85%/15% and 51 CSM layers and a 0.295 mm thickness layer we have a total laminate thickness of 29.8 mm and

everything that is needed to use the Bureau of Veritas method (see 5.3) to determine the mechanical properties of the laminate which are:

Table 5.14 Mechanical properties of the optimized GFRP laminate

E₁ (GPa)	E₂ (GPa)	E₃ (GPa)	G₁₂ (GPa)	G₂₃ (GPa)	G₃₁ (GPa)	v₁₂	v₂₃	v₁₃
21,699	13,335	6,483	4,264	1,944	1,944	0,255	0,306	0,287

A finite element analysis has been performed using these mechanical properties. The geometry of the specimen was the same as the BSC2 specimen geometry except for the GFRP laminate thickness which is increased to 29.8 mm. The number of elements used in the thickness direction of the GFRP was 10 with a total number of elements of 22400 and 98829 nodes. The load model that was used was configuration -1-. Analysis were made with the steel developing mainly tensile stresses and vice versa. As expected the results were almost the same. But the most important thing is the SRF which was the same in both cases. The calculated value was $SRF = 6.07$. This is a very impressive value, and in combination with the other very good properties of the GFRP plate, this configuration of material could make the entire solution very attractive.

7. CONCLUSIONS

In this chapter, the conclusions that were made based on the previous chapters will be presented.

A short review in what it was done will follow. In the first chapter the problem was described which was fatigue cracks in orthotropic steel bridge decks. The proposed solution was deck strengthening by the use of GFRP plates. Therefore, in the second chapter the materials, the properties and the manufacturing methods of FRP materials were reviewed.

In the third chapter, a simple preliminary analysis was performed, to evaluate the stress reduction factor that it was to be expected and to find out if it would be prudent to go on and perform the necessary experiments. Although the stress reduction factor of the steel stresses wasn't impressive, it was decided that the experiments should be performed, especially due to the fact that FRP is a material with excellent fatigue properties and also it can be further improved.

In the fourth chapter, the tests were presented. The tests that were performed were:

- Tensile tests on GFRP specimens
- Bending tests on GFRP plates
- Bending tests on steel plates reinforced by GFRP plates
- Fatigue tests on steel plates reinforced by GFRP plates
- Creep test on GFRP plate

From the tensile tests it was found that the modulus of elasticity of the GFRP (11.01 GPa) was very low in comparison to the steel, but still it was close to what it was expected. Nonetheless the interface layer proved to be very resilient and the GFRP's very good fatigue properties were verified.

In the fifth chapter the material properties were determined. For this a number of burn-out tests were performed and the bureau of veritas method was utilized for the determination of the material properties, making the assumption that it is a liner elastic orthotropic material. Comparing the theoretical Young's modulus in the x direction and the one that was found from the experiments, it became evident that the method is very accurate.

In the sixth chapter a finite element analysis was performed using the analysis software ANSYS. The models used had the same geometry as the specimens. The normal stresses parallel to the longitudinal direction from the analysis and the experiments were compared and the error was derived. In all the cases the error was sufficiently low; low enough to convince us that the finite element model and the analysis were successful. Based on that fact a rough optimization of the material was attempted. The fibre volumetric

fraction of the GFRP laminate was increased to a 40% using the vacuum assisted resin transfer moulding (VARTM) method. Furthermore, since the strengthening of the steel deck for the specific case was in the transverse direction, meaning in the longitudinal direction of the specimens, the fibre orientation was changed from 50%/50% to 85%/15%. The stress reduction factor that was achieved this way was a rather impressive 6.07. Combined with the excellent fatigue properties of the material, it makes the solution rather attractive. However, there is the financial issue as well. Therefore, a cost analysis must be performed, in order to find out how financially feasible the solution is. The financial analysis is out of the scope of this thesis and it will be left to future researchers.

REFERENCES

Lawrence C. Bank, 2006, Composites for construction: Structural design with FRP materials, John Wiley & Sons, Inc.

Advanced polymer composites for structural applications in construction, edited by R. A. Shenoi, S. S. J. Moy, L. C. Hollaway, 2002, Thomas Telford Publishing.

Thanasis C. Triantafillou, 2006, Strengthening and seismic retrofitting of concrete and masonry structures with composites, University of Patras.

Erdogan Madenci, Ibrahim Guven, 2006, The finite element method and applications in engineering using ANSYS, Springer Science & Business media.

F. B. P. De Jong, 2007, Renovation techniques for fatigue cracked orthotropic steel bridge decks, TUDelft.

Yang YuGuang, 2007, Bending behaviour of a high performance concrete overlay on an orthotropic steel deck, TUDelft.

Dr. A. Romeijn, 2006, Fatigue, TUDelft

M. H. Kolstein, 2003, Fatigue, TUDelft

J.G. Teng, J.F. Chen, S.T. Smith, L. Lam, 2002, FRP-strengthened RC Structures, John Wiley & Sons, LTD.

Markku Hentinen, Martin Hilderbrand, Maunu Visuri, 1997, Adhesively bonded joints between FRP sandwich and metal, Technical research centre of Finland.

2001, FRP composites – Life extension and strengthening of metallic structures, Thomas Telford

Deric John Oehlers, Rudolf Seracino, 2004, Design of FRP and steel plated RC Structures, Elsevier.

Structural analysis of laminate composites, James M. Whitney, Technomic Pub Co, 1987

Engineering mechanics of composite materials, Isaac M. Daniel, Ori Ishai, Oxford University Press, Usa, 2005

S. Koussios AE4-684 Lecture notes

Dr. A. Romeijn, 2006, Steel bridges, TUDelft

Bureau of Veritas, Rules for Yachts 2008, General requirements and Application Pt B, Ch12, Sec 3.

ASTM standards, Designation D 3039 – 76 “Standard test method for tensile properties of fibre-resin composites”.